DNA Programmed Assembly of Active Matter at the Micro and Nano Scales

Ibon Santiago González
St Catherine's College
University of Oxford

A thesis submitted for the degree of
Doctor of Philosophy
Trinity Term 2017

DNA Programmed Assembly of Active Matter at the Micro and Nano Scales

Ibon Santiago González

St Catherine's College, University of Oxford

Doctor of Philosophy, Trinity Term 2017

Abstract

Small devices capable of self-propulsion have potential application in areas of nanoscience where autonomous locomotion and programmability are needed. The specific base-pairing interactions that arise from DNA hybridisation permit the programmed assembly of matter and also the creation of controllable dynamical systems. The aim of this thesis is to use the tools of DNA nanotechnology to design synthetic active matter at the micro and nano scales.

In the first section, DNA was used as an active medium capable of transporting information faster than diffusion in the form of chemical waves. DNA waves were generated experimentally using a DNA autocatalytic reaction in a microfluidic channel. The propagation velocity of DNA chemical waves was slowed down by creating concentration gradients that changed the reaction kinetics in space.

The second section details the synthesis of chemically-propelled particles and the use of DNA as a "programmable glue" to mediate their interactions. Janus micromotors were fabricated by physical vapour deposition and a wet-chemical approach was demonstrated to synthesise asymmetrical catalytic Pt-Au nanoparticles that function as nanomotors. Dynamic light scattering measurements showed nanomotor activity that depends on H_2O_2 concentration, consistent with chemical propulsion. Gold nanoparticles/Origami hybrids were assembled in 2D lattices of different symmetries arranged by DNA linkers.

The third section details the design process and synthesis of nanomotors using DNA as a structural scaffold. 3D DNA Origami rectangular prisms were functionalised site-specifically with bioconjugated catalysts, i.e. Pt nanoparticles and catalase. Enzymatic nanomotors were also conjugated to various cargoes and their motor activity was demonstrated by Fluorescence Correlation Spectroscopy.

In the final section, control mechanisms for autonomous nanomotors are studied, which includes the conformational change of DNA aptamers in response to chemical signals, as well as a design for an adaptive dynamical system based on DNA/enzyme reaction networks.

Thesis Supervisor: Prof. Andrew J. Turberfield

Amama Clara eta Izeko Mari Carmen gogoan
Familia eta lagun maiteei eskeinia
bihotzetik bihotzera.

– –

Lehenik Aitari,
gero Amari
gero nire arrebari
t'azken orduan ixil-ixilik
nire Lulu politari.

'Au milieu de l'hiver, j'apprenais enfin qu'il y avait en moi un été invincible.'

ALBERT CAMUS, *Retour à Tipasa* (1952)

Bekoak goikoa ezkondu leidi,
ta txikiak handia benzi leidi,
asmoz ta jakitez.

i' vidi de le cose belle che porta 'l ciel,
per un pertugio tondo.
E quindi uscimmo a riveder le stelle.

DANTE, *La Divina Commedia* (Canto XXXIV)

Acknowledgements

Just like active matter, this thesis could only exist thanks to the input of energy, love and enthusiasm of many people, whom I would like to thank in the following lines.

First, I want to thank my incredible family, who have accompanied me on this journey (in the distance), all the way from Bilbao to Boston and now in Oxford. We have a long word to say this: *Eskerrik asko*. To my *Aita* Josu, who has been a constant support and a lighthouse in moments where my ship was lost. As it happens, marine biology is not that far from physics, and he has been an invaluable help in many aspects of this work and much more. To my *Ama* Amalia, whose love and energy are a constant driving force in anything I do. I thank her for teaching me the beauty of biology and for nourishing my passion for science. To my sister Jone, who became a real Doctor before me, I thank her for showing me the right way to do things and for always being there. In the loving memory of my grandmother *Amama* Clara and aunt Mari Carmen, who passed away while my time in Oxford, I would like to thank them for their love and support, and for the endless hours I spent in their bookstore, which contributed to my scientific curiosity. To them, *nire sendiari*, to my family, I dedicate this thesis.

I wish to thank my supervisor Andrew Turberfield for giving me the opportunity to work on this project in his laboratory. When I arrived, he promised exciting science and so it has been! I want to thank Andrew for his insightful comments, for the constructive feedback he has given me in the many discussion we had and for reading this thesis thoroughly. I thank him for the freedom he gave me and for helping me become a better scientist. His rigour and commitment to excellent science is something I value, and I am grateful for. Eskerrik asko, Andrew.

I thank the Basque Government and its Ministry of Education, Culture and Science for a doctoral scholarship that helped fund this research. I also thank other funding bodies, like the EPSRC, the Institute of Physics and St Catherine's College for financial support.

Over the years at Oxford, I had the good fortune to learn from and the pleasure to work with an exceptional group of people. There is no way I can fully express my gratitude in writing, but I will attempt to do so.

To my estimado compañero Jon Bath, heart and soul of the lab, I thank him for introducing me to the lab, for teaching me the fundamentals of DNA nanotech (including how to use a pipette) and for his generous help. Jon was at the inception of this project and his input has been very valuable throughout all my DPhil. He has been a great mentor and friend, capable of answering the most complicated molecular biology question in Spanish with a very funny uruguayan accent. Eskerrik asko, Jon!

I would like to thank Robert Schreiber for teaching me (almost) all the secrets of DNA Origami. He brought to the lab so many skills, and was generous and patient to share them with everyone. He is a talented scientist, teacher and great friend. It has been a joy to work with him on the nanoflower project. His enthusiasm for what he does is contagious, be it a new plasmonic project or an infamous lab clean-up day he so eagerly organised. Vielen Dank Robert!

I thank Antonio Garcia Guerra who provided many good ideas, biscuits and a wealth of biological knowledge. I cherish all the really bad (very good) jokes he has shared with me and I thank him for believing in this work. I thank Celine Journout for her enthusiasm and interesting science questions. The lab could not work without Natalie Haley and her expertise in every single apparatus. I thank her for our joint efforts with the microscope and for her tips about AFM. Many thanks to Wenjing Meng, the queen of chemistry, Florence Benn, my DPhil buddy, Mike Boemo, Alex Lucas, Juan Jin, Adam Wollman, Robert Machinek, Sam Tusk, Joel Spratt and the many DNA group members I have interacted with throughout these years. In the wider department, thanks to Maabur Sow and Anne Plochowietz.

I want to acknowledge all those who contributed to this research. To Achillefs Kapanidis and his group for letting me use their Snowdon microscope and shape it into an FCS setup, to Errin Johnson for running the best TEM facility (in the world?), to Neil Young for his help with STEM-EDX, to David Staunton for letting me use the DLS apparatus indefinitely, to Dirk Aarts for help with Janus particles, to Luisa Kneer for a wonderful month of joint exploration of DNA aptamers. Within the department, I thank Sonia Contera, Richard Berry and Sonia Trigueros for valuable discussions about physics and science in general.

Many thanks to John Foord, for his invaluable advice and encouragement throughout the last stages of this work. Several chemistry experiments in this thesis would have impossible without his support. I thank him for his interest in this work and for allowing me to develop it to its fullest.

Science is a global enterprise and I have been lucky to interact with many professionals who have helped me throughout this work. I would like to thank André Estévez-Torres for introducing me to DNA waves and for giving me the opportunity to tinker in his lab while learning so much about out-of-equilibrium phenomena with DNA. This would have been impossible without the help and enthusiasm of Anton Zadorin, who took the time to show me the experimental techniques relevant to this work with thorough detail. Many thanks to Jean-Christophe Galas for the hours in the machine shop and advice and to Adrian Zambrano and Jonathan Lee for allowing me to bother them in the lab with questions and steal their pipettes. I thank Georg Urtel for the work on wave localisation we did together, which I hope can continue at some point. Merci a tous!

Thanks to Pierre de Buyl, for his patience teaching me secrets of Python and the wonders of multiparticle collision dynamics. I thank Ayusman Sen, Ubaldo Figueroa, Raymond Kapral, Ramin Golestanian, Tung-Chun Lee and Franscesc Sagues for helpful discussions at different stages of this project. I also thank Mark Bathe, for showing me for the first time what one could do with nucleic acids and Jeff Gore for giving me the journey of Biophysics.

Part of the Oxford experience has definitely been the people I have met in this interesting city. I want to thank my flatmates Valentina Di Stasio, Marisa Storm, Jenny Shurville, Michael Hutchinson and Hanne Wouters, for making my life in Oxford more enjoyable. I praise my students at Hertford College for letting me share with them a passion for Physics and the wonders of Statistical Mechanics.

I want to remember and thank my friends who have been a source of inspiration and who have been there for me when I needed it. To Shamim (now Professor Nemati), for his help in all things MATLAB, for reminding me to be careful with Kafka's cat, to attach value to things and to be large, containing multitudes. "I did it my way". Kheyli mamnun! To my Olympic friends, Wieland Staessens, Claudio Geuna and Davide Scaini, for being there to help me see the stars again. To Ignacio Vazquez, for many good conversations and endless interest in all things science. To Roberto Galvan for joining me in a Synthetic Biology adventure in Germany. To Hasan Gökce for his friendship and love of Opera. To Igor Bragado because we care about Ithaka, even though we are lost somewhere in Troy. To Luismi Vicente, for his infinite curiosity in what I have been doing all these years.

And my biggest Eskerrik Asko, goes to my partner Luyun Jiang. I thank her for putting her heart and soul into this, for accompanying me on this long journey always with a smile, for convincing me it was worthwhile; for bearing me, my crazy schedules and my desk full of papers, for showing me the elegant science of electrochemistry and for helping me understand the chemistry of tiny motors with her experimental insight. It was fantastic working with her. Without her encouragement and excellent feedback, this manuscript would not have been possible. Xie xie Lulu. Maite zaitut.

Oxford, June 2017

List of publications

. Schreiber, R., **Santiago, I**., Ardavan, A., & Turberfield, A. J. (2016).Ordering Gold Nanoparticles with DNA Origami Nanoflowers. *ACS nano*, 10(8), 7303-7306. DOI: 10.1021/acsnano.6b03076

. **Santiago, I.** , Jiang L.& Foord J (2017).Observation of nanoimpact events of catalase on diamond ultramicroelectrodes by direct electron transfer *Chemical Communications 53.59 (2017): 8332-8335.* DOI: 10.1039/C7CC04085G

. **Santiago, I.** , Jiang L., Foord J & Turberfield A (2018).Self-propulsion of catalytic nanomotors synthesised by seeded growth of asymmetric platinum–gold nanoparticles *Chemical Communications.* DOI:10.1039/C7CC09436A

. **Santiago, I.** (2018).Nanoscale active matter matters: challenges and opportunities for self-propelled nanomotors *Nano Today.* DOI:10.1016/j.nantod.2018.01.001

Contents

Appendices

List of Figures

List of Abbreviations

A,G,C,T	Adenine, Guanine, Cytosine, Thymine
AFM	Atomic force microscopy
APD	Avalanche photodiode
ATP	Adenosine triphosphate
BSPP	Bis(p-sulfonatophenyl)phenylphosphine dihydrate dipotassium salt
CCD	Charge coupled device
DDLS	Depolarised dynamic light scattering
DFT, FFT	Discrete Fourier Transform, Fast Fourier Transform
DLS	Dynamic light scattering
DNA	Deoxyribonucleic acid
dsDNA	Double stranded DNA
DTT	Dithiothreitol
E. coli	Escherichia coli
EDC	1-Ethyl-3-(3-dimethylaminopropyl)carbodiimide
FAM	Fluorescein
fcc	Face-centered cubic
FCS	Fluorescence correlation spectroscopy
FKP	Fisher-Kolmogorov-Piskunov
FRET	Förster resonance energy transfer
GCE	Glassy carbon electrode
BDD	Boron-doped diamond ultramicroelectrode
IFFL	Incoherent Feed Forward Loop
MD	Molecular dynamics
ME	Microelectrode

MPCD	Multi-particle collision dynamics
MSD	Mean squared displacement
NMR	Nuclear magnetic resonance
NPs	Nanoparticles
NTA	Nanoparticle tracking
PAGE	Polyacrylamide gel electrophoresis
PBS	Phosphate-buffered saline
PDB	Protein Data Bank
PEG	Polyethylene glycol
RDE	Rotating disk electrode
RDF	Radial Distribution Function
Re	Reynolds number
RMPCD	Reactive multi-particle collision dynamics
RNA	Ribonucleic acid
SAXS	Small-angle X-ray scattering
SDS	Sodium dodecyl sulfate
SEM	Scanning electron microscopy
SP	Structure parameter
ssDNA	Single stranded DNA
sulfo-SMCC	sulfosuccinimidyl4-(N-maleimidomethyl)cyclohexane-1-carboxylate
TBE	Tris/Borate/EDTA buffer
TCEP	tris(2-carboxyethyl)phosphine
TEM	Transmission electron microscopy
UME	Ultramicroelectrode
XPS	X-ray photoelectron spectroscopy

1

Introduction: Active matter and DNA programmed assembly at the micro and nanoscales

multa minuta modis multis per inane videbis / corpora misceri radiorum lumine in ipso
et vel ut aeterno certamine proelia pugnas / edere turmatim certantia nec dare pausam [...]
quod tales turbae motus quoque materiai / significant clandestinos caecosque subesse.
multa videbis enim plagis ibi percita caecis / commutare viam retroque repulsa reverti [...]
a principiis ascendit motus et exit / paulatim nostros ad sensus, / ut moveantur illa quoque,
in solis quae lumine cernere quimus / nec quibus id faciant plagis apparet aperte.

You will see many minute bodies in many ways through the apparent void mingle in the midst of the light of the rays, and as in never-ending conflict skirmish and give battle combating in troops and never halting.[. . .] Such tumbling imply that motions also of matter latent and unseen are at the bottom. For you will observe many things there impelled by unseen blows to change their course and driven back to return the way they came now this way now that way in all directions round [...] and step by step issues forth to our senses, so that those bodies also move, which we can discern in the sunlight, though it is not clearly seen by what blows they so act.

LUCRETIUS, *De Rerum Natura* (On the Nature of Things), Book II, 116, (ca. 55 BC)

1.1 Motivation and objectives

Living matter is a source of inspiration for generations of scientists and engineers. Many have tried to find life-like properties in non-living (abiotic) matter [1]. However, the constituents of living organisms are no different from those found in inanimate objects, but they have properties that allow us to classify them as such. For example, living systems organise themselves, expand and replicate in constant thermodynamic openness with their surrounding. And above all, they move.

A feature shared by living organisms is the capacity of purposeful locomotion. When in 1828 the botanist Robert Brown first reported the jiggling of pollen grains in suspension, he thought that this activity was the ‘vital force’ that animated matter [2]. Boltzmann’s kinetic theory of gases [3], Einstein’s and Smoluchowski’s explanation of Brown’s observations [4, 5], and Perrin’s experiments with colloids [6] removed this vitalistic conception of random motion as the sole property of living organisms and assigned its cause to thermal fluctuations.

What characterises living matter is not random thermal motion and thermodynamic equilibrium, but its capacity to stay far from it, while consuming free energy in the environment to perform systematic movements, growth and replication. We know that these processes are mostly driven by the activity of molecular motors fuelled by hydrolysis of ATP [7]. This aspect of biology defines *active matter*, i.e. entities which move in a non-thermal fashion, dissipating the energy of the environment (or internally stored) to sustain an out-of-equilibrium state and perform mechanical work [8].

At the molecular level, progress in chemistry has enabled the synthesis of artificial molecular machines that can harness external energy and translate it into motion. Examples include chemical molecular rotors like ‘rotaxanes’ [9], that can perform nanoscale mechanical switching and rotation. More recently, DNA-based molecular motors have been shown to move along tracks, mimicking natural motors like kinesin [10]. Developments in material science have facilitated the assembly of numerous artificial devices that display activity at the micro and nanoscale [11]. These include catalytic self-propelled colloidal particles [12], artificial flagella driven by an external magnet [13], laser-driven microswimmers [14] and light-activated propulsive particles [15]. However, most of these synthetic swimmers developed in the last decade rely on external fields to alter their swimming behaviour and control their interactions. Therefore, they are not intrinsically self-driven and lack programmability. In order to obtain truly autonomous swimmers, new approaches are necessary for manufacturing synthetic propulsive devices.

This thesis introduces the tools of DNA nanotechnology to build synthetic active matter from the bottom-up at the micro and nanoscales. The specific base-pairing interactions that arise from DNA hybridisation permit the programmed assembly of matter and also the creation of controllable dynamical systems. This work aims to bridge the emerging fields of active matter and programmable materials. Together DNA nanotechnology provides new tools to create and control rationally-designed motors that can self-propel freely in solution.

In this chapter, a simple natural microswimmer is taken as a canonical example, *Escherichia coli (E. coli)* and its main properties are highlighted. DNA is presented as a programmable self-assembly tool, that in combination with active elements can serve to rationally design a device that mimics cellular locomotion.

1.2 *E.coli*, a canonical autonomous swimmer

E. coli is a paradigmatic example of a natural autonomous swimmer. This small bacterium is a model system in biology, analogous to the hydrogen atom in physics [17]. Because of its ease of manipulation, *E. coli* is an important tool in modern biological engineering and it has served as a model organism in many discoveries

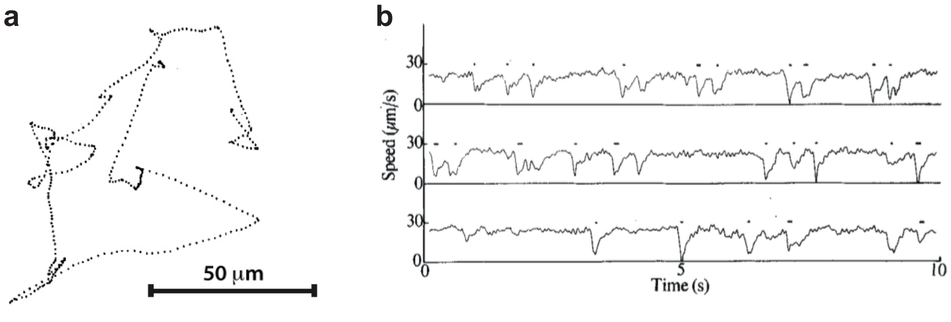

Figure 1.1: *E. coli* in motion. **a)** A projection of the track of a wildtype *E. coli* obtained with a microscope which automatically follows its motion in three dimensions. For 30 s bacteria perform a ‘run and tumble’ persistent random walk, alternating ballistic runs with reorientations in the absence of attractants. **b)** Speed of bacteria. Velocity drops to zero (marked with a dot) when a tumbling event occurs. (Figures extracted from [16]).

of molecular biology (e.g. lac operon, genetic recombination). Apart from its historical significance and apparent simplicity, there is nothing extraordinary about this organism.

Despite their small size (≈ 1 µm), they are capable of autonomous locomotion, while subject to strong thermal fluctuations. The molecular machinery that controls the motility of *E. coli* towards or away from food sources (a process called *chemotaxis*) is well understood and it can be generalised to other motile and sensory cells. The chemotactic pathway equips *E.coli* with sensing, memory and signalling abilities that allow them to migrate towards favourable environments and away from unfavourable ones [18]. Briefly, the chemotactic system works as follows: cells have chemoreceptors in their membranes that can bind to attractants and repellants to trigger the chemotactic pathway that controls the flagellar motor. Cells can either undergo 'runs', straight swims of about 1 s duration, or 'tumbles', random movements that can last 0.1 s for a reorientation of the cell in a random direction. If cells move towards a favourable environment, then the chemotactic pathway introduces longer runs and fewer tumbles, while if the environment is unfavourable, then cells quickly reorient towards a new swimming direction. This motion results in what is known as an *active biased random walk*, where ballistic motion coexists with Brownian motion. An example of the 'run and tumble' motion of *E. coli* taken from the pioneering work of H. Berg [16] is shown in Figure 1.1 (a). Tumbling occurs when the speed decreases in Figure 1.1 (b). The chemotactic pathway is shown in Figure 1.2. This bacterium exemplifies an autonomous swimmer capable of sensing its environment and responding to signals without the need of external control. Four properties stand out as basic ingredients for an artificial analogue that aims to mimic this swimming behaviour, which are described below and in Figure 1.2:

Structure: The selective value of bacterial morphology has been widely researched in microbiology [19]. Shape and size have a significant impact on resistance to

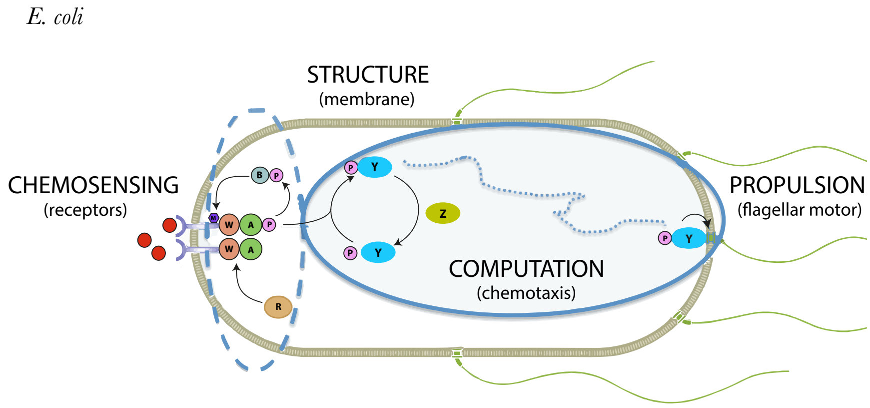

Figure 1.2: Schematic representation of *E. coli*, which highlights 4 characteristics that define an autonomous swimmer. The cell has a **structure** that determines the friction forces and thermal fluctuations it will be subjected to. **Chemosensing** allows the cells to detect attractants in the environment and trigger an internal **computation** process (chemotactic pathway) that controls the **propulsion** mechanism (flagellar motor).

motion. Most bacteria are spherical, ellipsoidal or rod-shaped and have acquired their geometry subject to selective pressure [20] to increase their swimming efficiency[1].

Propulsion: *E. coli* propels itself by rotating its flagella powered by molecular motors. If the flagellar motor rotates counterclockwise, the organism ‘runs’ by rotating together the left-handed helical flagella. However, when flagellar rotation abruptly changes to clockwise, flagella unbundle and the bacterium ‘tumbles’ in place. Propulsion strategies at low Reynolds number are reviewed in section 1.4.

Chemosensing: *E. coli* has localised chemoreceptor clusters that amplify small changes in ligand concentration. These signals are transmitted eventually to the rotary motors that control the flagella. For example, the phosphorylation levels of the CheY protein regulate the rotation direction of the flagellar motor.

Computation: The chemotactic pathway acts as a short-memory program that exhibits *adaptation*. The cell measures the concentration of chemoattractants over a few seconds and then resets its receptors for a new measurement. Robust adaptation,

---

[1] For example, growth in cell size of 0.1 µm can increase the energy required for chemotaxis by a factor of 10^5 [19, 21].

which can be implemented with integral feedback control, is a characteristic of most biosensors.

1.3 DNA nanotechnology for bottom-up self-assembly of active matter

This thesis introduces the tools of DNA nanotechnology in the design and study of synthetic active systems. The diagram in Figure 1.3 proposes four main areas that are developed throughout this thesis. *Structural DNA nanotechnology* focuses primarily on creating nanostructures of arbitrary shapes using the scaffolded DNA Origami technique (Figure 1.3 (a)). In addition, DNA can also act as a cargo or guide the assembly of particles attached to it, enabled by the specificity of Watson-Crick pairing. This thesis explores DNA programmed assembly of ‘passive’ and ‘active’ colloidal particles at the micro and nanoscales (e.g. 2D lattice of DNA/gold nanoparticle hybrids in Figure 1.3 (b)). Activity is achieved using catalytic metallic nanoparticles or enzymes. The mechanism of propulsion,-*self-diffusiophoresis*- is illustrated for the case of catalytic Janus particles in Figure 1.3 (c)).

Dynamic DNA nanotechnology permits the development of functional DNA devices capable of computational tasks (e.g. strand displacement reaction in Figure 1.3 (d)). The programmability of DNA devices in response to external signals opens the possibility of mimicking chemosensing and signalling properties of natural autonomous swimmers. Finally, DNA in combination with enzymes is studied as an active medium in itself, kept out-equilibrium through a reaction-diffusion process that results in a travelling chemical wave. Figure 1.3 (e) shows the propagation of an autocatalytic wave made out of DNA.

The rest of this chapter surveys the main ideas that have contributed to the work in this thesis. They are classified following the scheme in Figure 1.3: **Propulsion**: the physics of locomotion and propulsion strategies; **Structure**: DNA Origami and DNA mediated assembly of micro and nanoparticles; **Sensing and computation**: Dynamic DNA nanotechnology; and **Active media**: DNA autocatalytic travelling waves.

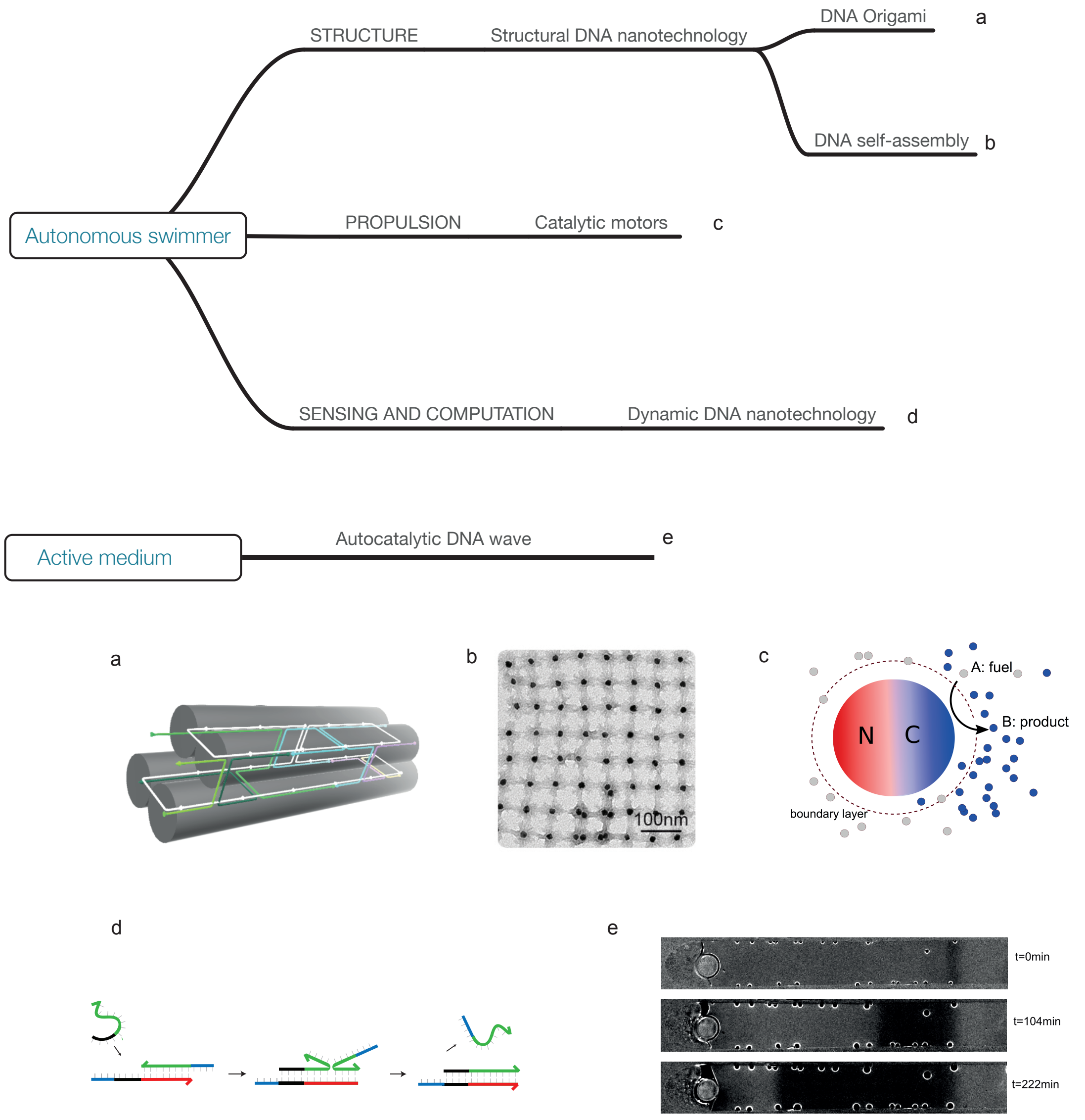

Figure 1.3: *Thesis outline: Ingredients for an autonomous swimmer.* **a)** DNA as a building block: Example of a 3D DNA Origami structure, a four-helix bundle assembled using a large *scaffold* (in white) bound to small *staples* (other colours). **b)** DNA as a molecular glue: self-assembled gold nanoparticles into square lattices with the aid of DNA linker strands. Figure from [22]. **c)** Propulsion mechanism: scheme of a Janus particle propelling by catalysing fuel. **d)** Example of thermodynamic control of DNA structures through *toehold-mediated strand displacement* reactions. **e)** Autocatalytic DNA wave propagation along a microfluidic channel recorded at different times.

1.4 Propulsion

The aim of this section is to describe the physical constraints facing locomotion at the micro and nano scales and to review the different propulsion mechanisms found in natural swimmers, as well as those developed for synthetic ones.

1.4.1 The physics of locomotion of natural and synthetic swimmers

When studying the microscopic world, even though the laws of physics remain the same, the relative importance of forces changes considerably. Therefore, a new intuition different from the one used in the macroscopic world is needed. For example, microswimmers swim in an environment where the role of inertia is negligible. When the fluid becomes too viscous or the immersed object is too small, then viscous forces dominate over inertial ones. The *Reynolds number* (*Re*) quantifies the ratio between inertial and viscous forces as follows:

$$Re = \frac{av\rho}{\eta} \tag{1.1}$$

where a is the size of the object and v its velocity, ρ is the density of the fluid and η its dynamic viscosity. High Reynolds number physics that rules macro-swimmers does not apply to the low Reynolds number regime that dominates swimming of microorganisms. The physicist E. M. Purcell pointed out in his paper *Life at Low Reynolds number* [23], that since flow is reversible at low Reynolds number[2], propulsion cannot be achieved by a reciprocal motion in which a rigid appendage with a single degree of freedom is moved back and forth, retracing its path no matter the rate at which this is done (also known as the *Scallop theorem* and illustrated in Figure 1.4). Scallops break symmetry by opening their shell slowly and closing them quickly. However, reciprocal movement as a swimming strategy does not work at low Reynolds number.

---

[2] The Navier-Stokes equation reduces to the Stokes equation when $Re \ll 1$,

$$\eta\nabla^2\mathbf{u} - \nabla\mathbf{p} = 0 \tag{1.2}$$

which is linear and independent of time. As a consequence, it presents kinematic reversibility.

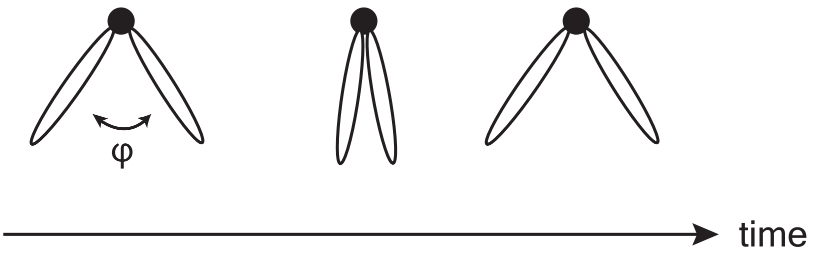

Figure 1.4: *The scallop theorem.* A scallop-shaped device with a single degree of freedom φ performing a reciprocal movement. At low Reynolds number, where inertia is negligible, a stroke forward is cancelled out by an identical stroke backward, resulting in no net displacement.

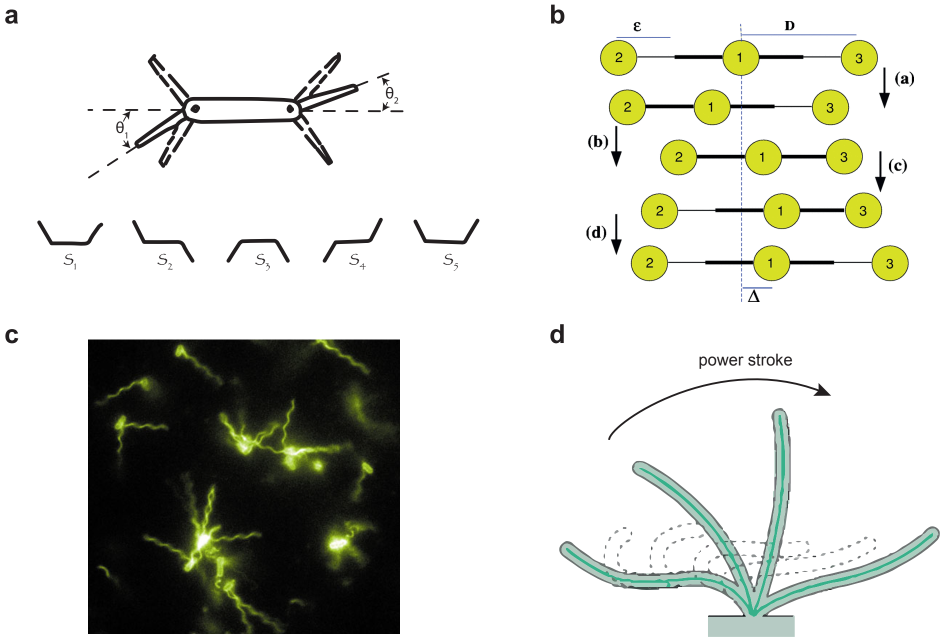

Figure 1.5: **a)** *Purcell's swimmer* consists of a body with two hinges. Changing configuration from S_1 to S_5=S_1 every cycle results in non-reciprocal motion. **b)** Complete cycle of the Najafi-Golestanian 1D swimmer, which is composed of four consecutive time-reversal breaking stages. By completing the cycle the whole system is displaced to the right side by an amount Δ. Figure from [24]. **c)** Real-time imaging of fluorescent flagellar filaments of *E. coli* undergoing 'run and tumble' events. Image from the Berg lab [25]. **d)** A cilium beats by performing a repetitive cycle, consisting of a power stroke, followed by a recovery stroke. Adapted from [26].

Breaking time-reversal symmetry is the only way to achieve propulsion without inertia. This can be done in non-Newtonian fluids[3] [27] or by introducing additional degrees of freedom. For example, the *Purcell swimmer* in Figure 1.5 (a) has two appendages and performs a sequence of movements in 2D that propels it forward. Najafi and Golestanian's three-spheres model linked by two arms of varying length, shown in Figure 1.5 (b), is another example of a synthetic swimmer. This one-dimensional swimmer propels by moving mass forward, mimicking amoebas, in four consecutive time-symmetry breaking steps [24].

In the biological world, microswimmers have acquired through the evolutionary process diverse strategies to break time-reversal symmetry and propel themselves, overcoming and even exploiting viscous drag. Two main propulsive mechanisms can be distinguished: on the one hand bacteria propel themselves by deforming their rigid, helical *flagella*. For example, Figure 1.5 (c) shows flagellated bacteria observed with fluorescence microscopy. On the other, whip-like beating of *cilia* (normally shorter than flagella and embedded to the cell body) are responsible for locomotion of larger cells, such as eukaryotes. Other forms of cellular motility exist, such as gliding and crawling [28]. In addition, human pathogens have developed intricate propulsion mechanisms to escape recognition from the immune system, e.g. trypanosome [28]. Microrganisms have served as inspiration to create many artificial swimmers in the laboratory. These are classified below as either externally propelled or subject to (self-)phoretic forces.

1.4.2 Externally-controlled propulsion

This section presents a few examples of recent realisations of bio-inspired microswimmers that mimic flagella and cilia. They are actuated externally by magnetic fields.

Dreyfus et al. presented in 2005 one of the first artificial microswimmers (see Figure 1.6 (a)) [13]. It is composed of superparamagnetic colloids of 1 µm size linked by DNA. These colloids assemble in the direction of a static magnetic field. A rotational magnetic field in the transversal direction creates a beating pattern

---

[3] The non-linearities in the inertial terms of the Navier-Stokes equation provide time-irreversibility.

analogous to cilia, which leads to the propulsion of the flagellar structure. Another example of an externally-controlled swimmer was reported by Gosh and Fischer in 2009 (Figure 1.6 (b)) [29]. This is a chiral rotor with magnetic properties and has a length of 2 µm. An external rotating magnetic field causes rotation of the helix and it reaches a propulsion speed up to $40\,\mu m\,s^{-1}$. Tierno et al. developed a conceptually similar swimmer by attaching two paramagnetic beads of different sizes with DNA [30]. Propulsion is observed when these anisotropic particles are subjected to a magnetic field that precesses around an axis parallel to the plate, as shown in Figure 1.6 (c).

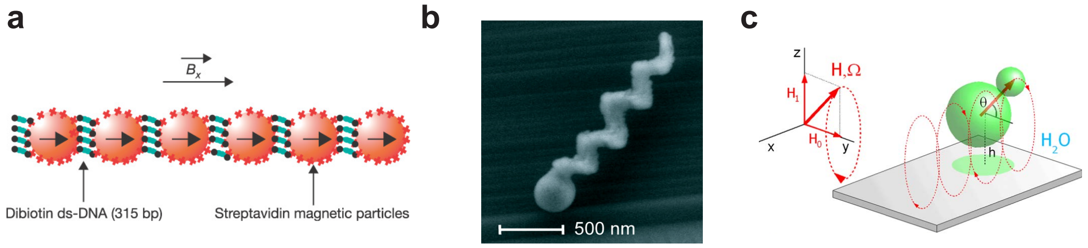

Figure 1.6: *Externally-controlled microswimmers*: **a)** Cilia-inspired swimmer composed of superparamagnetic colloids linked with DNA(by Dreyfus et al [13]). An oscillating external magnetic field actuates the filament. **b)** Flagella-inspired helical swimmer with a magnetic head (by Ghosh et al. [29]). **c)** DNA linked paramagnetic beads propelled by an external oscillating magnetic field (by Tierno et al. [31])

1.4.3 Phoretic propulsion

The previous examples of swimmers break time-reversal symmetry and propel at low Reynolds number successfully. However, they are fuel-free, rely on external forces, and therefore cannot be considered truly autonomous. There are alternative ways of breaking time-reversal symmetry that involve the modification of the surrounding medium by means of phoretic mechanisms. *Phoresis* refers to a type of transport that arises by external fields interacting with the interfacial layer of particles [32] (discussed in chapter 2). The phoretic force may be, for example, due to a temperature gradient (*thermophoresis*) or a chemical gradient (*diffusiophoresis*). In order for the particle to be autonomous, the gradient has to be formed by the particle itself. This type of self-generated phoretic forces will be referred to as *self-propulsion* in this thesis.

As opposed to previous examples that rely on external directional control, phoretic swimmers are subject to rotational Brownian motion and their directions are randomised. In this sense, the persistent random walk observed for these active particles resembles the 'run and tumble' motion described for *E. coli.* Its analogies have been studied by Cates et al.[33].

The first demonstration of the concept of swimming powered by asymmetric chemical reactions can be traced back to the work by Whitesides and co-workers, who made millimetre-scale chemically-powered disks coated with platinum, which catalysed the decomposition of hydrogen peroxide [34]. Ever since, the idea of an asymmetric catalytic chemical reaction to drive propulsion has been extended to smaller scales. The catalytic decomposition of H_2O_2 by Pt has been the preferred reaction for its effectiveness and high catalytic activity at room temperature. However, alternative fuels have been studied, as well [35].

Pt/Au nanorods are an early example of autonomous phoretic microswimmers, which were developed by Paxton et al. [36] (shown in Figure 1.7(a)). A phoretic nanorod is composed of a cylindrical bimetallic rod, which propels when suspended in a solution of H_2O_2. These rods are several micrometres long and a redox reaction between the two halves of the structure is what drives the motion. More specifically, H_2O_2 oxidises on the Pt side and is reduced into water on the Au side as illustrated in Figure 1.7(a). An electric field is created and transports H^+ ions along the outer edge of the rod. The steady production of H^+ creates a pressure gradient that translates into a fluid flow that propels the nanorod. This is an example of phoretic motion, which in this case is *self-electrophoresis.*

Another paradigmatic example of phoretic propulsion is the Janus swimmer developed by Howse et al. [12], inspired by the theoretical work of Golestanian and colleagues [37]. The Janus swimmer was fabricated by coating polystyrene beads with metallic caps, which catalyse a chemical reaction. The catalytic reaction implies an asymmetric, non-equilibrium distribution of products around the Janus particle, which generates phoretic forces (*self-diffusiophoresis*).

Palacci et al., have taken self-diffusiophoretic swimmers further by constructing photoactivated Janus swimmers. They achieved this using hematite cubes which upon ultraviolet illumination become active [15]. Another example of phoretic propulsion is the self-thermophoretic motion of half-coated Au/silica particles suspended in water [38]. Due to illumination with an infrared laser, a temperature gradient is formed around the Janus particle which translates into a propulsion velocity proportional to ∇T.

There are many other propulsion mechanisms that are out of the scope of this thesis. These include, active emulsions self-propelled by Marangoni stresses, tubes and spheres propelled by bubbles, microrods propelled by ultrasound etc. Comprehensive reviews can be found in [11, 28, 39]. Throughout this work only chemically-propelled particles are considered.

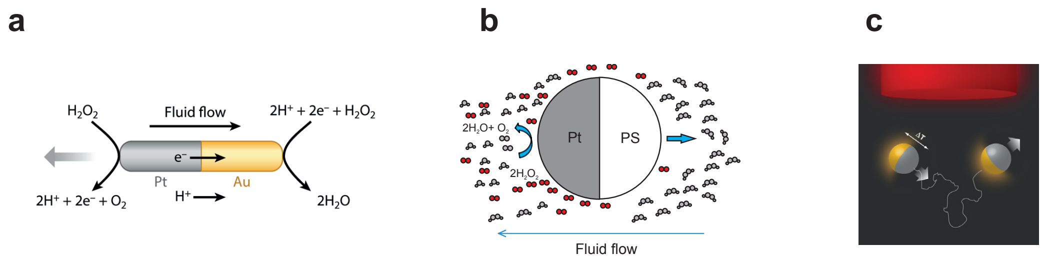

self-electrophoresis self-diffusiophoresis self-thermophoresis

Figure 1.7: *Phoretic swimmers:* **a)** Self-electrophoresis of an Au-Pt rod in a solution of H_2O_2. The redox reaction creates a flux of H^+ around the rod, causing propulsion to the left (indicated by the arrow) [36]. **b)** Decomposition of H_2O_2 at the boundary layer of a Pt-coated Janus particle. The particle moves due to self-diffusiophoresis [12]. **c)** Self-thermophoretic Janus particles moving due to irradiation with an infrared laser[38]. (Figure (a) and (c) are extracted from [36] and [40] respectively.

1.4.4 Nanomotors

'Swimming' implies direction and this is a hydrodynamic property associated with microorganisms and the microdevices discussed so far. Whether nanoscale swimmers exist is an open question that a number of research groups have started to address [41–43]. In this thesis, rather than *nanoswimmer*, the term *nanomotor* will be used, which refers to any molecule or nanoscale particle (e.g. enzyme, nanoparticle), free in solution, that converts chemical energy into motion. Molecular motor proteins, such as kinesin or dynein, that are anchored to tracks and convert ATP into mechanical work will not fall into this category. Mechanically interlocked artificial molecular machines, like 'rotaxanes' [9] will not be considered here neither.

A few experimental groups have reported that certain enzymes exhibit enhanced diffusion in the presence of their substrate [44, 45]. Chemotaxis of enzymes towards their substrate has also been reported [41]. A mechanistic explanation of these observations is still subject to debate by theoretical groups around the world [44, 46, 47]. Synthetic nanomotors of similar sizes have also been achieved: 30 nm Pt/Au [42] and 40 nm Pt/mesoporous silica Janus nanoparticles [48] are the smallest current examples of synthetic, self-propelled nanomotors. Several groups have used the catalytic activity of enzymes to propel larger structures, such as Janus particles coated by catalase and urease [49, 50]. Another example is the covalent attachment of the enzymes glucose oxidase and catalase to carbon nanotubes by the Feringa group [51].

Proposed mechanisms for enzymatic enhanced diffusion

Several enzymes, such as catalase, urease and alkaline phosphatase undergo enhanced diffusion in the presence of their substrate. This means they diffuse with an effective diffusion coefficient D_{eff} that is larger than its equilibrium value D_0. The observed increase in diffusion constant reaches $\frac{\Delta D}{D_0} \approx 0.5$ for some cases and this increase scales with substrate concentration [44, 45]. Some hypotheses, such as self-diffusiophoresis or local heat generation do not account for the observed increase in diffusion, as reviewed in [46]. The main mechanisms that have been put forward are listed in Table 1.1.

The *Chemoacoustic effect* hypothesises that the heat generated from each catalytic cycle is transmitted through the enzyme as a pressure wave. Exothermicity

Table 1.1: Main propulsion mechanisms for enzymatic nanomotors

Hypothesis	*Description*	*Reference*
Chemoacoustic effect	heat released during catalysis generates an asymmetric pressure wave	[44]
Self-(electro)phoresis	generation of local gradients of (charged) reaction products	[52]
Conformational change	non-equilibrium cyclic conformational changes create a force dipole	[53]
Collective heating	temperature rise of the buffer caused by the accumulation of reaction heat leads to protein denaturation	[46]

and catalytic activity are thought to be responsible for the enhanced diffusion, while enzymes like triose phosphate isomerase with low heat generation were shown not to exhibit this effect. Because the catalytic centre is not at the centre of mass of the enzyme, the pressure wave creates differential stress at the enzyme/solvent interface, which then propels the enzyme. This mechanism put forward by [44] does not explain the phenomenon fully, as pointed out in [46, 47].

Self-electrophoresis is the mechanism proposed in [52] to explain the enhanced diffusion of urease. There is strong theoretical support for this mechanism to work at the angstrom and nano scales for asymmetric catalytic nanomotors [54], however it is not clear if it can account for the observed enhanced diffusion in enzymes. Self-phoretic mechanisms are described in chapter 2.

The enhanced diffusion of single enzymes could also be attributed to cyclic *conformational changes* in the enzyme [53]. Proteins act as stochastic oscillating force dipoles that can influence the motions of other particles in the system. This hydrodynamic mechanism also predicts the enhanced diffusion of tracer particles. It is thought to play a role in highly crowded environments (e.g. in the cytoplasm).

For an isolated enzyme the relative change in temperature across the enzyme ΔT results in a negligible increase in diffusion. However, when a high concentration of enzymes is considered, *collective heating* could lead to the denaturation of the protein and a change in diffusion constant [46]. This effect is unlikely to explain the single-molecule measurements where enzyme concentration is low ($\ll nM$).

The investigation of the mechanisms underlying enhanced diffusion in enzymes is an ongoing research topic. There could be alternative explanations, or a combination of them. Enhanced diffusion of individual enzymes has been challenged by some groups [47], suggesting quenching of fluorescence by catalytic products as an explanation. The observation of enhanced diffusion for endothermic enzymes [55]as well as exothermic ones [44] suggests that heat generation is not a likely explanation of the molecular mechanism behind this phenomenon. On the other hand, stochastic oscillating force dipoles generating hydrodynamic flows that change the diffusion of particles is a stronger hypothesis, supported by experiments with tracer particles and enzymes immobilised on a surface [56] and free in solution [57]. This hypothesis could be verified by single-molecule experiments to unravel the conformational changes of enzymes. Alternative experimental methods, such as Nuclear Magnetic Resonance (NMR), have observed similar enhanced diffusion in other systems [58]. Collective effects, such as accumulation of enzymes or what has been coined as 'chemotaxis' of enzymes [45, 59] are yet to be explained mechanistically. More experiments and new methods to observe this phenomenon would contribute to a complete physical picture of enzymatic propulsion.

1.5 Structure: Structural DNA nanotechnology

1.5.1 DNA, a nucleic acid

The biological role of *deoxyribonucleic acid* (DNA) is well-known, as an information carrier principally responsible for coding the protein amino acid sequence and for regulation of protein expression. From a physical point of view, DNA is a linear polymer of monomer nucleotides. These units are composed of a nitrogenous base (base hereafter), a five-carbon sugar (deoxyribose) and a phosphate group, as illustrated in Figure 1.8 (a). The nucleotides are covalently linked together in a chain through the sugars and phosphates, which form a 'backbone' of alternating sugar-phosphate.

There are 4 different bases (adenine, guanine (purines), thymine, cytosine (pyrimidines)) and they follow *Chargaff's parity rule* [62], i.e. the amount of guanine is equal to cytosine and the amount of adenine is equal to thymine. The crystallographic structure of DNA, the double helix famously discovered by Franklin, Wilkins, Watson and Crick, reveals a specific pairing of bases that lies at the root of the mechanism that copies genetic information [60, 63]. The four bases are able

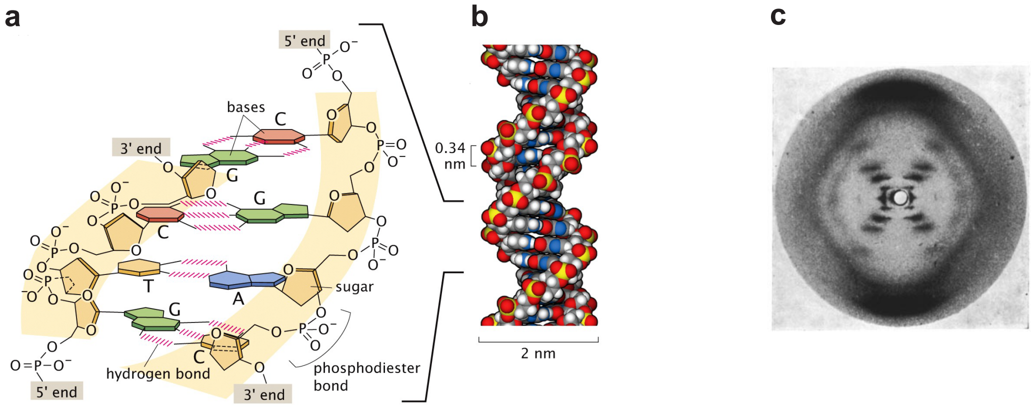

Figure 1.8: *The molecular structure of deoxyribonucleic acid (DNA):* **a)** Scheme of how bases are assembled to form DNA, a double helix structure with two backbones made of phosphate groups and deoxyribose sugar. The four bases are able to form stable hydrogen bonds uniquely with one partner, namely guanine (G) with cytosine (C) and adenosine (A) with thymine (T). G-C bases pair with three hydrogen bonds and A-T bases pair with two hydrogen bonds. The polarity of DNA is indicated by the $5'$ and $3'$ ends. **b)** Atomic model of the most common conformation of DNA (B-DNA), which twists in a right-handed double helix about 2 nm in diameter. One full turn of the helix is about 10 to 10.5 base pairs long (3.5 nm). **c)** Celebrated X-ray diffraction pattern of B-DNA by Gosling and Franklin [60]. The central Saint Andrew's cross is characteristic of a helical structure. (Figures (a) and (b) are adapted from [61].)

to form stable hydrogen bonds uniquely with one partner, namely guanine (G) with cytosine (C) and adenosine (A) with thymine (T). This mechanistic explanation of Chargaff's parity rule is known as *Watson-Crick base pairing.*

Apart from the genetic information encoded in the DNA sequence, the specificity of the base pairing interaction provides a means to selectively bind a single stranded DNA (ssDNA) to its complement in a process called *hybridisation.* For B-DNA, the most common form in nature, hybridisation results in a right-handed double helix with about 10-10.5 base pairs per turn (Figure 1.8 (b)) [61]. The cross in the X-ray diffraction pattern by Gosling and Franklin [60] in Figure 1.8 (c) is indicative of this helical structure.

Another key property of DNA is its polarity. As illustrated in Figure 1.8 (a), the $5'$ end bears a phosphate group on the 5^{th} carbon of the sugar ring, while the $3'$ end bears a hydroxyl group on the 3^{rd} carbon of the sugar ring. It is conventional to write sequences from the $5'$ to $3'$ end. The double helix is formed when two anti parallel strands hybridise. The stability of double-stranded DNA (dsDNA) comes from base pairing interactions, which are mediated by hydrogen bonds (A forming two hydrogen bonds with T, and C forming three hydrogen bonds with G), as well as from stacking interactions between bases of the same strand. Two complementary strands can come apart resulting in two single-stranded DNA molecules (ssDNA) in a process known as melting.

DNA, as other macromolecules present in living organisms, has a complex structure. However, its biological function and the inner chemical complexity at the atomic level can be abstracted away thanks to the robustness of the base pairing mechanism. From a physical-chemistry perspective, DNA is a polymer that can be considered as a rigid rod for length scales smaller than its persistence length ($\xi_{dsDNA} \approx 50$ nm for double stranded DNA (dsDNA)) [61]. ssDNA is more flexible than dsDNA ($\xi_{ssDNA} \approx 0.8$ nm [64]), its bases can pair along its backbone and form hairpins, which depend on sequence and salt concentration.

1.5.2 DNA as a building block

Apart from its biological relevance, nucleic acid hybridisation offers specific and strong interactions that can be used for self-assembly. In 1982 Nadrian Seeman proposed that immobile junctions could be generated from DNA. He envisioned that individual structures could be combined using simple sticky-end base pairing (Figure 1.9 (a) to assemble complex, multidimensional objects [65]. The most successful motif in structural DNA nanotechnology is a 4-branch junction, also known as *Holliday junction* (Figure 1.9 (b)). Holliday junctions found in nature have symmetric pairs of arms and the junction can migrate, while preserving base pairing. Artificial Holliday junctions, however, are immobile by design.

A key idea in *structural DNA nanotechnology* consists in combining branched junctions into larger three-dimensional structures. For example, Figure 1.9 (b) shows the assembly of artificial Holliday junctions into a larger lattice structure by means of sticky-end complementarity between their four arms, namely X, Y and their complementary X′ and Y′.

Pioneering examples in the field that developed this idea further are shown in Figure 1.9 (c) and (d). Seeman and coworkers were able to construct a molecule with the connectivity of a cube [66] by hybridising and ligating six strands. Goodman et al., later demonstrated a single-pot reaction with high yield to construct 3D tetrahedra by annealing four strands [67].

DNA Origami has been a significant milestone in DNA nanotechnology that has improved a bottom-up approach to nanofabrication. In 2006 Paul Rothemund developed a new technique for constructing DNA nanostructures using numerous short *staple* strands to direct the folding of a longer single stranded *scaffold* ($\sim$ 7000 nucleotides) [71]. Figure 1.10 (a) illustrates a simplified cartoon of the scaffolding strategy and shows Atomic Force Microscopy images of the first 2D DNA Origami.

Rothemund's research on scaffolded DNA Origami demonstrating 2D DNA structures of arbitrary shape was followed by Douglas et al. [72], who reported the assembly of solid 3D DNA Origami using the scaffolding method. The principle,

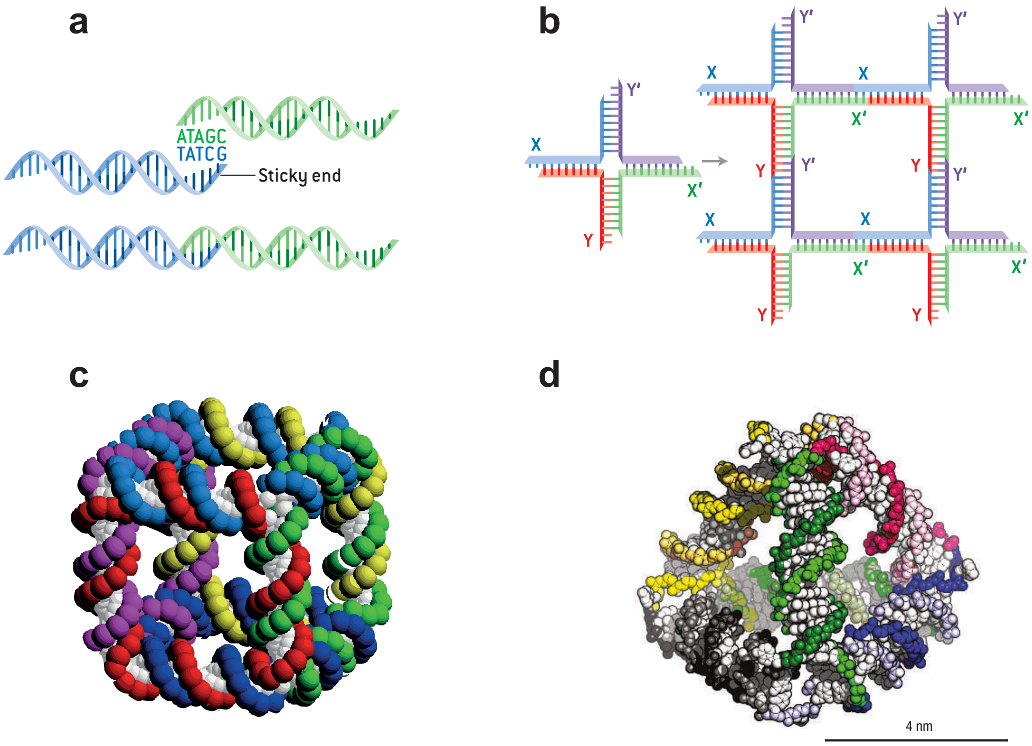

Figure 1.9: *Central ideas in structural DNA nanotechnology*: **a)** *Sticky-ends* are single-stranded overhangs that hybridise through hydrogen bonding with a complementary overhang. **b)** Artificial *Holliday junctions* can be combined to assemble larger stable structures. The left hand side shows a branched junction formed with 4 strands with sticky ends, namely X, Y and their complementary X′ and Y′. Four of these junctions have been combined to form the structure on the right. **c)** DNA self-assembled structure with the connectivity of a cube constructed by hybridizing and ligating six strands [66]. Each corner is a three-arm junction and the DNA backbones are shown in colour. **d)** DNA self-assembled tetrahedron by annealing 4 strands [67]. (Figures (a) and (b) were extracted from [68], (c) was adapted from [69] and (d) was extracted from [70]).

illustrated in Figure 1.10 (b) and (c) consists of folding layers of helices constrained to a honeycomb lattice. Figure 1.10 (d) shows some examples of 3D Origami structures.

Scaffolded DNA Origami has become a standard tool in nanotechnology laboratories to create bottom-up DNA nanostructures. Progress in the field has been extended to the realm of RNA, and first RNA Origami structures have been reported [73]. Software-aided design of DNA Origami structures is possible with open-source programs that have facilitated the diffusion of the technique. *caDNAno* is a DNA origami design software that outputs a list of staple oligonucleotides [74]. *canDo* is a tool that computes 3D DNA origami shapes based on caDNAno design files [75].

Synthetic swimmers are normally manufactured following top-down approaches. They are commonly made of polymers, such as polystyrene or materials like silicon oxide and the required asymmetries are obtained using traditional lithography techniques. The tools of scaffolded DNA Origami will be used in this thesis to create nanostructures of desired shapes that will constitute the body of a self-assembled nanomotor. One of the advantages of using bottom-up assembly techniques is the possibility of simultaneous synthesis of many structures with desired shape.

1.5.3 DNA as a programmable molecular glue

One of the grand challenges in material science is the ability to build structures with great control over the arrangement of the individual components. The motivations are numerous, for example, achieving control over the assembly of building blocks would permit designing materials with desired physical, chemical and optical properties. The possibility of binding catalytically active materials onto a larger structure at specific locations would be a first step towards creating rationally designed nanomotors.

The same principles that hold for DNA Origami and other DNA self-assembled structures can be extended to micro and nano-objects, if these are linked to hybridising DNA strands. In this section, the attention turns to the research area of DNA nanotechnology that focuses on creating DNA-functionalised materials and studying their self-assembly. In contrast to the rich diversity of materials, only

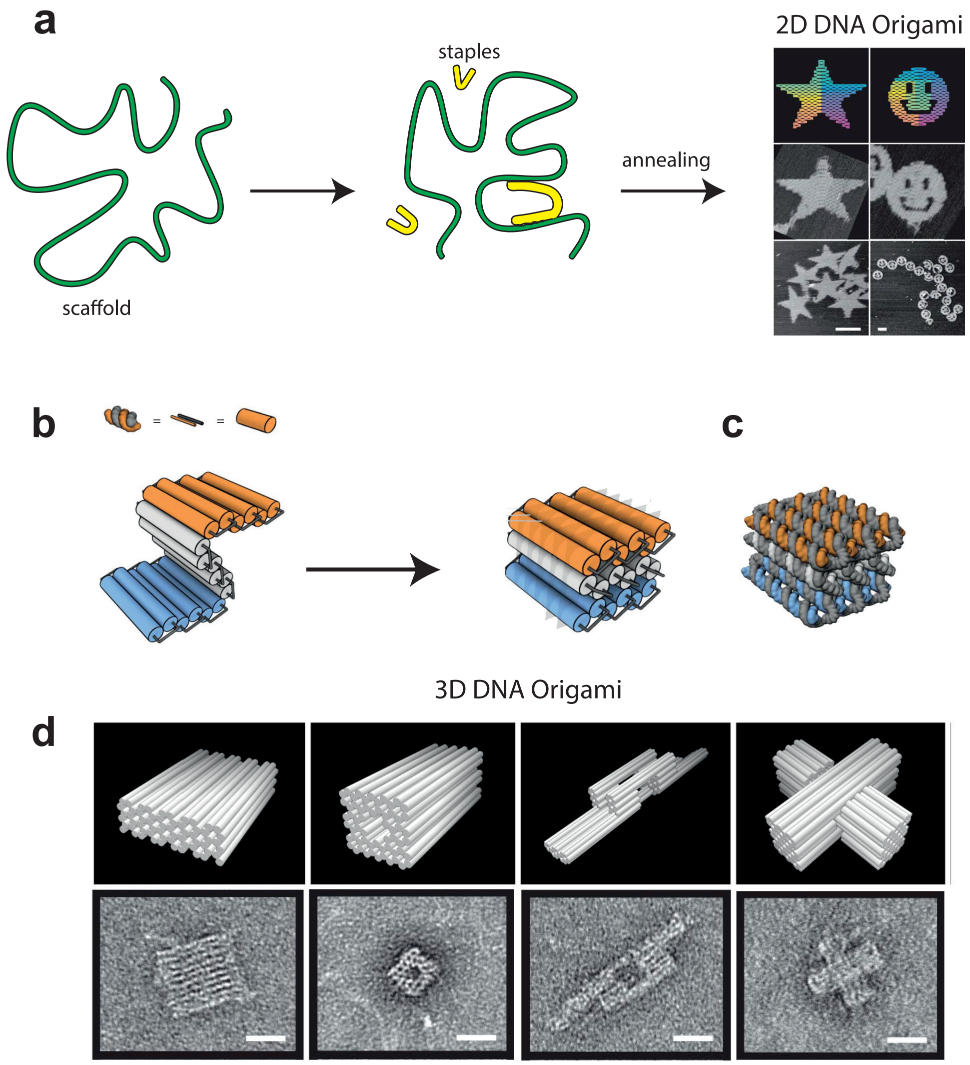

Figure 1.10: *Scaffolded DNA Origami in 2D and 3D:* **a)** Simplified cartoon shows the principle of scaffolded DNA Origami. A long DNA strand (*scaffold* in green), normally m13 viral ssDNA , folds into a structure aided by short oligonucleotides (*staples* in yellow). AFM images of the first 2D Origami structures by Ruthemond are shown [71].**b)** 3D Origami: Scheme of double helices, represented by cylinders, comprised of scaffold (grey) and staple strands (orange, white, blue). The honeycomb arrangement of parallel helices is shown in a cylinder model [72]. **c)** Atomistic model of the shape in b) is shown. **d)** Examples of 3D Origami structures: monolith, square nut, railed bridge and cross. (2D Origami images in a) have been taken from [71] and b), c) and d) have been modified from [72].)

a few have been amenable to DNA-mediated assembly so far, the most prominent one being gold nanoparticles [76] and to a lesser degree, other nanomaterials, such as carbon nanotubes [77], quantum dots [78], silver and platinum nanoparticles [79].

The earliest example of using DNA to guide the assembly of particles was reported independently by two different groups in 1996. Mirkin and coworkers demonstrated the reversible aggregation of gold nanoparticles using DNA [76]. They used a binary mixture of gold nanoparticles coated with 2 different thiolated ssDNA oligonucleotides and they induced aggregation by adding DNA duplexes to link the two strands (see Figure 1.11 (a)). The target DNA duplex aggregated gold nanoparticles in a temperature-dependent way and it resulted in a clear change of colour from red to blue (see Figure 1.11 (b)). These properties were used in a colourimetric DNA sensor successfully [80]. Further studies [81] indicated that, while hybridisation of DNA strands in solution is a gradual function of temperature (Figure 1.11 (c) in black), DNA-functionalised particles transition from a dispersed state to an aggregated one over a very narrow temperature window (Figure 1.11 (c) in grey). This is due to the ability of DNA-coated particles to form many DNA bridges cooperatively. The melting temperature T_m can be tuned by changing the length of strands [82].

Parallel to the work of Mirkin et al., Alivisatos and coworkers demonstrated the controlled arrangement of individual gold nanoparticles bearing single DNA strands on a template oligonucleotide [83]. These experiments showed that the distance between particles could be manipulated by changing the sequence of DNA. Figure 1.11 (d) shows the assembly principle of what were dubbed as 'nanocrystal molecules'.

This research introduced the use of DNA as a programmable glue to bind together colloidal particles and construct 3D crystals of desired symmetry from the bottom-up. However, researchers had to consider other interactions at play and optimise the conditions that would favour crystallisation [84]. Among many parameters, temperature is an important one. Biancaniello et al. assembled DNA-coated microparticles into a face-centred cubic (fcc) crystal by incubating the particles for days just below the melting temperature T_m (shown in Figure 1.11 (e)).

Similar efforts at the nanoscale permitted the first crystallisation of DNA-grafted gold nanoparticles by Nykypanchuk et al. [85] and Park et al. (Figure 1.11 (e)).

Despite successful assemblies of diverse materials, achieving valency or directional control in interactions has remained elusive. Significant progress was made at the microscale by Wang et al. [86], who synthesised patchy colloidal polystyrene spheres with interactions that are specific (through Watson-Crick pairing) and directional. Figure 1.11 (f) shows colloidal analogues of molecules (e.g. AB_4) that were assembled with patchy colloids functionalised with complementary DNA.

Patchy particles have not been developed at the nanoscale, where anisotropy can be achieved during synthesis but it is challenging to control. However, Janus nanoparticles have been realised by some groups [87] and new strategies are starting to emerge. DNA Origami presents a promising way towards achieving controlled directional valency at the nanoscale. Figure 1.11 (g) gives an example of progress in tailor-made DNA nanostructures with designed physical and optical properties. Kuzyk et al. [88] obtained high-yield production of plasmonic structures that contained gold nanoparticles arranged in nanometre-scale helices. These exhibited defined circular dichroism in agreement with theoretical predictions. Another example was given by Edwardson et al. in [89], where they used DNA nanostructures as temporary scaffolds to transfer a designed pattern to gold nanoparticles. This bottom-up technique provides control over the number of DNA strands and their relative placement, directionality and sequence asymmetry.

Apart from nanomaterials, proteins can also be functionalised with oligonucleotides and they can be assembled onto Origami structures [90]. For example, enzymatic cascades show enhanced catalytic activity when the proteins involved in the cascade are immobilised close to each other on DNA Origami structures [91]. A successful implementation of this approach requires careful protein-DNA crosslinking strategies.

The tools of DNA nanotechnology described above can serve to position catalytic particles, either nanoparticles or enzymes, on devices of desired geometries. This is explored further in chapter 6, in the context of a self-assembled nanomotor.

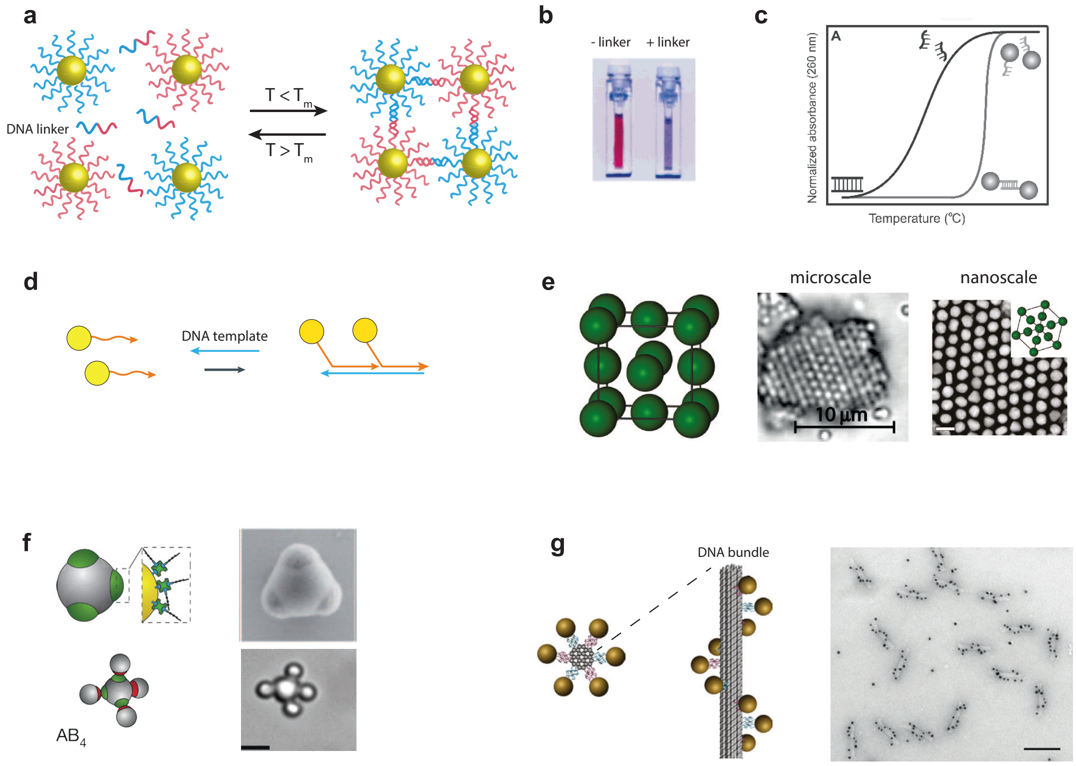

Figure 1.11: *DNA programmed assembly of micro and nano particles:* **a)** Mirkin et al. showed that a binary mixture of uniformly coated gold nanoparticles (13 nm diameter) with different ssDNA (blue and red) aggregate in the presence of a linker strand in a temperature-dependent way [76]. **b)** Adding a linker strand in a) results in aggregation, which changes the colour of the solution from red to blue. **c)** The dissociation of DNA grafted to colloids follows a narrower curve than DNA free in solution as studied in [81]. **d)** Alivisatos et al. [83] showed that gold nanoparticles bearing single DNA strands could assemble together into 'nanocrystal molecules'. **e)** First DNA-assembled crystals into face-centred-cubic (*fcc*) lattices using DNA coated microparticles by Biancanello et al. [92] and using DNA coated gold nanoparticles independently by Park et al. [93] and Nykypanchuk et al. [85]. **f)** Patchy colloids developed by Wang et al. [86] that mimic molecular analogues (AB_4) by providing valency with DNA patches at symmetrically arranged positions on the surface of micron-sized particles. **g)** DNA Origami hybrid nanostructures: DNA grafted nanoparticles can be located site-specifically on Origami structures. This example by Kuzyk et al. [88] shows the assembly of gold nanoparticles onto DNA origami 24 helix bundles. They assemble into nanohelices of defined handedness and circular dichroism. TEM micrograph shows left-handed nanohelices. (Figures (a),(b) have been modified from [94], (c) has been extracted from [82], (e) has been modified from [95] and [92], (f) has been modified from [86] and (g) has been modified from [88])

1.6 Sensing and computation: Dynamic DNA nanotechnology

Analogies between cells and computers abound. In many ways, digital computing has influenced the systems approach to understanding biology. The analogy can be misleading, as the complex biochemical reaction networks responsible for cellular decision are far from a digital yes/no conception borrowed from digital computers. Jacques Monod likened gene regulation to 'microscopic cybernetics' [96], introducing concepts like feedback, inhibition, regulation borrowed from electrical engineering. However, the cell contains no electric circuitry or transistors. Instead, thousands of enzymes diffusing in the cell are responsible for performing logic computations and reacting to stimuli. They do so by controlling the activation energies of numerous biochemical reactions, and speeding up some of them when necessary. For example, the chemotactic network shown in Figure 1.2 consists mostly of kinases and phosphatases that increase or reduce the phosphorylation levels of other proteins that end up controlling the flagellar motor. The sensitivity of the chemosensing system, which is the subject of chapter 7, is also controlled by enzymes that regulate the methylation levels of signalling proteins. This biological system, highly nonlinear and orchestrated by the specificity of enzymes, is an example of cellular information processing.

In this context, we have seen that DNA has a cellular role of information carrier, and it has immense potential as a building block and self-assembly tool *ex vivo*. However, DNA is also endowed with functional properties that can allow it to perform computational tasks. This was first acknowledged in a seminal paper by Adleman [97], where he solved the *Hamiltonian path problem*, which is a version of the *travelling salesman* problem[4] using the self-assembly properties of DNA to perform computation at the molecular level. As any other molecule, DNA strands can participate in chemical reaction networks with other strands through

---

[4] Given a graph with directed edges and specific start and end vertices, one says there is a *Hamiltonian path*, if there is a path that goes through each vertex exactly once. The Hamiltonian Path Problem is to decide if given a graph, such a path exists or not.

hybridisation. Reactant and product strands can be addressed by their specific DNA sequence. The advantage is that the kinetic rates of such DNA reactions are very easy to predict and design, just by changing the sequence. In addition, many of these reactions can take place simultaneously.

An important tool in *dynamic DNA nanotechnology*, is the concept of *toehold mediated strand displacement reaction*. This idea was developed by Yurke and collaborators in Bell Laboratories [98] and introduced non-equilibrium dynamics into what, until then, was equilibrium thermodynamics of static DNA structures. Strand displacement happens when two strands with partial or full complementarity hybridise, displacing in the process one or more pre-hybridized strands. This is illustrated in Figure 1.12 (a), where the displacement is initiated in a single-stranded overhang (*toehold*), and progresses through a branch migration process. By varying the length of toeholds the rate of strand displacement reactions can be controlled over 6 orders of magnitude [99]. Such reactions have opened the possibility of creating logic gates with DNA, extending its computational capabilities [100].

The DNA tweezer shown in Figure 1.12 (c) developed by Yurke et al. [98] is one of the first functional DNA devices. It uses strand displacement reactions to control the open/close conformation of a 7 nanometre DNA tweezer. By adding set strands (fuel) in solution, the tweezer was forced into a closed conformation. Unset strands brought the tweezer back to the open conformation generating irreversible waste. This oscillatory open-close conformation was observed by FRET.

Mimicking chemoreceptor proteins, certain DNA sequences can also react to chemical stimuli and change conformation. *DNA aptamers* are oligonucleotides that bind to specific ligands (in analogy with antibodies). They could also be RNA or peptide aptamers. One early example was given by Huezinga and Szostak, who reported a DNA aptamer capable of binding to adenosine and ATP [101]. One application of this aptamer is shown in Figure 1.12 (b), where it is used as a colorimetric sensor of adenosine. In the presence of the ligand the aggregation state of aptamer-coated gold nanoparticles changes [102]. DNA aptamers, introduce sensing abilities to DNA nanodevices, as was used with functional DNA Origami devices by Douglas et al. [103], where an aptamer enabled the opening of a DNA cage.

Another example of dynamic DNA devices is given by *DNA motors* or walkers. The *burnt-bridges* motor developed by Bath et al. [10], shown in Figure 1.12, produces, unidirectional motion of a single-stranded *cargo* along a track of single stranded *stators*. The mechanism uses a nicking enzyme that specifically cuts the stator/cargo duplex, revealing a toehold that facilitates a branch migration to the next stator. These motors have been shown to walk on a network of tracks embedded in DNA Origami tiles [104]. The motors receive external stimuli and move following a designed path at a speed of 0.1 $\mathrm{nm\,s^{-1}}$ [5].

In principle, arbitrary networks of chemical interactions between DNA strands can be programmed. These, however, are slow compared with the time scales observed for cellular decision making and so far they have not achieved the nonlinear complexity found in natural systems. Fuji and Rondelez [106] introduced nonlinearities in chemical reaction networks by combining DNA strands with polymerases, exonucleases and nickases, extending the molecular programmability of DNA with the specificity of enzymatic catalysis. The Predator-Prey oscillatory system reproduced in Chapter 7 is an example of this kind of reaction network.

In addition to temporal patterns like oscillations, nonlinear systems coupled to diffusion give rise to interesting spatial patterns, such as wave propagation or Turing patterns. These DNA-based synthetic systems bear close resemblance with intercellular signalling mechanisms and are ideal candidates to provide artificial autonomous devices with sensing and signalling capabilities.

---

[5] Molecular motors like kinesin move on microtubules at speeds of 1800 $\mathrm{nm\,s^{-1}}$ [105], enzyme nanomotors free in solution and their phoretic analogues reach ballistic velocities of $\sim$ 1$\mathrm{mm\,s^{-1}}$.

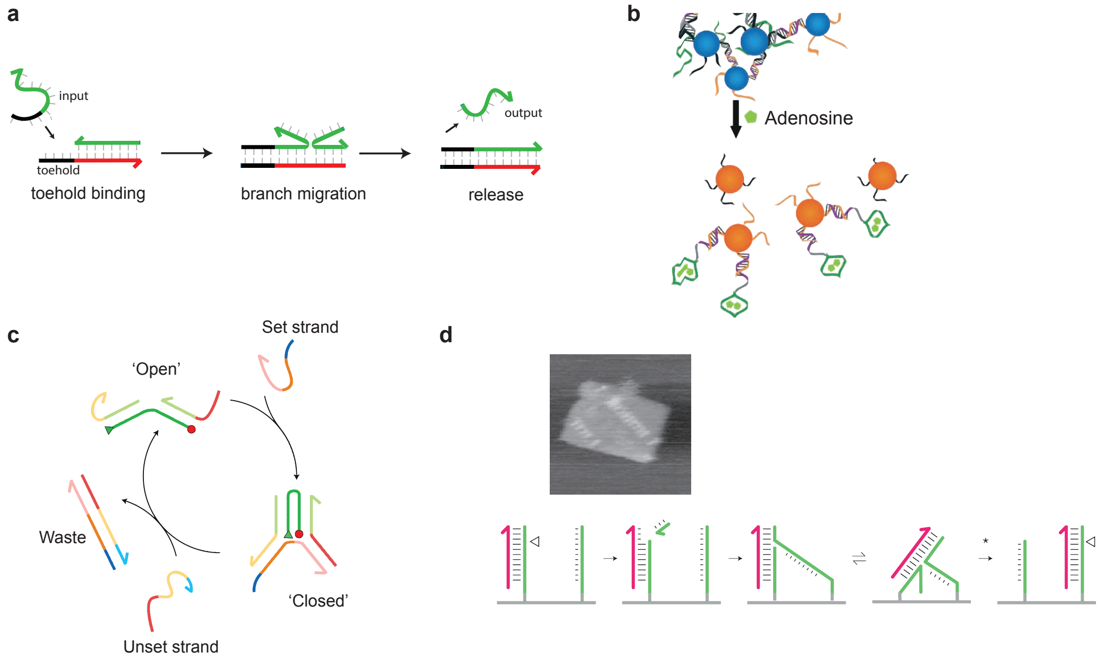

Figure 1.12: *Dynamic DNA nanotechnology:* **a)** Toehold-mediated strand-displacement reaction. An input strand with a toehold domain and a displacement domain, drives the displacement of a target strand. **b)** Adenosin-induced disassembly of nanoparticle aggregates (blue) into dispersed aggregates (red). Adenosin induces a conformational change in the DNA aptamer that coats the nanoparticles [102]. **c)** Full cycle of the DNA tweezer device developed by Yurke et al. [98], one the of the first examples of a functional DNA device. Using the toehold mediated strand displacement, when a set strand is added it forces the tweezer into a close conformation. An unset strand brings the tweezer back to the open conformation generating irreversible waste. This oscillatory open-close conformation was monitored by FRET. **d)** Design of a DNA motor and AFM observation of a track on an origami scaffold by Shelley et al. [104]. Scheme of the *burnt-bridges motor* mechanism [10]: a nicking enzyme cuts the motor-bound stator revealing a toehold at the 3' end of the motor (magenta) that facilitates transfer of the motor to the adjacent intact stator by branch migration. (Figure (b) was modified from [102], Figure (c) was extracted from [70], Figure (d) was taken from [104]).

1.7 Outline of this thesis

Chapter 2 introduces the reader to phoretic propulsion mechanisms. Self diffusiophoresis is presented as an effective propulsion mechanism for chemically-propelled particles. A continuum hydrodynamic model is discussed using Janus and dimer particles as working systems. Experimental observables for self-propelled particles are shown, such as enhanced diffusivity. The implications of diffusiophoresis at the nanoscale are studied using particle-based numerical simulations.

Experimental methods for characterising the activity of micro and nanomotors are presented in **Chapter 3**. Two main experimental approaches are treated: firstly, diffusion constants are extracted by analysing fluctuating signals coming from scattered light (Dynamic Light Scattering (DLS), Nanoparticle Tracking (NTA), emitted fluorescence (Fluorescence Correlation Spectroscopy (FCS)) and nanoimpact voltammetry. Secondly, if particles can be tracked by optical methods, then full trajectories can be reconstructed (bright field microscopy). A theoretical discussion of the techniques is given, together with descriptions of the experimental setups used throughout this work.

Chapter 4 turns the attention to active media, rather than active particles. Using a DNA autocatalytic system, chemical wave propagation of DNA strands is studied both theoretically and experimentally. The DNA reaction network used in this chapter is an example of a DNA active system, out-of-equilibrium and capable of transporting information faster than diffusion. A theoretical discussion of the problem using a simple reaction-diffusion equation is presented, together with the experimental system and analysis tools. The velocity of the travelling wave is shown to be tunable by altering the kinetics of the autocatalytic reaction. This is also done by propagating waves in controlled gradients of spatially varying autocatalytic rates. Numerical simulations and experiments with different shapes of gradients are shown, which result in propagating waves with nonlinear wave velocities that depend on space.

Chapter 5 describes the synthesis of micro and nanomotors and presents the use of DNA to control their assembly. Janus particles and Au/Pt nanoparticles are synthesised using physical vapour evaporation and wet chemical techniques, respectively. Their activity is characterised using the methods described in chapter 3. DNA conjugation strategies are introduced both at the micro and nanoscales using cross-linking chemistry. DNA-mediated interactions between colloids are studied. Finally, the use of DNA Origami to arrange gold nanoparticle/Origami hybrids in 2D lattices of different symmetries is demonstrated.

The focus of **Chapter 6** is the use of DNA as a structural component of the nanomotor, as well as its role as a cargo. The chapter first discusses the DNA Origami design of a monolith structure, its assembly and purification methods. The structures are visualised and characterised by negative staining Transmission Electron Microscopy (TEM) and Atomic Force Microscopy (AFM). Then various choices of catalysts (metallic and enzymatic) are treated and their catalytic activities are assessed by electrochemical methods. Experimental techniques to synthesise DNA-catalyst hybrids follow, with a description of used functionalisation methods. Cargoes of diverse molecular weight are bound to enzymatic nanomotors and characterised. Finally, measurements of the diffusion of nanomotors bound to cargoes are presented using fluorescence correlation spectroscopy (FCS). Enhanced diffusion of catalase-based DNA structures in the presence of H_2O_2 is reported.

Chapter 7 deals with mechanisms of control of autonomous swimmers, namely chemosensing and computation. The focus switches from structural DNA nanotechnology to dynamic aspects. Experiments with DNA aptamers are shown, to induce geometrical changes in DNA nanodevices in response to changes in ligand concentration. A theoretical discussion of a minimal model for robust adaptation in chemotaxis is presented using DNA reaction networks. An enzyme and DNA toolbox is used to realise Lotka-Volterra oscillatory dynamics experimentally with a DNA system. Finally, a potential DNA implementation of a DNA adaptive system is discussed.

2

Phoretic propulsion mechanisms for nanomotors

2.1 Introduction

The development of small devices capable of self-propulsion has potential applications in many areas of nanoscience, where autonomous locomotion and programmability are needed. However, their study also motivates fundamental questions in motility at low Reynolds number, as well as in out-of-equilibrium statistical physics. On the one hand, most self-propelled particles move in a fluid and generate interesting hydrodynamic interactions (at the single-particle and collective levels) [107]. On the other, self-propelled particles are paradigmatic examples of *active matter* and can provide new insights into yet inaccessible and poorly understood out-of-equilibrium phenomena.

One of the goals of this chapter is to identify the experimental conditions that give rise to self-propulsion and to list the physical observables that indicate this property and that distinguish it from mere Brownian motion. Most synthetic self-propelled motors rely on catalytic activity at their surface to achieve motion through various mechanisms that convert chemical energy in the environment into mechanical work. These include bubble propulsion and a large variety of phoretic effects, among which self-diffusiophoresis stands out as an effective propulsion mechanism [39].

Here we discuss the general features of a continuum model for diffusiophoresis and apply it to cases of self-induced phoresis (e.g. Janus and dimer geometries). An analysis of the role of orientational loss due to Brownian motion follows, together with a description of the fluid flow fields that self-propelled particles generate. Enhanced diffusion and mean-squared displacement measurements are presented as evidence for self-propulsion.

Continuum models for phoretic propulsion are useful to describe large motors, but it is not obvious that those principles apply at the nanoscale, where the focus of this thesis is. Therefore, the chapter concludes with particle-based numerical simulations that address this issue and show how self-diffusiophoretic mechanisms also hold at the nanoscale.

2.2 Motility by (self-)diffusiophoresis

We will consider the motion of dispersed particles in a fluid. Colloidal particles move in the presence of gradients due to phoretic effects. *Phoresis*[1] means migration under any type of gradient. A steady-state motion arises from the coupling between a non-equilibrium spatial variation of a thermodynamic field (e.g. temperature, chemical potential) and the interactions of molecules in solution with colloids (interfacial forces). Examples include electrophoresis, driven by an electrical potential, diffusiophoresis due to a concentration gradient of ionic or neutral species, thermophoresis caused by a temperature gradient, and osmophoresis arising from an osmotic pressure gradient.

Diffusiophoresis consists of the motion of dispersed particles induced by a gradient of molecular substances dissolved in a fluid. The same principles underlying this phenomenon (reviewed by Anderson in [32]) can be used to understand the propulsion of particles by self-generated concentration gradients. In the following, diffusiophoresis is explained following derivations in [108] and [109], always emphasizing the physical picture of the phenomenon. First, the mechanism of diffusiophoresis caused by an externally-generated concentration gradient is

---

[1] from Greek, φέρειν=to carry

considered and then this result is applied in the case of self-induced gradients, such as those encountered in chemically-propelled particles.

Diffusiophoresis, as other phoretic mechanisms, has its origin in the coupling between surface forces and fluid fields in the vicinity of the particle. To illustrate this phenomenon, we consider a simple case of a hard colloidal sphere with radius a immersed in a solvent and a dilute neutral solute with an inhomogeneous concentration field $c(\mathbf{r})$ (see Figure 2.1 (a)). The surrounding solvent is described as a viscous continuous fluid[2]. The solute molecules interact with the surface of the particle through a short-range potential of mean force W (obtained by coarse-graining over all solvent molecules) and the characteristic range of interaction is given by $L = R_0 - a$, where R_0 is the radius of the boundary-layer and a is the radius of the particle (see Figure 2.1 (a)). This potential can be attractive $W < 0$ or repulsive $W > 0$. L defines the interfacial region where surface-solute interactions take place. If the particle is large compared to the few nm range of the interfacial layer (thin surface film approximation [32]), then we can consider the surface to be locally flat (Figure 2.1 (a) and (b)). In this approximation, we introduce a local coordinate frame, where the vector $\mathbf{y} = y\hat{\mathbf{n}}$ is along the normal, $\mathbf{s}$ is tangential and $y = 0$ at the surface of the particle. With this coordinate system we can describe how $c(\mathbf{r})$ varies in space. The next derivations demonstrate that the concentration field induces a pressure gradient, which is balanced by forces from the fluid flow. This results in an effective slip velocity $\mathbf{v}^{(\mathbf{s})}$ of the fluid which, in turn, translates the particle with a velocity $\mathbf{V}$.

How a concentration field $c(\mathbf{r})$ translates into a pressure gradient

The surface applies a force to the liquid via its interaction with the solute within the interfacial layer L. For an ideal solute, we can write the concentration distribution from the surface in terms of the Boltzmann factor $c(\mathbf{s}, y) = \tilde{c}(\mathbf{s})e^{-\beta W(y)}$, where

---

[2] For particles of radius $R \sim 1\,\mu$m and typical velocities $|V| \sim 1 - 10\,\mu\mathrm{m\,s}^{-1}$ observed experimentally, the corresponding Reynolds number is small $Re = \frac{\rho R V}{\eta} \lesssim 10^{-5}$. Thus, the Navier-Stokes equation is greatly simplified, as the inertial terms can be neglected. Similarly, the role of advection of the solute, as measured by the Péclet number $Pe = \frac{|V|R}{D}$, is on the order of $Pe \approx 10^{-3} - 10^{-1}$ and therefore negligible. This allows a decoupling of the solute diffusion dynamics from the Stokes flow of the fluid.

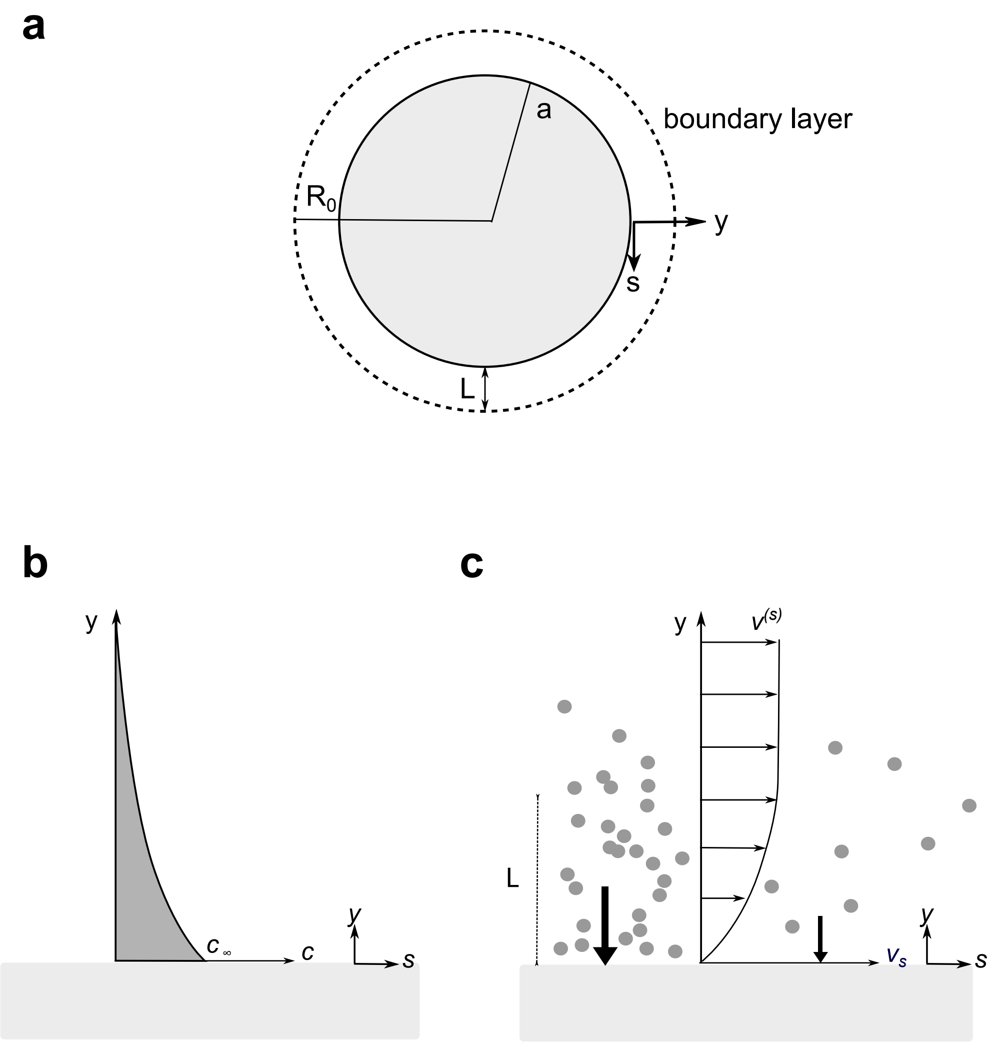

Figure 2.1: *Diffusiophoresis* **a)** Diagram showing a particle of radius a immersed in a fluid. A boundary layer of thickness L is shown, where interaction with the solute is non-zero. The outer radius of the particle is R_0 and a coordinate frame of reference is chosen on the surface of the particle. **b)** Solute concentration distribution along the direction of the surface normal $c(\mathbf{s}, y) = \tilde{c}(\mathbf{s})e^{-\beta W(y)}$. **c)** Diffusiophoresis for a neutral solute attracted to the surface. A concentration gradient is imposed with higher solute concentration on the left side (the thickness L indicates the interface) ‘pushing’ the fluid against the surface. A pressure gradient results in the interfacial layer, which creates a flow opposite to the concentration gradient, from high concentration to low. An apparent slip velocity builds up around the particle with its asymptotic value reached at $\mathbf{v}_s(s, y = L) = \mathbf{v}^{(s)}$.

$\beta = \frac{1}{k_B T}$ (see Figure 2.1 (b)). For $a \gg L$, the concentration along the surface $\mathbf{s}$ varies over a longer length scale than those over which the interfacial forces operate. Then we can consider that equilibrium along $\mathbf{y}$ is much faster than along the tangential plane $\mathbf{s}$.

A solute particle experiences a force $-\frac{dW(y)}{dy}$ which, through force balance, is transmitted to the fluid and leads to a pressure field $p(\mathbf{s}, y)$. The pressure can be determined from:

$$\frac{\partial p(\mathbf{s}, y)}{\partial y} + c(\mathbf{s}, y)\frac{dW(y)}{dy} = \frac{\partial}{\partial y}(p(\mathbf{s}, y)) - k_B T c(\mathbf{s}, y) = 0 \tag{2.1}$$

which yields a pressure

$$p(\mathbf{s}, y) = p_\infty + k_B T \tilde{c}(\mathbf{s})(e^{-\beta W(y)} - 1)$$

Slip velocity and the Derjaguin length λ_D

The tangential variation in pressure due to the change in concentration along $\mathbf{s}$ creates a solvent flow. The viscous stress of this flow balances the tangential pressure gradient. This can be expressed by the Stokes equation[3] as,

$$\eta \frac{\partial^2}{\partial y^2}\mathbf{v}_s - \nabla_s p = 0 \tag{2.2}$$

where η is the shear viscosity, $\mathbf{v_s}{=}\mathbf{v}_\parallel{=}\mathbf{1}-\mathbf{v}_\perp$ is the tangential component of the fluid velocity and $\nabla_\mathbf{s} = (\mathbf{1} - \hat{\mathbf{y}} \cdot \hat{\mathbf{y}}) \cdot \nabla$. The velocity field $\mathbf{v_s}$ is obtained by integrating twice equation (2.2) subject to the following boundary conditions:

$$\mathbf{v}_s(y=0) = 0 \qquad \text{(no slip on the surface)} \tag{2.3}$$

$$\lim_{y \to \infty}\left(\frac{\partial \mathbf{v}_s}{\partial y}\right) = 0 \qquad \text{(no pressure gradient in the bulk)} \tag{2.4}$$

yields a velocity field $\mathbf{v_s}$, given by:

$$\mathbf{v_s}(\mathbf{s}, y) = -\frac{k_B T}{\eta}\left(\nabla_s \tilde{c}(\mathbf{s})\right)\int_0^y dy' \int_{y'}^{\infty} dy'' \left(e^{-\beta W(y'')} - 1\right) \tag{2.5}$$

Even though the velocity field is zero at the surface of the particle, because of the small thickness of the boundary layer compared with the size of the particle

---

[3] The Stokes equation is the linearisation of the Navier-Stokes Equation at low Re and relates the pressure and viscous stresses through momentum balance: $\eta\nabla^2\mathbf{u} - \boldsymbol{\nabla} p + \mathbf{f} = 0$

$a \gg L$, from the point of view of the particle, the fluid velocity has a value $\mathbf{v_s}(\mathbf{s}, y)$ at a short distance, and therefore acts as an effective *slip* velocity. $\mathbf{v_s}(\mathbf{s}, y)$ reaches its asymptotic value $\mathbf{v}^{(s)}$ at $y \approx L$, we can then integrate (2.5) by taking the limit $y \to \infty$ [4]

$$-\mathbf{v}^{(s)}(\mathbf{s}) = \frac{k_B T}{\eta} \left(\nabla_s \tilde{c}(\mathbf{s})\right) \int_0^\infty dyy \left(e^{-\beta W(y)} - 1\right) = \frac{k_B T}{\eta} \left(\nabla_s c(\mathbf{s})\right) \lambda_D^2 \tag{2.6}$$

This expression for the slip velocity was derived by Derjaguin in [110]. The *Derjaguin length* $\lambda_D \equiv \left(\int_0^\infty dyy \left(e^{-\beta W(y)} - 1\right)\right)^{1/2}$ is a measure of the interaction potential ($\lambda_D^2 < 0$ for repulsive interactions and $\lambda_D^2 > 0$ for attractive).

Equation (2.6) shows that the coupling between surface forces and fluid dynamics leads to a flow of solvent around the particle with effective slip velocity $\mathbf{v}^{(s)}(\mathbf{s})$. For an attractive interaction (as shown in Figure 2.1 (c)), the flow moves from high concentration of solute to low concentration. In the reference frame of the fluid, this means that the particle moves up the concentration gradient[5].

Particle velocity

The previous calculation can be used to determine the velocity of the particle $\mathbf{V}$. As mentioned above, the flow field outside the boundary layer is described by the Stokes equation for a viscous force-free incompressible fluid:

$$\boldsymbol{\nabla} \cdot \mathbb{P} = 0, \qquad \boldsymbol{\nabla} \cdot \mathbf{v} = 0 \tag{2.7}$$

where the pressure tensor is given by $\mathbb{P} = -p\mathbf{1} + \eta(\nabla\mathbf{v} + \nabla\mathbf{v}^T)$ and the flow field is subject to the boundary conditions: $\mathbf{v}(R_0) = \mathbf{V} + \mathbf{v}^{(s)}$ at the surface of the particle and $\lim_{r\to\infty} \mathbf{v}(\mathbf{r}) = 0$.

---

[4] We evaluate this integral by noting that if $f(y') = \int_{y'}^\infty dy'' \left(e^{-\beta W(y'')} - 1\right)$, then by differentiating under the integral sign we have $\frac{df(y')}{dy'} = -\left(e^{-\beta W(y')} - 1\right)$. Now (2.5) can be evaluated by parts:

$$\int_0^\infty f(y')dy' = [y'f]_0^\infty - \int_0^\infty y\frac{df}{dy'}dy' = \int_0^\infty ydy \left(e^{-\beta W(y)} - 1\right)$$

[5] The opposite is true with repulsive interactions. For example, wax particles dispersed in a non-uniform glucose solution, migrate toward lower sugar concentration because of their unfavourable interaction $\lambda_D^2 < 0$ [111]. This is one of the first observations of diffusiophoresis.

We now introduce an auxiliary field with $\mathbb{P} = \mathbb{P}' + \mathbb{P}''$ and $\mathbf{v}$=$\mathbf{v}'$+$\mathbf{v}''$, where $\mathbf{v}$ satisfies the boundary condition $\mathbf{v}'(R_0) = \mathbf{v}^{(s)}$ and $\mathbf{v}''$ satisfies $\mathbf{v}''(R_0) = \mathbf{V}$, corresponding to a passive particle with no slip velocity. One way to solve (2.7) is to invoke the Lorentz reciprocal theorem [11]. This theorem states that any two flow fields $\mathbf{v}'$ and $\mathbf{v}''$, which are solutions to the force-free Stokes equation (2.7) within the same domain, obey the relation:

$$\int_{S_0} dS\hat{\mathbf{n}} \cdot \mathbb{P}' \cdot \mathbf{v}'' = \int_{S_0} dS\hat{\mathbf{n}} \cdot \mathbb{P}'' \cdot \mathbf{v}' \tag{2.8}$$

where the surface integral is defined as $\int_{S_0} dSf(\mathbf{r}) = \int d\mathbf{r}\delta(r - R_0)f(\mathbf{r})$. We can now apply this result to a simple solvable case, such as a sphere moving at a velocity $\mathbf{v}'' = \mathbf{V}$. The pressure tensor on the surface of a sphere moving at $\mathbf{V}$ can be solved analytically [112] and is given by $\hat{\mathbf{n}} \cdot \mathbb{P}''|_{r=R_0} = -\frac{6\pi\eta R_0\mathbf{V}}{4\pi R_0^2}$ (*Stokes' law*).

Given the boundary conditions imposed on the fields, (2.8) can be rewritten as:

$$\int_{S_0} dS\hat{\mathbf{n}} \cdot \mathbb{P}' \cdot \mathbf{V} = \int_{S_0} dS\hat{\mathbf{n}} \cdot \mathbb{P}'' \cdot \mathbf{v}^{(s)} = 6\pi\eta R_0 \mathbf{V} \cdot \left\langle \mathbf{v}^{(s)} \right\rangle_S \tag{2.9}$$

where the angle brackets indicate a surface average $\left\langle \mathbf{v}^{(s)} \right\rangle_S = \frac{\int_{S_0} dS\mathbf{v}^{(s)}}{4\pi R_0^2}$. Using Gauss' law in (2.7) we have,

$$\int_{S_0} dS\hat{\mathbf{n}} \cdot \mathbb{P}' = -\int_{S_0} dS\hat{\mathbf{n}} \cdot \mathbb{P}'' \tag{2.10}$$

and inserting in (2.9) we obtain the important relation between the particle velocity and the slip velocity $\mathbf{V} = -\langle \mathbf{v}^s \rangle_S$. This expression shows that the velocity of the particle is the negative of the phoretic slip, averaged over the surface of the particle. Using the expression for the slip velocity in (2.6), the velocity of the particle is given by:

$$\mathbf{V} = \frac{k_B T}{\eta} \left\langle \nabla_s c_0(\mathbf{s}) \right\rangle_S \lambda_D^2 \tag{2.11}$$

which expresses the particle velocity in terms of the viscosity of the solution η, the Derjaguin length squared λ_D^2 and the gradient of the concentration field along the surface $\langle \nabla_s c_0(\mathbf{s}) \rangle_S$.

Self-diffusiophoresis

The result in (2.11) can be used for particular cases where the concentration gradient is self-generated, rather than externally imposed. This is the case of many chemically active phoretic motors, which rely on at least two principles for their motion: 1) asymmetric catalytic activity and 2) product-particle interactions. These are the ingredients for the self-diffusiophoretic particle model introduced by Golestanian in [37].

For a Janus particle as the one shown in Figure 2.2, one hemisphere is catalytically active (C) and the other is not (N), while both sides have interactions with the solute. The inhomogeneous concentration field of solute can be found by solving the reaction-diffusion equation outside the boundary layer, subject to boundary conditions that reflect the creation of new product on one hemisphere. We will consider that particle motion is slower than solute diffusion ($Pe \ll 1$); this implies that the reaction-diffusion process reaches steady-state.

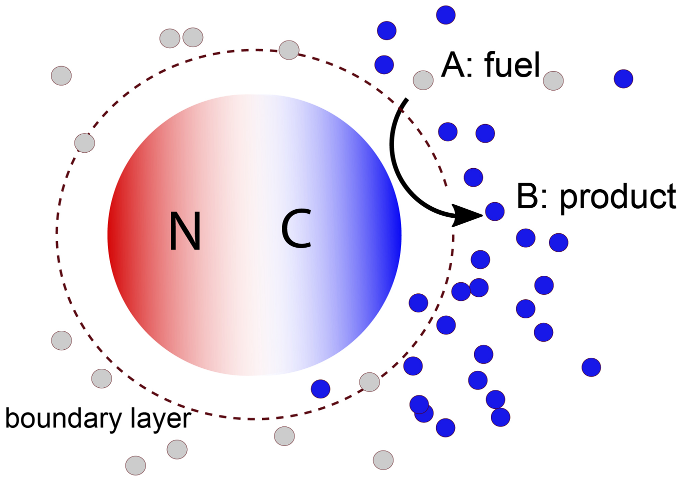

Figure 2.2: Janus particle composed of an inert hemisphere (N) and a catalytic hemisphere (C) which converts fuel particles (A) into (B) creating an inhomogeneous distribution of product. The boundary layer is shown, where interfacial forces between solute and surface take place.

Taking $\hat{\mathbf{z}}$ as the vector from the centre of the particle to the pole of the catalytic hemisphere (C), the projection of the velocity in this direction is given by [43, 113]:

$$V_z = \frac{k_B T}{\eta} \frac{c_0}{3R_0} (\lambda_C^2 + \lambda_N^2) a_1 \tag{2.12}$$

where

$$\lambda_j^2 = \int_0^\infty dyy(e^{-\beta W_{Aj}(y)} - e^{-\beta W_{Bj}(y)})$$

are the Derjaguin lengths that depend on the interactions between fuel (A) and product (B) with the two hemispheres of the Janus particle ($j = C, N$). In (2.12) c_0 refers to the total concentration of initial fuel, while the coefficient a_1 depends on the solution of the steady-state diffusion equation $D\nabla^2 c(\mathbf{r}) = 0$.

The solution of the reaction-diffusion equation can be expressed as a series of Legendre polynomials:

$$c(r, \theta) = c_0 \sum_l a_l f_l(r) P_l(cos\theta) \tag{2.13}$$

Further, this solution must fulfil $\lim_{r\to\infty} c_A(r, \theta) = c_0$ and the 'radiation' boundary conditions[6] which account for the catalytic reaction $A \rightarrow B$ on the surface of the particle.

$$4\pi R_0^2 D \frac{\partial c_A(r, \theta)}{\partial r}|_{R_0} = \kappa c_A(r, \theta)\Theta(\theta) \tag{2.14}$$

where $\Theta(\theta)$ is unity on the catalytic hemisphere and zero otherwise and D is the diffusion constant of the solute (same for both species). (2.14) states that the flux at contact is proportional to the local reactant concentration. The intrinsic reaction rate at the surface κ determines the degree of diffusion control.

For a diffusion-controlled reaction (diffusion-limited), the chemical reaction occurs so quickly that the reaction rate is dominated by the diffusion coefficient and is given by the Smoluchowski rate constant $k_D = 4\pi R_0 D$. In this case the velocity of the Janus particle takes the form:

$$V_z \sim \frac{k_B T}{\eta} \frac{c_0}{3R_0} (\lambda_C^2 + \lambda_N^2) a_1^D \tag{2.15}$$

where a_1^D is a constant. Therefore in this limit the velocity of the particles scales as $1/R_a$, which has been experimentally observed by Ebbens et al. in [113].

---

[6] The Collins-Kimball radiation boundary conditions [114] are a generalisation of the Smoluchowski model of bimolecular reaction rates. Colliding molecules are modelled as isotropically reactive spheres and instead of a perfectly absorbing boundary condition $c_A(R_0) = 0$ (assumed by Smoluchowski), the radiation boundary conditions consider a partially absorbing surface.

The expressions of the velocities that were derived here are a useful measure of the departure from equilibrium that self-propelled particles exhibit. The propulsion velocity is highly dependent on $(\lambda_C^2 + \lambda_N^2)$, which are given by the nature of the interaction potentials (repulsive $\lambda_C^2 < 0$ or attractive $\lambda_C^2 > 0$, for λ_N=0). Their sign determines the direction of propulsion. Similar arguments hold for a dimer system (shown in Figure 2.5). The dimer geometry has been extensively studied by particle-based simulations [115]. This geometry is used as a model system for experimental realisations of DNA-based nanomotors in section 2.4.

Ballistic velocity calculations from a continuum model like in equation (2.15) or from particle based simulations are often masked by thermal fluctuations, which dominate at the nanoscale. The contribution of orientational randomisation and its effect in measurable observables is the subject of section 2.3.

Self-propelled particle vs. dragged particle

In an experimental setting, the natural observables of the systems are either the velocity of the particle or the mean squared displacement (MSD) that result from particle tracking measurements. Alternative approaches involving light-scattering or single-molecule experiments can probe the rotational and translational diffusion of the particles, too. However, these measurements also hold for motile particles that do not self-propel. One may ask what distinguishes a self-propelled particle from one subjected to an external field, as in principle, particle trajectories and velocities alone do not shed light on their propulsion mechanism. An answer to this question lies in the different flow fields that phoretic particles and dragged particles create around them. For example, the velocity field, that a particle moving under an external force creates is given by 'the stokeslet' and scales as $v \sim r^{-1}$ (Figure 2.3 (b)), whereas a sphere moving at a speed $\mathbf{V}$ by phoretic mechanisms, acts as a force dipole ('stresslet') (Figure 2.3 (a)) and creates a flow velocity field that decays much faster $v \sim r^{-2}$. This is why self-propelled particles have weaker long-range hydrodynamic interactions than particles dragged by an external force. Further, phoretic particles together with their boundary layer are subject to a net zero force.

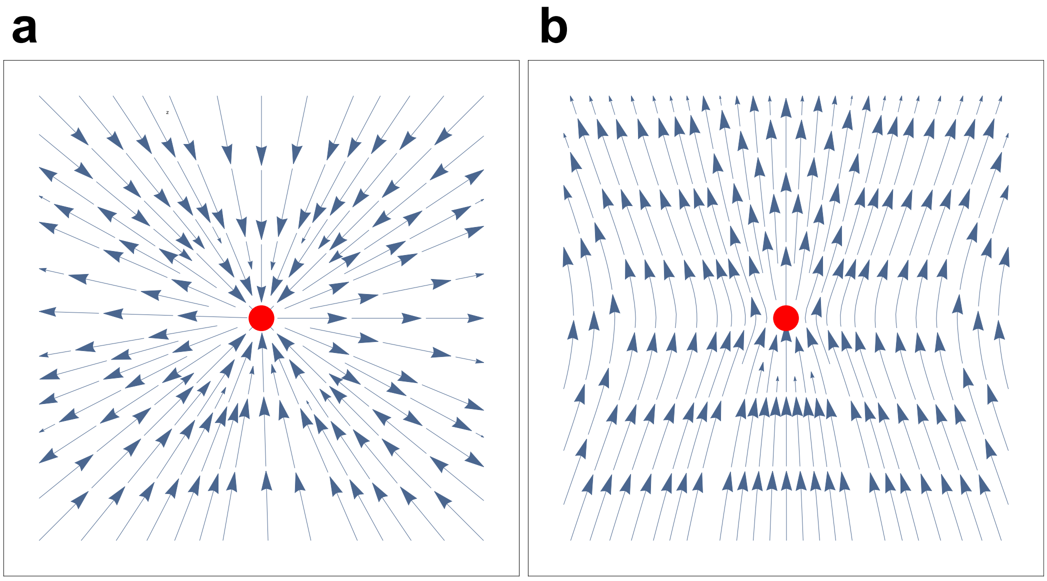

Figure 2.3: **a)** Fluid flow caused by a self-propelled particle moving in the $\hat{\mathbf{y}}$ direction $\mathbf{v}(\mathbf{r}) = \frac{A_{strs}}{r^2}[3(y/r)^2 - 1]\hat{\mathbf{r}}$ ('stresslet'). **b)** Fluid flow caused by a particle moving under an external force in the $\hat{\mathbf{y}}$ direction, $\mathbf{v}(\mathbf{r}) = \frac{A_{stokes}}{r}(\mathbf{I} + \hat{\mathbf{r}}\hat{\mathbf{r}})\hat{\mathbf{y}}$ ('stokeslet').

2.3 Orientational Brownian motion in self-propelled particles

Chemically-powered motors propel themselves in solution with a constant velocity when they reach steady-state. Without Brownian motion, these particles would show a ballistic mean-squared displacement ($MSD \sim V^2t^2$). However, thermal fluctuations due to collisions with the fluid play important roles in the dynamics of self-propelled particles, as they are subject to translational and rotational diffusion, in addition to their ballistic propulsion. The tumbling of particles due to rotational Brownian motion is a key ingredient that contributes to the MSD of the motor. Ballistic events combined with diffusive ones result in *active Brownian motion*, which contains properties from both types of motion. For longer times compared with the rotational diffusion time, the motion is essentially diffusive, with a larger diffusion constant than that of passive particles.

The Stokes-Einstein relation gives an expression for the rotational diffusion time, which is the time it takes for the particle to lose direction and reorient[7]. It is related to the rotational diffusion coefficient D_R as,

$$\tau_R = \frac{1}{2D_R} = \frac{4\pi\eta R^3}{k_B T} \tag{2.16}$$

where R is the radius of the particle. For time scales below $t \ll \tau_R$, the motion is ballistic, however for time scales $t \gg \tau_R$ it is purely diffusive. In order to understand this effect better, it is useful to calculate the mean squared displacement and study how it behaves in those two limits.

The velocity of the self-propelled particle $\mathbf{V}(t)$ can be decomposed into the average propulsion velocity V_u along the direction $\hat{\mathbf{u}}(t)$, and deviations from this quantity due to fluctuations, $\mathbf{V}(t) = V_u + \delta\mathbf{V}(t)$. The velocity correlation function is then given by:

$$C_V = \frac{1}{3}\langle \mathbf{V}(t)\cdot\mathbf{V}\rangle \approx \frac{1}{3}\left(V_u^2\langle \hat{\mathbf{u}}(t)\cdot\hat{\mathbf{u}}\rangle + \langle \delta\mathbf{V}(t)\cdot\delta\mathbf{V}\rangle\right) \tag{2.17}$$

where the average is taken in the steady-state and the cross-correlation terms between orientation and velocity fluctuations have been neglected. Knowing the velocity correlation function, we can compute the diffusion coefficient[8] by $D = \int_0^\infty C_V(t)dt$. For this computation, we need a measure of how orientation is lost in the time scale τ_R. Assuming the orientational correlation function decays exponentially with time

---

[7] For a hard sphere the friction term is given by $\xi_r = 8\pi\eta R^3$ in $D_r = \frac{k_B T}{\xi_r}$. Rotational diffusion can be analysed in the same fashion as translational diffusion. For example, the mean-square angular deviation $\langle\theta^2\rangle = 2D_r t$ is analogous to the 1-D translational MSD, $\langle x^2\rangle = 2Dt$ [116].

[8] From Einstein's relation $D = \frac{1}{6}\frac{\langle \mathbf{r}^2\rangle}{t}$, we can express the diffusion coefficient (macroscopic property) in terms of time correlation functions, that represent the microscopic fluctuation of the system. We rewrite the displacement from the initial position as $\mathbf{r} = \int_0^t \mathbf{V}(t')dt'$ and substitute into Einstein's relation:

$$D = \lim_{t\to\infty}\frac{1}{6t}\int_0^t dt'\int_0^t dt''\langle \mathbf{V}(t')\cdot\mathbf{V}(t'')\rangle = \lim_{t\to\infty}\frac{1}{3t}\int_0^t dt'\int_0^{t'} dt''\langle \mathbf{V}(t')\cdot\mathbf{V}(t'')\rangle \tag{2.18}$$

Because the fluid is in equilibrium, any ensemble average should not change with time, hence $\langle \mathbf{V}(t')\cdot\mathbf{V}(t'')\rangle = \langle \mathbf{V}(t)\cdot\mathbf{V}(0)\rangle$ where $t = t'' - t'$ and we obtain the *Green-Kubo* expression for the diffusion coefficient, showing a clear link between the motion of the particle and its diffusion coefficient.

$$D = \frac{1}{3}\int_0^\infty dt\langle \mathbf{V}(t)\cdot\mathbf{V}\rangle \tag{2.19}$$

constant τ_R as $\langle(\hat{\mathbf{u}})(t)\cdot\hat{\mathbf{u}}\rangle \approx e^{-t/\tau_R}$, we obtain for the diffusion coefficient:

$$\begin{aligned} D &= \frac{1}{3}\int_0^\infty \langle\delta\mathbf{V}(t)\cdot\delta\mathbf{V}\rangle dt + \frac{V_u^2}{3}\int_0^\infty \langle(\hat{\mathbf{u}})(t)\cdot\hat{\mathbf{u}}\rangle dt && (2.20)\\ &= \frac{1}{3}V_u^2\tau_R + D_0 && (2.21)\end{aligned}$$

where $D_0 = \frac{1}{3}\int_0^\infty\langle\delta\mathbf{V}(t)\cdot\delta\mathbf{V}\rangle dt$ is the diffusion coefficient when there is no propulsion. This is equivalent to the Stokes-Einstein relation, if we assume an exponential decay of fluctuation correlations with time constant $\tau_v = \frac{M}{6\pi\eta R}$, i.e. $D_0 = \frac{k_BT}{6\pi\eta R}$.

It is also useful to calculate the mean-squared displacement $\Delta L^2(t)$ of the motor, which is the most experimentally accessible observable when particle tracking is available. From the Einstein relation, we have $D = \frac{1}{6}\frac{\langle\mathbf{r}^2\rangle}{t}$, and using the expression (2.17), we express the MSD in terms of the velocity correlation function as:

$$\begin{aligned} \Delta L^2(t) &= 6\int_0^t dt' D(t') = 6\int_0^t dt'\int_0^{t'} dt''\frac{1}{3}\langle\mathbf{V}(t)\cdot\mathbf{V}\rangle && (2.22)\\ &= 6\int_0^t dt'\left[\int_0^{t'} dt''\frac{1}{3}\left(V_u^2 e^{-\frac{t}{\tau_R}}\right) + \int_0^{t'} dt''\frac{1}{3}\langle\delta\mathbf{V}(t)\cdot\delta\mathbf{V}\rangle\right] && (2.23)\end{aligned}$$

for $t \gg \tau_v$, we substitute the last term for $D_0 = \lim_{t'\to\infty}\frac{1}{3}\int_0^{t'}\langle\delta\mathbf{V}(t)\cdot\delta\mathbf{V}\rangle dt$ and the integral yields[9]

$$\Delta L^2(t) \approx 6\left(D_0 + \frac{1}{3}V_u^2\tau_R\right)t - 2V_u^2\tau_R^2(1 - e^{\frac{-t}{\tau_R}}) \qquad (2.25)$$

This equation shows two important limits, corresponding to ballistic and diffusive regimes, separated by the time scale set by the rotational diffusion τ_R. On the one hand, for short times $t \ll \tau_R$, ballistic motion dominates and $\Delta L^2(t) \approx V_u^2 t^2$. On the other, for long times $t \gg \tau_R$, it exhibits a mean squared displacement linear with time, i.e. diffusive behaviour $\Delta L^2(t) \approx 6\left(D_0 + \frac{1}{3}V_u^2\tau_R\right)t$. We obtain the effective diffusion coefficient calculated in (2.20).

---

[9] This equation is normally cited in experimental work related to active particles. When 2D diffusion measurements are taken, the expression in (2.25) changes to:

$$\Delta L^2(t)_2D \approx 4\left(D_0 + \frac{1}{2}V_u^2\tau_R\right)t - 2V_u^2\tau_R^2(1 - e^{\frac{-t}{\tau_R}}) \qquad (2.24)$$

There is a general discrepancy in the literature regarding this expression that can be traced back to the definition of τ_R (either $\tau_R = \frac{1}{2D_R}$ or $\tau_R = \frac{1}{D_R}$). Howse et al. introduce in [12] an effective diffusion constant for swimmers in 2D given by $D_{eff} = D_0 + \frac{1}{4}V^2\tau_R$. This expression does not apply to results obtained in 3D ((2.20) should be used). The discrepancy in the prefactor has extended to some experimental work, such as [42, 117].

This results in a persistent random walk, due to the competition between ballistic propulsion and directional randomisation due to rotational Brownian motion. The violation of the Stokes-Einstein law is a sign of the out-of-equilibrium properties of self-propelled particles. Experimentally, the effective diffusion coefficient D_{eff} is obtained by measuring the slope of the mean square displacement at times $t \gg \tau_R$.

Examples with nano and micro motors

Here we list some examples of synthetic motors of different sizes and experimental velocities, to illustrate the effect of size in the effective diffusion and separation of ballistic and diffusive regimes. Figure 2.4 shows the computed mean-squared displacement for micro and nanomotors. The crossover between ballistic and diffusive regimes occurs at a timescale determined by the rotational diffusion time τ_R. While micron-sized particles lose orientation in a measurable timescale of seconds, nanosized particles randomise their direction after μs. This makes a direct measurement of nanomotor velocities experimentally challenging. Table 2.1 lists several motor geometries and their observed enhanced diffusion, as measured experimentally in this thesis. The larger the particles the stronger the ballistic contribution to the enhanced diffusion.

Table 2.1: Characteristic dynamic parameters for some experimental motors explored in this thesis

Motor	Radius (nm)	D_0 (µm^{2}s^{-1})	velocity[10]	τ_R	D_{eff}(µm^{2}s^{-1})	$\frac{D_{eff}}{D_0}$	Chapter
Janus micromotor	1000	0.2	5 μm s^{-1}	3 s	26	124	5
Pt/Au nanomotor	15	14	2.2 mm s^{-1}	2.5 μs	18	1.3	5
Catalase	5	42	10 mm s^{-1}	0.75 μs	63	1.5	6

2.4 Multiparticle collision dynamics of nanomotors

The computation of motor velocities using phoretic theory is possible for simple geometries (e.g. Janus sphere in equation (2.15)). Still, testing alternative geometries for motors which are subject to strong thermal fluctuations is best done with

---

[10] For Pt-Au and catalase the velocity was obtained from the equation 2.20

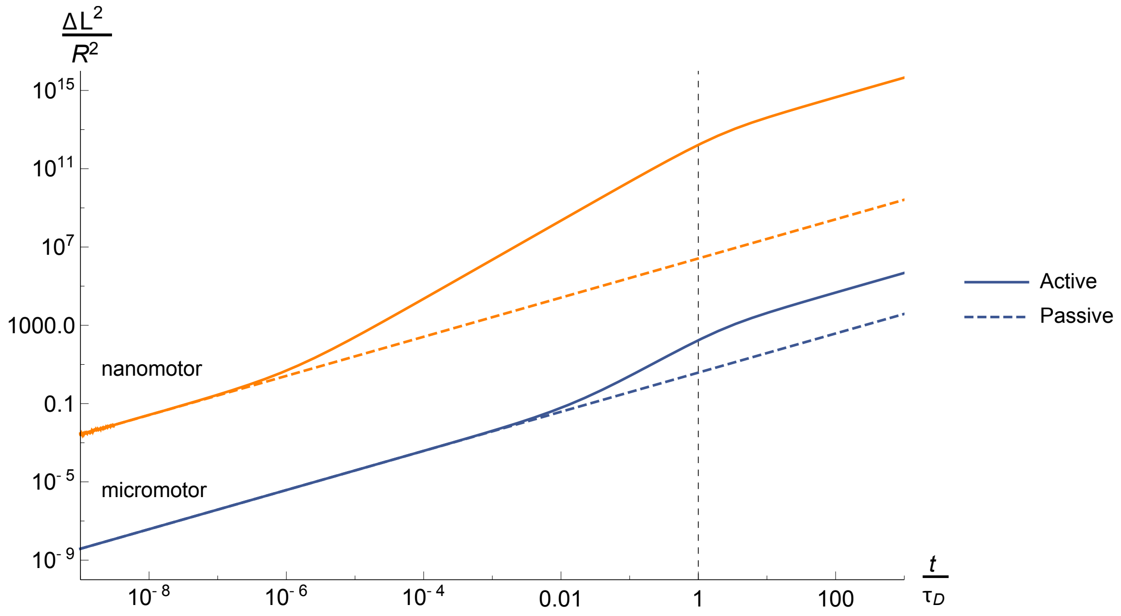

Figure 2.4: Computed mean-squared displacement (MSD) from (2.25) for a R=1 µm particle with characteristic rotational diffusion time τ_R=3 s propelling at a velocity of 5 µms^{-1} (in blue) and for a R=30 nm nanomotor with τ_R=84 µs and propelling at 0.66 mms^{-1}. τ_R distinguishes the ballistic regime (indicated by dashed lines) and diffusive regimes (solid line).

numerical simulations, as continuum theories break down[11] at the nanoscale. A successful particle-based modelling strategy is the Multiparticle Collision Dynamics (MPCD) algorithm [119]. Briefly, this approach can be described as a hybrid scheme that contains certain properties of a full (and computationally costly) Molecular Dynamics (MD). The major difference of MPCD with full MD is that solvent-solvent interactions are not explicitly computed and are replaced by cell-wise collisions at fixed time intervals. However, collisions of solvent particles with embedded objects (e.g. nanomotors) are computed using full MD. This renders otherwise untractable problems feasible, such as the propulsion of catalytic motors. A major improvement of MCD is the addition of reaction events (fuel $A \rightarrow B$) at the surface of a motor. This addition to the algorithm is the basis of the Reactive Multiparticle Collision

---

[11] The breakdown of the Navier-Stokes description can be quantified by the *Knudsen number* $K_n \equiv \frac{\lambda_{free}}{L}$, where λ_{free} is the molecular mean free path and L is the characteristic length scale of the fluid flow. Important non-continuum effects appear for $K_n \gtrsim 0.1$ [118]. For the case of an enzyme with characteristic length of 5 nm surrounded by water molecules (with mean-free path $\lambda_{free} \approx 3$ Å), $K_n \sim 0.06$, which is in a regime where effects of the discrete nature of the fluid should appear.

Dynamics (RMPCD) algorithm used in this chapter to model a dimer nanomotor [12].

A fluid described by Multiparticle Collision Dynamics (MPCD) consists of N point particles with defined mass, position and velocity. The particles evolve in two steps: (i) independent streaming of the particles for a duration τ and (ii) cell-wise collision of particle velocities. For example, particle i will undergo the following steps:

$$x'_i = x_i + v_i \tau \tag{2.26}$$

$$v'_i = v_\xi + \omega_\xi (v_i - v_\xi) \tag{2.27}$$

where the prime denotes the quantities after the corresponding step. ξ is a cell and ω_ξ is a rotation operator and v_ξ is the centre-of-mass velocity in the cell. All cells constitute a regular lattice in a box and each simulation step conserves mass, energy and linear momentum.

The dimer nanomotor

In the following, we consider the Rückner-Kapral dimer [115] as a model for the construction of a DNA nanomotor. A dimer structure consists of a catalytic and non-catalytic spheres as shown in Figure 2.5, where sphere C converts fuel molecules (A) into products (B). The boundary layer represents the region where interactions take place. The goal is to simulate the motion of a nanomotor with such dimer geometry and to obtain the average propulsion velocity and mean-squared displacement. We then use these results to study the enhanced diffusion for the chosen structure and interaction parameters.

All quantities reported here are in dimensionless simulation units[13]. Units of length are defined from the simulation box (L=32 a_0), energies in units of $k_B T$, and time in units of $t_0 = \sqrt{m a_0^2 / k_B T}$. The simulation volume also contains solvent A (fuel) and B (product) with mass $m = 1$ and temperature $T = 1/3$. The total number of solvent molecules in the volume is 300 000 giving an average number

---

[12] The RMPCD algorithm was developed by Pierre de Buyl and colleagues. Full details can be found in [120] and [121].

[13] In MPCD there is no unique relation to physical units, e.g. increasing temperature is equivalent to rescaling time. However, a mapping is possible by considering selected quantities (e.g. self-diffusion of the fluid, viscosity). Possible mapping strategies are reviewed in [118]

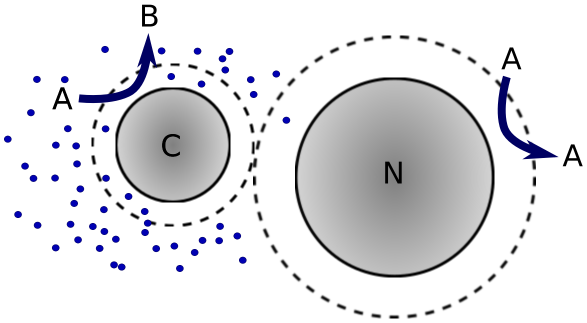

Figure 2.5: Rückner-Kapral dimer consisting of a catalytic sphere C and a non-catalytic N separated by a distance d. A is converted into B in the vicinity of the catalytic hemisphere. Solute-particle interactions (Lennard-Jones type) only take place in the boundary layer (dashed lines). Diagram adapted from [115].

density of $n = 9$ particles/cell. The diameter of the catalytic sphere is R=4 and the non-catalytic sphere R=8, with a centre-to-centre distance of d=6.5. The total energy of the system is conserved by refuelling the solvent A in every simulation steps in order to guarantee that non-equilibrium is maintained.

The total force on the motor can be expressed as the sum of the forces acting on the catalytic sphere C and non-catalytic sphere N:

$$F = -\sum_{\alpha} \int d^3 x c_\alpha(x) \left(\frac{dV_{\alpha C}(x_C - x)}{dx} + \frac{dV_{\alpha N}(x_N - x)}{dx} \right) \tag{2.28}$$

where $\alpha = A, B$ are fluid particle species and $V_{\alpha C}$ and $V_{\alpha N}$ are the interaction potentials of the fluid species with the C and N spheres respectively. The potential is of Lennard-Jones-type[14] and for this simulation repulsive interactions were used with LJ prefactors $\epsilon_A = 1$ and $\epsilon_B = 0.1$ for interactions with A (fuel) and B (product) respectively, as the ones used in [115]. To simulate a passive dimer the interaction parameters were chosen as $\epsilon_B = \epsilon_A = 1$, which effectively is relabelling of the solvents and it creates no effect on the forces.

The departure of the dynamics from equilibrium can be tracked by the average speed of the motor along the axis of the dimer $< V_z >$. The distribution of the speed

---

[14]

$$V^j_{LJ}(r) = 4\epsilon_j \left[\left(\frac{\sigma_S}{r} \right)^{12} - \left(\frac{\sigma_S}{r} \right)^6 + \frac{1}{4} \right], \quad r \leq r_c$$

where, where ϵ is the depth of the potential well and $\sigma = R_0$ the size of the sphere, r the interparticle distance and r_c the distance at which the potential is truncated for the repulsive LJ (bottom of the well).

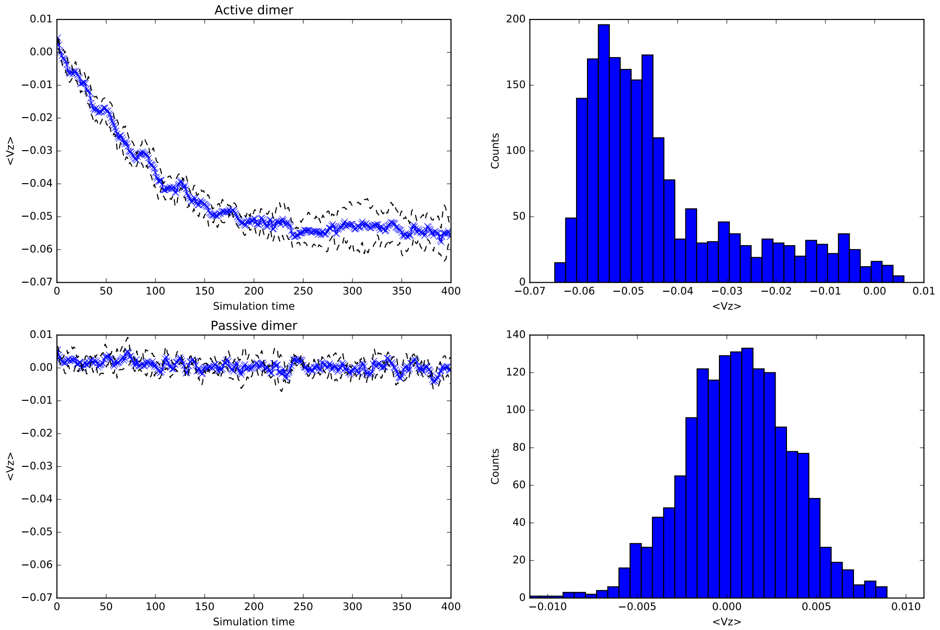

Figure 2.6: Time evolution of the running average of the centre-of-mass velocity of the dimer along its axis V_z (left) and its distribution (right) for an active (up) and passive (bottom) dimer nanomotor. After a transient, the running average velocity stabilises around a constant non-zero value of $< V_z > \sim -0.055$, showing the existence of directed motion. In simulation units the thermal velocity of a dimer is given by $v_{th} = \sqrt{\frac{k_B T}{M}}$ ≈0.004. These results are obtained from an average of 5 independent simulations (standard deviation in dashed lines).

$P(V_z)$ and the mean squared displacement (MSD) are shown in Figures 2.6 and 2.7. These results are averaged values of 5 simulations. After a short transient, Figure 2.6 shows that the active dimer reaches a directional velocity, whereas a passive dimer is close to the thermal velocity ($v_{thermal} = \sqrt{\frac{k_B T}{M}} \approx 0.004.$). This effect can also be seen in the averaged MSD, where the active dimer shows a clear initial ballistic behaviour. Comparing the slopes of the MSD in Figures 2.7 a and b, there is $\frac{D_{active}}{D_0} \approx 140$ increase in the diffusion coefficient. A snapshot of the dimer is shown in Figure 2.8 (a) inside its simulation volume together with the product distribution, while the simulated trajectory for the active dimer is shown in Figure 2.8 (b).

We can relate the simulation units to physical units by choosing a model of the fluid. Following the same strategy as in [122], we choose a dense fluid Argon-like

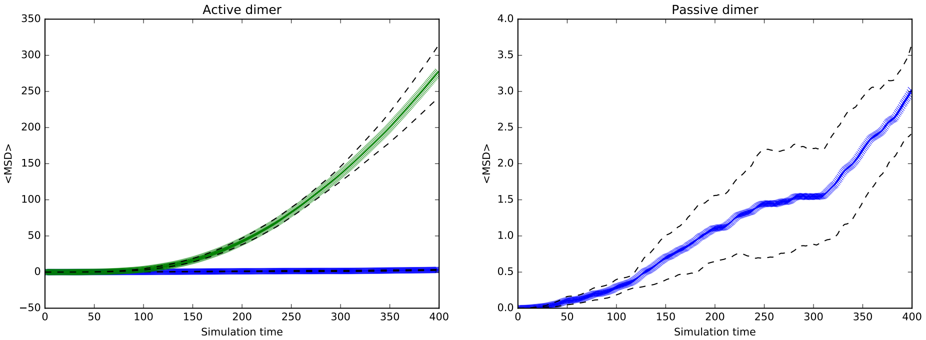

Figure 2.7: Mean-squared displacement (MSD) averaged over 5 simulation runs (standard deviations in dashed lines) for active (green) and passive (blue) dimers. Passive dimers are simulated by choosing ϵ_A=$\epsilon_B = 1$.

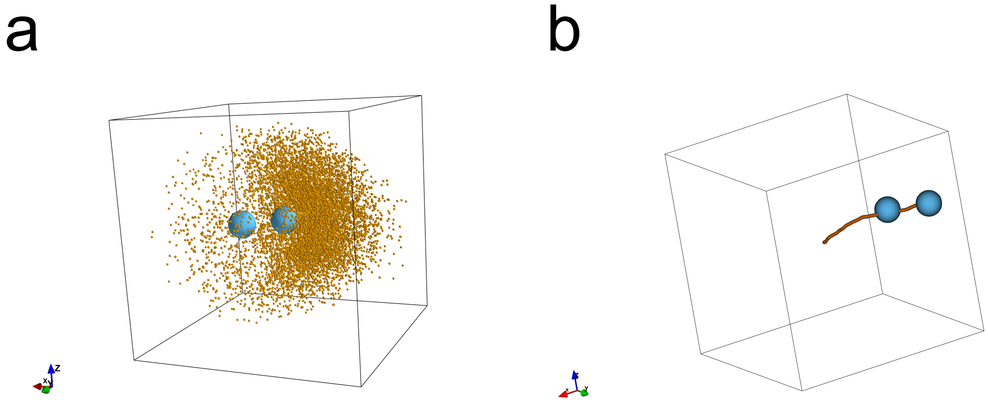

Figure 2.8: **a)** Snapshot of RMPCD simulation showing the dimer (in blue) inside the simulation volume. Product solvent particles (in yellow) are being produced around the catalytic sphere as it propels. **b)** 3D trajectory of the dimer from the origin at the centre of the simulation box after 400 t_0. The sizes of the spheres are not in scale. Figures have been rendered using MayaVi data visualiser.

solvent with parameters σ =0.34 nm, ϵ =120K k_B and m =39.95 u and t =2.15 ps [123]. With this choice of fluid, the sizes of the dimer spheres are 1.3 nm and 2.6 nm, with a centre-to-centre distance of 2.2 nm. The average running velocity for such a system would be $< V_z > \sim -8.6\,\mathrm{ms}^{-1}$.

2.5 Conclusion

The fundamental mechanisms of nanomotor propulsion are still not fully understood. This chapter summarised the main known basis of operation of chemically propelled synthetic particles, namely self-diffusiophoresis. In addition, computational simulations, first coded by Raymond Kapral et al. and further developed in this work to address the dimension of DNA nanodevices, clearly stated the different behaviours between passive nanoparticles and active nanomotors, by comparing their simulated mean-squared displacements and average velocities. The Janus and dimer geometries were presented and treated theoretically. Multi-particle dynamics simulations of dimer nanomotors showed that small motors exhibit self-propulsion with ballistic velocities one order of magnitude higher than their thermal velocity.

Reported experimental results were also collected, analysed and summarised to provide an experimental insight into quantifying the difference between externally driven particles, active and passive particles at different length scales. As sizes become smaller, rotational Brownian motion randomises the direction. However, the ballistic velocity increases for smaller motors. This analysis showed that nanoparticles, while dominated by thermal motion, can be expected to exhibit an increased diffusion coefficient, which can be measured experimentally. Together, this chapter concludes that for the purposes of a bottom-up assembly of a DNA-based nanodevice, its size, geometry, interaction strength with solute and catalytic activity are the key parameters to achieve significant and measurable nanomotor propulsion.

3

Techniques for measuring diffusion at the micro and nano scales

3.1 Introduction

Most studies on active matter involve the observation of a few natural or synthetic motors in an optical microscope, followed by an analysis of their trajectories. As particles get smaller, it becomes experimentally more challenging to characterise the dynamics of these motors and new approaches need to be considered that go beyond fast CCD cameras and improved optics. As discussed in chapter 2, a hallmark of active particles, including those at the nanoscale, is the increase in their diffusivity for times longer than the orientation randomisation time. Active catalytic motors show higher diffusivity in the presence of their substrate, coming from the self-propulsion that is randomised by rotational Brownian motion (see Figure 3.1).

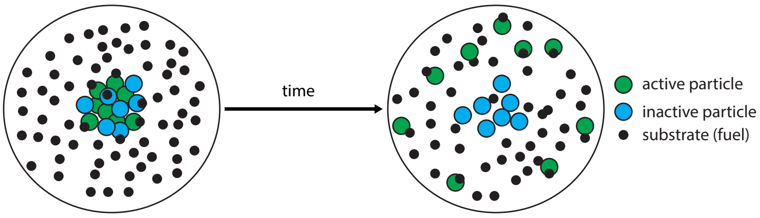

Figure 3.1: Active catalytic particles show higher diffusivity in the presence of their substrate (fuel). (Diagram adapted from [124].)

The following chapter presents experimental methods that find use in measuring the diffusion of particles and that have been implemented for the work in this thesis for characterising self-propelled devices. Some techniques are better suited than others for studying the motion of motors, depending on their characteristics (e.g. size, composition, propulsion mechanism). Two main experimental approaches are presented in this work: on the one hand diffusion constants can be extracted from a careful analysis of fluctuating signals (either by scattered light, emitted fluorescence or electric current) and on the other, if particles can be tracked by optical methods, then full trajectories can be reconstructed together with the full dynamics of motors.

3.2 Dynamic Light Scattering

3.2.1 Theory

In Dynamic Light Scattering (DLS), a coherent light source (e.g. laser) passes through a sample and the scattered light is recorded by a photodiode at a fixed angle θ (Figure 3.2 (a)). If the particles suspended in the sample are small compared to the wavelength of the laser (typically $d < \frac{\lambda}{20}$), then the scattering from a particle will be essentially isotropic with an intensity given by: $I \propto \frac{d^6}{\lambda^4}$ (*Rayleigh scattering*), where d is the particle diameter and λ is the laser wavelength [1]. Static scatterers would give a constant interference pattern (a 'speckle pattern' as shown in Figure 3.2 (b)), however this is not the case for scatterers in solution subject to Brownian motion. Diffusing particles cause fluctuations in the interference signal between scattered electric fields E_s. This translates into random speckles, which are detected as fluctuating dark and white spots in a camera or a fluctuating intensity signal in a photodiode (normally placed at either 173^0 or 90^0). A correlator computes the autocorrelation function of the scattered light intensity $g_2(\mathbf{q}, \tau)$, which is a

---

[1] The intensity I of light scattered by a dielectric sphere of diameter d and refractive index n from a beam of unpolarized light of wavelength λ and intensity I_0 is given by [125]:

$$I = I_0 \frac{1 + \cos^2\theta}{2R^2} \left(\frac{2\pi}{\lambda}\right)^4 \left(\frac{n^2 - 1}{n^2 + 2}\right)^2 \left(\frac{d}{2}\right)^6 \tag{3.1}$$

measure of how correlated a signal is with itself after a time delay τ at a scattering wave vector $\mathbf{q}$, corresponding to the detector position:

$$g_2(\mathbf{q},\tau) \equiv \frac{< I(t) \cdot I(t+\tau) >}{< I(t) >^2} \tag{3.2}$$

Fluctuations in position are encoded in the fluctuations in the phase of the scattered electric field E_s. However the photodiode can only detect the wave intensity. The *Siegert relation* recovers this phase information by relating the second-order autocorrelation function with the square of the first order autocorrelation function [125]:

$$g_2(\mathbf{q},\tau) = 1 + \beta[g^1(q,\tau)]^2 \tag{3.3}$$

where the first order autocorrelation is given by $g^1(\mathbf{q},\tau) = \frac{<E(t) \cdot E(t+\tau)>}{<E(t)>^2}$, and β is a correction factor which depends on laser parameters and geometry of the setup. The quadratic dependence comes from the relation between the amplitude of the electric wave and the intensity.

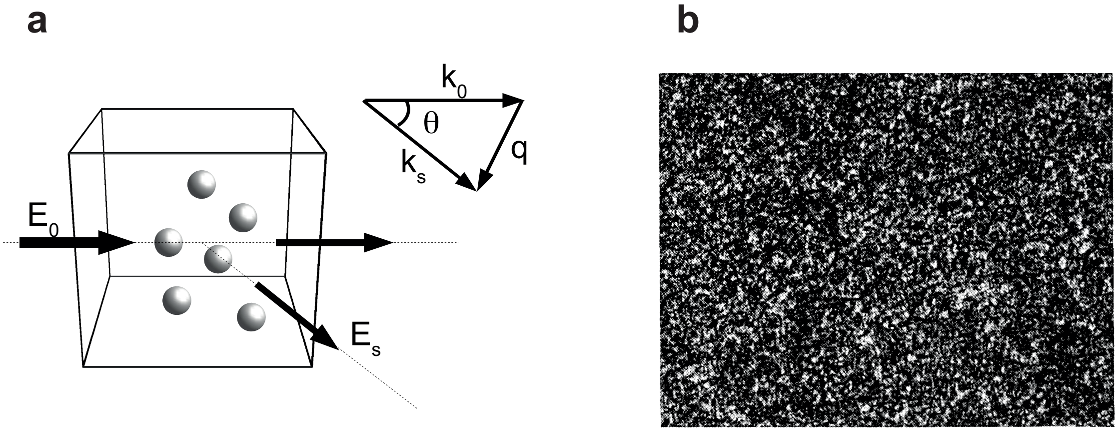

Figure 3.2: **a)** Incident light E_0 is scattered by particles. The scattered electric field amplitude E_s is detected at an angle θ. $\mathbf{q}$ is the scattering wave vector. **b)** Typical speckle pattern observed in the image of a uniformly white reflecting object illuminated by a CW laser. Figure (b) was extracted from [126].

For monodisperse non-interacting spherical scatterers the autocorrelation $g_1(\mathbf{q},\tau)$ is given by a decaying exponential function [125]:

$$g_1(\mathbf{q},\tau) = e^{-\Gamma\tau} = e^{-Dq^2\tau} \tag{3.4}$$

where Γ is the relaxation rate, $\mathbf{q} = \frac{4\pi n}{\lambda}\left(\sin\frac{\theta}{2}\right)$ is the scattering wave vector, n is the refractive index of the sample, θ is the angle at which the detector is located with respect to the transmitted beam (scattering angle), λ the laser wavelength and D is the translational diffusion constant, which is the parameter we seek from this measurement.

The *Stokes-Einstein* equation relates the diffusion coefficient to the radius of spherical particles by:

$$D = \frac{k_B T}{6\pi\eta r} \tag{3.5}$$

where k_B is Boltzmann's constant, T is the absolute temperature, η is the dynamic viscosity, and r is the radius of the particle, which is the usually reported hydrodynamic radius.

Knowing the physical properties of the particles and the environment in which they are suspended, then the diffusion constant can be calculated from the relaxation rates Γ. If the sample contains nanomotors, one should observe an increase in the relaxation rate when particles, in addition to Brownian motion, undergo self-propulsion.

The relaxation rates for the translational and rotational diffusion of a Stokes sphere with radius R are given by [125]:

$$\Gamma_{tr} = D_{tr}q^2 = \frac{k_B T}{6\pi\eta R}q^2 \tag{3.6}$$

$$\Gamma_{rot} = 3\tau_{rot}^{-1} = \frac{3k_B T}{4\pi\eta R^3} \tag{3.7}$$

The previous discussion refers to spherical isotropic particles. If a particle has an anisotropic shape or if a spherical particle has a refractive index anisotropy (e.g. Janus particle), then the rotational diffusion can be measured with DLS. When using optically anisotropic particles (e.g. ellipsoids), the rotational and translational relaxation times can be separated in the intensity autocorrelation functions [42]. Depolarised dynamic light scattering (DDLS) can also be used to measure translational and rotational relaxation diffusion coefficients [125]. When scattering is angle dependent (e.g. *Mie scattering*), multi-angle dynamic light scattering gives improved measurements [127].

3.2.2 DLS simulation

In Figure 3.3 (a) the scattered light intensity of 50 diffusing particles of radius 200 nm is simulated. For all experiments and simulations we performed, the incident light (λ=830 nm) travels in the x-direction and the scattered light is recorded at θ=90°. The simulation box has a volume of 8 µm^3 (i.e. particle concentration of µM). Using this simulated data, the autocorrelation function $g_2(\tau)$ is calculated and plotted on a semi-logarithmic graph (see code in Appendix B.1). A faster diffusing particle (5D) loses correlation earlier than a slowly diffusing one (D) in Figure 3.3 (b). If we assume that particles are monodisperse and non-interacting, then the intensity autocorrelation function $g_2(\tau)$ is described by a single exponential. In Figure 3.3 (c) we see how the simulated data fits into an exponentially decaying correlation function and the hydrodynamic radius calculated from the fit agrees with the particle radius.

For a polydisperse system, however, $g_1(\tau)$ can no longer be represented as a single exponential decay. Instead, an intensity-weighed integral over a distribution of rates $G(\Gamma)$ is used:

$$g_1(\tau) = \int_0^\infty G(\Gamma)e^{-\Gamma\tau}d\Gamma \tag{3.8}$$

where, $\int_0^\infty G(\Gamma)d\Gamma = 1$. The fitting process is usually carried out using the cumulant method (by expanding the term $e^{-\Gamma\tau}$ around a mean value of $\bar{\Gamma}$) or the CONTIN algorithm, which involves an inverse Laplace transform of $g_1(\tau)$ [128]. This results in a final calculation of $G(\Gamma)$, which is then translated into a distribution of particle sizes.

3.2.3 DLS experimental setup

The Viscotek 802 (Malvern Instruments), equipped with a 50 mW 830 nm diode laser, was used to collect dynamic light scattering data. The avalanche photodiode is located at 90°, and detects photons with a bandwidth of 10 MHz. A quartz cuvette of 20 µl is used to place the sample and a thermostat maintains it at a constant temperature of 25 °C. Ten measurements of 10 s are taken, and an average autocorrelation curve is calculated by a digital correlator. The built-in

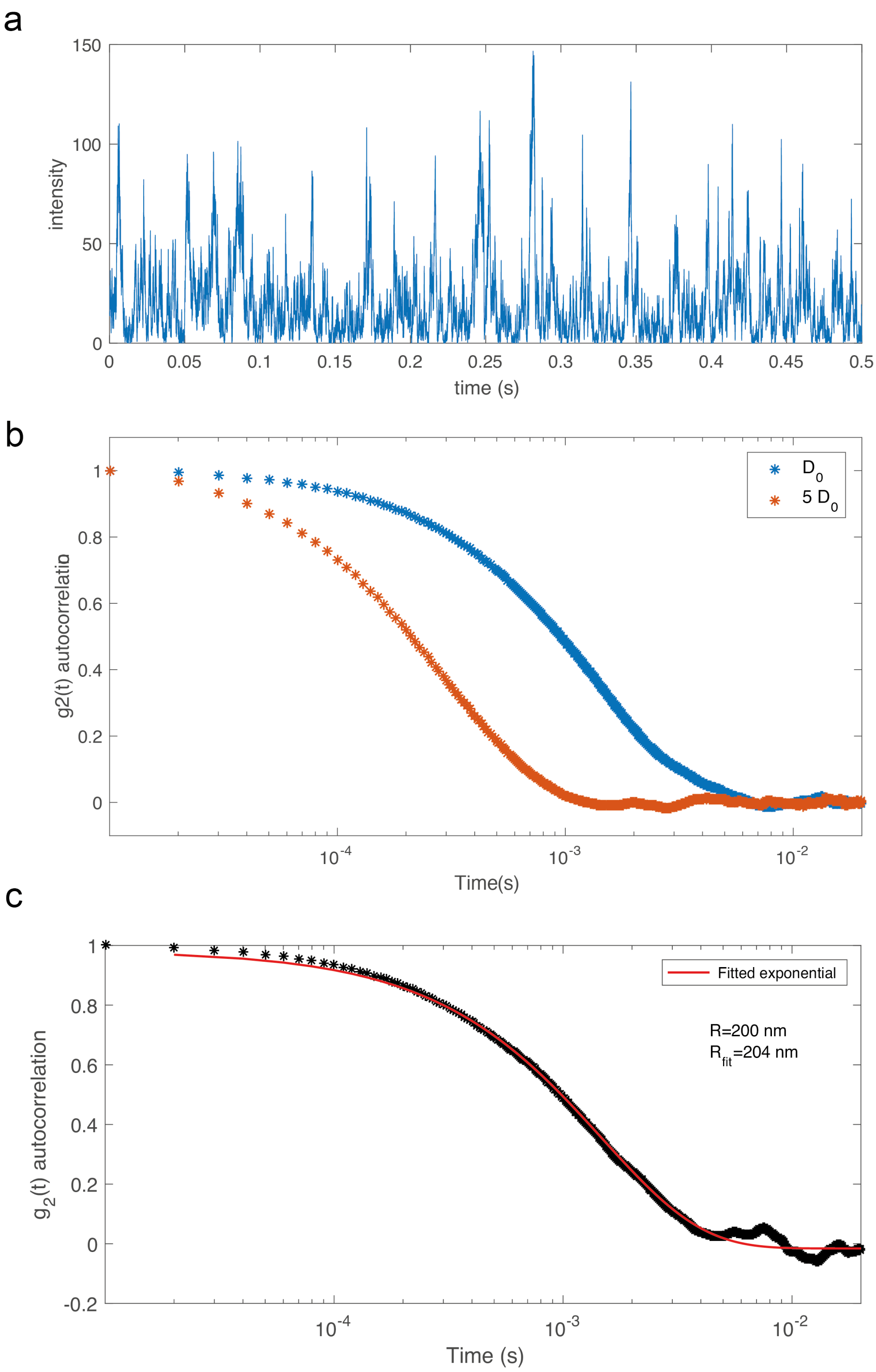

Figure 3.3: **a)** Simulated intensity of scattered light from 50 particles of radius 200 nm measured at 90°. **b)** Autocorrelation function for the signal in a) and particles that diffuse 5 times faster. **c)** The autocorrelation function is fitted to the Siegert relation $g_2(q,\tau) = 1 + \beta e^{-2Dq^2\tau}$.

OmniSIZE program (Malvern) gives a distribution of particle sizes by processing the autocorrelation functions.

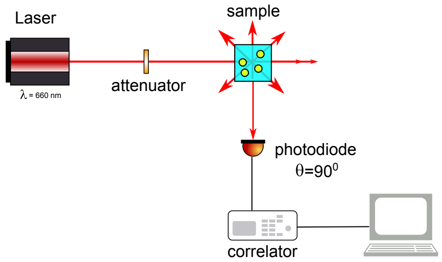

Figure 3.4: *Dynamic Light Scattering experimental setup* A laser beam is passed through a polarizer and into a sample. The scattered light is collected by a photomultiplier. A correlator generates the autocorrelation of the intensity trace.

3.2.4 DLS measurement of gold nanoparticles

20 µl of 20 nm diameter Au NPs (BBI) were analysed with DLS at a concentration of 10^{11} particles/ml. A TEM micrograph in Figure 3.5 (a) shows the morphology of Au NPs. The autocorrelation function in Figure 3.5 (b) is fitted to the Siegert relation given in (3.3), $g_2(q,\tau) = 1 + \beta e^{-2Dq^2\tau}$. The fitted exponential gives the relaxation rate $\Gamma = Dq^2$, while the system parameters are included in the scattering wave vector q. Together, this analysis yields a hydrodynamic radius of $R_h = 11 \pm 1$ nm, a comparable result to the CONTIN algorithm performed by the commercial software in Figure 3.5 (c).

3.3 Fluorescence Correlation Spectroscopy

Fluorescence Correlation Spectroscopy (FCS) is a single-molecule method that relies on the measurement of fluctuations in fluorescence intensity as a result of particles diffusing in and out of a confocal volume. The advantage of this method lies in its selectivity, as only the motion of fluorescent particles is detected, while unlabelled impurities remain undetected.

Although the technology for the measurement and analysis of fluctuations in FCS was originally derived from those developed for DLS, the physical principle

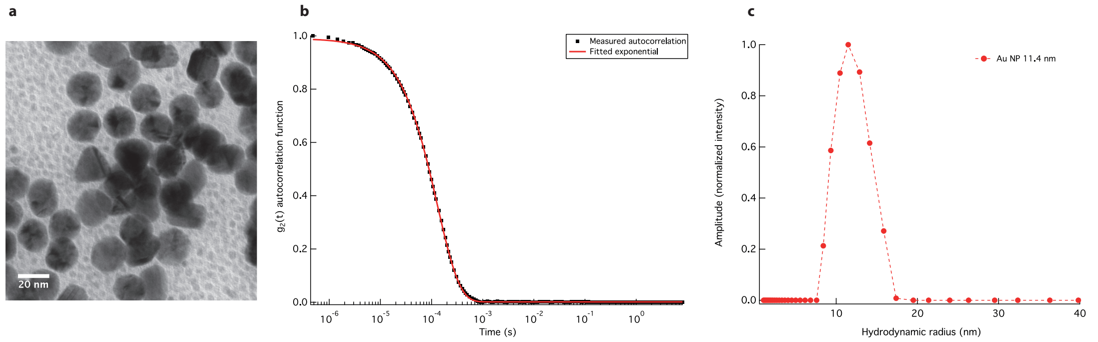

Figure 3.5: **a)** TEM micrograph of 20 nm Au NP taken with FEI Tecnai 12. **b)** Autocorrelation function measured in Viskotek DLS 802 (Malvern) and fitted exponential yielding a relaxation factor $\Gamma = Dq^2 = 3980 \pm 7\mathrm{s}^{-1}$. Using the setup parameters of $q = \frac{4\pi n}{\lambda} sin\left(\frac{\theta}{2}\right)$ =$1.4239 \times 10^7\,\mathrm{m}^{-1}$ gives a hydrodynamic radius of $R_h = 11 \pm 1$ nm. **c)** Intensity distribution using built-in software OmniSIZE yielding a similar result.

producing fluctuations in FCS is very different: DLS is an ensemble measurement coming from the scattered light of diffusing particles. However, the FCS fluctuating signal originates from fluorescent molecules passing through a very small illumination volume defined by a confocal volume. Single molecules in this volume of excitation (usually around 1 femtolitre or 1 $\mu\mathrm{m}^3$) are sufficient to produce a signal. This corresponds to concentrations in the pM-nM range, which are optimal for FCS measurements. The FCS principle is illustrated in Figure 3.6.

FCS data analysis uses correlation functions (Figure 3.6 (c)), following a similar approach to that found in DLS, to extract the diffusion constant from a fluctuating signal. However, the relationship between diffusion and loss of correlation involves coupling the fluorescent excitation with the diffusion of a particle in the 3D confocal volume. The most basic models with a minimum set of parameters that are used in this work are presented below. Comprehensive reviews can be found in the work of those who pioneered the technique, e.g. E. Gratton [129] and P. Schwille [130].

3.3.1 Theory of FCS

In this section we consider the diffusion of N fluorescent particles in a 3D volume. Fluctuations in the fluorescence signal from excited molecules in the confocal volume (here represented as an ellipsoid) are continuously occurring. There are many factors

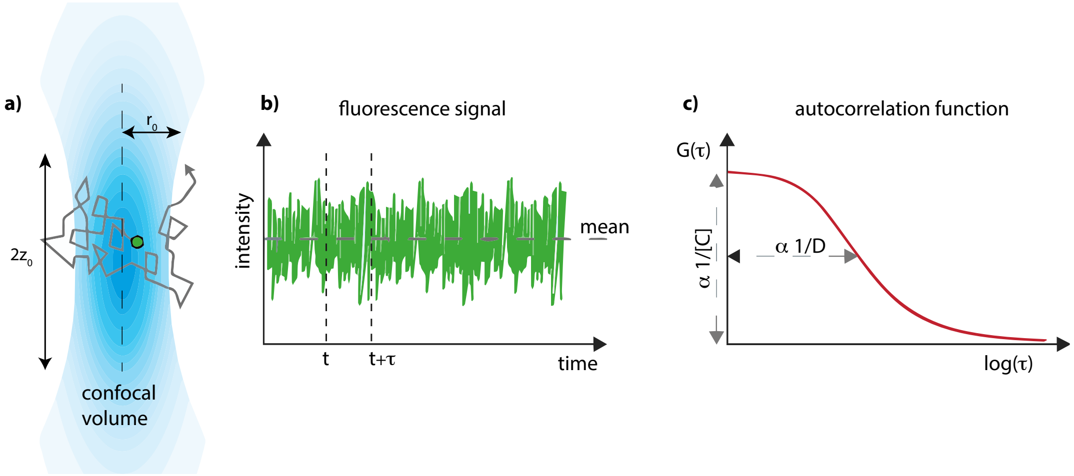

Figure 3.6: *Description of Fluorescence Correlation Spectroscopy.* **a)** A fluorescent particle moving in and out of a confocal volume creates a fluctuating intensity signal in **b)**. The (temporal) autocorrelation function $G(\tau)$ in **c)** is the correlation of a time series with itself shifted by time τ and expressed as a function of τ on a semilogarithmic plot. The width of $G(\tau)$ is inversely proportional to the diffusion and its amplitude is inversely proportional to the average concentration of dyes in the confocal volume.

involved in the noise patterns found in the measured fluorescent signal, which include photophysical effects. However, the fluctuations of interest, those related to the diffusion of the particles, can be quantified by calculating a temporal autocorrelation $G(\tau)$. This measure of self-similarity in the signal provides a means to decode the stored information about the diffusion of particles.

The normalised autocorrelation function of the fluorescence time trace $F(t)$ is defined as [130]:

$$G(\tau) = \frac{< F(t) \cdot F(t+\tau) >}{< F(t) >^2} = \frac{< \delta F(t) \cdot \delta F(t+\tau) >}{< F(t) >^2} + 1 \qquad (3.9)$$

with

$$\delta F(t) = F(t) - < F(t) > \qquad < F(t) > = \frac{1}{T}\int_0^T F(t)dt \qquad (3.10)$$

This routine[2] is the temporal average of the signal F at time t multiplied by the signal F at a later time $t+\tau$, normalised by the square of the average of F over the acquisition time T.

Particles are diffusing in a 3D confocal volume which is modelled as a simple three-dimensional Gaussian profile [131]. For a Gaussian confocal volume (Figure

---

[2] There are different conventions that choose $G(\infty) = 0$ instead of $G(\infty) = 1$. This depends on the definition in (3.9)

3.6 (a)), in the radial direction, the $1/e^2$ radius is given by r_0; in the axial direction, it is given by z_0. The effective confocal volume V_{eff} can be defined as an ellipsoid:

$$V_{eff} = \pi^{3/2} \cdot r_0^2 \cdot z_0 \tag{3.11}$$

If we consider translational diffusion for a single fluorescent species inside a 3D Gaussian volume, the autocorrelation function in (3.9) is then given by [130]:

$$G(\tau) = \frac{1}{< N >} \left(1 + \frac{\tau}{\tau_D}\right)^{-1} \cdot \left(1 + \frac{\tau}{SP^2 \tau_D}\right)^{-1/2} \tag{3.12}$$

where $\tau_D = \frac{r_0^2}{4D_t}$ is the lateral diffusion time (i.e. the time it takes for a molecule to diffuse through the confocal volume), and SP is the *structure parameter* or axial ratio defined as $SP = \frac{z_0}{r_0}$ (this is also the eccentricity of the ellipsoid).

Provided that the dimensions of the confocal volume are known after calibration, the amplitude of the measured autocorrelation function $G(0) = \frac{1}{<N>} = \frac{1}{<C>V_{eff}}$ can be used to determine the local concentration of fluorescent molecules (Figure 3.6 (c) shows the relationship between amplitude $G(0)$ and concentration <C>).

Fitted diffusion times τ_D can be converted into absolute values of diffusion coefficients if a reference dye is used in the measurement (e.g. Rhodamine 6G). In this way the translational diffusion coefficient of interest is given by:

$$D_{sample} = \frac{\tau_{reference}}{\tau_{sample}} D_{reference} \tag{3.13}$$

Other parameters, such as photophysical effects have not been considered in this discussion for the sake of simplicity. The assumption that fluorescence intensity is constant inside the confocal volume might not hold as many dyes change their fluorescent properties over time. Therefore, additional sources of fluctuations must be added into the model. It should be noted that one of the keys to a successful diffusion measurement is the right choice of fitting function G(τ) to the measured autocorrelation curves. Independent measurements of the confocal volume, together with a good understanding of the species involved in the solution and their photophysics are essential for a correct analysis of the FCS data.

3.3.2 FCS Simulation of diffusive particles in a volume

Let us consider a box filled with N particles performing a random walk. We simulate the diffusion of spherical particles with n number of dyes entering a confocal volume specified by the ellipsoid (MATLAB, Mathworks). At each simulation step, the position of each particle is used to calculate the emitted fluorescence depending on the shape and position of the illumination beam. The total intensity for a given particle configuration is calculated and recorded to produce an intensity trace.

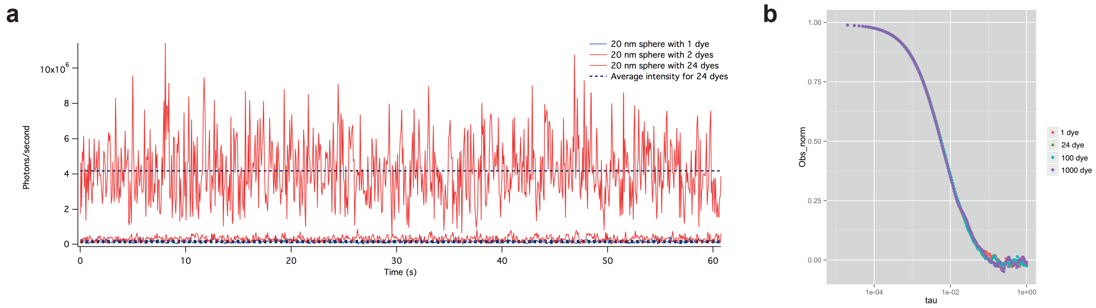

Figure 3.7: **a)** Intensity time plot for a 20nm sphere with 1, 2 and 24 dyes. **b)** Normalised correlation functions, showing that the number of dyes does not alter the diffusion constant.

In this simulation, we can change the number of dyes per particle by modifying its brightness. This gives higher intensity peaks, as can be observed in the simulated data in Figure 3.3.2 a. However, after normalisation, the autocorrelation functions superpose (Figure 3.3.2 b.), indicating that the diffusion coefficient is independent of the brightness of the particle. $g_2(0)$ is a measure of the number of particles in the confocal volume and does not give any information about their brightness.

This simulation shows that the number of dyes on the diffusing particle changes the average intensity but does not affect the autocorrelation function, as long as there is a single population of particles with the same diffusion constant. Therefore, in the experiments in this thesis a careful purification is needed to achieve a single-species solution. After normalisation of the autocorrelation functions, the number of dyes per nanomotors does not determine the measured diffusion.

3.3.3 FCS experimental setup

The diagram in Figure 3.8 illustrates the custom-built confocal microscopy setup used for FCS measurements in this work. The confocal setup consists of two laser lines, a 638 nm diode laser (Cube, Coherent), and a 532 nm Nd:YAG laser (Samba, Cobolt).

For single-dye FCS measurements, an incident 532 nm laser beam in continuous-wave mode is coupled with a 60x, 1.35 NA, UPlanSApo oil immersion objective (Olympus), which focusses the beam into the sample to produce a fluorescent signal. A dichroic mirror (630DRLP, Omega) spectrally separates excitation and emission beams and directs the latter into a pinhole, which filters out-of-focus-light. Avalanche photodiodes (SPCM-AQR14, Perkin Elmer) collect single photons and the produced signal is processed in a multiple-tau digital correlator [3] (Flex, Correlator) to generate an autocorrelation function. These curves are then fitted to models of single or double species diffusion using a least-square regression algorithm.

A general workflow designed for performing FCS measurements and analysing data produced in the confocal setup shown in Figure 3.8 is listed below. As part of this thesis, an R code was written by the author to analyse the files recorded by the digital correlator (see appendix B.2).

1. Dissolve sample in a buffer of choice and dilute until the fluorescence intensity produces a typical autocorrelation curve (nM concentrations). The laser power should be chosen so that fluorescence intensity scales with laser power to avoid saturation of the dye and distortion of the confocal volume (linear regime, ≈50 µW).
2. Receive and convert data from digital multiple tau hardware correlator (.SIN file format, Flex Correlator).

---

[3] The multiple-tau correlation technique, originally implemented for digital correlators, calculates temporal correlations in real time by limiting the number of calculated correlation time lags. In practice, one does not compute $G(\tau)$ for all possible values of lag-time τ, but at increasingly spaced lag-time values [132]. If the temporal resolution of the photon detection is, for example 100 ns, and one desires to follow a correlation process up to a minute, possible values of lag time τ are any values between 100 ns and 100 s in intervals of 100 ns, which results in $6 \cdot 10^8$ possible lag time values. Calculation of $G(\tau)$ for all these values is computationally very expensive. Instead, the autocorrelation is calculated for only few, approximately logarithmically-spaced values of τ. This method was developed by Schätzel [133].

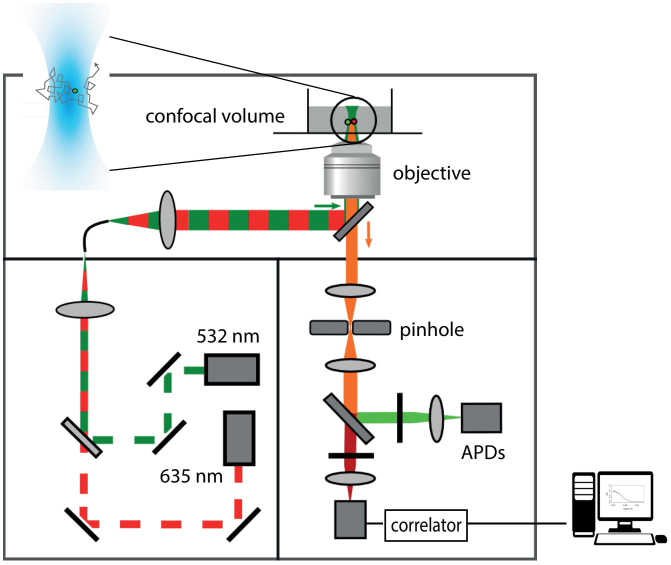

Figure 3.8: *Custom-built confocal setup for FCS measurements.* A 600 nm diode laser and a 532 nm Nd:YAG laser coupled with a 60x objective. A dichroic mirror separates excitation and emission, which is then filtered through the confocal pinhole and detected in 2 APDs. A digital correlator computes the autocorrelation function (or cross-correlation if more than one laser is used). (This microscope was originally built for FRET measurements by the A. Kapanidis group.)

3. Short timescales data are removed from the autocorrelation signal (from $t<10^{-5}$s). The threshold is set to two orders of magnitude less than typical diffusion time of a dye in a femtolitre volume (i.e. ms).
4. Fit diffusion model (3D diffusion of single species in a Gaussian volume) using non-linear least square fitting method (e.g. Levenberg–Marquardt algorithm). Examine goodness of fit with residuals and if necessary choose a different fitting model involving more than one species.
5. Extract diffusion time τ_D for each measurement and report the average and standard deviation. A comparison with a reference dye gives an absolute value of measured diffusion.
6. Normalise correlation curve by fitted $G(0) = \frac{1}{<N>}$ and superpose normalised autocorrelation curves for visualisation.

3.3.4 FCS measurement of Rhodamine 6G

Let us consider a typical example concerning the molecule of reference, Rhodamine 6G, with a well-known diffusion coefficient D=$2.8 \times 10^{-10}\,\mathrm{m}^2\,\mathrm{s}^{-1}$ (η=1.0 cP at 20 °C) [134]. 5 measurements were taken with the FCS setup described above for different concentrations from the same source (200 nM Rhodamine 6G). No triplet state effects[4] were taken into account and the chosen data range was from $t = 10^{-5}$s onwards [130]. (N, τ_D) were the only free parameters and the Levenberg-Marquardt algorithm was used to find a local minimum of the least-squares fitting. The structure parameter was held at SP=10.

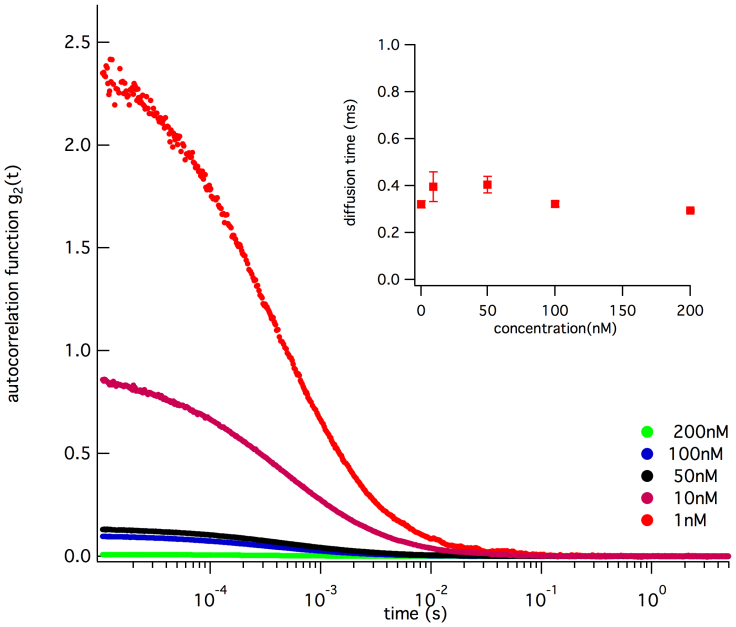

Figure 3.9: Autocorrelation functions for different concentrations of rhodamine dye. The inset graph shows the average diffusion time measured from fitting the autocorrelation function to single-species diffusion $G(\tau)$ given in (3.12). The concentration changes the amplitude of the correlation function $G(0)$. (Error bars indicate the standard deviation of 3 measurements).

The autocorrelation curves are plotted in Figure 3.9. G(0) is inversely proportional to the average number of particles in the confocal volume. On the other hand, the diffusion time is similar for all concentrations of Rhodamine. This type of

---

[4] A common cause for unwanted fluctuations in the fluorescence intensity is the transition of the dye into the first excited triplet state. During the interval it takes to relax back to the ground state, the dye cannot emit any fluorescence photons.

measurement is used as a reference to obtain absolute values for diffusion coefficients. For relative comparisons it suffices to compare diffusion times τ_D, as the confocal volume remains constant, given the same laser and optics settings.

3.4 Particle tracking methods

3.4.1 Optical microscopy

This is the simplest method to characterise a suspension of active motors. It is a modern version of Jean Perrin's experiment with colloidal particles (1923) [135]. It relies on imagining and tracking the 3D trajectories of N particles to obtain statistically significant values of their diffusion and ballistic velocities. For particle i the velocity is given by:

$$\mathbf{v}_i t = \frac{d\mathbf{s}_i}{dt} \approx \frac{s_i(t+\delta t) - s_i(t)}{\delta t} \tag{3.14}$$

and the ability to measure these velocities depends on the spatial and time resolution of the microscope. 3D tracking also poses experimental challenges, which require a feedback mechanism to maintain particles in focus. This is why 2D tracking is more common, especially for synthetic particles, like the ones developed by the Sheffield group in [12].

Obtaining a list of coordinates as a function of time, allows a direct computation of the mean-squared displacement (MSD), obtained as an average of all steps corresponding to a single lag time τ:

$$MSD =< L^2 > (\tau) = \frac{1}{n}\sum_{i=1}^{n} \Delta r_i^2(\tau) \tag{3.15}$$

where $\Delta r_i(\tau) = r_{i+1} - r_i$. From this calculation the diffusive and ballistic properties of the particles can be determined by analysing the functional form of the MSD. Tracking methods with optical microscopy are suitable for particles larger than the resolution limit set by diffraction (e.g. assuming green light, this limit is ≈ 250 nm). However, this can be overcome with dark field microscopy or super-resolution fluorescence methods. Another limitation is set by the rotational diffusion, that is the smaller the particle is, the faster the camera needs to be to capture ballistic events [5].

In the example of Figure 3.10 the 2D diffusion of a 1 µm beads in water placed on a glass surface is tracked using an inverted microscope (iX81 Olympus) and a digital camera (Andor iXon). Particles are detected by an ImageJ program, which automatically applies a threshold to each frame and converts them into binary images. Then the (x, y) coordinates of the centroid of the beads along with the time for each frame are recorded. With this procedure the tracking script computes the MSD of each particle. For the case of particles diffusing in 2D, $< L^2 >_{diffusive} = 4Dt$ holds for passive particles, while ballistic behaviour would be identified by $< L^2 >_{ballistic} = v^2t^2$. Active particles show a combination of both regimes which contribute to a characteristic functional form of the MSD as discussed in chapter 2. The velocity term contributes to an ‘effective diffusion coefficient’.

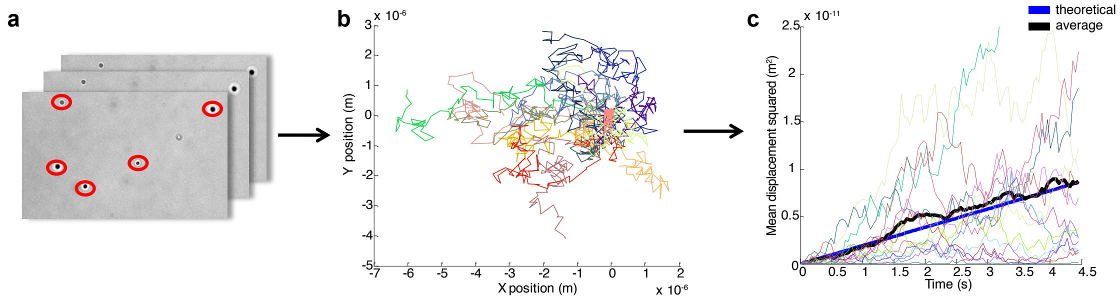

Figure 3.10: Particle tracking workflow for measuring the 2D diffusion of a 1 µm polystyrene bead. **a)** Movie clips of the particles are recorded using optical microscopy and a digital camera (iXON Andor). **b)** Particle tracking algorithms identify spherical particles and track their position over time. **c)** The mean squared displacement is calculated from the measured trajectories and an average is computed. For this example a diffusion constant of $D = 0.38 \pm 0.2\ \mu\mathrm{m}^2\,\mathrm{s}^{-1}$ was obtained from the relation $MSD = 4Dt$.

3.4.2 Nanoparticle tracking

One of the drawbacks of DLS is that it is very sensitive to the presence of large particles, as the scattered light is proportional to the sixth power of the particle size. This can be useful for detecting small amounts of large particles, but it is

---

[5] For a CCD camera with a maximum capture frame of 66 Hz, a minimum length of the swimmer is of the order of 250 nm.

a serious problem when aggregates or large impurities mask the main component of the solution that needs to be measured.

Nanoparticle tracking analysis (NTA) provides a tracking method for measuring the diffusion and concentration of particles from about 30 to 1000 nm, with the lower detection limit being dependent on the dielectric properties of the nanoparticles. The technique consists of a laser scattering setup similar to DLS but with a custom-made microfluidic device and a CCD camera, which permits the visualization of nanoparticles by recording their scattered light (see Figure 3.11 (a)). The core of the method is the commercial software that is able to identify the position and track individual particles under Brownian motion. This technique can be used to study the enhanced diffusion of self-propelled particles [136].

In Figure 3.11 (b) a measurement of 200 nm polystyrene beads (Bangs laboratories) is shown. Beads were diluted in deionized water until the concentration was acceptable for NTA measurements, i.e. between 10^7 and 10^9 total particles/ml. 3 consecutive measurements were taken and an average distribution was obtained.

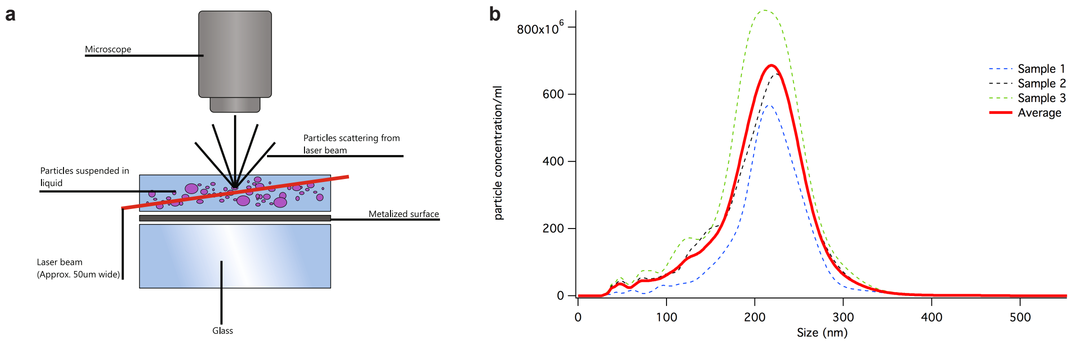

Figure 3.11: a) Schematic diagram of Nanosight NTA apparatus (adapted from Malvern Instruments). The particles contained in the sample are visualized by virtue of the light they scatter when illuminated in an angle by laser light. The light scattered by the particles is captured using a digital camera and the motion of each particle is tracked from frame to frame. **b)** Particle size distribution from 3 NTA measurements of 200 nm beads in deionized water.

NTA can measure the signal from single particles, but it has a fundamental limitation due to the low scattering of small particles. Also, NTA data acquisition and analysis remain prone to user input and bias on account of the high number of acquisition and analysis parameters available in the custom-built software [137, 138]. NTA may also be used to track fluorescent particles by detecting the fluorescence signal rather than scattered light.

3.5 Nanoimpact voltammetry

Electrochemistry provides an alternative to optical microscopy and scattering methods, for detecting particles in solution. The field of particle-electrode collisions (also known as nanoimpact [139]) is a rapidly growing research discipline opening up a broad range of potential applications[140]. This method allows in-situ direct detection of single nanoparticles in solution [141, 142]. In a typical nanoimpact experiment an electrode under a controlled potential is immersed in a solution containing the freely-diffusing analyte. Particles collide stochastically on the electrode where they may directly adsorb, react (reduce or oxidise) or trigger an intermediate redox reaction, all resulting in characteristic current spikes out of which properties of the particle can be extracted, such as concentration, size and shape [140]. This method has been used with inorganic and organic nanoparticles, such as Ag[142] and Pt [141], emulsion droplets [143], vesicles[144], DNA[145], and virus[146]. It has also been used to measure the motion of micron-size self-propelled particles[147].

Most tools available today for enzyme nanomotor detection rely on single-molecule fluorescence measurements, which require enzyme labelling. Nano-impact experiments allow single-enzyme measurements in their native state, without molecular modifications, using cost-effective experimental setups [140]. Nanoimpact voltammetry could be used to study the self-propulsion of enzymatic nanomotors like catalase in their native state.

3.6 Conclusion

This chapter presented and compared most of the well-established experimental methods that are suitable for characterising nano and micromotors by measuring their diffusion coefficient. These include dynamic light scattering (DLS), fluorescence correlation spectroscopy (FCS) and dark-field optical microscopy with nanoparticle tracking analysis (NTA). In this thesis, all of these techniques are used. The detailed experimental setup that was used together with one experimental result are included for each technique. Advantages and disadvantages of these methods from both theoretical and practical aspects are stated and compared. Simulations of DLS and data analysis methods for FCS are developed and described fully in the appendix. A summary of all techniques is shown in the table below.

Table 3.1: List of experimental methods for characterising micro/nano motors

Technique	**Working principle**	**Size range**	**Suitable for**	**Disadvantages**
Dynamic Light Scattering (DLS)	Fluctuations in scattered light	<10 µm	Monodisperse colloids	Signal masked by aggregates ($I \propto d^6$)
Fluorescence Correlation Spectroscopy (FCS)	Fluctuations in fluorescence	<200-300 nm	Fluorescent particles	Needs fluorescence. Limited by confocal volume.
Optical microscopy	Optical tracking with camera	>200 nm	Large particles	Limited by microscope resolution
Nanoparticle Tracking (NTA)	Tracking of scattered light	10 nm-2 µm	Nanoparticles	Limited by low scattering of small particles
Particle collision voltammetry (Nanoimpact)	Particle collisions with electrode	1.5-100 nm (UME) >1 µm(ME)	Metallic NP and proteins	Limited to certain NP and proteins

In short, FCS is the most suitable method to measure the diffusion of fluorescently labelled proteins or hybrid nanostructures, such as a DNA based nanomotors. Since FCS is a small-ensemble detection method that only requires low concentrations, it can avoid the interference caused by aggregation of particles. For unlabelled metallic nanomotors, DLS is a suitable choice as they scatter light strongly. The last part of this chapter pointed out a recently developed electrochemical single-particle detection method, namely nanoimpact voltammetry, and suggested it has the potential to be developed into a new method in the nanomotor research area, which has not been used in any reported work yet.

4

DNA travelling waves in controlled concentration gradients

4.1 Introduction

The creation of localised gradients of products by catalysing a reaction of a fuel in the environment is a strategy shared by many artificial phoretic microswimmers, allowing them to overcome diffusion and self-propel. In this chapter the attention focusses on chemically active media instead of active particles. DNA itself becomes active, by sustaining a reaction-diffusion process in the environment, rather than on the surface of a particle. Catalysed by enzymes, DNA waves arise, which can be considered as propagating signals. Using DNA as the active autocatalytic component, chemical wave propagation is made into a tunable mechanism for transmitting information (but no cargo) faster than by diffusion[1].

4.1.1 Chemical waves

Spatial structures may form in nonlinear systems far-from-equilibrium. Chemical waves, which are concentration variations of chemical species propagating in a system, are an example of such structures [148].

---

[1] The work in this chapter is in collaboration with Dr. Andre Estevez-Torres, CNRS and Georg Urtel, LMU

As first introduced in 1906 by Robert Luther in his seminal work ‘Propagation of Chemical Reactions in Space’ [149], travelling waves with constant velocity emerge when an autocatalytic species is allowed to diffuse. The autocatalytic reaction creates an excess product that then diffuses to an unreacted region, triggering further proliferation of the species in front of the wave. In his lecture demonstration, Luther showed a propagating front in the permanganate oxidation of oxalic acid, with the purple solution becoming colourless at the moving boundary. Later in 1952, Alan Turing laid the mathematical foundations of morphogenesis in his work ‘The chemical basis of morphogenesis’ [150], where he described the spontaneous formation of spatial patterns in systems undergoing reaction and diffusion of their ingredients.

Today, many systems are known to exhibit such spatial patterns. The biological world is full of phenomena where autocatalytic chemical waves transmit biochemical information inside and outside the cell. Cytosolic Ca^{2+} signalling [151] and cAMP waves for chemotactic aggregation of social amoebas like *Dictyostelium discoideum* [152] are a few examples.

Autocatalytic waves are important precursors to developmental processes such as complex spatio-temporal patterning found in embryogenesis [153] and they are believed to be one of the main contributors to the emergence of order in living systems [154]. Autocatalytic waves are not restricted to the molecular scale, but are also important interacting population models in ecology where spatial effects play a role, like in epidemic propagation [155].

In inorganic chemistry, chemical oscillators like the Belousov-Zhabotinsky (BZ) reaction offer an example of an excitable medium capable of generating chemical waves [156]. Similar spiral patterns are found in the biological realm, for example in the growth pattern of *Dictyostelium discoideum*, as shown in Figure 4.1. The BZ reaction involves more than 18 steps, including the generation and inhibition of an autocatalyst which changes the oxidation state of an intermediate iron complex, thus making the solution oscillate between red and colourless. However, the phase space where this reaction can survive is very limited and normally it only occurs at a very restricted combination of concentrations of simple reactants with fixed kinetics, making control of wave dynamics limited.

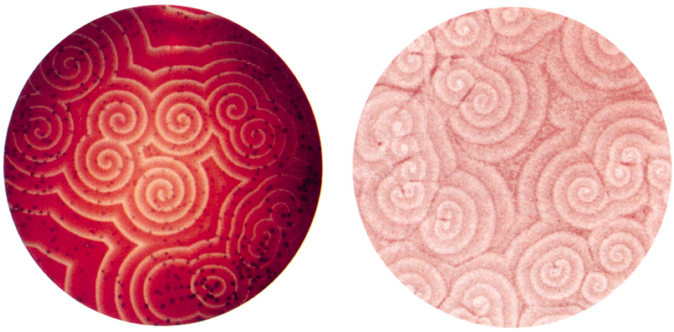

Figure 4.1: Chemical waves in the Belousov–Zhabotinsky reaction (Left) and in *D. discoideum* (Right). Image reproduced from [157].

DNA-based chemical reaction networks, in combination with enzymes, allow an exquisite control over nonlinear chemical effects [106]. Spatio-temporal patterns described by reaction-diffusion equations, like the ones governing the BZ reaction, can be programmed by changing the DNA sequence, their network topology, reaction rates and diffusion constants.

The work presented in this chapter builds on previous research on the synthesis of reaction-diffusion wave fronts with DNA [158, 159] and aims to introduce control over its dynamics. DNA propagating fronts were generated using an autocatalytic amplification reaction in a microfluidic channel. The velocity of the fronts depends on the growth rate and diffusion coefficients of the species involved in the autocatalytic reaction. This chapter studies mechanisms of control of wave propagation in two different ways: on the one hand, by altering the reaction network topology and on the other, by imposing spatially inhomogeneous concentration gradients. A description of gradient generation and wave characterisation in a microfluidic channel is presented and the nonlinear behaviour that emerges when the autocatalytic rate changes in space is analysed.

4.1.2 Autocatalytic chemical reactions

In an autocatalytic reaction, one of the products (or a reaction intermediate) catalyses its own formation. This leads to an acceleration in the production rate of the autocatalyst as a function of time. There are many mechanisms that have the potential to exhibit autocatalysis, but only do so for some values of the parameter space. A practical definition of autocatalysis, given by Plasson et al. in [160], is one in which the kinetic behaviour of the system is described by the following rate equation:

$$\frac{dx_i}{dt} = k(\mathbf{X}) \cdot x_i^n + f(\mathbf{X}) \tag{4.1}$$

where $\mathbf{X}$ is the vector of all the concentrations of species involved in the reaction. Autocatalysis for the compound x_i exists when the conditions of equation (4.1) are fulfilled. The term $k(\mathbf{X}) \cdot x_j^n$ describes the autocatalytic process itself, while $f(\mathbf{X})$ describes the sum of all other contributions coming from the rest of the chemical system. For autocatalysis to happen $|k| \gg |f|$ needs to be fulfilled. n indicates the order of autocatalysis. In this work only quadratic autocatalysis will be considered ($n = 2$), however higher order autocatalytic systems are known to exhibit chemical waves as well [161].

The simplest example of a single-step autocatalytic process is illustrated in Figure 4.3 (a) and involves two species:

$$A + D \xrightarrow{k} 2D \tag{4.2}$$

Here, A is the reactant, D is the autocatalyst, and the rate equation is non-linear (this is an example of quadratic autocatalysis):

$$r \equiv \frac{d[D]}{dt} = k[A][D] \tag{4.3}$$

The differential equation (4.3), combined with mass conservation $[A] + [D] = [A_0] + [D_0] = C$ is also known as the *logistic equation*, often expressed as:

$$\frac{d[D]}{dt} = k(C - [D])[D] \tag{4.4}$$

The autocatalyst D, with initial concentration D_0, speeds up the reaction rate as it is being produced. A solution to the differential equation (4.3) yields

$$\begin{aligned} [A] &= [A_0] - x \qquad (4.5) \\ [D] &= [D_0] + x \qquad (4.6) \end{aligned}$$

where

$$x = [D_0]\frac{e^{bt} - 1}{1 + \frac{[D_0]}{[A_0]}e^{bt}} \qquad (4.7)$$

and $b = Ck$.

At first the reaction rate is slow, but as more autocatalyst D is produced the reaction rate increases. As the concentration of the reactant A starts to decrease, the rate decreases as well until the reaction ends. The functional form of the autocatalytic growth is a sigmoidal curve (exponential at initial times) and the growth rate follows a bell-shaped curve, as shown in Figure 4.2.

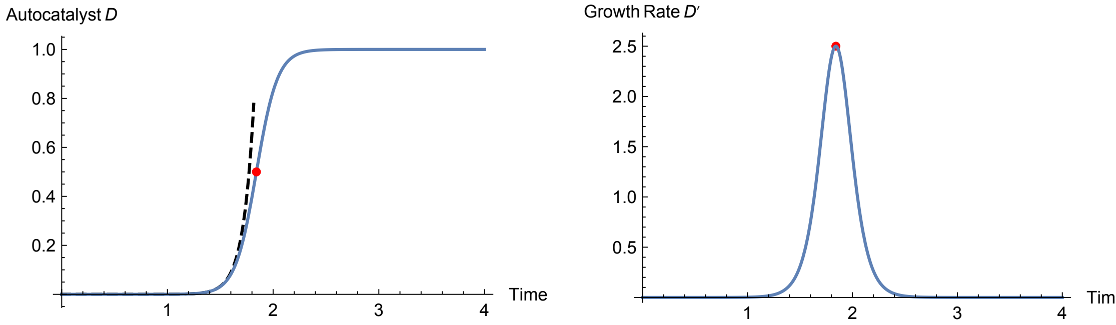

Figure 4.2: The left graph shows a sigmoidal curve, which represents the growth of autocatalyst D. The following parameters have been chosen $b = 10$, $[D_0] = 10^{-4}$ and $[A_0] = 1$. For initial times with little autocatalyst ([D]«[A]) the growth follows an exponential function (dashed line). The graph on the right shows the growth rate $\frac{d[D]}{dt}$. The red point shows where template and product concentration are equal [D]=[A].

Autocatalysis mechanisms

Following the classification by Plasson et al. [160], equation (4.2) is an example of *template autocatalysis* (Figure 4.3 (a)), where a direct association between the

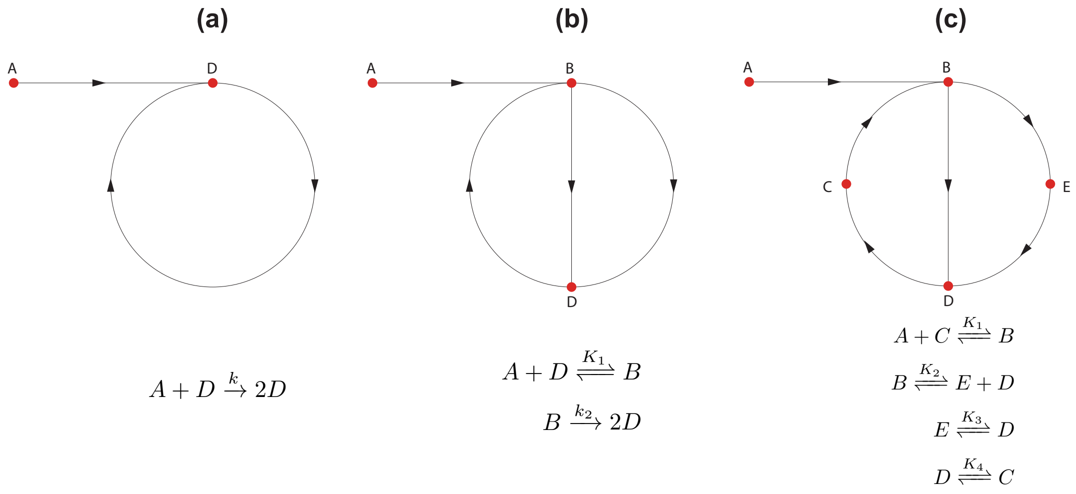

Figure 4.3: Diagrammatic representation of 3 autocatalytic mechanisms, adapted from [160]. **a)** Direct template autocatalysis. **b)** Direct template autocatalysis with an intermediate. **c)** Indirect autocatalysis.

product and reactants occurs, as opposed to *indirect autocatalysis*, such as the case illustrated in Figure 4.3 (c), where reactants and autocatalyst never interact directly.

Direct template autocatalysis normally incorporates an intermediate species B, formed by the template A and autocatalyst D (Figure 4.3 (b)).

$$A + D \underset{k_1^-}{\overset{k_1^+}{\rightleftharpoons}} B \tag{4.8}$$

$$B \xrightarrow{k_2} 2D \tag{4.9}$$

Assuming B is an unstable intermediate and that its variation can be neglected compared to A and D (quasi steady-state approximation), from the law of mass-action the growth is given by the rate expression:

$$r \equiv \frac{d[D]}{dt} = 2k_2[B] = 2k_2 \cdot K_1[A][D] = k_{eff}[A][D] \tag{4.10}$$

where $K_1 = \frac{k_1^+}{k_1^-} = \frac{[B]_{eq}}{[A]_{eq}[D]_{eq}}$ is the equilibrium binding constant and $k_{eff} = 2k_2K_1$ is an effective rate constant. The system is equivalent to the direct autocatalysis in (4.2), with a rate given by k_{eff}.

The PEN DNA toolbox implementation of an autocatalytic reaction (introduced in section 4.2.1) is a complex example of template autocatalysis, where association between reactants and autocatalyst occurs through Watson-Crick pairing. This system, which exhibits exponential growth at initial times, contains several intermediate species, enzymes and monomer oligonucleotides to sustain the reaction. In the next section the onset of reaction-diffusion fronts is described, namely when autocatalytic reactions are allowed to diffuse.

4.1.3 Mathematical description of chemical travelling waves

Travelling waves can arise when reaction kinetics are coupled with diffusion. In the following, the evolution of the concentration of an autocatalytic species in a one-dimensional reactor will be considered. The changes in concentration in space and time of a reacting species are governed by a reaction-diffusion equation, as derived from the mass-balance equation:

$$\frac{\partial d}{\partial t} = r(d) + D\frac{\partial^2 d}{\partial x^2} \tag{4.11}$$

where the autocatalyst concentration is expressed by $d(x,t)$, $r(d)$ is the autocatalytic reaction rate and D is the diffusion coefficient of the autocatalyst.

Note that if the reaction term $r(d)$ vanishes, then the equation represents a purely diffusive process (*Fick's 2ndlaw*). When the reaction term describes an autocatalytic process through the logistic function introduced in (4.4), $r(d) = kd(C-d)$, then for $C = 1$ the equation becomes the *Fisher-Kolmogorov-Piskunov (FKP)* equation and is rewritten as:

$$\frac{\partial d}{\partial t} = kd(1-d) + D\frac{\partial^2 d}{\partial x^2} \tag{4.12}$$

Coupling of autocatalytic growth and diffusion in the form described by equation (4.12) can give rise to travelling waves, as these are solutions to the equation. These type of waves propagate without changing shape. A mathematical description of such waves is given by solutions to (4.12) of the form $d(x,t) = d(x-vt) = d(z)$, where v is the speed of wave propagation and $z = x - vt$. When observed in a moving coordinate frame at velocity v, the wave appears stationary.

The formal solution to the FKP equation in (4.12) was first given by Kolmogorov, Petrovsky and Piskunov in [162]. They demonstrated that travelling wave solutions exist for wave velocities higher than a critical velocity $v \geq v_{min} = 2\sqrt{kD}$. They also showed that localised initial input of autocatalyst, mathematically expressed as initial conditions with compact support[2], evolve into travelling waves with the minimum speed v_{min}. Higher velocity waves arise when there is an initial gradient of the autocatalyst.

This result can be generalised to other cases, where the reaction term $r(d)$ takes a different form from the logistic function [158, 163]. Importantly, if the reaction term $r(d)$ fulfils certain criteria[3], then

$$v = 2\sqrt{r'(0)D} \tag{4.14}$$

corresponds to the velocity of the single stable asymptotic travelling wave solution, where r' is the derivative of r with respect to d and $r'(0)$ is taken at the limit where $d = 0$. In this case, v does not depend on details of the growth function $r(d)$, but only on its behaviour at low values of autocatalyst $d \approx 0$. This result will be useful in Section 4.2.1, where $r(d)$ is described by a Michaelis-Menten equation (4.23) rather than by the logistic equation (4.4).

In the FKP model, $r'(0) = k$ and we obtain $v = 2\sqrt{kD}$, which is known as *Luther's equation.* A heuristic argument by R. Fisher without the full mathematical rigour can be found in [164] and adapted to a context of chemical travelling waves in [165]. In the next section, we arrive at this result for the FKP model by performing a linear stability analysis for stationary solutions of (4.12) [155].

Derivation of Luther's equation for the speed of a travelling wave

Let us consider the following rescaling to simplify the FKP equation

$$\tilde{t} = kt, \quad \tilde{x} = x\left(\tfrac{k}{D}\right)^{1/2} \tag{4.15}$$

---

[2]

$$d(x,0) = d_0(x) \geq 0 \qquad d_0(x) = \begin{cases} 1 & \text{if } x \leq x_1 \\ 0 & \text{if } x \geq x_2 \end{cases} \tag{4.13}$$

where $x_1 < x_2$ and $d_0(x)$ is continuous in $x_1 < x < x_2$.

[3] 1. $r(0) = 0$, 2. bounded growth (i. e. there exists $d_{max} > 0$ such that $r(d_{max}) = 0$), 3. $r(d) > 0$, 4. $r'(0) > 0$, 5. $r'(d) < r'(0) \in (0, d_{max})$

and, omitting the tildes for notational simplicity, we rewrite equation (4.12) as:

$$\frac{\partial d}{\partial t} = d(1-d) + \frac{\partial^2 d}{\partial x^2} \tag{4.16}$$

We look for travelling waves of stationary form as solutions to the FKP equation by substituting $d(z) = d(x - vt)$ in (4.16) to transform a partial differential equation in x and t into an ordinary differential equation in z:

$$d''(z) + vd'(z) + d(z)(1 - d(z)) = 0 \tag{4.17}$$

where primes indicate differentiation with respect to z. Not all values of v or boundary conditions for $d(z)$ admit solutions. A wavefront solution that satisfies the boundary conditions $\lim_{z\to-\infty} d(z) = 1, \quad \lim_{z\to\infty} d(z) = 0$, can only exist for certain values of v. This sets up an eigenvalue problem that will determine the allowed values for v (to be specific, only $v > 0$ will be considered).

The second-order differential equation can be rewritten as:

$$d' = u \tag{4.18}$$

$$u' = -vu - d(1-d) \tag{4.19}$$

This system in the $(d, u) = (d, d')$ phase plane has two singular points, namely the steady states (0,0) and (1,0). By Taylor expanding around the singular points and retaining only linear terms, a linear stability analysis gives the following eigenvalues for the singular points:

Singular points	Eigenvalues	Stability
(0,0)	$\lambda_\pm = \frac{1}{2}[-v \pm (v^2-4)^{1/2}]$	stable node ($v^2 > 4$) and stable spiral ($v^2 < 4$)
(1,0)	$\lambda_\pm = \frac{1}{2}[-v \pm (v^2+4)^{1/2}]$	saddle point

Figure 4.4 shows the phase plane trajectories for different values of v. Negative values of autocatalyst concentration d are considered here as non-physical. The origin is only a stable node for values of $v \geq 2$. For $v < 2$ it becomes a stable spiral, where in the vicinity of (0,0) values of d oscillate. Following the argument in [155], a travelling wave solution exists for all values of $v \geq v_{min} = 2$, represented by

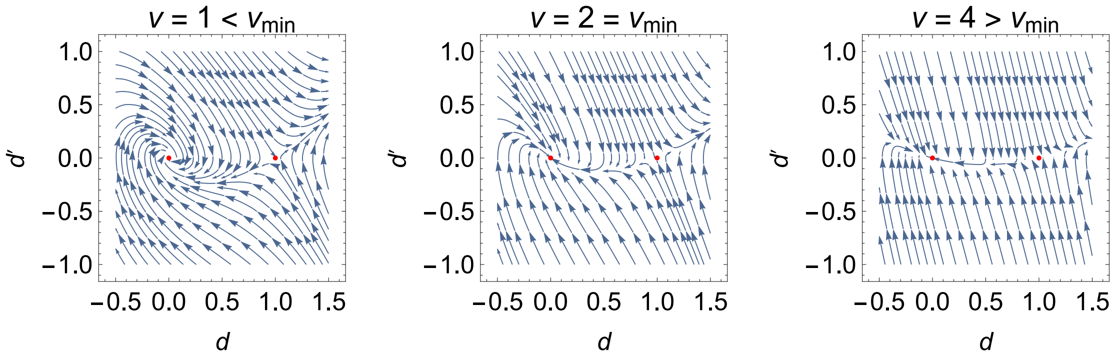

Figure 4.4: Phase-plane trajectories for equation (4.17), solved for $v = 1$, $v = 2$ and $v = 4$. The red points show the two singular points (0,0) and (1,0).

trajectories from (1,0) to (0,0) that lie in the quadrant $d \geq 0$, $d' \leq 0$, with $0 \leq d \leq 1$. In terms of the original dimensions, the range of allowed propagation speeds are:

$$v \geq v_{min} = 2\sqrt{kD} \tag{4.20}$$

which is *Luther's equation.*

The FKP equation is solved numerically (see appendix B.6) and wave profiles at different time steps are shown in Figure 4.5 (a). A kymograph is constructed in Figure 4.5 (b) by plotting wave profiles as a function of time, which shows the constant propagation speed of the wave.

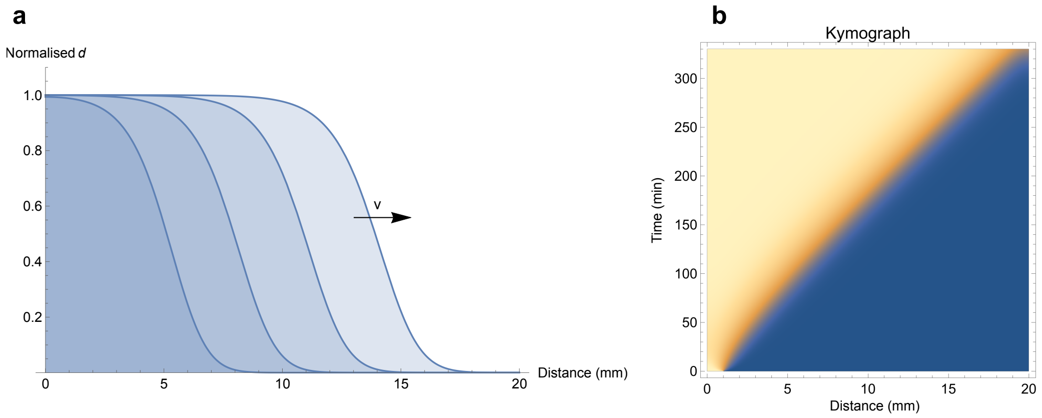

Figure 4.5: **a)** Propagation of a travelling wave, after solving the FKP equation for $k = 0.067$ min^{-1} and $D = 150$ μm^2 min^{-1}. The initial condition is a step function $d(x, 0) = \theta(x - 1)$. Profiles correspond to multiples of $t = 100$ min. **b)** Kymograph that shows the constant propagation velocity of the wave (in yellow), $v = 2\sqrt{kD} = 0.063$ mm min^{-1}.

Speed selection rule

The previous stability analysis reveals an infinite range of allowed wave propagation velocities, but it does not offer a selection criterion. For initial conditions that are not spatially localised (without compact support as expressed in equation (4.13)), the solution strongly depends on the profile of $d(x,0)$ [166]. The wave speed is governed by a selection rule [4] that states that if the initial profile decays more steeply than $d(x,0) \sim e^{-\lambda^* x}$, where $\lambda^* = v_{min}/2D$, then $v = v_{min} = 2\sqrt{kD}$; whereas if $d(x,0)$ decays less steeply than $e^{-\lambda^* x}$, then $v > v_{min}$.

---

[4] One way to understand this result is by analysing the leading edge of the wave, where autocatalyst concentration $d \ll 1$ is negligible. Then, the linearised version of FKP about $d = 0$ can be written as:

$$\frac{\partial d}{\partial t} = kd + D\frac{\partial^2 u}{\partial^2 x}$$

This equation can be solved exactly [167] and for the initial condition of an exponential profile $d(x,0) = e^{-\lambda x}$ for $x > 0$, the solution reads:

$$u(x,t) = \frac{1}{2}e^{-\lambda(x-v(\lambda)t)}\left[1 + \operatorname{erf}\left((x - 2D\lambda t)/(2\sqrt{Dt})\right)\right]$$

where $v(\lambda) = D\lambda + \frac{k}{\lambda}$. This solution reveals that different parts of the wave profile move at different speeds. On the one hand, at the far tip of the wave, $x \gg 2D\lambda t$, the error function is approximated by $\operatorname{erf}(y) \approx 1$ for $y \gg 1$ and the solution simplifies to $u(x,t) \approx e^{-\lambda(x-v(\lambda)t)}$. Then, the tip of the wave moves at a speed $v(\lambda)$, which depends on the initial steepness. However, for regions where $x \ll 2D\lambda t$, i.e the back of the wave profile, we can expand the error function $erf(-y) \approx -1 + \frac{e^{-y^2}}{\sqrt{\pi y}} + ...$ and the solution reduces to $u(x,t) \approx e^{-\lambda^*(x-v^*t)-(x-v^*t)^2/(4Dt)}$, where $v^* = v_{min} = 2\sqrt{kD}$.

The crossover point x_c between these two regimes occurs when $x_c = 2D\lambda t$. For values of $\lambda > \lambda^* = v_{min}/2D$ the crossover moves faster than the tip of the wave, therefore the core of the wave will move at speed v_{min}. However, if $\lambda < \lambda^*$, then the crossover point remains behind the tip of the wave, and for long times it will be the speed of the tip $v(\lambda)$ that will control the speed of the wave. This is illustrated in the two profiles in the figure below for (a) $\lambda = \lambda^*/2$ and (b)$\lambda = 2\lambda^*$.

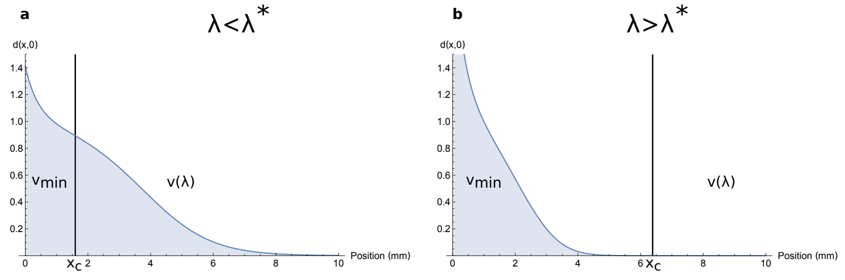

Figure 4.6: $d(x,t_1)$ solution to the FKP equation with initial conditions **a)** $d(x,0) = e^{-\lambda^*/2}$ and **b)** $d(x,0) = e^{-2\lambda^*}$. The horizontal line marks the crossover $x_c = 2D\lambda t$, which separates regions moving at v_{min} $(x \ll x_c)$ and at $v(\lambda)(x \gg x_c)$. For steep initial conditions the crossover point moves faster than the tip of the wave, and the wave front has speed v_{min}.

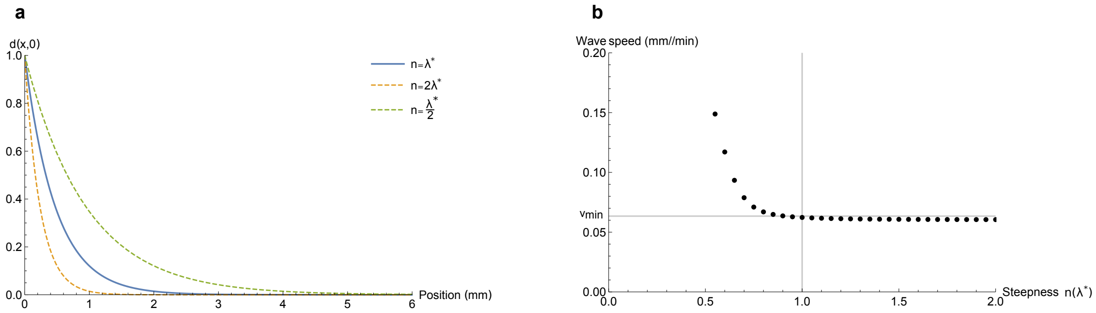

Figure 4.7: *Velocity selection for initial condition of varying steepness.* **a)** Initial conditions of the exponential form $d(x,0) = e^{-n\lambda^* x}$ where $\lambda^* = v_{min}/2D$. **b)** Wave front velocities for numerical solutions to the FKP equation with initial conditions of the form $d(x,0) = e^{-n\lambda^* x}$. For steepness $n \geq 1$, wave velocities evolve to v_{min}.

.

To illustrate this selection principle, we solve the FKP equation for initial conditions of varying steepness $d(x,0) = e^{-n\lambda^* x}$ (shown in Figure 4.7 (a)). Wave profiles that are solutions to the equations were then fitted with a sigmoidal function to extract the wave front position as a function of time. Wave velocities plotted in Figure 4.7 (b) show that for steep initial conditions $\lambda > \lambda^*$, the wave velocity collapses to the critical velocity given by Luther's equation $v = v_{min} = 2\sqrt{kD}$. Less steep initial conditions, however, $\lambda < \lambda^*$, display faster velocities $v > v_{min}$. The relevance of this result is that for sufficiently steep initial profiles, the wave velocity is independent of initial conditions and it will only depend on kinetic and transport parameters, such as k and D. Translated into an experimental setting, these results show that sufficiently steep initial conditions (e.g. Heaviside-type step function) yield the same wave speeds.

4.1.4 Chemical waves in inhomogeneous template concentrations

What happens when the autocatalytic growth rate $r(d)$ varies in space? This chapter addresses the question of chemical waves propagating in spatially inhomogeneous media. A useful analogy to illustrate the problem is one of a propagating wave in 'on' and 'off' regions. 'On' regions correspond to areas where autocatalysis and wave propagation are possible, whereas 'off' regions do not sustain autocatalysis.

This setting would lead to ballistic wave propagation in 'on' regions and to mere diffusion in 'off' regions. At the interface between 'on' and 'off' regions there would be different non-linear wave dynamics worth exploring.

In order to tackle this problem computationally, to serve as a guide for experiments in section 4.5, we introduce a spatial dependence in the reaction term $r(d) = kd(1-d)f(x)$ of the FKP equation (4.12). This spatial dependence can be interpreted, for example, as a spatially varying concentration of template for autocatalysis (A in equation (4.2)) or as the presence of a spatially varying inhibitor species. For convenience, the spatial dependence is absorbed into $k = k(x)$, allowing us to rewrite the FKP equation as

$$\frac{\partial d}{\partial t} = k(x)d(1-d) + D\frac{\partial^2 d}{\partial x^2} \tag{4.21}$$

Figure 4.8 shows the wave front profiles at different times for a chemical wave propagating in a decreasing gradient of template concentration.

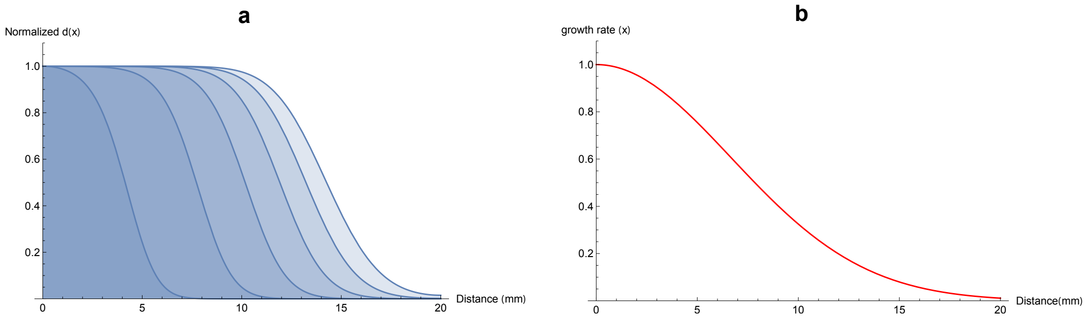

Figure 4.8: *Propagation of a travelling wave with spatially varying autocatalytic rate* **a)** Propagation of a travelling wave, after numerically solving equation (4.21) for $k = k_0 f(x)$, $k_0 = 0.067\ \mathrm{min}^{-1}$ and $D = 150\,\mu\mathrm{m}^2\,\mathrm{min}^{-1}$. Profiles correspond to multiples of $t = 100$ min. **b)** Exponential-type gradient $f(x) = e^{-3x^2/L}$.

A full numerical solution for equation (4.21) yields the kymographs in Figure 4.9 for the shown gradient profiles. We explore two types of gradients in this work, both computationally and experimentally: Exponential-type gradients $k(x) = e^{-x^2/A}$ and Heaviside-type gradients, $k(x) = k\theta(x-10)$. The latter sharply distinguishes a region of ballistic propagation from a diffusive one (in the context of a travelling wave, 'ballistic' here refers to propagation at constant speed). The results indicate that a deviation from ballistic velocities for wave fronts is to be expected in experimental systems described by equation (4.21).

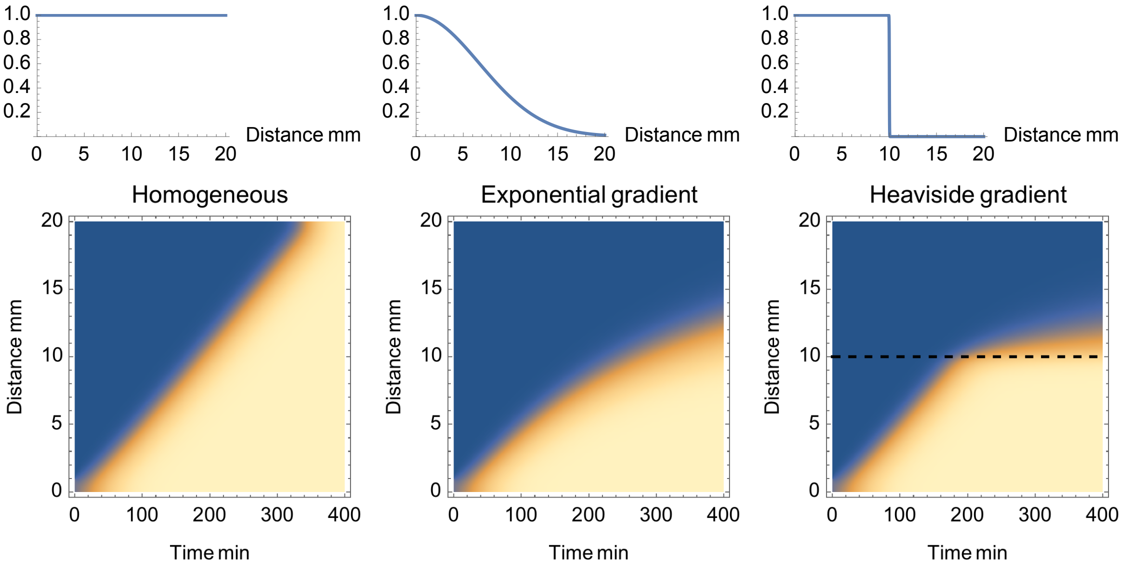

Figure 4.9: Numerical solutions to the FKP equations for $k = 0.067$ min^{-1} and $D = 150$ μm^2 min^{-1}. The upper graphs represent how $k(x)$ changes in space, while the density plots in the bottom represent kymographs. The dashed line distinguishes a ballistic region, where the wave front velocity is linear, from a diffusive one. Simulation code is given in the appendix B.6.

With these results as a guide, the next section is devoted to the experimental study of a DNA-based autocatalytic system. Propagating waves are generated in homogeneous and inhomogeneous media, mimicking the conditions described in Figure 4.9.

4.2 Experimental system

4.2.1 Autocatalytic DNA amplification reaction

For all experiments in this chapter, we consider an autocatalytic system based on the self-growth of an oligonucleotide **d** in the presence of DNA polymerase (Bst, New England Biolabs (NEB)), nickase (Nt.Bst, NEB), a template strand **T** and monomer nucleotides (dNTP, NEB). This autocatalytic system is based on the PEN DNA toolbox (Polymerase Exonuclease Nickase, Dynamic Network assembly toolbox) [106], described in chapter 7. Figure 4.10 illustrates the autocatalytic mechanism.

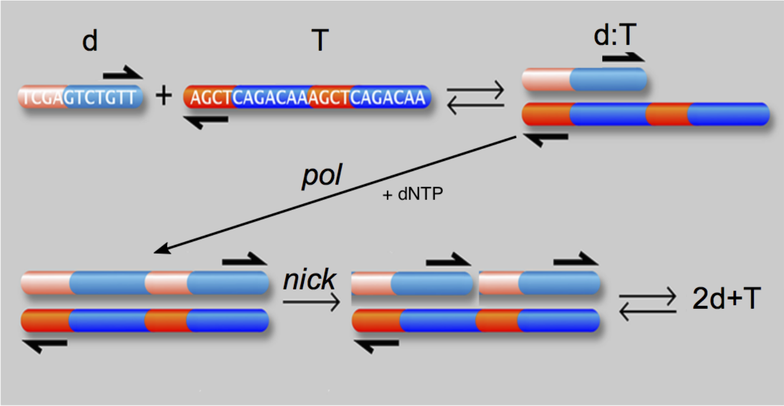

Figure 4.10: *Autocatalytic mechanism*: **d** reversibly hybridises with the **T** template to form the complex **d:T**. This complex is extended by the polymerase, *pol*, to form a dsDNA, which is recognised by the nicking enzyme, *nick*, yielding two copies of **d**. (Diagram adapted from [158]).

The net reaction is $d \rightarrow 2d$ and it shows exponential growth at short times (at least for 20 min) [158]. The growth rate $r(d)$ depends on the concentration of autocatalyst, template strand, polymerase and nickase concentrations. An excess of dNTPs acts as a reservoir of free energy keeping polymerization rate constant over long periods of time ($100-1000$ min). A typical amplification curve for this reaction (Figure 4.11) shows initial exponential amplification, followed by faster exponential growth, linear growth and eventually saturation. Saturation can occur if, for example, the template saturates when bound to excess autocatalyst or if the nucleotide monomers that sustain the reaction are consumed.

The linear autocatalytic model $d \rightarrow 2d$ is a simplification that does not reflect the full amplification mechanism shown in Figure 4.12, although it is a faithful representation at short times. Superexponential growth, such as the one observed in Figure 4.11, arises when linear processes are suppressed in autocatalytic cycles, allowing higher-order processes to take place (i.e. association between more than two species to create a third species) [168]. The linear growth after saturation of template observed in Figure 4.11 is due to the accumulation of single-stranded autocatalyst in solution, which is weakly fluorescent in these conditions. However, in the presence of exonuclease *RecJ* (not used in this work), single stranded DNA can be digested and the reaction reaches a flat steady state instead, as shown in [169]. Templates used in this autocatalytic system contain phosphorothioates to avoid exonuclease activity.

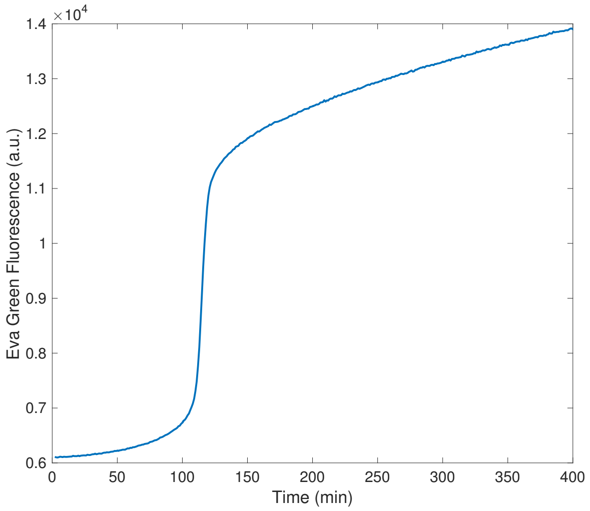

Figure 4.11: Characteristic growth profile of autocatalyst d with initial template T at 100 nM, as measured by fluorescence of a DNA intercalating dye (EvaGreen). The amplification is exponential for at least the first 20 min.

To explain the amplification process for the autocatalytic system outlined in Figure 4.12 we follow a similar mechanism proposed by Fuji and Rondelez in [106] and [169]. The approach to finding the reaction term $r(d)$ is the following: we assume that all association and disassociation reactions between DNA strands (reactions 1-4) are much faster than enzymatic reactions; i.e. DNA species are in quasi-equilibrium. The polymerisation process in Figure 4.12 (5), as a rate-limiting step, imposes an upper limit on the maximum rate of the autocatalytic process[5]. Bst polymerase can also recognize and elongate nicked substrates. In this case, strand displacement occurs and the reaction is slower because the enzyme needs to unwind the forward strand before it can add a new nucleotide to the nascent strand. [169].

We can then express the production rate of d empirically by the Michaelis-Menten expression as:

$$r(d) = k_{pol} \cdot pol \cdot \frac{B}{K_M + B} \tag{4.22}$$

---

[5] The polymerisation rate is $k_{pol} = 6 \cdot 10^{-3}$ s^{-1} [169] and the duplex dissociation rate is on the order of $k_{off} \sim 1$ s^{-1}, considering a $k_{on} \sim 10^7$ M^{-1}s^{-1}. Since $\frac{k_{pol}}{k_{off}} \ll 1$, then the quasi-equilibrium approximation is justified.

where $B \equiv B_1 = B_2$ is the concentration of the complex *d:T*, k_{pol} is the polymerisation rate constant, *pol* the concentration of polymerase and K_M is the Michaelis-Menten constant for the saturation of polymerase by the template.

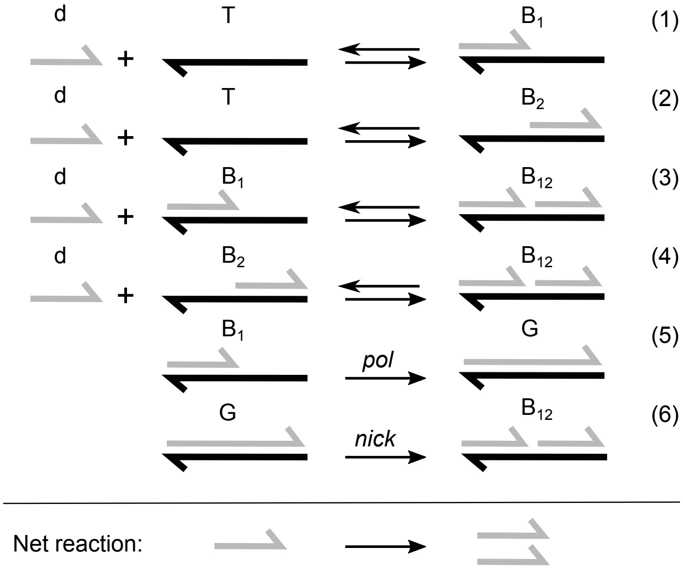

Figure 4.12: *Mechanism of DNA autocatalysis $d \to 2d$.* The 11-base long autocatalyst d hybridizes with 22-mer T, which bears two contiguous sites complementary to d. Reactions (1-4) represent possible hybridisation reactions generating species B_1, B_2 and B_{12}. B_1 and B_2 may be extended by a polymerase, *pol*, to form species G. G carries a recognition site for a nicking enzyme, *nick*, such that the upper strand is cut at its midpoint, yielding species B_{12}, which can then dissociate into $2d$. (Diagram adapted from [158] and [106]).

From reaction (1) in Figure 4.12, and considering fast equilibrium, we have $B = K_a \cdot d \cdot T$, where K_a is the equilibrium association constant [6], we can then write:

$$r(d) = k \cdot pol \frac{K_a \cdot d \cdot T}{K_M + K_a \cdot d \cdot T} \tag{4.23}$$

The experimental conditions normally occur at a concentration range of template T below 200 nM, in a regime where polymerisation does not reach saturation of the enzyme [7]. We can then approximate the rate equation as:

$$r(d) \approx k \cdot pol \frac{K_a \cdot d \cdot T}{K_M} \tag{4.24}$$

---

[6] For $d + T \leftrightharpoons B$, NUPACK (http://www.nupack.org) predicts an association constant of K_a=$13 \cdot 10^7$ M^{-1}

[7] (Bst polymerase $K_M > 1\mu$M)

For low concentration of autocatalyst, we can integrate the previous expression that yields the exponential growth $d = d_0 e^{r'(0)t}$, where $r'(0) = k_{eff} \cdot pol \cdot T$ and k_{eff} is an effective constant. The linear dependence of the growth rate with template and polymerase concentration is experimentally demonstrated in [158] and confirmed for the system used in this work in section 4.4.

In section 4.1.3, we showed that the behaviour of the growth rate $r(d)$ at $d \approx 0$ governs wave dynamics, independent of its full functional form, if some criteria are met. In particular, travelling wave solutions for Michaelis-Menten-type growth exist with velocities given by equation (4.14) [170]. When the function $r(d)$ differs from the one of FKP, a multiplicative constant greater than unity may appear in the expression of the velocity (see for example [161]). To take this into account, the authors in [158] introduce a corrective factor γ in the wave velocity, together with an effective diffusion coefficient :

$$v_{corr} = \gamma v = 2\gamma\sqrt{r'(0)D_{eff}} \tag{4.25}$$

Substituting $r'(0)$ into equation (4.25), we obtain $v = v = 2\gamma\sqrt{r'(0)D_{eff}} \propto \sqrt{pol \cdot T \cdot D}$.

This section has served as a description of a DNA based autocatalytic system with tunable growth rate. In the next section, the properties of this DNA autocatalytic system will be used to create propagating waves and to control its dynamics, taking into account that the reaction kinetics can be altered by changing the template T and polymerase *pol* concentrations. We will then introduce spatially varying template concentrations $T(x)$ in order to study new wave dynamics.

Modified autocatalytic DNA amplification reaction with inhibitor and reporter strands

We introduced two modifications to the system in Figure 4.10 in order to control the growth of this reaction and to visualise the propagating front on a channel when the template T concentration changes in space: On the one hand, an inhibitor strand that competes with the autocatalyst to bind to the template was used (inh). The inhibitor slows down the autocatalytic growth, as illustrated in Figure 4.13

and prevents self-starting autocatalysis (a recurrent problem in all DNA wave experiments). On the other, a fluorescent reporter strand (f2ie-Dy530) that binds to d was added to monitor autocatalyst generation. The reporter strand is labelled with a dye (Dy530) and its fluorescence is quenched when bound to d. By measuring a reduction in fluorescence, the propagating front could be tracked in regions with little or no template. Autocatalyst quantification is normally achieved with an intercalating dye (EvaGreen), which effectively reports autocatalyst generation when it binds to a template strand to form a duplex, but not in the case of ssDNA. A full list of oligonucleotides used for the modified reaction network in Figure 4.13 is given in Table 4.1.

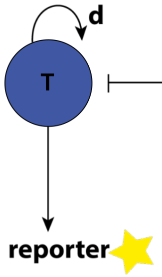

Figure 4.13: *Diagrammatic representation of the modified reaction network.* Template T generates autocatalyst d, which binds to reporter f2ie and quenches its fluorescence. d competes with inhibitor inh to bind to T.

Table 4.1: List of used oligonucleotides (from Biomers Gmbh)

DNA strand name	Sequence	Description
T-biotin	AACAGAC-TCGA AACAGAC-TCGA-TTTTT	template (with spacer+biotin)
d	TCGA-GTCTGTT	autocatalyst
inhibitor **inh**	AGTCTGTT-TCGAGTAA	growth inhibiting strand
reporter **f2ie**-Dy530	T*T*A*CTCAGCCAAGACAACAACAGACTCGA-DY530	binds to d

4.2.2 Microfluidic chamber for the observation of DNA wave fronts

DNA wavefronts were created and monitored in reaction chambers assembled with polystyrene slides cut out of sterile Petri dishes (10 mm thick). This material was chosen for its proven compatibility with enzymes and buffer mix, as opposed to commercial slides with treated surfaces. 1 mm diameter holes were drilled in the upper slide to facilitate filling the chamber using a micropipette. Two layers of parafilm were sandwiched between two polystyrene slides and heated at 80°C for one minute. Each assembled slide contained 4 to 5 reaction chambers and served for setting up simultaneous wave front experiments (Figure 4.14 (a)). To create a DNA wave, a chamber was filled with enzyme, template and Predator-Prey (PP) buffer mix (see appendix A.9). Once the chamber was ready, a small amount of trigger autocatalyst *d* was placed at the inlet of each channel to initiate the reaction, followed by sealing of the chamber with epoxy to prevent evaporation.

The reaction chambers were approximately 1.3 cm long, 2 mm wide and 0.25 mm thick. Longer channels were used in some experiments to allow for continued wavefront propagation.

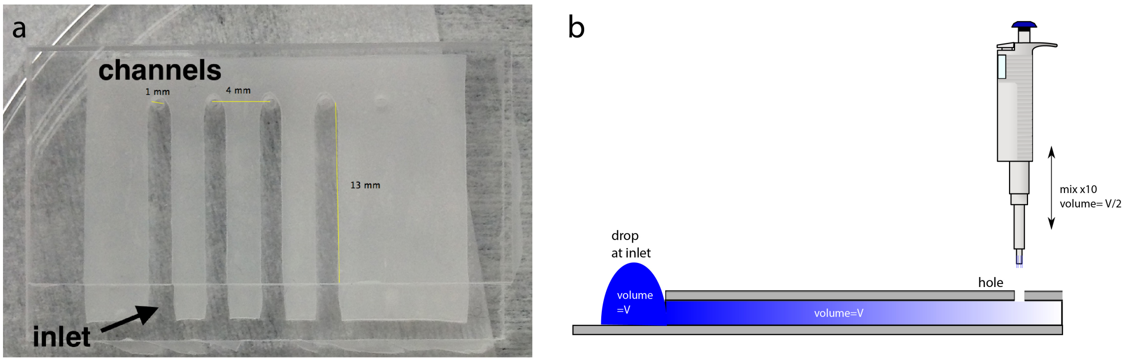

Figure 4.14: a) Microfluidic setup with 4 reaction chambers, assembled with parafilm and polystyrene slides. **b)** Gradient generation protocol through *Taylor dispersion* by partially mixing two solutions with a pipette.

An inverted microscope (Zeiss Axio Observer Z1) was used for the observation of wave fronts. The microscope was equipped with a 2.5× lens, a LED excitation light, a motorised stage with a transparent heating plate kept at 38°C and a CCD camera. Acquisition and analysis were done with μmanager, ImageJ and MATLAB (see section 4.5.1).

4.2.3 Creating gradients of template oligonucleotides (in solution and immobilised on a surface)

Gradients can be generated free in solution or they can be immobilised on a surface. These two approaches are presented and discussed.

Gradients in solution

Gradients were generated in reaction chambers using pipettes and tips that fitted the 1 mm hole in the chamber. For the dimensions of the chamber and the approximate flow created with pipettes ($10\,\mu l\,s^{-1}$), a Reynolds number on the order of $Re \approx 50$ indicates that the regime is laminar and therefore Poiseulle's law applies. Holes on both ends of the chamber facilitate the generation of gradients in two steps: firstly, the chamber is filled with a common buffer and then the same volume of the desired component is placed at the inlet in contact with the common buffer as illustrated in Figure 4.14 (b). Secondly, a gradient forms through *Taylor dispersion*, the combined effect of convection and molecular diffusion, and flow reversal.[8] This is achieved by placing the pipette in the hole and aspiring and mixing backwards and forwards at a constant rate more than 10 times. Figure 4.15 shows examples of this gradient generation technique using methylene blue as a test dye.

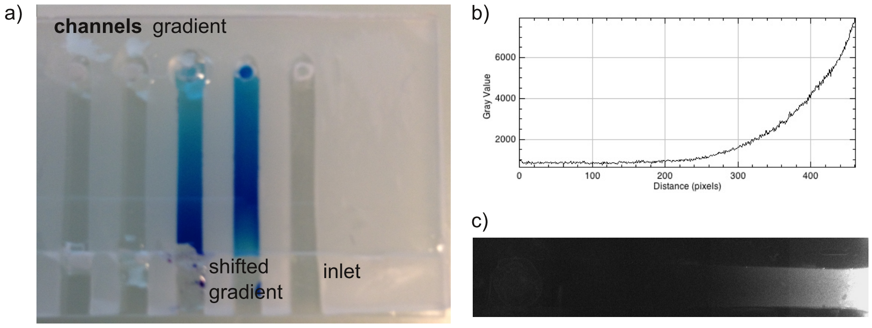

Figure 4.15: a) Gradients of methylene blue in reaction chambers assembled with polystyrene and parafilm. **b)** and **c)** Exponential-type template oligonucleotide gradient in solution as reported by ROX dye fluorescence.

For the timescale of wavefront experiments (which can range from 5 to 10 hours) a change in the shape of the gradient is expected as dictated by the law of diffusion and simulated in Figure 4.16. Heaviside-type gradients change more significantly than exponential-type gradients making tracking of the template strand as it diffuses a necessary ingredient in the experiments.

---

[8] In the axial direction, the chemical transport is mainly due to convection; since the flow is essentially axial in the direction of the channel, the transport in the transverse direction is mainly due to diffusion. This type of chemical spreading, involving both axial convection and transverse molecular diffusion, is called *Taylor dispersion* [171].

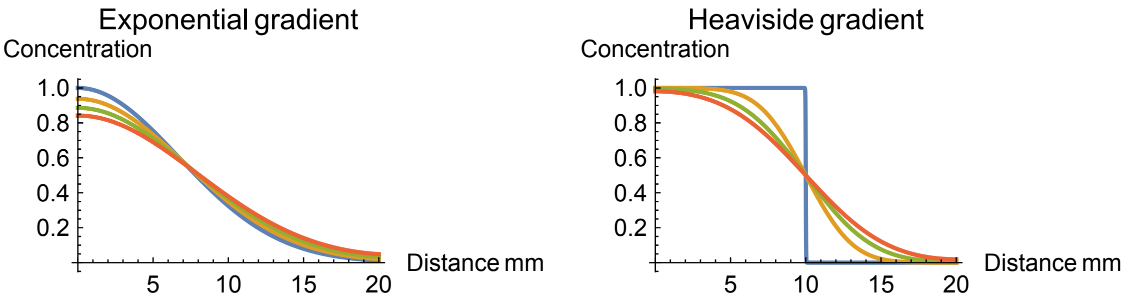

Figure 4.16: Profile snapshots taken every 200 min showing the evolution for two types of gradients by numerically solving the diffusion equation for given initial conditions of template strand concentrations (in blue).

Immobilised gradients on a surface

The previous technique can be extended to permanently immobilise a gradient of oligonucleotides on a surface. For this approach, PEGylation of a microscope slide was necessary (full protocol in [172]). After this process, which involves silanisation of the substrate, Biotin-PEG was added homogeneously, followed by 1µM streptavidin in 1xTE buffer with 1M NaCl. This ensured a homogeneous coating of streptavidin on the biotinylated surface. After incubating the mixture for 30 min, a gradient of biotinylated fluorescent template strand biotin-T-DY530 was created, followed by several washing steps. In Figure 4.17 the gradient formation of immobilised fluorescent template strands is shown. Inhomogeneous immobilisation of template strand T on a surface could faithfully resemble a spatially varying $k(x)$ in the FKP equation. However, in this case autocatalysis would only be limited to the surface and

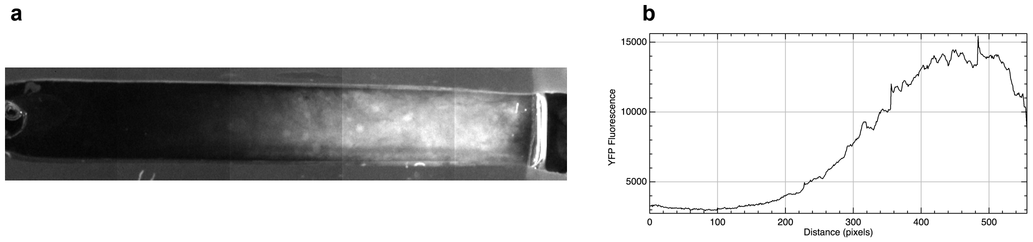

Figure 4.17: Example of a successful generation of a gradient of fluorescent biotinylated T-dy530. **a)** is a fluorescence image of the channel (YFP channel) and **b)** its horizontal intensity profile after averaging in the y-direction

no reaction would happen in the bulk, as the wave propagates. Experiments with the immobilised template gradient shown in Figure 4.17 did not render measurable wave fronts. This is why no further surface immobilisation was attempted in experiments and the former approach for creating gradients free in solution was taken.

4.2.4 Measurement of DNA wave propagation

First, we study DNA waves in a homogeneous medium, where template concentration is constant in space. The chambers were filled with 10 µl of a reactive solution containing PP buffer (see appendix A.9) and template T (when gradients were formed no T was added at this step). A small volume (1 µl) of a highly concentrated solution of autocatalyst (1 µM) mixed with PP buffer was added in the inlet of the chamber to initiate wave generation. The chambers were sealed with epoxy to prevent evaporation and they were immediately transferred to a transparent hotplate (Tokai-Hit) set at 38°C, ready for observation in the microscope.

Fluorescence of EvaGreen (a DNA intercalating dye) at the GFP channel and Dy530 fluorescence at the YFP channel were recorded, as reporters of autocatalyst concentration. A μmanager code was written to program the microscope stage to take several consecutive recordings overnight. Figure 4.18 shows an example of wave propagation as reported by quenching of Dy530.

4.3 Kinetic control of DNA wave propagation

As mentioned in the introduction, one approach towards control of DNA propagation is to alter its kinetics of autocatalysis. The reaction kinetics has a direct impact on the speed of the travelling wave, as given by Luther's equation (4.20) $v = 2\sqrt{kD}$. The results in section 4.2.1 indicate that by tuning diffusion and autocatalytic rates, control over the propagation speed can be achieved. In this section a DNA wave is successfully created and an inhibitor strand is introduced, which slows down the speed of the wave. This convoluted approach to tuning the reaction rate is motivated by an attempt to hinder self-starting autocatalysis (non-triggered initiation of wave propagation), which is a recurrent problem in this autocatalytic system.

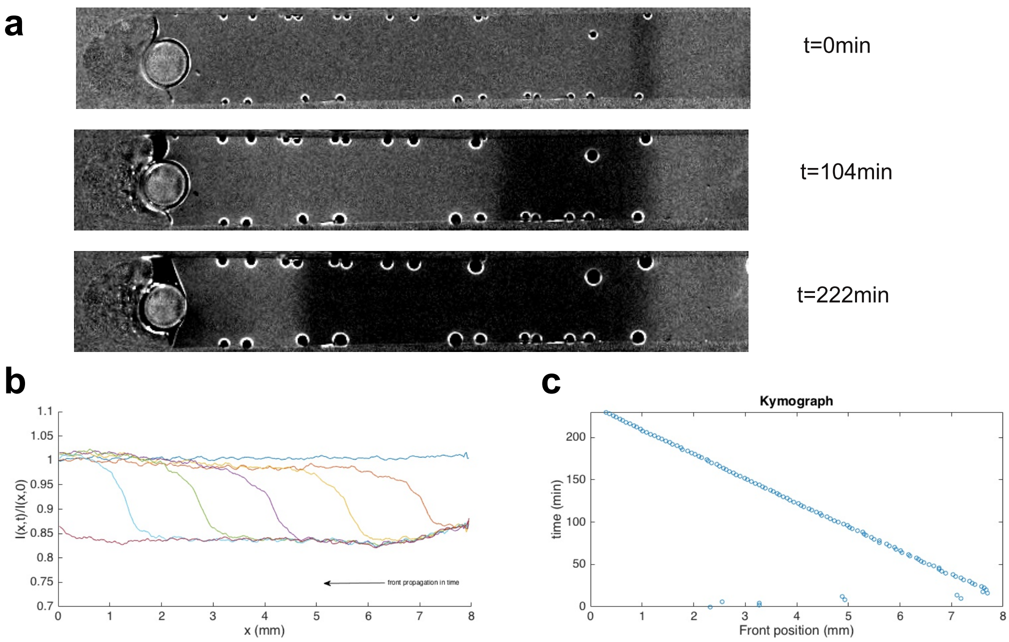

Figure 4.18: Channel filled with homogeneous T template 100 nM, 100 nM inhibitor strand, 50 nM and reporter Dy530. Input autocatalyst d 1 μM was added at the right inlet of the channel to initiate the wave. **a)** Dy530 fluorescence of microfluidic channel recorded at different times. **b)** Normalized intensity showing wave front propagation (from right to left). **c)** The position of the wave front over time at a velocity $v = 35$ $\mu\mathrm{m\,min}^{-1}$.

4.3.1 Autocatalytic reaction kinetics in a well-mixed solution

The kinetics of the autocatalytic reaction was first characterised using a CFX96 Touch Real-Time PCR Detection System (Bio-Rad) with a thermostated fluorescence reader kept at 38°C. Two fluorescence channels were monitored, one for EvaGreen (λ_{abs}=500 nm, λ_{emi}=525 nm) and the other one for Dy530 (λ_{abs}=539 nm, λ_{emi}=561 nm).

PP buffer was mixed with 3% final concentration of nickase (Nt.Bst), and 1% of polymerase (Bst) while the T template was kept at a concentration of 100 nM. d was used as a trigger at 1 nM final concentration and with none in a control experiment. Figure 4.19 shows the autocatalytic growth of d, exponentially amplified until it reaches saturation of the template. After this the growth is linear. We observe that the non-triggered reaction starts after 60 min, a process known as *self-start*, which can be due to contamination of small amounts of d.

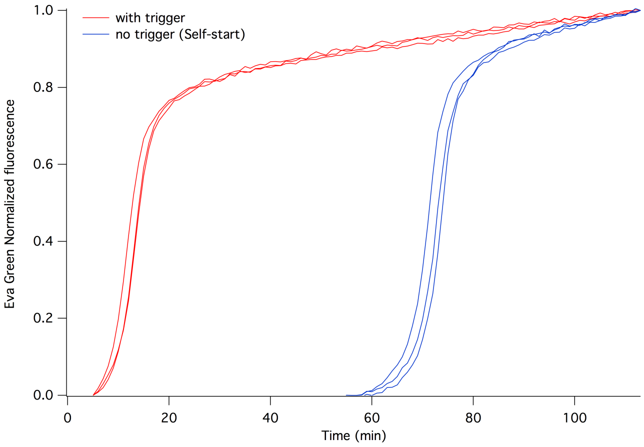

Figure 4.19: Autocatalytic growth of d in the presence of an autocatalyst trigger, as monitored by EvaGreen fluorescence. A non-triggered reaction starts after 60min (self-start).

4.3.2 Inhibition changes the kinetics of autocatalytic reaction

The first approach that we considered to reduce the self-start in this system was to introduce an inhibitor strand inh, that competes with d to bind to the template, thereby hindering growth. This delay in growth was characterised by measuring EvaGreen fluorescence in a well-stirred solution. The mixture protocol in Table 4.2 was followed.

Table 4.2: Mixture protocol for CFX growth experiment with 100nM inhibitor strand

	1	2	3	4
	-d -inh	-d +inh	+d -inh	+d +inh
PP Master Mix (2X)	10ul	10ul	10ul	10ul
d (20nM)	-	-	2ul	2ul
Inhibitor (2uM)	-	1ul	-	1ul
H_2O	10ul	9ul	8ul	7ul
Total	20ul	20ul	20ul	20ul

Figure 4.20 shows the kinetics of this reaction, as monitored with fluorescence measurements in qPCR (CFX, BioRad). We notice that the addition of the inhibitor strand delays the self-start by 400 min. However it also delays the triggered autocatalytic growth.

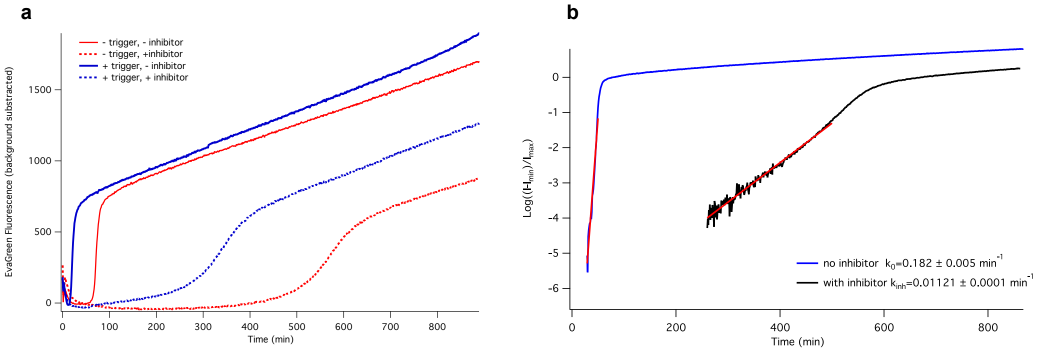

Figure 4.20: **a)** Eva Green Fluorescence monitoring of autocatalytic growth in the presence or absence of an inhibitor strand. Triggered and self-started growth are shown. **b)** Logarithmic plot of normalized intensity values for triggered reactions with an without inhibitor. A linear fit gives an estimate of the autocatalytic rate $r'(0)$.

In addition, the growth kinetics changes. Linear fits to the logarithm of normalized intensities in Figure 4.20 (b) show a change in the rate of $\frac{k_0}{k_{inh}} \approx 16$, which translates (using equation (4.25)) into a change in velocity of a DNA front of $\frac{v_0}{v_{inh}} \propto \sqrt{\frac{k_0}{k_{inh}}} \approx 4$. The addition of the inhibitor strand translates into a slower propagating wave as can be seen in the kymographs from Figure 4.21.

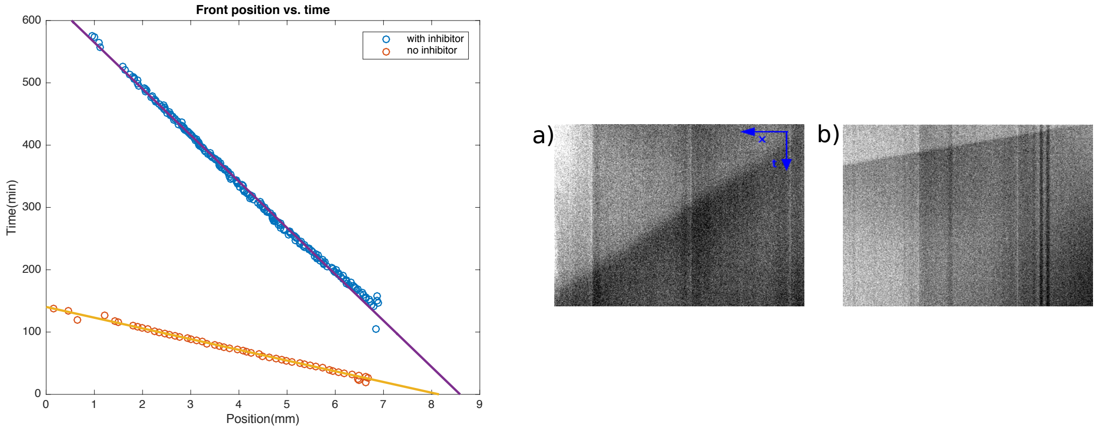

Figure 4.21: Kymographs representing average Dy530 fluorescence intensity in space and time for channels with homogeneous template distribution (100nM) with **a)** and without inhibitor **b)**. Velocities are $v_{inhibitor}$=13.4 µm min^{-1} and $v_{noinhibitor}$=58.1 µm min^{-1}

4.4 Spatial control of DNA wave propagation

In section 4.1.4 we saw that spatially changing autocatalytic growth rate led to nonlinear wave propagation. In the following, first the autocatalytic growth rate dependence on template concentration is measured experimentally for this system. Then, wave front propagation in Heaviside-type and exponential-type gradients of template oligonucleotides are studied.

4.4.1 Growth rate dependence on template concentration

The reaction buffer mix was prepared with polymerase (Bst 1%) and nickase (Nt.Bst 3%) with 50 nM reporter strand. The final template concentration was varied from 0 to 200 nM. All samples were initiated with 1 nM autocatalyst. Figure 4.22 shows EvaGreen fluorescence (as a reporter of autocatalyst concentration) measured in qPCR (CFX, BioRad) at 1 min intervals. These results show different autocatalytic growth rates for varying template concentrations.

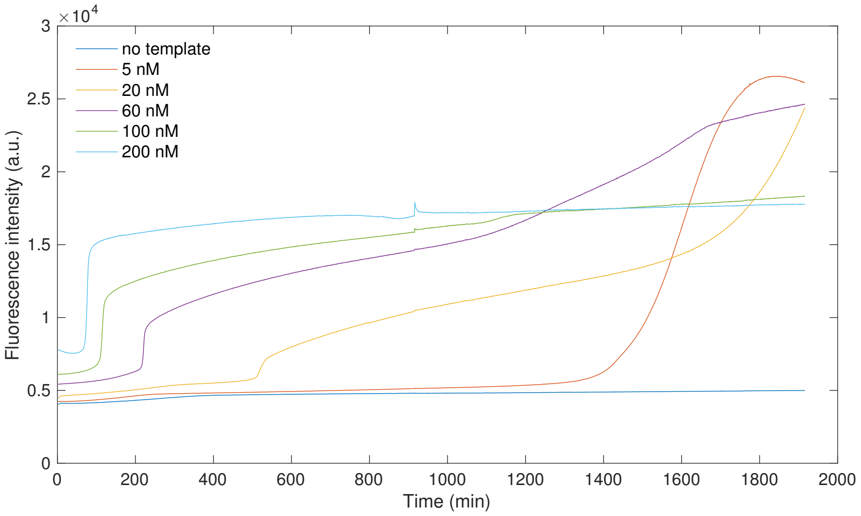

Figure 4.22: Raw fluorescence data from reaction mixes with varying concentrations of template.

As only growth at initial times is relevant for wave propagation, we follow the same fitting procedure as in [158] to obtain the value of $r'(0)$. The minimum fluorescence intensity was subtracted to the raw signal and normalised. We fitted the initial part of the autocatalyst growth curve to an exponential function. Figure 4.23 shows the logarithm of the normalised fluorescence intensity $\ln \frac{I-I(t=0)}{I_{max}}$.

We obtain a linear relationship between exponential growth rate at low autocatalyst concentration $r'(d \approx 0) = k$ and template concentration. This dependence is shown in Figure 4.23 (b). This result is in agreement with the linear relationship reported in [158] for concentrations smaller than 100 nM. Therefore, in the next experiments $r'(0) = \alpha T$ is considered to create a spatially inhomogeneous growth rate by creating gradients of template strands in a channel.

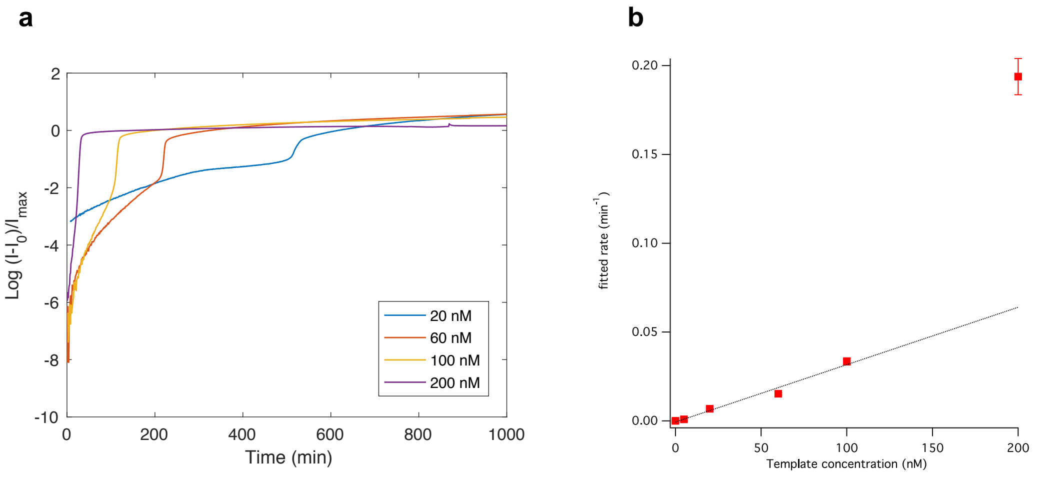

Figure 4.23: **a)** $\ln \frac{I-I(t=0)}{I_{max}}$ for reaction mixes with 200 nM, 100 nM, 60 nM and 20 nM template. **b)** Fitted growth rates vs template concentration. Growth rate scales with template concentration for template concentrations up to 100 nM in agreement with [158].

4.5 Wave front propagation in Heaviside and Exponential gradients of template

4.5.1 Dynamic variables from microscopy data

Dynamic variables were extracted from microscopy data using ImageJ and MATLAB analysis tools. These variables fully characterise the wave at a given time t. In the following lines, a description of the analysis that was performed for all wave experiments is presented.

Front position

The front position was obtained after normalisation of the wave profile, dividing the fluorescence raw data by the frame with maximum fluorescence (for Eva Green GFP fluorescence this was the last recorded frame and for Dy530 quenched fluorescence it was the first recorded frame). To calculate the front position the following steps were taken: first normalised profiles were generated from the raw data (Figure 4.24 (a)) to profiles with intensity values ranging from 0 to 1 by $\frac{I-I_{min}}{I_{max}}$ (Figure 4.24 (b)), then 0.5 was subtracted to these profiles so that their values remained between -0.5 and 0.5 (Figure 4.24 (c)). After taking the absolute value of the shifted profiles, an algorithm searched for the minimum point, which was then defined as the front position of the profile (Figure 4.24 (d)). From here, plots of front position as a function of time were obtained. It should be noted that fronts shown here propagate from right to left and that high intensity fluorescence corresponds to an unquenched fluorophore, i.e. no autocatalyst.

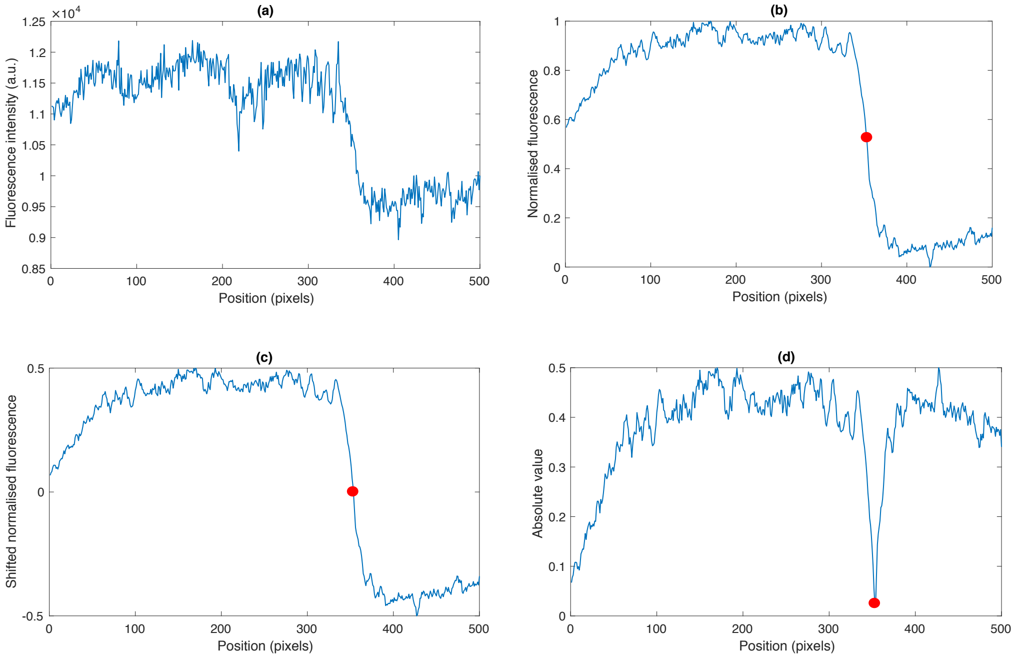

Figure 4.24: *Method for determining the wavefront position*: raw fluorescence intensity **a)** is first normalised by $\frac{I-I_{min}}{I_{max}}$, **b)**, then 0.5 is subtracted **c)** and the absolute value of the function is calculated **d)**. An algorithm searches the minimum value of the function identifying and recording the position of the front. The red dot indicates the front position.

Front velocity

A cubic function ($x = At^3 + Bt^2 + Ct + D$) was fitted to obtain an analytic expression for the front position as a function of time. The derivative of this function yielded the front velocity as a function of time and space as shown in Figure 4.25.

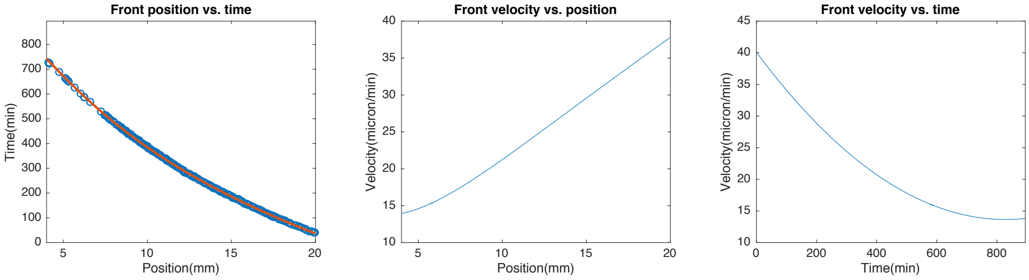

Figure 4.25: Wavefront position is fitted with a 3^{rd} order polynomial (left) to obtain velocities as a function of space (middle) and time (right).

Front width

For a travelling wave solution of the FKP equation, the wave profile can be approximated by a sigmoidal function $f(x) = \frac{A}{1+e^{(x-x_0)s}}$. The steepness of the profile (defined as s) is inversely proportional to the velocity of the wave [155]. The faster the velocity v, the less steep the wavefront is, as can be seen in Figure 4.26, where numerical solutions for the FKP for different front velocities are shown. A practical measure of the front width L is the inverse of the steepness $L = \frac{1}{s}$. To obtain the front width, a sigmoidal function of steepness s centred at the front position x_0 was fitted to every profile. After fitting a sigmoidal function to the normalised wave profiles, the front width as a function of position was plotted.

Template concentration at front

One way to measure the shape of the gradient is by using fluorescently labelled template oligonucleotides. This approach, however, presented changes in the kinetics of the autocatalytic reaction to the extent of hindering growth and wave formation. As shown in Figure 4.27, a reporter sequence labelled with Cy35 altered the kinetics and prevented the formation of travelling waves. On the other hand, if this same

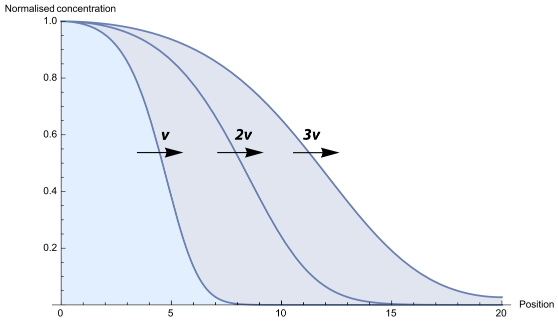

Figure 4.26: Snapshot of three simulated travelling waves that propagate at v, $2v$ and $3v$ velocities. The slower the wave propagates, the steeper the profile.

sequence was functionalised with Dy530, then sigmoidal growth was observed at different template concentrations. A possible explanation of this effect is that Cyanine dyes like Cy35 interact with DNA preventing the optimum performance of polymerisation and nicking.

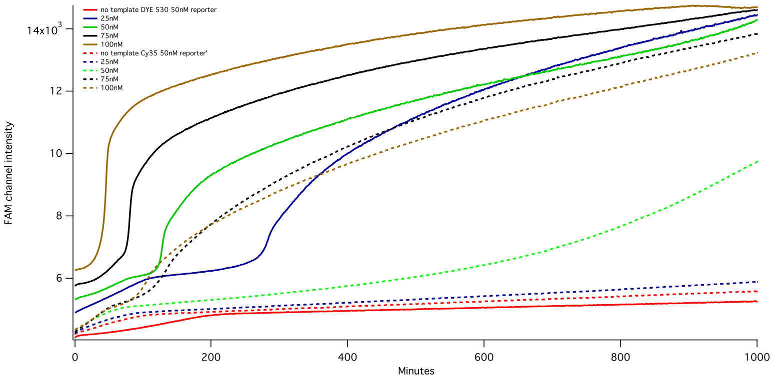

Figure 4.27: Autocatalytic growth as measured by Eva Green fluorescence in the presence of different concentrations of the template with 50 nM Cy35-labelled reporter strand (dashed lines) and 50 nM Dy530-labelled reporter strand (thick lines).

To avoid altering the working template/reporter autocatalyst mixture, we mixed ROX dye (carboxy-X-rhodamine, Thermo Fischer) in a ratio of 1× ROX per 100 nM template in all experiments. By mixing ROX dye and template strand, the fluorescence of ROX served as an indicator of template concentration. A calibration was done to translate ROX fluorescence intensity into template strand concentration. This calibration was performed by adding the mixture in 4 channels at concentrations of 0, 25, 50 and 100 nM and by measuring the average fluorescence intensity at the chosen exposure time of the experiments (12 ms, for RFP channel). With the calibration in Figure 4.27 a mapping from ROX dye concentration to template oligonucleotide concentration was possible.

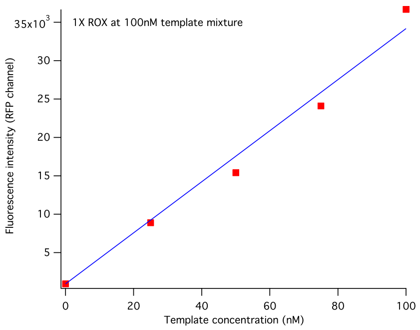

Figure 4.28: Calibration of ROX fluorescence at 12 ms exposure time for different DNA template concentrations.

Using recorded spatial changes in ROX fluorescence we extracted the change in concentration of the template at the wave front $\Delta C(x)$. The change in concentration scales with the diffusion coefficient $\frac{\Delta C(x,t)}{C(x,0)} \propto D$, where $\Delta C(x) = C(x, t_f) - C(x, 0)$. Since this quantity scales with the diffusion coefficient ($D^{38^0}_{ROX} = 4.17 \cdot 10^{-10}$ m^2 s^{-1} and $D^{38^0}_{template} = 2 \cdot 10^{-10}$ m^2 s^{-1}), we obtain the template concentration at the front by:

$$C_{template}(x,t) = (C_{ROX}(x,t) - C_{ROX}(x,0))\frac{D_{template}}{D_{Rox}} + C_{template}(x,0) \tag{4.26}$$

assuming that the initial concentration of ROX at $t = t_0$ is the same as the template $C_{template(x,0)} = C_{ROX(x,0)}$, after applying the fluorescence calibration in Figure 4.28. With this calculation, the template concentration at the wavefront position is reported at every frame.

4.5.2 Heaviside gradients

In a short channel (13 mm long and 1.5 mm wide) Heaviside-type gradients of autocatalyst template were created, after filling the chamber with a homogeneous mixture of PP buffer, reporter strand at 50 nM, nicking and polymerase enzymes. No inhibitor strand was used in gradient experiments, as ‘self-start’ was not observed for any of the gradient experiments. ROX dye was mixed at a concentration of 1× per 100 nM of template and an initial autocatalyst was added at 1 µM to trigger the

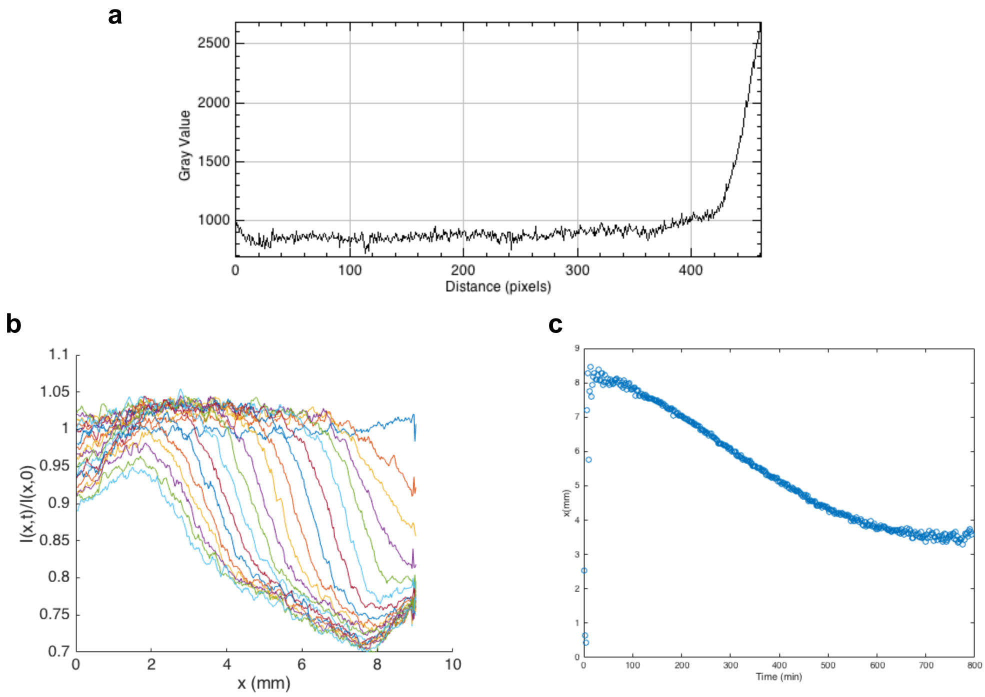

Figure 4.29: *Wavefront propagation in Heaviside-type template gradient* **a)** Initial template distribution as reported by ROX dye. **b)** Wave propagation (from right to left) after normalisation **c)** Kymograph showing wave position over time.

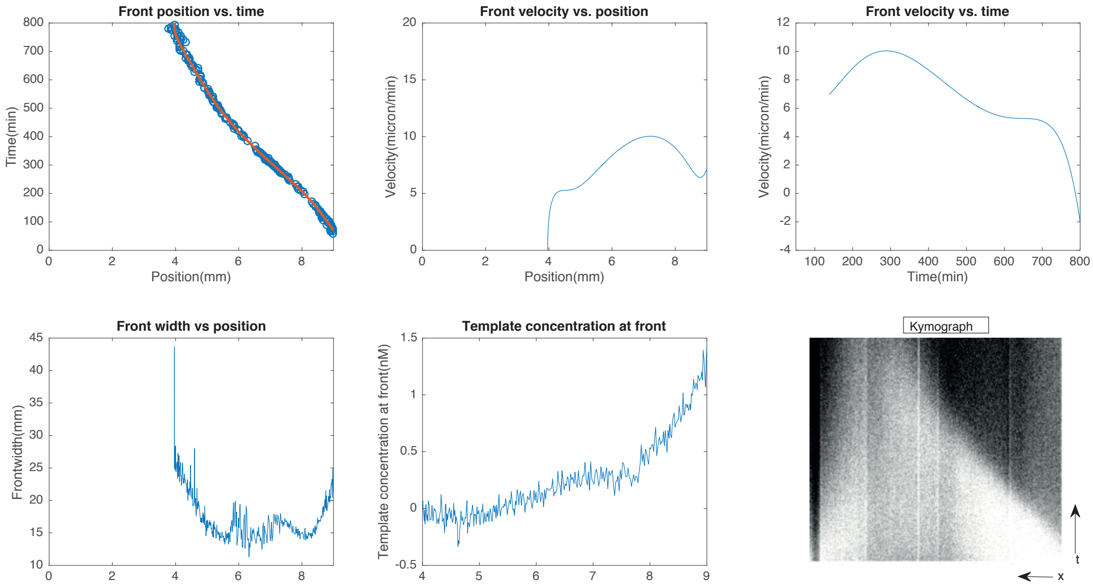

Figure 4.30: Dynamic parameters after image processing recorded data of wave propagation in a Heaviside-type gradient of template. The wave propagates from right to left. A kymograph shows changes in fluorescence as a function of time.

reaction. Figure 4.29 shows a non-linear wave propagation speed. A full analysis of dynamic parameters is reported in Figure 4.30.

4.5.3 Exponential gradients with varying polymerase concentrations

Experiments with exponential gradients of template in short channels did not yield significant results that would distinguish them from DNA waves in homogeneous media. To better observe the effect, in this experiment a longer channel was used and the polymerase concentration was changed, in order to test its effect on wave dynamics.

In a long channel (16 mm long and 1.5 mm wide) gradients of autocatalyst template were created after filling the chamber with a homogeneous mixture of PP buffer, 50 nM Dy530-labelled reporter strand and 3% nicking enzyme. Polymerase enzyme was mixed in the buffer at varying concentrations (1%-4%) in different chambers. ROX dye was mixed at a concentration of 1× per 100 nM of template prior to setting up an exponential-type template gradient. An initial 100nM autocatalyst was added on one side of the channel to start the reaction.

Figure 4.31 superposes results for channels with (4%,2%,1%) polymerase, (blue, green,red) respectively. The velocity as a function of template concentration at the front (ROX diffusion scaling has been done to 38^0C) is reported. A clear non-linear change in velocities is observed, in agreement with the theoretical expectation shown in Figure 4.9.

From equation (4.25) and confirmed in Figure 4.23 (b), we know that the velocity of the wave scales as $v \propto \sqrt{T \cdot pol \cdot D}$, where T is the template concentration and pol the polymerase concentration. We plot v^2/pol to see if a universal $r(T)$ emerges, as a linear dependence between $r(d)$ and pol is also known [158]. This agrees with the data from polymerase 4% and 2% but not for 1% (in red).

Considering $v = \sqrt{\alpha \cdot T \cdot pol}$, we try to obtain a universal α by fitting a linear function in v^2/pol vs. T. We obtain a similar α for pol 2% and pol 4%, but not for pol 1%.

Table 4.3: Values from fitting the data in Figure 4.31

pol%	v_{max} (μm min^{-1})	A at $v_{max}(nM)$	Fitted α
4	47	35	32.7± 0.1
2	38	33	33.9 ± 0.6
1	26	45	20.7± 0.3

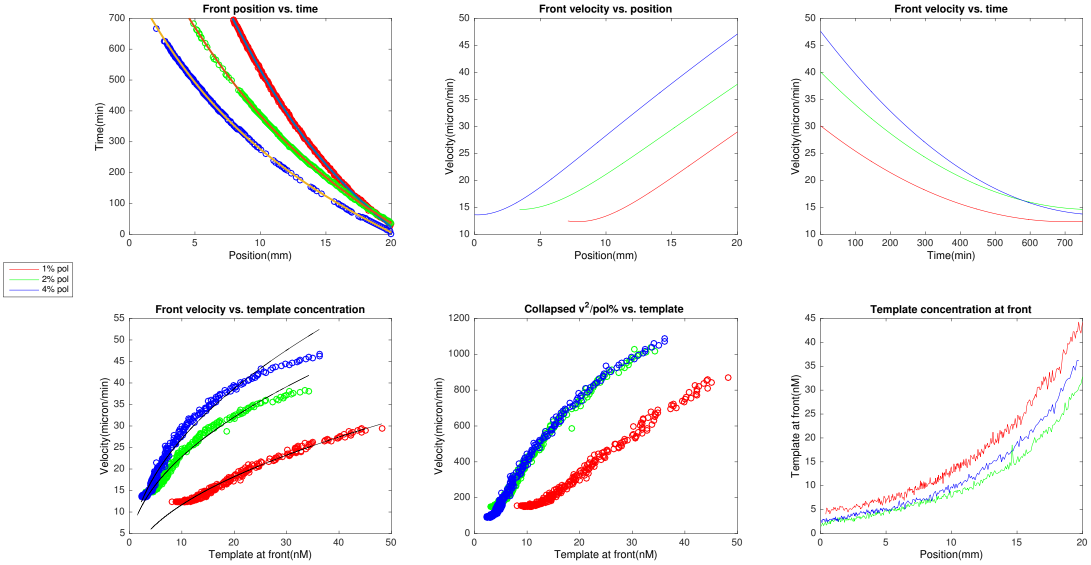

Figure 4.31: Superposition of front analysis for DNA travelling waves in long template gradients at different polymerase concentrations. (1%(red), 2%(green),4%(blue)). Waves propagate from right to left starting at x=20mm.

4.6 Wave front propagation in repressor concentration gradients

In the previous sections we have imposed gradients of template strands to create a spatially varying autocatalytic rate. A propagating wave slows down as autocatalysis is hindered in regions of low concentrations of template strands. An alternative way to create inhomogeneities in the medium is achieved by introducing a repressor gradient, that instead of promoting growth, it inhibits it. Here a repressor template strand binds to the autocatalytic species and is elongated by polymerase to create a pseudospecies. This in turn binds to the template, but is not recognised by the nicking enzyme, therefore repressing autocatalytic growth.

We can model this bistable system by a reaction-diffusion equation comprising self-activation, an external repression gradient and degradation. Only the external repression gradient varies in space, while activation and degradation are homogenous throughout the channel. Here we assume Michaelis-Menten kinetics, where k_p, k_r and k_d represent maximum rates and K_p, K_r and K_d are Michelis-Menten constants for activation, repression and degradation respectively.

$$\frac{\partial d(x,t)}{\partial t} = d(x,t)\left(\frac{k_p}{1+K_p d(x,t)} - \frac{k_r e^{x/\xi}}{K_r e^{x/\xi} + d(,xt)} - \frac{k_d}{K_d + d(x,t)}\right) + D\frac{\partial^2 d(x,t)}{\partial x^2} \tag{4.27}$$

Such a bistable system (illustrated in Figure 4.32), can lead to wave localisation, as studied in [173]. However, in this work the focus is on wave dynamics, i.e. how wave propagation speed evolves along an inhomogeneous medium. To this end, we solve the reaction-diffusion equation in 4.27 numerically and obtain the wave front position by fitting a sigmoidal function $\frac{A}{1+e^{-k(x-x0)}}$ to solutions and by recording the position x_0 as a function of time. We plot position vs time for different repression gradients $e^{x/\xi}$ with varying steepness ξ (shown in Figure 4.33 a). Differentiating Figure 4.33 b gives a velocity profile, which is then plotted as a function of position in Figure 4.33 c. We see that for steeper repressor gradients waves tend to localise quicker. Figure 4.33 c shows the non-linear velocity profiles, which are more pronounced for less steep gradients.

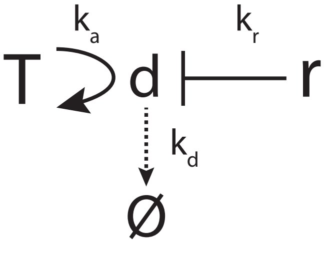

Figure 4.32: Scheme of a bistable reaction comprising self-activation (Template autocatalyses the production of d), inhibition (repressor r binds to autocatalyst and turns it into waste) and degradation (by exonucleases). Wave propagation is from left to right.

Figures 4.33 e, f show similar dynamics observed in two experimental settings with gradients of repressor of different shape (Figure 4.33 d). Figure 4.33 e shows a deceleration of the wave fronts as it moves from left to right. The velocity decreases in a non-linear way in regions where the repressor concentration is high. The steepest gradient (Figure 4.33 d in black) makes the wave decelerate faster in agreement with the simulation above.

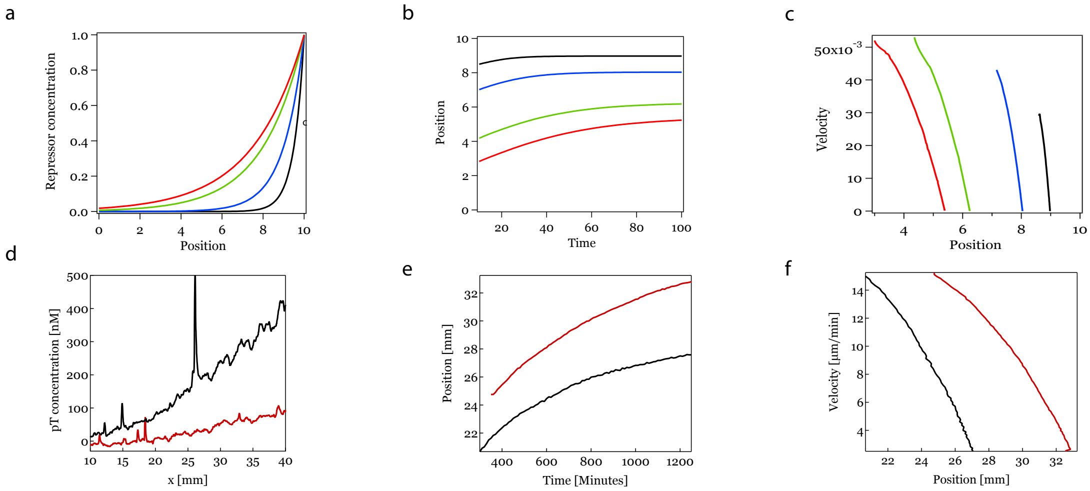

Figure 4.33: *Wave propagation in repressor concentration gradients.* **a)** Repressor gradients with different steepness **b)** Wave front position vs. time after solving (4.27) numerically **c)** Velocity vs position. **d)** Experimental gradient of repressor **e)** measured wave front position and **f)** velocity vs. position. Wave propagation is from left to right.

4.7 Conclusion

This chapter developed the idea of making DNA and its surrounding medium active. For this purpose, a reaction-diffusion system has been presented, based on the autocatalysis of DNA that, coupled to diffusion, generates propagating waves. Most experiments and theoretical descriptions of chemical waves take place in homogeneous media, where wave propagation occurs at a constant velocity. However, heterogeneities are always present in natural environments, for example in the form of obstacles or inhibitors, which can alter the reaction kinetics, thereby resulting in different wave dynamics. Therefore, here we developed a new implementation of this system, whereby wave propagation can be controlled either by changing the reaction kinetics or by introducing spatial inhomogeneities in autocatalytic rates.

This work goes beyond the original DNA wave system with constant velocity shown in [158] and develops a method to control the wave propagation velocity.

Our goal here is to study how the front speed of reaction-diffusion waves is influenced by heterogeneities in the medium, in particular, when the reaction rates change in space. This new system is first presented theoretically and computationally, after introducing the mathematical framework to study autocatalytic waves, namely the Fisher-Kolmorov-Piskunov (FKP) equation. Numerical simulations are followed by experiments, where spatial inhomogeneities in growth rate are achieved by creating concentration gradients of template oligonucleotides inside microfluidic chambers.

These experiments have shown that:

- The propagation velocity of homogeneous DNA waves can be increased or slowed down, by altering the reaction kinetics, i.e. promoting growth or inhibiting it, respectively.
- The propagation velocity of the front is slowed down as the wave propagates in a chamber where gradients of template oligonucleotide have been generated (Heaviside-type and exponential-type), as predicted by the modified FKP equation.
- Autocatalytic growth is hindered by introducing gradients of repressor oligonucleotides. The speed of the wave front was shown to decrease in agreement with a modified FKP equation.

These results indicate that template concentration gradients could serve to create regions of different wave propagation velocities (including diffusive regions with no autocatalysis). Inhomogeneities here are analogous to obstacles, that hinder wave propagation.

The DNA reaction network used in this chapter acts as an active system, out-of-equilibrium and capable of transporting information faster than diffusion. We have shown that the programmability of DNA can be used to tune the velocity of chemical waves, which is harder to achieve in conventional autocatalytic systems.

5

Synthetic micro and nanomotors and DNA conjugation

5.1 Introduction

Janus and dimer geometries were introduced in chapter 2 as necessary ingredients for phoretic propulsion. In this chapter, two different experimental approaches to manufacturing synthetic motors are developed (see Figure 5.1): on the one hand, Janus microparticles were fabricated by coating one hemisphere with platinum by physical vapour deposition and on the other, asymmetric nanoparticles were synthesised by wet chemical methods.

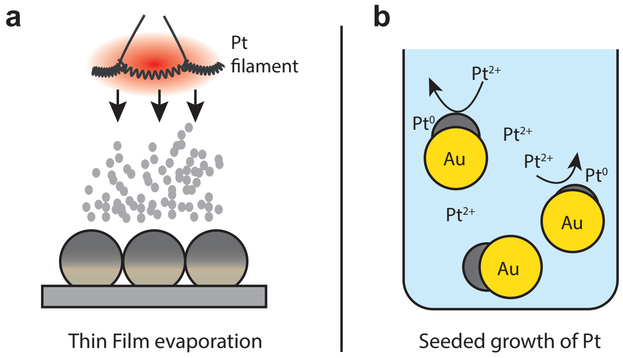

Figure 5.1: **a)** Physical vapour deposition of Pt onto microparticles to create Janus micromotors. **b)** Chemical synthesis of dimer nanomotors by reducing Pt ions onto the surface of Au nanoparticles in solution.

Next, this chapter reports successful conjugation of DNA to the surface of both micro and nanoparticles, and therefore control their assembly using DNA as a programmable 'molecular glue'. For microparticles, DNA mediated aggregation and disassembly of polystyrene beads was achieved. For nanoparticles, DNA Origami was used to provide a directional bond between Au NP and form assembled lattices of various symmetries.

5.2 Janus micromotors

5.2.1 Synthesis of Janus micromotors

This section is dedicated to experimental work on micron-sized Janus particles. These were synthesised by depositing Pt onto a monolayer of 1 µm polystyrene beads on a clean glass substrate. Monolayer formation of colloids can be achieved by several means, such as convective assembly [174], spin-coating [175] and dip-coating [176]. In this work, loosely-packed monolayers were obtained by evaporating a solvent on a tilted substrate at a constant temperature, following the work of Micheletto et al. [177]. The homogeneity of the monolayer strongly depends on the wettability of the substrate and on how the process of evaporation takes place. A hydrophilic surface improves the formation of a monolayer. Therefore, glass slides were plasma etched for 5 min (Plasma Cleaner-002, Harrick Plasma, Inc) prior to the formation of the monolayer, which rendered their surfaces hydrophilic. Hydrophilicity was tested by placing a drop of water to check the wettability. Similar results were obtained using the chemical etchant Hellmanex (2% solution).

To enhance evaporation, 10 µl of commercial polystyrene beads (Bangs laboratories) were diluted 200 times in isopropanol, a volatile solvent and sonicated. 200 µl of this solution were pipetted on a glass slide placed on a tilted peltier at constant temperature and left in a fume hood under laminar flow until the solvent evaporated completely (Figure 5.2 (a)).

After evaporation, slides with beads were observed under the optical microscope to assess the quality of the monolayer. Failure to form a monolayer resulted in heterogeneous coating and a mixture of Janus and uncoated beads. Best results were

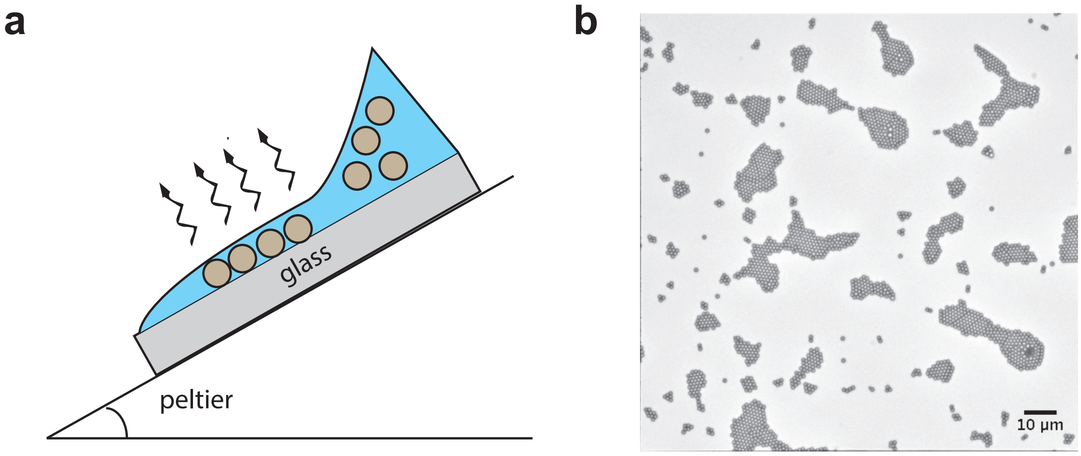

Figure 5.2: **a)** Evaporation of colloidal dispersion on glass placed on a tilted peltier heater. Laminar flow, gravity and constant temperature contribute to the formation of a monolayer. **b)** Submonolayer of polystyrene beads observed in bright-field microscopy.

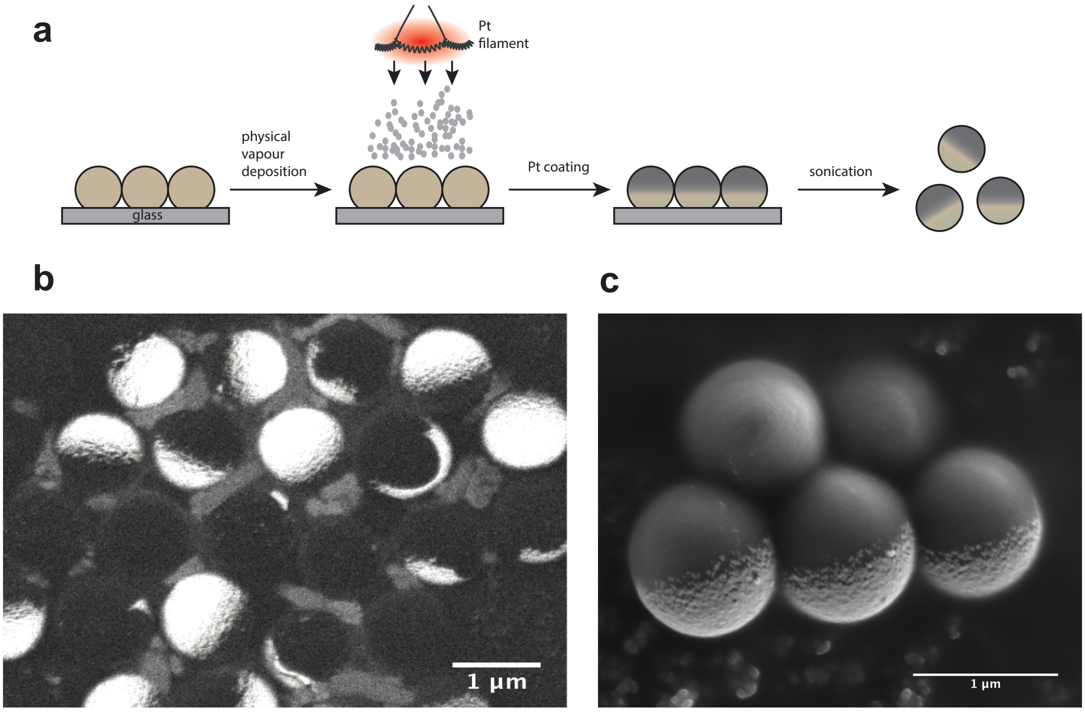

Figure 5.3: In **a)** the road to Janus particle synthesis is described: 1) monolayer formation 2) platinum thin film evaporation in a vacuum chamber and 3) sonication to release the Janus beads in solution. In **b)** and **c)** SEM images of obtained Janus beads are shown at different magnification. A Hitachi S-4300 Field Emission SEM was used.

obtained when forming submonolayers, i.e. monolayers with low surface coverage, such as the one shown in Figure 5.2 (b).

Samples were then placed under vacuum and a thin layer of platinum ($\approx$ 10 nm) was evaporated onto the particles by applying a high current to a Pt filament[1]. The thickness of the deposited Pt layer could be monitored with a quartz oscillator, which changed frequency with increasing mass deposition. Coated beads were recovered via mild sonication in deionized water [2].The coating process is illustrated in Figure 5.3 (a).

The Janus particles were then examined using Scanning Electron Microscopy (Hitachi S-4300, Field Emission) and successful masking of polystyrene was confirmed (Figure 5.3 (b) and (c)). The contrast between polystyrene (in black) and platinum (in white) was enhanced when coating with a layer thicker than 10 nm and by accelerating the SEM electron beam at a higher voltage (3 keV).

5.2.2 Particle tracking of micromotors

Janus particles next to a glass surface were tracked and their 2D mean-squared displacement was measured, following the particle tracking algorithm described in chapter 3, with an optical microscope (Olympus iX81) and a digital camera (Andor iXon). When dispersed in water the motion was purely diffusive, whereas for a solution with H_2O_2 the short-time MSD was purely ballistic, i.e. MSD=v^2t^2 (with v= 4.25 $\mu\mathrm{m\,s^{-1}}$), evidencing self-propulsion, as seen in the trajectories of Figure 5.4 (c). At times longer than the rotational diffusion time τ_R, rotational Brownian motion randomises the direction of the swimmer and the motion becomes diffusive, but with an enhanced diffusion constant (see chapter 2). For a 1 µm sized particle shown here, the rotational time scale is on the order of $\tau_R = \frac{4\pi\eta R^3}{k_B T} \approx 0.4\,\mathrm{s}$. In Figure 5.4 (a) and (b) we see the diffusion patterns of a swimmer in hydrogen peroxide and in water, respectively.

---

[1] A layer of chromium (2 nm) improved the stickiness of platinum. When available, first Cr was evaporated and then Pt.

[2] Alternatively the edge of a wet lens tissue was used to collect beads from the glass slide. Then the tissue was left in water and beads were recovered after mild sonication [178].

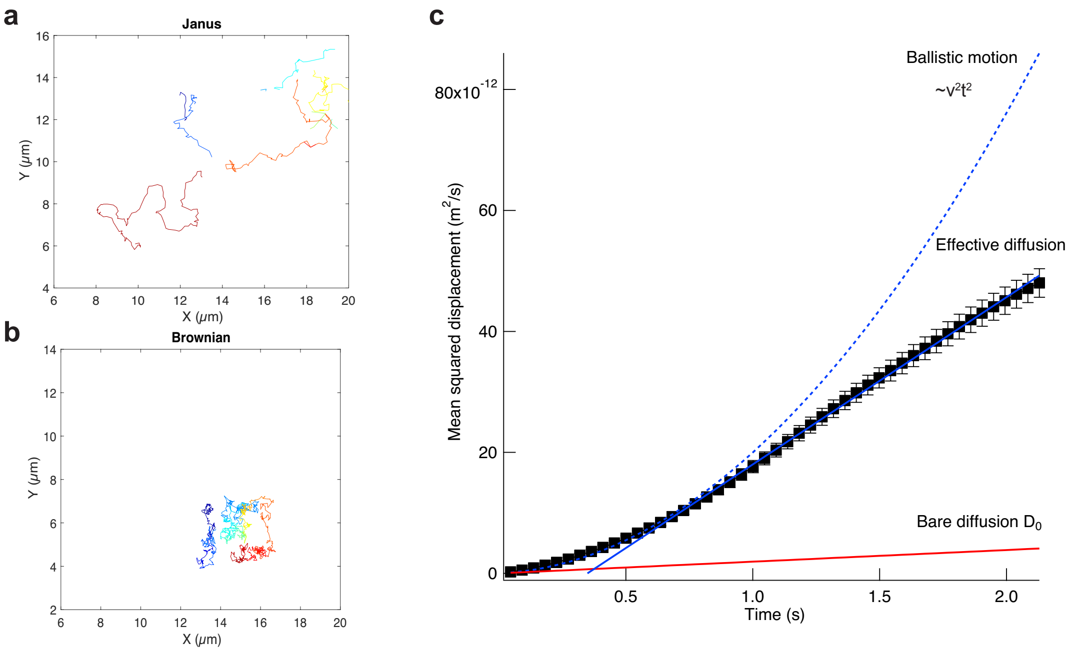

Figure 5.4: *X-Y trajectories of Janus motors in fuel (*H_2O_2) **a)** and in water **b)** as observed in bright-field microscopy. **c)** Mean-squared displacement (MSD) averaged for 5 trajectories shows the ballistic and diffusive regimes of the propelled swimmer. After τ_R =0.4 s ballistic motion becomes diffusive with a larger effective diffusion constant. This is an example of a persistent random walk.

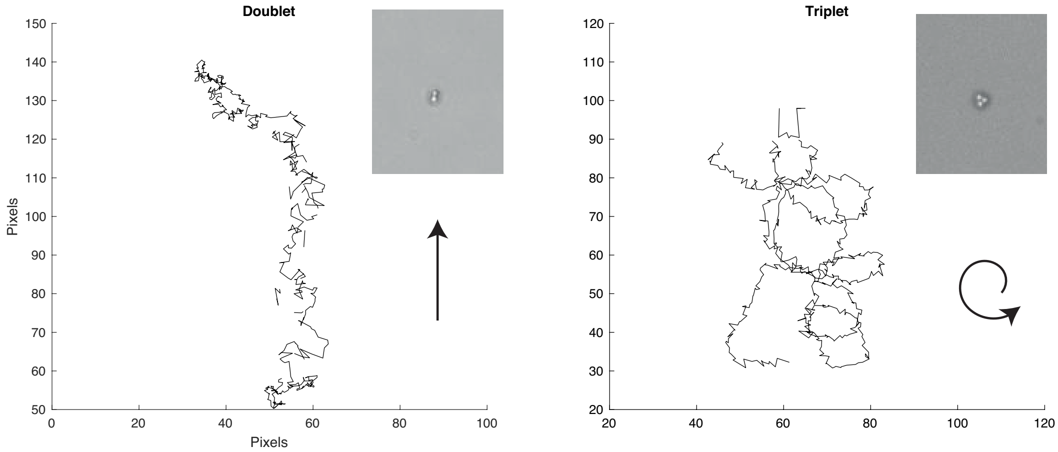

Figure 5.5: 2D Trajectories of self-assembled Janus doublet (*left*) in fuel exhibiting a persistent random walk in a preferred direction and triplet (*right*), with spiralling rotational motion.

Doublet and triplet Janus motors

Janus particles self-assemble in different configurations when left in solution over long periods of time (overnight incubation). This assembly is non-specific and it is not directed by any other component other than the colloidal interactions at play. Janus particles, because of their metallic coating, are subject to higher van der Waals attraction forces[3]. In Figure 5.5 we see characteristic trajectories of doublet and triplet structures. Rotational and translational motion have competing contributions depending on the arrangement [181]. On the one hand, the doublet structure shows less rotational diffusion and longer translational motion, before its direction is randomised. On the other, the triplet structure performs a spiralling rotational motion.

5.3 Nanomotors

5.3.1 Introduction

Experimental realisations of motors with dimensions of microns or hundreds of nanometres are abundant [39]. However, the fabrication of even smaller synthetic motors presents experimental challenges, it is hard to create geometric anisotropy at the nanoscale using traditional top-down synthesis methods, such as e-beam lithography or physical vapour deposition [182].

Asymmetric bimetallic nanoparticles have been synthesised by various wet chemical methods with controlled shape, size and composition[183, 184]. Seeded-growth is a well-established wet-chemical approach to achieve bimetallic nanoparticles (NP), by reducing a precursor metal salt in the presence of a metallic seed nanoparticle that provides a nucleation site [185, 186]. The size and symmetry of the growth process can be tuned by controlling the ratio between the precursor source and seed concentrations [184].

---

[3] The strength of the van der Waals interaction is quantified by the *Hamaker constant* A, which is 10 times larger for Pt and Au compared with polystyrene (values in vacuum [179]). This type of aggregation has been avoided in other non-catalytic Janus systems by using coating materials with low Hamaker constants, such as carbon [180].

In this section a wet-chemical synthesis approach is proposed to create asymmetric Pt-Au catalytic nanomotors. While other methods aim at achieving homogeneous coating of seed particles (so-called *core-shell* particles), we aim to obtain asymmetric growth of Pt on Au. First, the synthesis method is explained, followed by physical and chemical characterisations of the particles. Finally, we show that these particles exhibit enhanced diffusion in a fuel concentration-dependent manner, both in water and in viscous media.

5.3.2 Synthesis method: seeded growth of platinum on gold nanoparticles

We fabricated Pt-Au NP by a seeded-growth method, reducing Pt salt precursor on Au NP (growth scheme is shown in Figure 5.6). In order to obtain an asymmetric distribution of catalyst on a seed particle, a necessary condition for catalytic self-propulsion, in this work the ratio of precursor to seed was reduced allowing only partial coverage of Pt.

Starting with a monodisperse solution of 15 nm Au NP, Pt growth was achieved by adding K_2PtCl_4, followed by slowly mixing with a reducing agent $NaBH_4$. The following redox reaction took place, whereby the platinum salt was reduced from Pt(II) to Pt(0) on the surface of Au by $NaBH_4$:

$$\text{Au NP} + Pt^{2+} \xrightarrow{\text{NaBH}_4} Pt^0 Au \tag{5.1}$$

Pt-Au NP were synthesised by stirring 1 mL of monodisperse 15 nm Au nanoparticles (concentration of 1.40×10^{12} particles/mL, in 2 mM sodium citrate, BBI) and 100 µl 1 mM K_2PtCl_4 (Pt:Au atom ratio of 1:3) for 15 min, then slowly adding 20 µl 1 mM $NaBH_4$ dropwise, while stirring until a colour change from red to dark red occurred. The NP before and after the reaction are shown in Figure 5.6 a and b. Core-shell Pt-Au NP samples (Figure 5.6 c and d) were prepared by the same protocol by adding 100 µl and 300 µl 10 mM K_2PtCl_4 respectively.

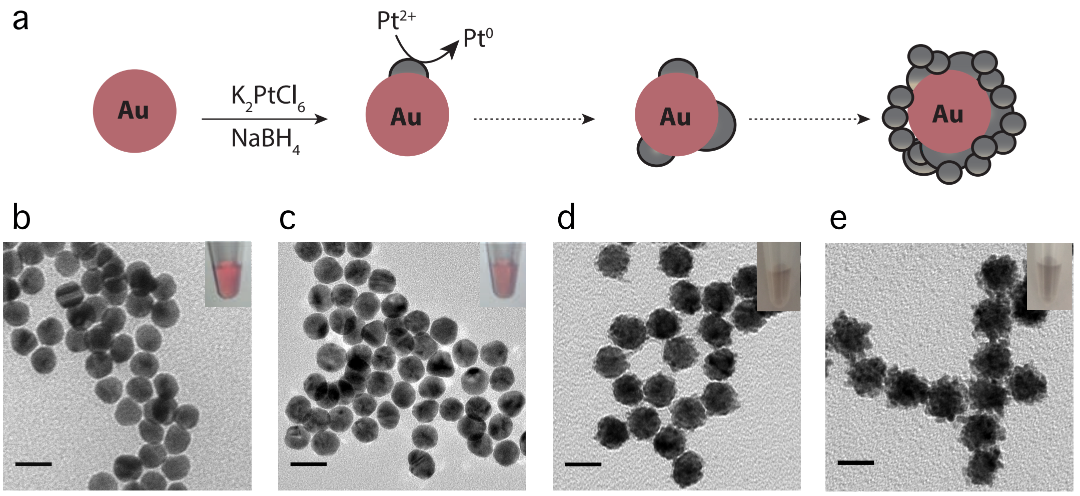

Figure 5.6: *Chemical synthesis of Pt-Au nanoparticles.* **(b-e)** Transition electron micrographs of Pt-Au nanoparticles obtained using K_2PtCl_4 precursor concentrations of: **c)** 0.1 mM, **d)** 1 mM and **e)** 3 mM. Micrographs show particles after evaporation on carbon grids. Insets show the characteristic colour of the suspension, turning from red (Au NP) to dark (core-shell Pt-Au NP). Scale bars: 20 nm.

5.3.3 Characterisation of Pt-Au nanoparticles

Pt-Au nanoparticles were analysed by physical and chemical methods to determine their morphology, composition and catalytic activity. Synthesised Pt-Au NP were filtered (100kDa centrifugation Amicon Filters) to remove residual Pt salt and a drop of 5 µl of solutions containing Pt-Au NP was cast onto a copper-carbon TEM grid and left in a fume-hood for evaporation under constant air flow.

TEM micrographs (FEI Tecnai 12 at 120 keV) were taken for Au NP (Figure 5.6 a) and for samples reacted with 0.1 mM, 1 mM and 3 mM Pt precursor final concentration (Figure 5.6 b, c, and d respectively). Insets in Figure 5.6 show the visible colour of post-reacted solutions. As more Pt precursor was added, the morphology of the Pt-Au NP changed from a smooth surface to rough indicating partial coverage by Pt, and eventually showed a raspberry-shaped core-shell structure indicating complete encapsulation.

Nanoparticle size distribution from TEM micrographs and Dynamic Light Scattering analysis (Figure 5.7) show an increasing particle size distribution that

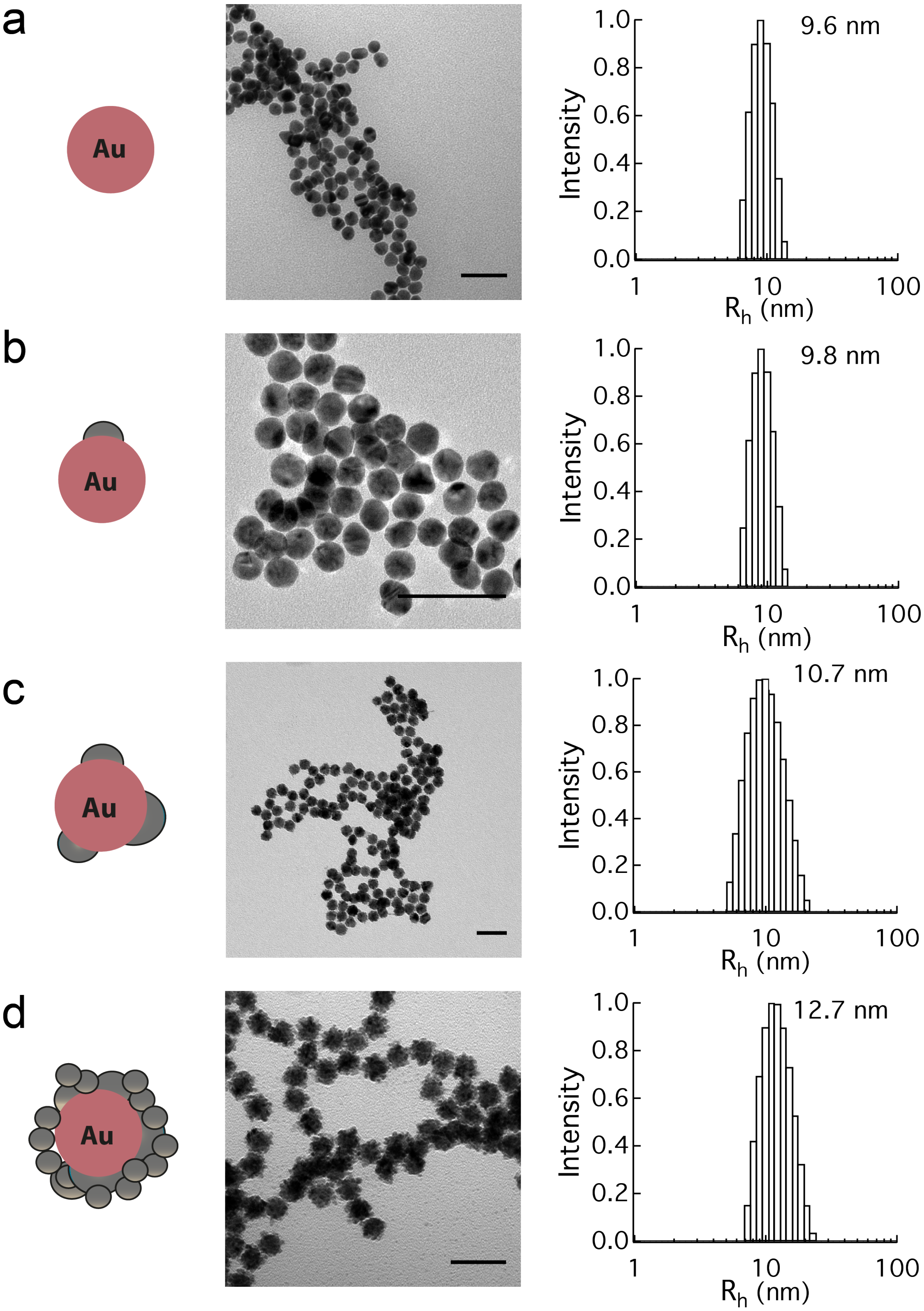

Figure 5.7: *Size distribution of Pt-Au nanoparticles* TEM micrographs and Dynamic Light Scattering size distribution of 15 nm Au nanoparticles (**a**) and Pt-Au NP with increasing concentrations of K_2PtCl_4, (**b** 0.1 mM, **c** 1mM and **d** 3mM).

scales with the concentration of Pt precursor. An average of 3 nm increase was measured for core-shell particles (Figure 5.7 d) from DLS and TEM size distributions.

The chemical composition of the particle surface was measured using X-ray photoelectron spectroscopy (XPS). As-prepared Pt-Au nanoparticle solutions were dried on conductive carbon substrate and placed under vacuum. XPS was performed using a VG Escalab XPS Spectrometer equipped with an Al-Kα X-ray source (1486.3 eV). XPS energy spectra of ejected electrons were processed using CasaXPS software for peak fitting and identification. The XPS analysis in Figure 5.8 shows that after Pt deposition, peaks characteristic of both metallic Pt and Pt oxide are observed. The latter is likely to arise simply from some superficial oxidation of deposited Pt in the ambient atmosphere prior to analysis and therefore, as expected, for the thicker Pt loadings (Figures 5.8 d), the signal from metallic Pt dominates, while the Au signal (at 84 eV) disappears.

As $NaBH_4$ is a strong reducing agent, small Pt NP might form in the solution. To rule out the possibility that the Pt precursor mainly formed Pt NP in the solution rather than by growth on Au NP, samples were filtered using a centrifugation filter (Amicon 30 kDa, approximately 5 nm) to remove unreacted Pt salt and possible small Pt NP forming in the solution. Bubble formation was observed in a sample containing filtered nanoparticles when H_2O_2 was added, however this was not observed in the supernatant. Further, to discard the possibility of Pt NP forming in solution and then being adsorbed onto Au, a control experiment was done by reacting the Pt precursor and reducing agent first and then physically mixing the solution with 15 nm Au NP. TEM micrographs in Figure 5.9 show that the physically mixed control NP are different from the seed-grown Pt-Au NP. In particular, while Pt NP are observed separately from Au NP, the Au NP remained in their initial shape rather than forming raspberry-like structures.

Unlike the distinctive raspberry-shaped NP, the detection of Pt on the surface of Pt-Au NP grown with a small concentration of Pt precursor is challenging using conventional TEM, where contrast is achieved by phase differences in transmitted and diffracted waves. However, some features can still be distinguished as shown

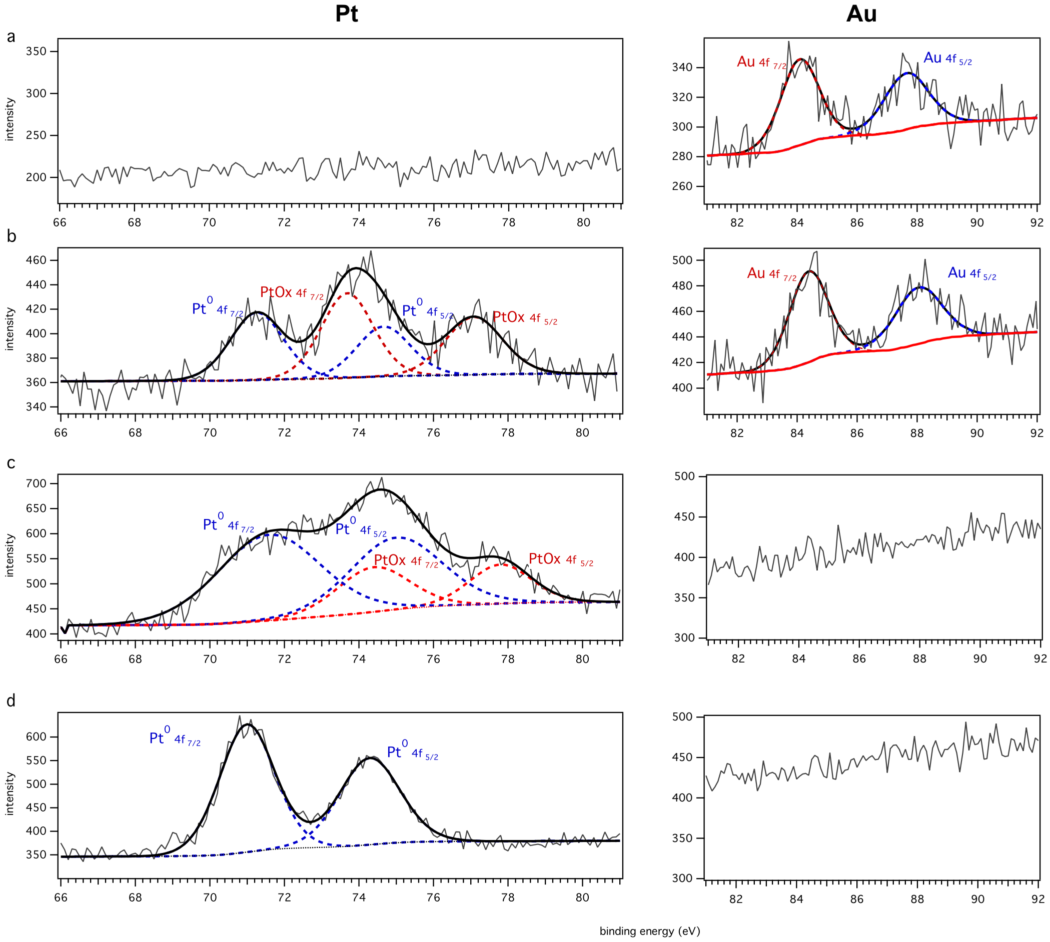

Figure 5.8: *X-ray photoelectron spectroscopy (XPS) analysis of core-shell Pt-Au NP* 15 nm Au nanoparticles (**a**) and Pt-Au NP with increasing concentrations of K_2PtCl_4, (**b** 0.1 mM, **c** 1mM and **d** 3mM).Grey lines represent the raw data, while solid and dashed lines refer to the curve-fitting results. The left column shows high resolution scans around Pt peak positions (71 eV), while the right column shows Au peak positions (84 eV).

in Figure 5.10. Therefore, to confirm the elemental composition of Pt-Au NP, high angle annular dark field scanning transmission electron microscopy (HAADF-STEM) was used equipped with energy dispersive X-Ray (EDX) (JEOL ARM 200F). In STEM, the electron beam is scanned over a defined area of the sample. The beam can be localised on a certain point in the image and used to collect emitted X-ray to form an EDX spectrum. Because of better atomic contrast in aberration-corrected STEM-EDX mode, lattice fringes corresponding to Au and Pt could be distinguished as shown in the inset of Figure 5.11 a. Line scans along the particles in Figure 5.11 b show net counts (background subtracted signals)

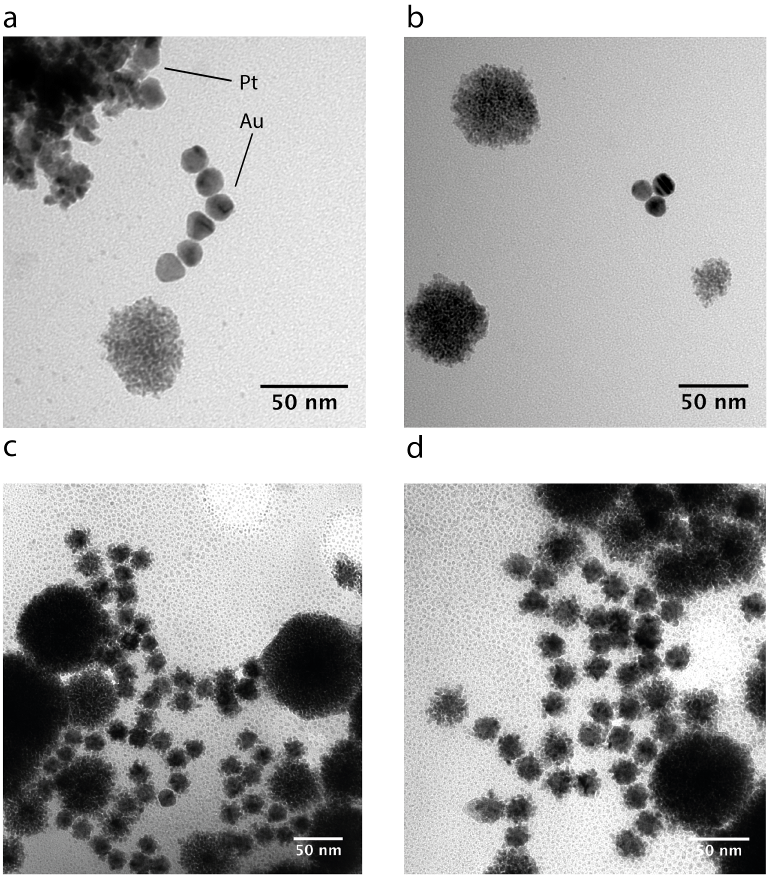

Figure 5.9: (**a,b**) TEM micrographs of unfiltered physical mixtures of reduced Pt and Au NP. Reduced Pt and unchanged Au NP can be distinguished as two different phases. (**c,d**) TEM micrographs of unfiltered core-shell Pt-Au nanoparticles dried on a grid. Raspberry-like Pt-Au NP can be seen together with Pt NP that formed during the drying process.

indicating an asymmetric distribution of Pt along the particle. EDX point analyses in Figure 5.11 c show the presence of three distinct phases in the sample, pure Au, pure Pt and Pt with Au. Although the EDX analysis cannot directly identify the metallic bond between Au and Pt, together with the previous characterisations, the most likely scenario is the one where Pt has grown directly on Au NP rather than by physical contact or absorption on the surface.

In addition, a characterisation of the grown Pt-Au in solution with UV-Vis spectroscopy showed that the absorption peak of gold at 518 nm decreased significantly, which is attributed to Pt growth onto Au NP. Figure 5.12 b shows the disappearing peak for core-shell Pt-Au NP, compared with 15 nm Au NP.

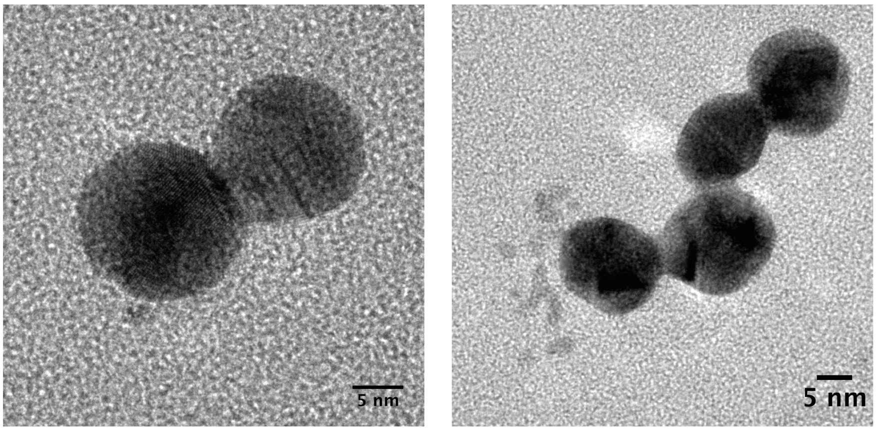

Figure 5.10: TEM micrographs of Pt-Au NP dried on a carbon grid. Some features (later identified as Pt) can be identified on the surface.)

The catalytic activity of nanoparticles is normally measured by casting them onto an electrode surface, or by using UV-vis spectroscopy. However, our interest lies on the catalytic activity in solution and metallic NP strongly scatter and interfere with the UV absorption measurement. Using an adapted electrochemical method described in chapter 6 the catalytic activity of Pt-Au NP was measured in solution. The nanoparticles were added to a 25 mM H_2O_2 solution, and the decreasing concentration of H_2O_2 over time was measured in-situ by a H_2O_2 sensor (silver-coated glassy carbon electrode). Pt-Au NP were 9 times more catalytically active than the control solution with equimolar Pt precursor as shown in Figure 5.12 a.

5.3.4 Motor activity of Pt-Au NP measured with DLS

Motor activity is normally assessed by measuring an enhanced diffusion coefficient in the presence of fuel [182]. Methods for measuring diffusion have been reviewed in chapter 3. Briefly, these include microscopy tracking methods (NTA), single-molecule methods (FCS) and scattering methods (DLS). For non-fluorescent metallic particles of 15 nm DLS presents itself as the most suitable choice.

Here, H_2O_2 was used as a fuel for Pt-Au NP, where Pt acted as a catalyst for the decomposition of H_2O_2, while Au remained inactive, thereby generating a gradient of product around the particle. The propulsion force is mainly attributed to a phoretic mechanism (explained in more detail in chapter 2), where a chemical

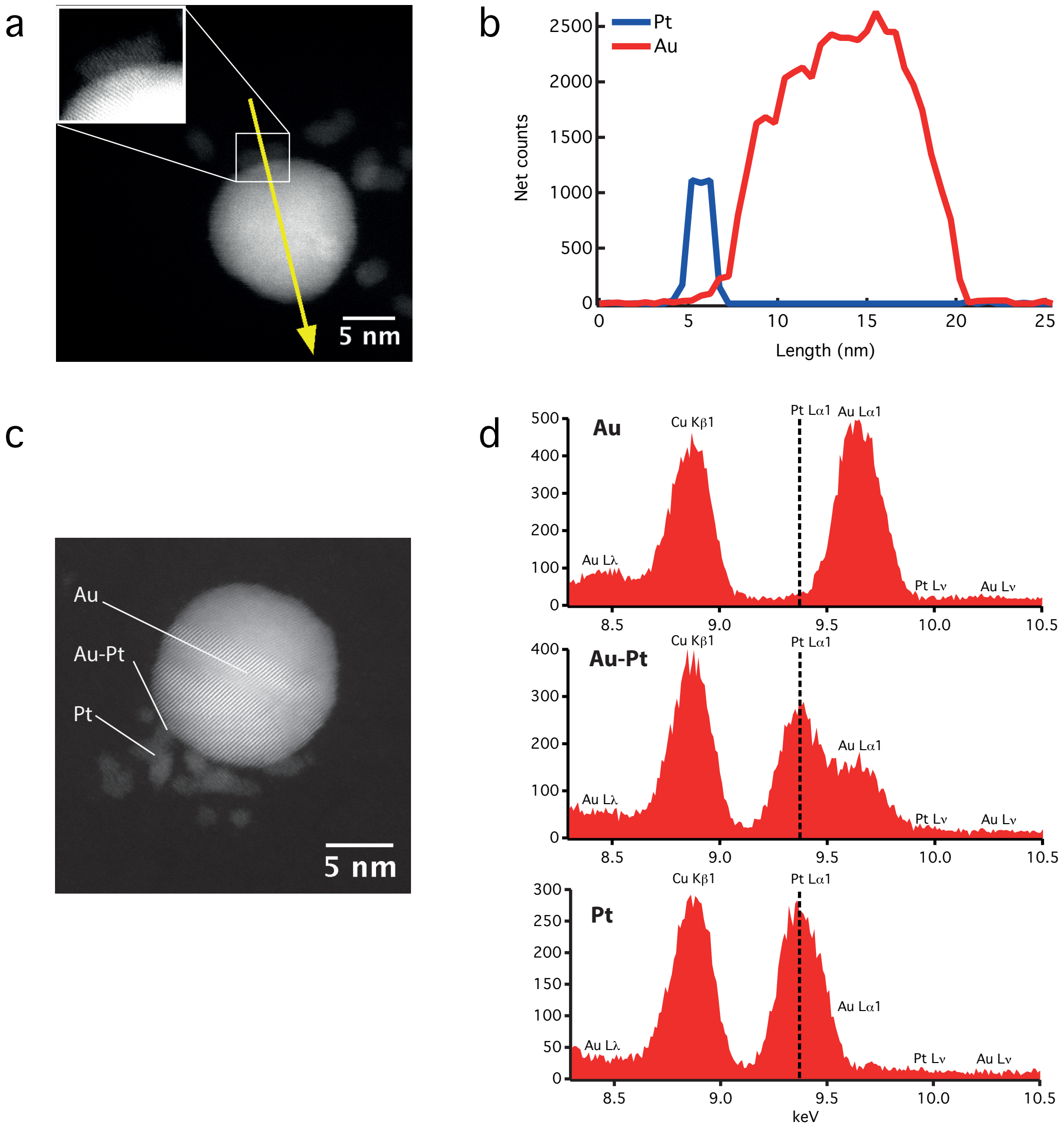

Figure 5.11: *HAADF-STEM and Energy dispersive X-ray analysis of Pt-Au NP.* **a)** Linescan along indicated arrow over one particle. Inset shows high resolution image of Pt on Au. **b)** Compositional analysis, showing the electron net count (background subtracted) along the line scan. **c)** HAADF-STEM micrograph showing 3 phases in the sample, Au, Pt and Pt-Au. **d)** Representative EDX spectra of point analyses centred around the Pt peak (9.4 keV).

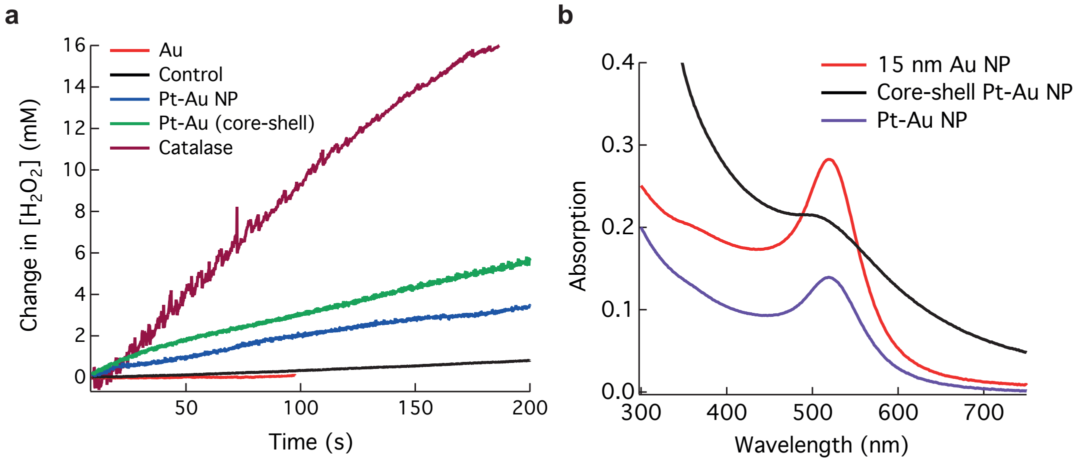

Figure 5.12: a) Electrochemical measurement to detect the decrease of H_2O_2 over time after addition of catalytic nanoparticles at t=0. Amperometric graph at a fixed potential of -0.6 V in solution of 25 mM H_2O_2 and 0.1 mM KCl using a silver-modified electrode after adding 2.3 nM Pt-Au NP, 1.2 nM core-shell Pt-Au NP and 0.25 nM catalase and 2.3 nM control solution. **b)** UV-vis spectra for 15 nm Au NP, Pt-Au NP and core-shell particles. A decrease in absorption is observed and as Pt grows the characteristic Au plasmon resonance peak disappears.

gradient of oxygen product is asymmetrically generated around the particle and induces a flow field that results in self-propulsion. In the case of bimetallic particles, self-electrophoresis is the main cause for a ballistic velocity component, as was observed for other bimetallic nanoparticles [36, 42]. While these nanoparticles are subject to strong thermal motion that randomises their direction, the nanomotor activity is observed in an increase in apparent diffusion, $D = D_0 + 1/3V^2\tau$, where V is the ballistic velocity coming from the catalytic activity and τ is the rotational diffusion time determined by the size of the particle [43].

DLS measurements showed an increase in apparent diffusion of Pt-Au NP when mixed with H_2O_2 (Figure 5.13). The measured diffusion coefficient of Pt-Au NP D_0 =(14.4 ± 0.2) µm^2 s^{-1} increased in a H_2O_2 concentration-dependent manner, until a plateau at D=1.25 D_0 was reached at around 3% (v/v). Normalised $g_2(\tau)$ autocorrelation functions (Figure 5.13 a) showed a distinct shift towards faster relaxation rates, which translate into an increase in diffusion constant of Pt-Au NP of up to 30% (Figure 5.13 b in black and distribution curves in Figure 5.14 a). The control group of 15 nm Au NP did not show a significant change in diffusion when

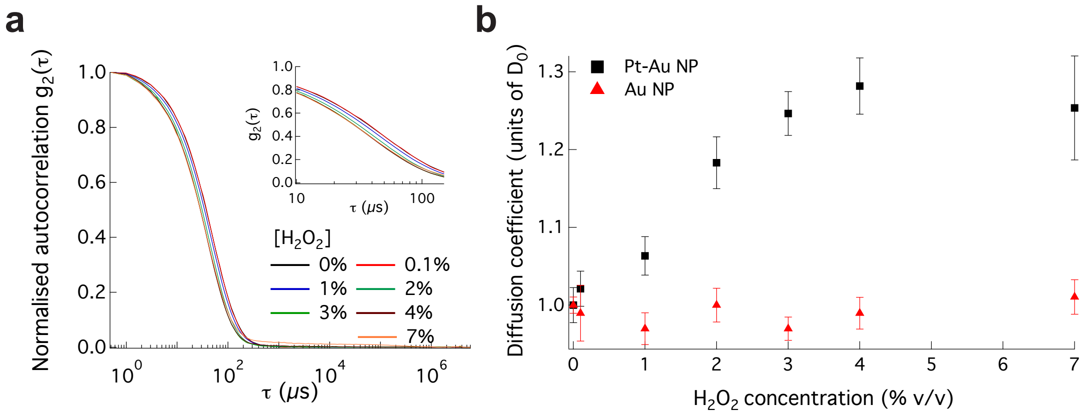

Figure 5.13: DLS diffusion measurement of motor activity of Pt-Au NPs. Dynamic Light Scattering measurement of 15 nm Au-Pt particle solution at a range of hydrogen peroxide concentrations. a Normalised autocorrelation functions as a function of H_2O_2 concentration (%v/v). b Relative diffusion coefficients for Pt (black, in units of $D_0 = (14.2 \pm 0.2)\,\mu\mathrm{m}^2\,\mathrm{s}^{-1}$) and Au (black, in units of $D_0 = (14.4 \pm 0.2)\,\mu\mathrm{m}^2\,\mathrm{s}^{-1}$) as a function of H_2O_2 concentration averaged over 3x14 experimental runs. Error bars indicate standard deviations.

mixed in the same concentrations of H_2O_2 (Figure 5.13 b, in red). No significant change in diffusion was observed for physically mixed Au NP and control solution when adding H_2O_2 (Figure 5.15 a). For comparison, the diffusion of core-shell Pt-Au NP was also measured with and without fuel. Figure 5.15 b shows that addition of H_2O_2 did not increase its diffusion. It should be noted that, due to the high catalytic activity of fully coated Pt-Au NP the onset of bubbles in the presence of H_2O_2 complicates the DLS measurement. These yield autocorrelation functions with elevated baselines such as the ones shown in Figure 5.15 b, which were automatically removed from the analysis.

Motor-activity in viscous media

The use of viscous media to slow down the motion of self-propelled particles is common, especially when using tracking microscopy [42]. Here, we use an ionic liquid as a viscous medium to increase the sensitivity when measuring changes in diffusion.

Pt-Au NP were mixed in 25% (v/v) of ionic liquid (1-Ethyl-3-methylpyridinium perfluorobutanesulfonate, Sigma-Aldrich) achieving a viscosity of about 20.9 cP

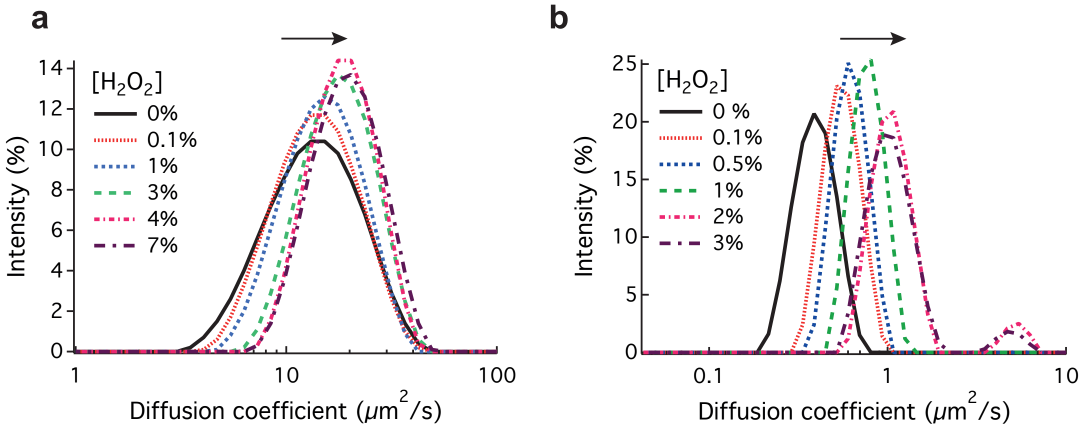

Figure 5.14: DLS diffusion coefficient distribution curve of Pt-Au NP with increasing concentrations of H_2O_2 **a)** in water and **b)**in high viscosity media.

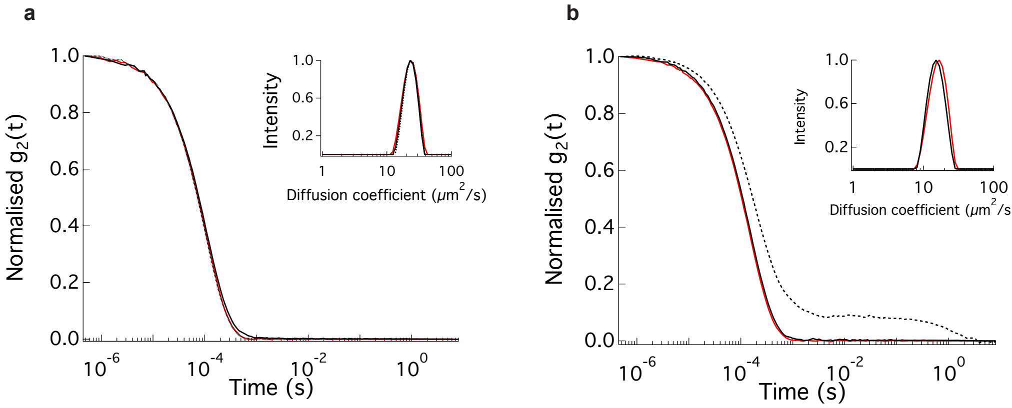

Figure 5.15: DLS autocorrelation functions and diffusion coefficient distributions in H_2O_2 for: (a) Au NP (red) and control solution of Au NP physically mixed with reduced Pt with 2% (v/v) H_2O_2 (dashed black) and without (solid black) ; (b) core-shell Pt-Au NP with 0.1% (v/v) H_2O_2 (red) and without (solid black). An erroneous autocorrelation function is shown (dashed lines) as an illustrative example of invalid data affected by bubble formation or aggregation, which does not meet the quality criteria and is removed from the analysis.

at 20 °C as measured in DLS. We observed a twofold increase in diffusion for 15 nm Pt-Au NP when mixed with H_2O_2 (Figure 5.16 a).

We also used this method to measure the diffusion of highly catalytic 5 nm Pt NP. We have observed a decrease of 40% in diffusion in 2%(v/v) H_2O_2 (Figure 5.16 b), which is unexpected as these particles are expected to have approximately isotropic catalytic properties. Similar observations were reported by other groups for the case of 30 nm Pt NP [42], attributing this effect to a slight increase in viscosity due to H_2O_2. While viscosity does increase with H_2O_2, it does not account for the measured change in diffusion (1.01 cP of 8% (m/m) H_2O_2 vs. 1.001 for H_2O at 20 °C)[187]. An alternative hypothesis to explain the apparent decrease of diffusion would be the symmetric catalytic activity of the nanoparticles, or bubble formation.

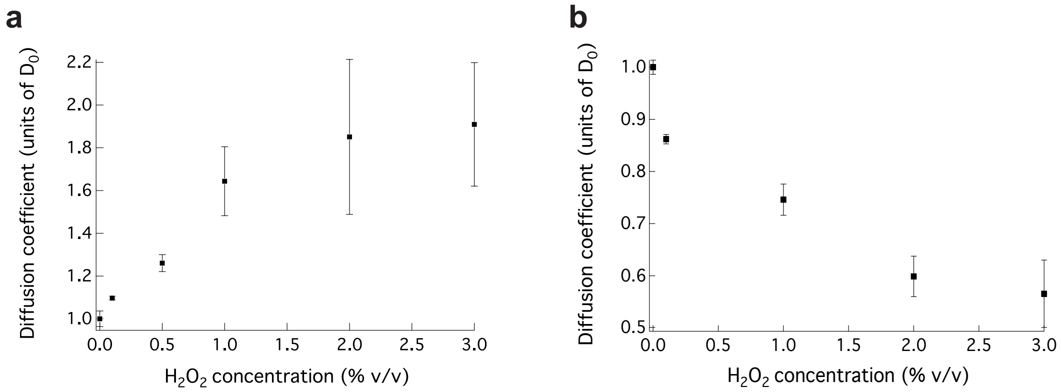

Figure 5.16: DLS diffusion measurement of motor activity of **a)** Au-Pt nanoparticles and **b)** 5 nm Pt nanoparticles in high viscosity solution. Relative diffusion coefficients for Pt-Au NP (D_0=(0.34 ± 0.01) $\mu m^2\,s^{-1}$) and Pt (in units of D_0=(0.87 ± 0.01) $\mu m^2\,s^{-1}$) as a function of H_2O_2 concentration averaged over 3 × 14 experimental runs. Error bars indicate standard deviations.

5.4 DNA conjugation methods and DNA-assisted colloidal interactions

In this section we focus on using DNA as a programmable ‘molecular glue’ to mediate the interactions between particles. In the case of motors, as the metallic side of the Janus or dimer particles is catalytically active, only the non-metallic side is available for DNA immobilisation.

DNA conjugation is uncoupled here from the task of synthesising active particles. Regarding conjugation chemistry, we made use of the diverse methods available for immobilising oligonucleotides on surfaces. Strategies that involve non-specific interactions, such as DNA surface adsorption will not be considered here. Oligonucleotides immobilise on a surface if they are modified with a functional group that can attach to a reactive group on a solid surface. For example, commercially available microspheres that are synthesised via emulsion polymerization can be terminated with surfaces covered with carboxyl groups (-COOH), streptavidin, amine groups (-NH_2) or other desired modifications that facilitate DNA bonding. Similarly, a variety of modifications can be incorporated into an oligonucleotide at the time of synthesis. In this work, three different conjugation methods were explored to graft DNA onto colloidal particles: streptavidin-biotin linking, water-soluble carbodiimide linking and thiol-metal bonding, which are summarised in Table 5.1. Full protocols can be found in Materials and Methods A.3 .

Table 5.1: List of DNA conjugation methods

Conjugation method	**Functional group on DNA**	**Functional group on colloid**	**Procedure**
Streptavidin-Biotin conjugation	Biotinylated DNA	Streptavidinated colloid	Spontaneous (non-covalent bond)
Carbodiimide crosslinking (EDC)	Amino modified DNA (-NH_2)	-COOH carboxyl group	activated carboxyl groups react with amines to form amide bond
Thiol-metal	Thiol modified DNA (-SH)	Au	Spontaneous thiol-Au bond

5.4.1 DNA assisted assembly of microparticles

In this section, proof-of-principle experiments are presented that show how oligonucleotides aggregate colloids in a sequence-dependent way. The design in Figure 5.17 shows active DNA strands referred to as *sticky ends* that mediate interactions between colloids. These are not directly linked to the colloidal surface, but instead, they are separated by a *spacer* that here takes the form of a 50 base pair duplex. The role of this spacer is to increase the volume explored by the active sticky end, in order to facilitate DNA-mediated bonding [188].

We chose streptavidin-biotin binding as DNA conjugation method. Oligonucleotides end-functionalised with biotin attach to the surface of colloids that carry streptavidin proteins. This approach has been widely used in the soft matter community studying DNA mediated colloidal interactions, such as the Pine and Chaikin groups [189]. The biotin-streptavidin bond is one of the strongest non-covalent bond known, it has a dissociation constant, $K_d \approx 4 \cdot 10^{-14}$ M and it is highly specific, making it a very attractive choice for DNA-colloid binding. However, this bond is reversible and it can be broken at temperatures higher than 70 °C [190].

For these experiments, streptavidin-coated superparamagnetic polystyrene colloids with diameter of 1.43 µm, fluorescently labelled with FluoRed dye (530/ 607 nm) and biotin-binding capacity of ∼1500 pmol mg^{-1} were purchased from Microparticles GmbH (Berlin). These were mixed together with biotin-functionalised oligonucleotides (in 10× excess) in a hybridisation buffer (10 mM phosphate buffer, 50 mM NaCl, Poloxamer 407, 0.5%(w/w), pH 7.5) and incubated at room temperature for 30 min. To remove the excess of non-specifically absorbed oligos, particles were washed and resuspended twice, heating the sample in between for 30 min at 55 °C.

Beads were then mixed with complementary strands that contained sticky ends in their $5'$ end. Red and green sticky ends are complementary to each other (see Table 5.2 for sequences), however none of them are complementary to a 'nonsense' sticky end. With this protocol, colloids were bound to a 50 bp duplex strand with a PEG spacer in-between and a sticky end as illustrated in Figure 5.17. Red and green beads were incubated in hybridisation buffer and shortly after one hour, aggregates started to form (Figure 5.18). We use the radial distribution function $g(r)$, which measures how pixel intensity varies as a function of distance from the centre of a particle in Figure 5.18, to assess the degree of aggregation. In Figure 5.18 we see successful aggregation of a red/green mixture (a), whereas mixtures with beads with 'nonsense' strand remained monodisperse (b), thus confirming DNA-induced colloidal assembly.

Table 5.2: List of oligonucleotides for assembly experiment (sequences taken from [191]).

DNA strand name	Sequence
Biotin TEG Main	5′-BiotinTEG/ATCGCTACCCTTCGCACAGTCAATCCAGAGAGCCCTGCCTTTCATTACGA-3′
Sticky end red	5′-CCTACTTCTAC|TCGTAATGAAAGGCAGGGCTCTCTGGATTGACTGTGCGAAGGGTAGCGAT-3′
Sticky end green	5′-GTSGSSGTAGG|TCGTAATGAAAGGCAGGGCTCTCTGGATTGACTGTGCGAAGGGTAGCGAT-3′
Nonsense strand	5′-TGTGTGTGTGT|TCGTAATGAAAGGCAGGGCTCTCTGGATTGACTGTGCGAAGGGTAGCGAT-3′

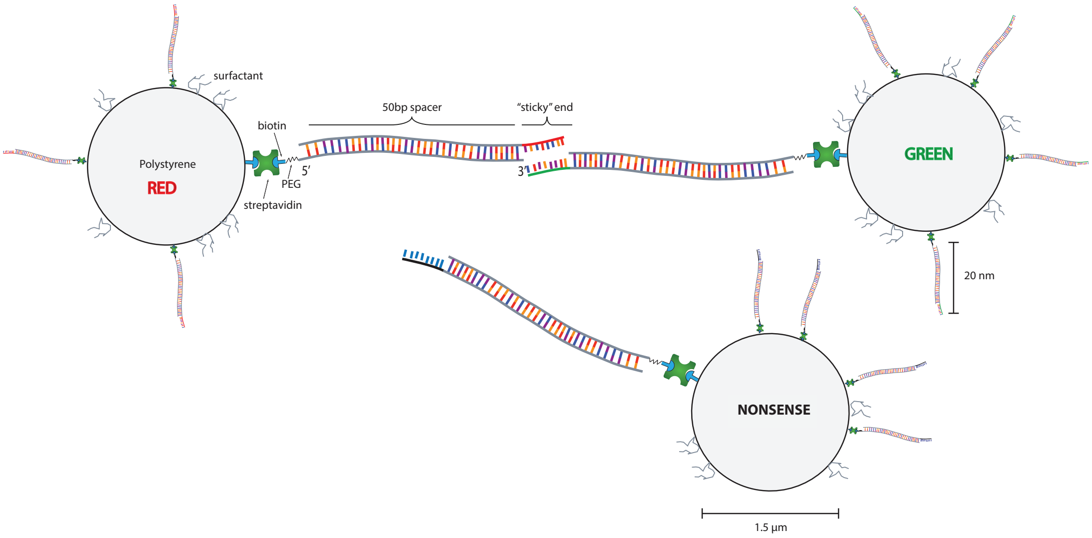

Figure 5.17: *Sequence design for biotin-streptavidin bound microspheres.* A PEG spacer and a 50 bp duplex, shown out-of-scale, act as spacers. Red and green complementary sticky ends are shown, together with a 'nonsense' strand, which is not complementary to either.

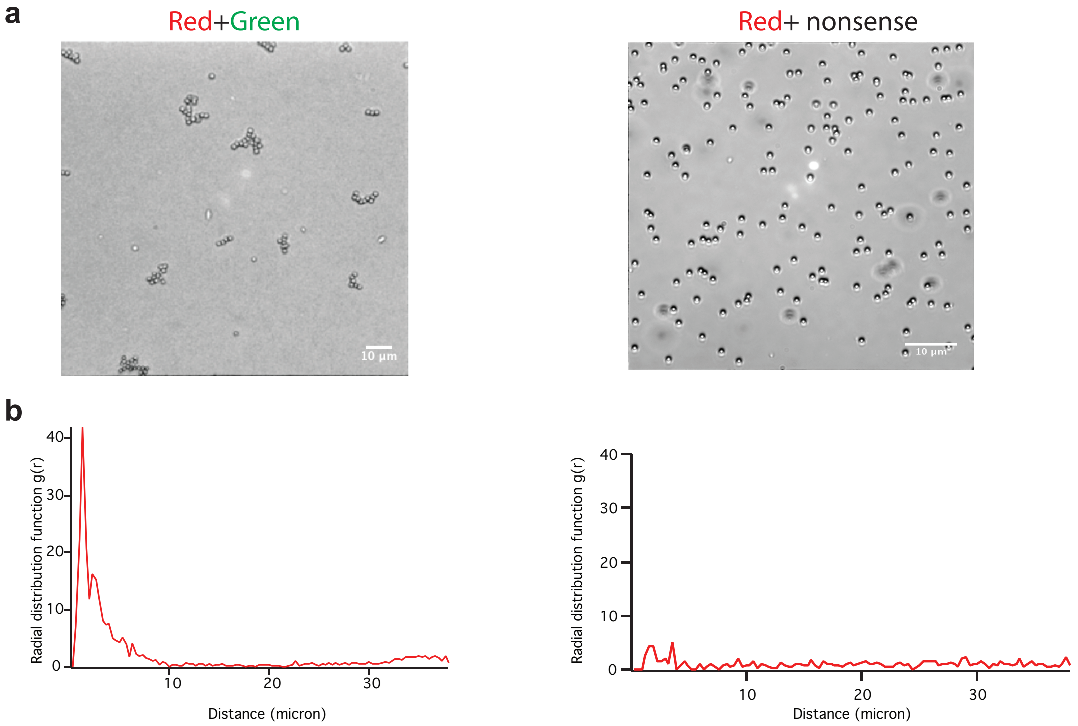

Figure 5.18: a) Aggregation experiments of streptavidinated beads (1.43 μm diameter) and corresponding radial distribution functions $g(r)$ in **b)**, calculated with ImageJ by plotting the integrated pixel intensity as a function of distance from the centre of particles. Peaks for Red+Green are indicative of the formation of clusters due to strand complementary.

5.4.2 DNA assisted aggregation and disassembly of microparticles

Disassembly of clusters of DNA grafted colloids can be induced by using restriction enzymes [192] or by heating above the DNA melting temperature [193]. An isothermal alternative, which is the preferred option to introduce a DNA-based control of the assembly, can be achieved by introducing competition with displacer oligonucleotide strands. Assembly and disassembly kinetics depend on sequence length and DNA surface density; so that a fine balance needs to be found between steric repulsion and DNA-mediated attraction as shown for the case of colloids in [194].

In contrast to the experiments in Figure 5.17, a simplified scheme with shorter and fewer oligonucleotides and covalent functionalisation is better suited to introduce strand-displacement reactions at the colloidal level. Therefore, a simpler generic strand was designed with a ‘nonsense’ sequence as a spacer (thymine chain), together with a 6 carbon spacer that separated the amine group from the oligonucleotide (see Table 5.3 and Figure 5.19). The nonsense spacer was followed by a toehold and a sticky end (called red). In the same way, a complementary strand with no toehold was designed (green). A displacer strand was complementary to both the toehold and the red sticky-end and could reverse the hybridisation between red and green beads, as illustrated in the diagram of Figure 5.20.

Aminated red and green strands were conjugated to carboxylated polystyrene beads of 2.8 µm and 1 µm diameter using an optimized water-soluble carbodiimide (EDC) crosslinking protocol (see Materials and methods A.3), as shown in Figure 5.19. Beads were resuspended in a phosphate buffer, which also served as a hybridization buffer. After incubation of complementary beads for 12 hours, self-assembled structures were observed. Upon addition of an excess of displacer strand, successful disassembly of clusters was observed after incubation for 6 hours (Figures 5.20 (b) and (d)).

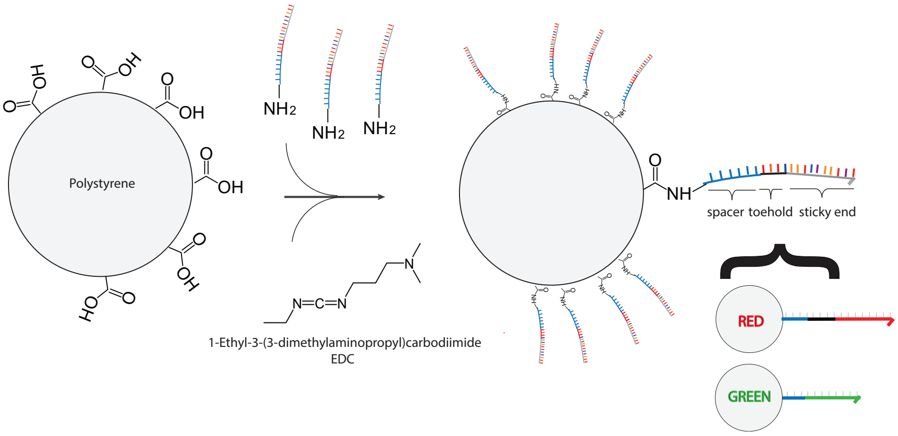

Figure 5.19: *Sequence design for amine-carboxyl bound microspheres.* Polystyrene beads, functionalised with carboxyl groups undergo activation with EDC to form a peptide bond with aminated oligonucleotides. Red and green complementary sequences are shown.

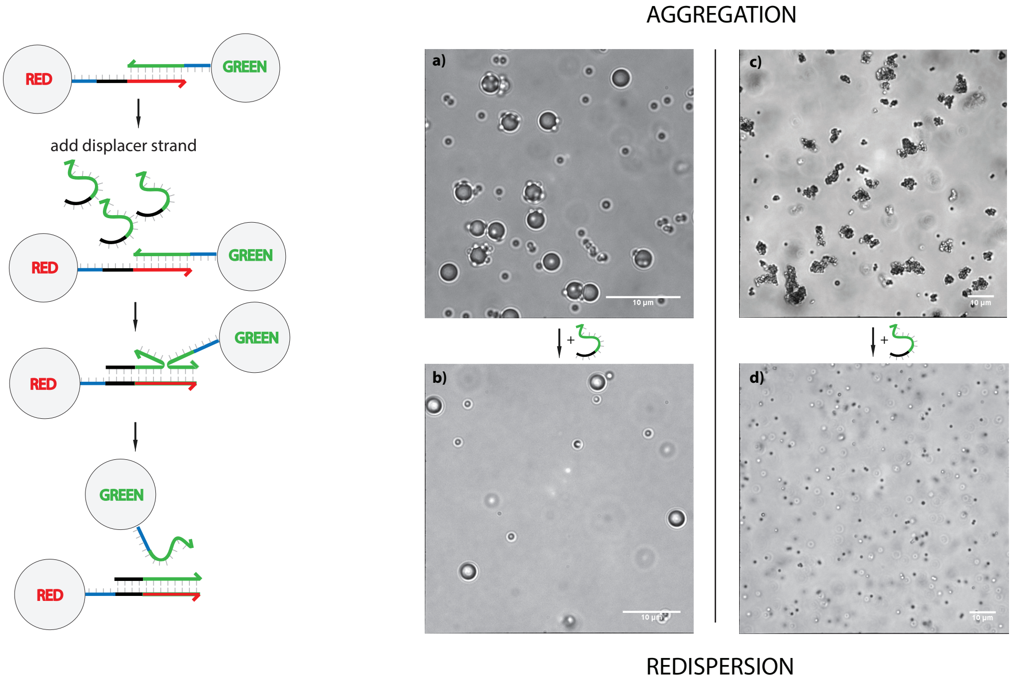

Figure 5.20: Strand displacement scheme with colloids (*left*). Confocal microscopy images show in **(a)** 2.8 µm diameter red beads hybridised to complementary 1 µm diameter green beads after 12 hour incubation, and 1 µm diameter red and green beads in **(b)**. Addition of displacer strands disassembles both structures in **(b)** and **(d)**. Images were taken after 6 hours of incubation with a displacer strand.

Table 5.3: List of used oligonucleotides for disassembly experiment. Sequences taken from [194].

DNA strand name	Sequence
Red A20	5’-Amine-TTTTTTGGATTGCGGCTGAT-3’
Green B20	5’-Amine-TTTTTTTTTTATCAGCCGCA-3’
displacer	5’-ATCAGCCGCAATCCAAAAAA-3

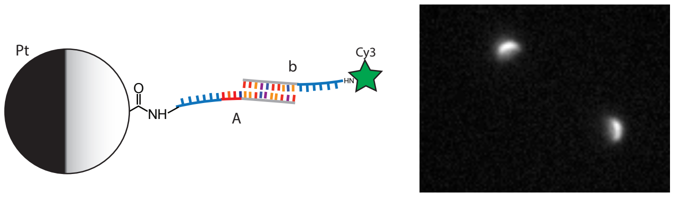

Figure 5.21: Carboxylated 2.8 µm diameter DNA conjugated Janus beads after incubation with a complementary Cy3 strand. Observed with a fluorescence microscope (iX81 Olympus).

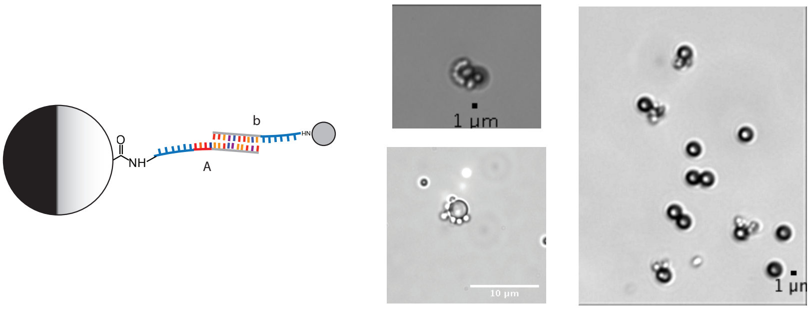

Figure 5.22: Carboxylated 2.8 µm diameter DNA conjugated Janus beads after 6-hour incubation with complementary 1 µm diameter satellite beads. Observed with a bright-field microscope (iX81 Olympus). More than 50% of the particles showed satellites.

5.4.3 DNA conjugation of Janus particles

To achieve functionalisation of DNA on a platinum-coated Janus particles, the following scheme was followed: prior to coating with platinum, colloids were first conjugated with desired oligonucleotides [4]. A covalent bond was chosen (amide bond), as opposed to a weaker streptavidin-bond. After monolayer formation, thin layers of chromium (2 nm) and platinum (10 nm) were evaporated in this order onto colloids. Beads were recovered with a wet lens tissue and resuspended in solution. After mild sonication, centrifugation and filtering, beads were washed and resuspended in water. Swimming capacity was tested by mixing a solution with hydrogen peroxide. To assess that DNA hybridisation capacity was not harmed during the evaporation process two different methods were used: on the one hand Janus beads were conjugated with complementary Cy3 fluorescent strands in hybridization buffer (Figure 5.21). On the other, Janus beads were conjugated with smaller complementary beads. After 6 hours of incubation, structures like the ones in Figure 5.22 were seen using fluorescence microscopy (iX81 Olympus), whereas control Janus beads incubated with beads with non-complementary strands did not form. More than 50% of the particles showed satellites, which indicates that not all particles retained their binding capacity after Pt evaporation. These results show successful functionalisation of DNA onto Janus particles, which could be used to mediate their interaction or as a mechanism to attach cargo to motors.

5.5 Ordering Au NP with DNA Origami nanoflowers

The use of DNA as a molecular glue at the nanoscale is presented in this section, whereby DNA Origami acts as a directional bond between Au nanoparticles, creating hybrid structures with ‘valency’. The Au-DNA Origami hybrid nanostructure introduced in this section can be reprogrammed through a small number of linker strands to create lattices of different symmetries. In the following lines, the lattice

---

[4] When reversing the order (first evaporation and then DNA conjugation) the stability and conjugation capacity of the beads was diminished. As a result large aggregates formed.

formation of Au-DNA Origami hybrids is described (a.k.a. ‘nanoflowers’), together with an analysis of the obtained TEM micrographs. Radial distribution functions and Discrete Fourier Transforms were used to study the assembled lattices. All codes that the author developed for this analysis can be found in the appendix[5].

5.5.1 Isotropic DNA conjugation of Au NPs

In this section we first describe methods to conjugate oligonucleotides onto Au NPs mainly following [78]. A variation of this protocol is later used for Pt NPs in section 6.4. We then present a Au NP-DNA Origami hybrid structure capable of arranging gold nanoparticles in 2D lattices of different symmetries.

The Au NPs were conjugated with thiolated ssDNA strands as follows: First Au NP were concentrated by mixing 2.5 mM bis(p-sulfonatophenyl) phenylphosphine dihydrate dipotassium salt (BSPP, Sigma Aldrich) with citrate-stabilized colloidal Au NPs. Au NPs were resuspended in 2.5 mM BSPP solution to a concentration of 200 nM. This is a ligand-exchange reaction that facilitates binding of thiols on the surface of gold.

Thiolated oligonucletides were prepared by reducing the disulfide bonds to monothiol by incubating with 10 mM final concentration of tris (carboxyethyl) phosphine hydrochloride (TCEP, Sigma Aldrich) for at least 30 min at room temperature.

Au NPs and thiolated oligonucleotides (100 µM, incl. the TCEP) were mixed in 0.5 × TBE buffer at a ratio of 1:1000 (Au NPs:DNA) for 15 nm sized Au NPs. A higher excess of thiolated DNA would be needed for larger Au NPs corresponding to the increased surface of larger Au NPs (scales as r^2). The mixture was incubated with continuous salt titration with NaCl up to 700 mM overnight (*salt-ageing method*) [195], the DNA-functionalised Au NPs were then purified from the excess of DNA using 100 kDa spin filters (Amicon Ultra from Millipore).

---

[5] This work is a collaboration with Dr. Robert Schreiber. The contribution from the author include purification and characterisation of DNA-nanoparticle hybrid structures with electron microscopy and their image analysis

5.5.2 DNA Origami nanoflower and 2D lattices

The directionality of DNA-mediated interactions is hard to control, as the functionalisation methods discussed so far are mainly isotropic, with the exception of Janus particles and patchy colloids [196]. However, DNA patches do not work for nanoparticles, where introducing valency proves more challenging. The DNA origami structures presented here wrap around a Au NP forming a nanoflower and ssDNA handles enable control of the bonding valency and geometry for an otherwise symmetric particle, allowing the formation of different lattice symmetries.

The nanoflower shown in Figure 5.23 has a 15 nm Au NP surrounded by radial 'petals', approximately 20 nm in length, formed by bundles of four DNA helices. The DNA scaffold forms one strand of each helix, so each has a unique base sequence and can be specifically functionalised. Petals are linked at the centre of the structure by scaffold and staple crossovers. The four helices of each petal are tightly bound to each other by staple crossovers. There are 32 petals, alternately arranged in two layers of 16. The petals meet in the centre to form a hole of approximately 15 nm diameter, around which the DNA helices are stacked close together. On the inner end of each petal, two staples are extended to provide A_n (n = 4-8) ssDNA overhangs positioned at the edge of the hole. These hybridize to multiple 19×T oligonucleotides that are covalently attached to the surface of the 15 nm Au NP through 5' thiol modifications, binding the Au NP in the centre of the nanoflower. The whole structure self-assembles in a single-pot reaction after an annealing process. More details about the design of the nanoflower structure and step-by-step protocols are found in [22].

Each part of the DNA origami is identifiable through its unique DNA base sequence, allowing selective functionalisation of the outer ends of some petals with ssDNA linkers to allow control of subsequent lattice formation. To create the lattices shown in Figure 5.23, we separately assembled two batches of nanoflowers, each with one of two complementary linking sequences (A or B type) repeated at two or four sites. Lattices were assembled by mixing nanoflowers A and B in equal concentrations and after an annealing process. Figure 5.23 shows three different lattices, corresponding to three different choices of functionalisation sites. Two attachment sites separated by 180° produce a linear chain of NPs (Figure 5.23 (b)). Four attachment sites separated by 90° produce a square NP lattice (Figure 5.23 (c)). Hexagonal NP lattices were achieved by using four attachment sites separated by approximately 120° and 60°. The quality of these lattices was then characterised by image analysis of TEM micrographs, which is discussed in the next section.

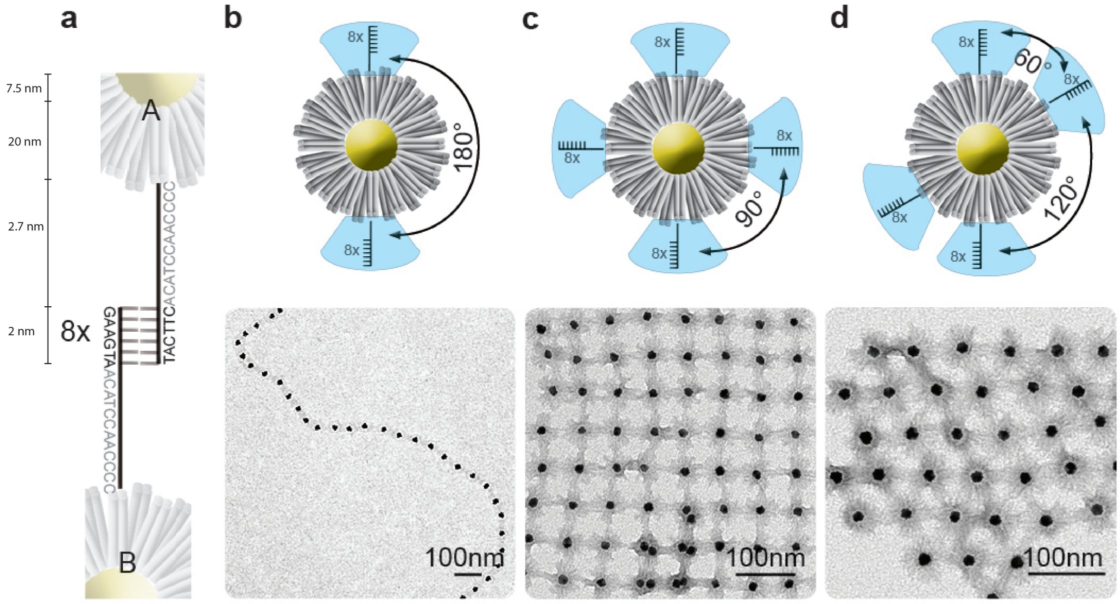

Figure 5.23: *Ordering Au NPs into different lattices by changing the valency of the nanoflowers.* **a)** Hybridization scheme (not to scale): A- and B-type nanoflowers are linked by hybridization of complementary linker oligonucleotides (8 handles per attachment site). **b)** Chains of Au NPs were obtained by providing A and B nanoflowers with two hybridization sites separated by 180°. **c)** Square lattice obtained with four hybridization sites at 90°. **d)** Hexagonal lattices obtained with four hybridization sites with approximately 60° and 120° separation.

5.5.3 Characterisation of DNA Origami-nanoparticle 2D lattices

DNA-assisted assemblies of nanoparticles are normally formed in solution. Because of their size (few nm) conventional microscopy does not reveal lattice structures and alternative methods are needed. Small-angle X-ray scattering (SAXS) has been widely used to probe the lattice properties of 3D DNA crystals. Using SAXS, the interparticle distance can be extracted from an analysis of peak positions in reciprocal space. Normally the data in SAXS is plotted against the scattering vector $q = \frac{4\pi}{\lambda} \sin\left(\frac{\theta}{2}\right)$, which is directly related to the characteristic lattice d spacing, as $q = \frac{2\pi}{d}$. The scattering intensity is proportional to the structure factor $S(q)$, which reveals symmetry properties of 3D lattices. The positions and relative intensities of peaks provide insights into the internal organisation of assemblies in solution, while the number of peaks and their widths reflect their degree of ordering. $S(q)$ is related to the Fourier transform of the *radial distribution function* $g(r)$, which is a measure of the probability of finding a particle at a distance r away from an arbitrary central particle:

$$S(q) = 1 + \rho \int_V \mathrm{d}\mathbf{r}\, \mathrm{e}^{-i\mathbf{q}\mathbf{r}} g(r) \tag{5.2}$$

Unlike 3D crystal lattices, 2D Au NP lattices formed with nanoflowers can be readily observed in the TEM microscope and it is not necessary to extract information from the reciprocal space given by scattering experiments. By measuring the radial distribution function (RDF) $g(r)$ for each lattice directly, they can be classified into one of the 2D Bravais lattices. Due to their long-range order, lattices exhibit RDFs with peaks corresponding to their nearest-neighbours, next-nearest neighbours etc. Each type of lattice has a characteristic nearest-neighbour distribution as illustrated for 3 types of lattices in Figure 5.24.

To analyse the obtained TEM micrographs, first they were converted to binary images using ImageJ (NIH; Bethesda, USA). We then used a MATLAB routine (‘regionprops’) to locate centroids of nanoflowers and to compute a list of pair distances by looping over all pairs of particles (see Appendix B.4). Centre-to-centre distances were plotted on a histogram and normalised by the maximum count. A peak finder algorithm was used to detect peaks and plot a Gaussian for each detected peak. In Figure 5.24 the obtained radial distribution functions for three types of nanoflower lattices are shown: i.e. a), square, b), hexagonal, and c), linear chains.

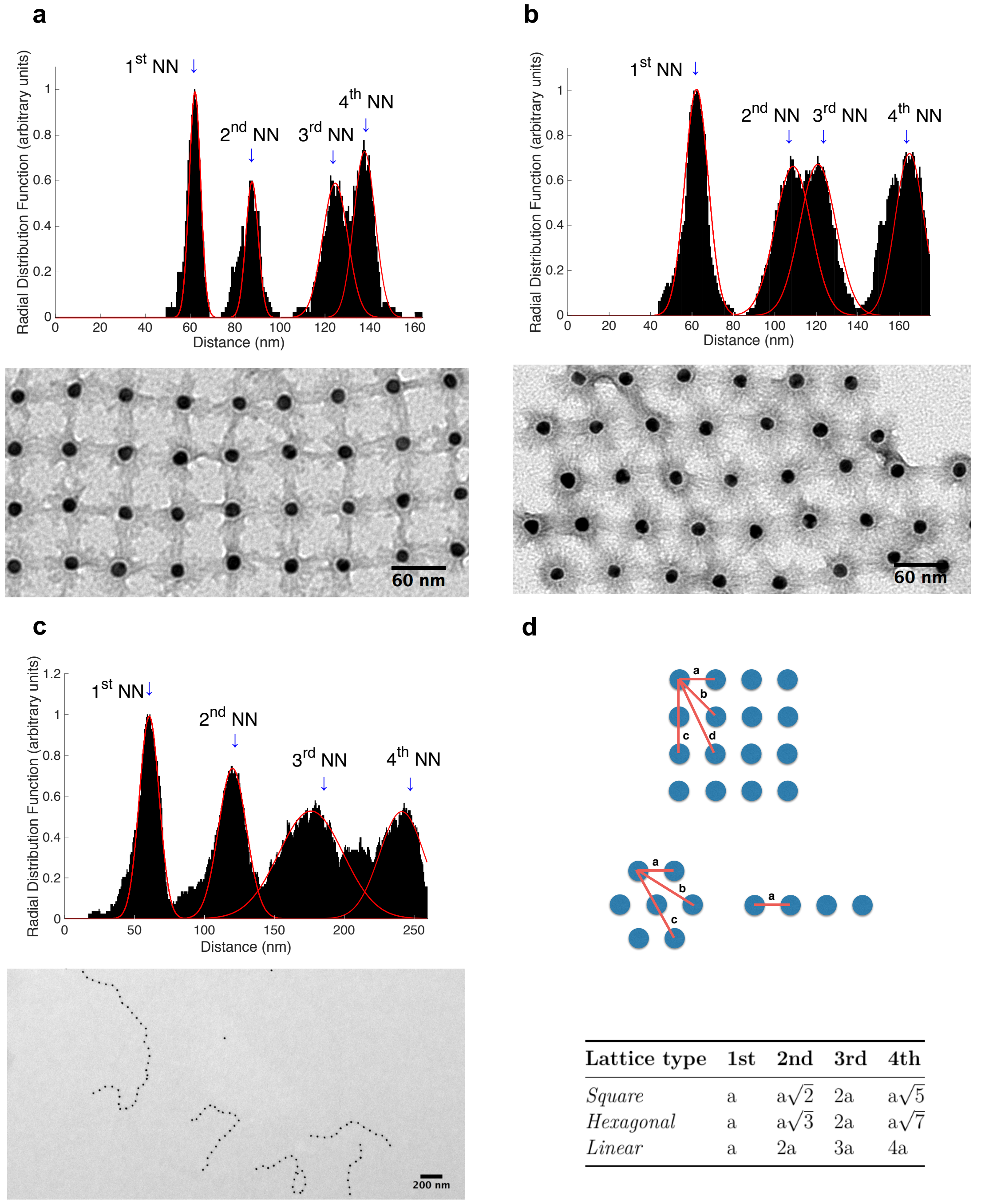

Lattice type	1st	2nd	3rd	4th
Square	a	a$\sqrt{2}$	2a	a$\sqrt{5}$
Hexagonal	a	a$\sqrt{3}$	2a	a$\sqrt{7}$
Linear	a	2a	3a	4a

Figure 5.24: *Radial distribution functions for nanoflower lattices.* **a)**, square, **b)**, hexagonal, and **c)**, linear chains. Images analysed are shown in each case. Each micrograph was converted to a binary image using ImageJ (NIH; Bethseda, USA); MATLAB (Mathworks) routine "regionprops" was used to locate centroids of nanoflowers. Gaussians were fitted to peaks in the radial distribution function (i.e., the histogram of centre-to-centre separations). An average inter-particle spacing of 62(±4) nm was measured for all lattices: corresponding expected separations between nearest neighbours (NN) for each lattice type shown in d) are indicated with a blue arrow in the diagrams.

2D Fourier transform of lattices

Another image processing tool to assess the quality of a lattice is to calculate its 2D Fourier transform [197]. As we are only concerned with digital images from TEM micrographs, the Discrete Fourier Transform (DFT) will be considered. For a MxN image the 2D DFT is given by:

$$F(u,v) = \frac{1}{MN}\sum_{x=0}^{M-1}\sum_{y=0}^{N-1} f(x,y)\exp[-2\pi i\left(\frac{xu}{M}+\frac{yv}{N}\right)] \tag{5.3}$$

where $f(x, y)$ is the image in the spatial domain and the exponential term is the basis function corresponding to each point $F(u, v)$ in the Fourier space. The 2D Discrete Fourier Transform is applied to raw images obtained from Transmission Electron Microscopy (see Appendix B.3). Briefly, a Fast Fourier Transformation (FFT) algorithm is used in the X and Y dimensions and the results are visualised by plotting the logarithm of the power spectrum. To centre the spectrum, a shift is applied that brings the low frequency components to the centre. An example is illustrated with a single disk of 15 nm in Figure 5.25. The Fourier transform of a disk of radius R is given by the Airy disk:

$$F_{disk}(k_R) = 2\pi R^2 \frac{J_1(k_R a)}{k_R a} \tag{5.4}$$

where $k_R = \sqrt{k_x^2 + k_y^2}$ is the wavevector and J_1 is the Bessel function of 1^{st} kind.

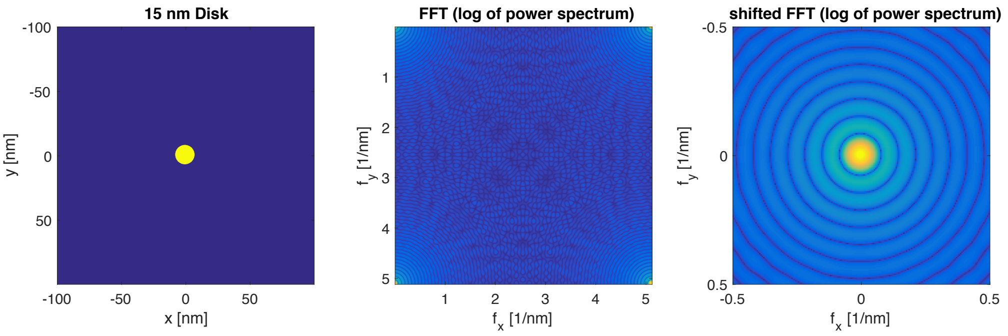

Figure 5.25: a) 2D Fast Fourier Transform (FFT) of a 15 nm disk (left). FFT after shifting the zero-frequency component to the centre of the array (centre), which results in the Airy disk pattern (right). Only low-frequency components are shown.

In the case of the rectangular lattice in Figure 5.24 (a), its reciprocal lattice is also rectangular (Figure 5.26). The same applies to the hexagonal lattice Figure 5.24 (b), which transforms into another hexagonal lattice in reciprocal space[6]. A disk (representing a nanoparticle), repeated over a 2D Bravais lattice (e.g. rectangular or hexagonal), yields a Fourier transform given by:

$$f(\vec{r}) = 2\pi a \sum_{\vec{k}} \frac{J_1(k_R a)}{k_R} e^{i\vec{k}\cdot\vec{r}} \tag{5.5}$$

where the first zero of the $J_1(k_R a)$ for a=7.5 nm is given at k_R ≈0.081 cycles nm^{-1}, indicated by a blue circle in Figure 5.26.

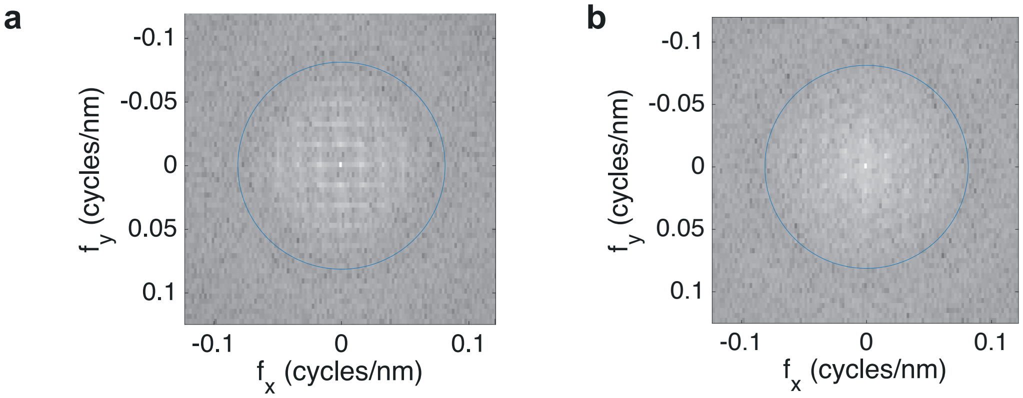

Figure 5.26: Low-frequency components of the log magnitude of the 2D Fast Fourier Transform for **a)** square and **b)** hexagonal lattices. The blue circle represents the first zero of the Bessel Function of First Kind for a sphere of 15 nm diameter.

5.5.4 Electroless deposition of metal ions onto assembled nanoflower chains

Here we describe a way to increase the size of nanoparticles by electroless deposition of Au ions onto assembled nanoflower lattices. The process is similar to what is described in section 5.3.2 for Au@Pt NP.

A 10 µl amount of 5 nM nanoflowers assembled into chains, was applied to a carbon-Formvar copper TEM grid for 30 s. Excess sample was removed with filter paper, and the grid was allowed to dry. A 10 µl amount of EM GoldEnhance

---

[6] The rectangular and hexagonal 2D Bravais lattices are of the same type in their Fourier domain representation, i.e. the reciprocal lattice of a Bravais lattice is also a Bravais lattice.

(Nanoprobes) was applied to the dried nanoflower chains. This mixture consists of Au salts and a reducing agent that triggers an autocatalytic reaction on the surface of gold, increasing its size. After 5 s the enhancement was stopped by rinsing with 10 µl of water. Nanoflowers were stained with uranyl acetate and imaged by transmission electron microscopy (FEI Tecnai 12 at 120 kV).

Figure 5.27 (a) shows the result of gold enhancement after assembly of the chain. The diameter of the gold nanoparticles was increased from 15 nm to ∼60 nm and the particle spacing remained approximately constant at 60 nm, as shown in the radial distribution function in Figure 5.27 (b).

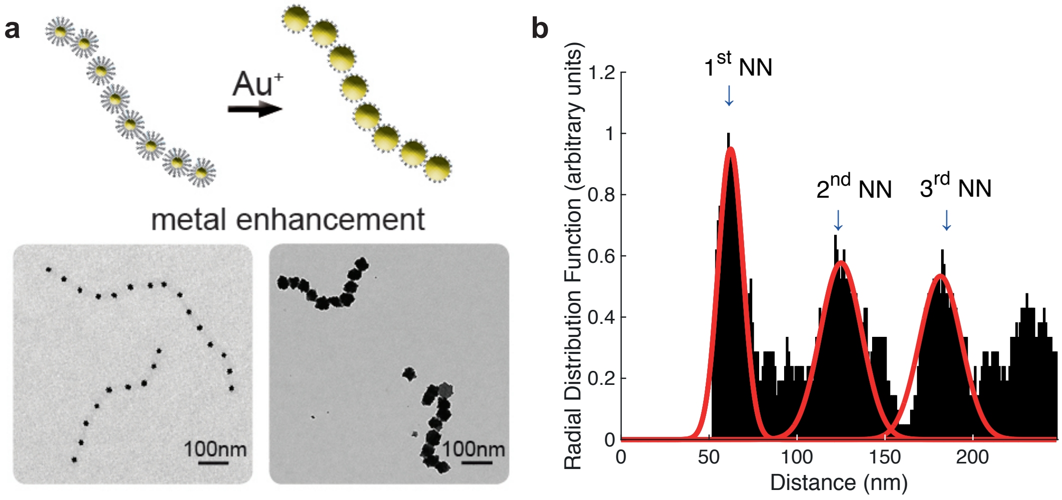

Figure 5.27: a) Gold enhancement of nanoflower chains. The diameter of the gold nanoparticles was increased from 15 nm to ∼60 nm, after assembly of the chain, by electroless deposition of Au. The particle spacing remained approximately constant at 60 nm as from the radial distribution function shown in **b)**.

5.5.5 DNA Origami nanoflowers give valency to nanoparticles

We have introduced origami nanoflowers, a class of composite gold-DNA nanostructure with flexible origami petals wrapped around single AuNPs. These are true composite structures: a nanoflower will not unfold unless it has a AuNP at the centre. The origami structures enable control of the bonding valency and geometry for otherwise symmetric NPs, allowing facile control of lattice symmetry.

Further control of particle size and spacing through electroless gold deposition after assembly could be used to control photonic properties: for example, self-assembled chains with tunable particle size could be used as plasmonic wave guides [198]. Three-dimensional nanoflowers with radial petals can be envisaged, allowing the construction of three-dimensional NP crystals. Directional control of the assembly of NPs is an essential tool for the further exploration of functional nanostructures such as optical metamaterials [199] and catalytic superlattices [200].

5.6 Conclusion

This chapter has described two different methods to synthesise metallic motors at the micro and nano scales. On the one hand, Janus micromotors were fabricated using a traditional thin-film evaporation method. On the other, a wet-chemical approach was used to grow platinum on gold nanoparticles in an asymmetric fashion and produce catalytic nanomotors. The obtained structures were characterised and the activity of micro and nanomotors was measured by tracking microscopy and by dynamic light scattering (DLS), respectively. The second part of this chapter was dedicated to achieving DNA conjugation on both micro and nanoparticles, in order to control their shapes and assembly. The main conclusions of this work are summarised below:

- Micron-sized Janus particles were synthesised by evaporating Pt onto a monolayer of 1 μm polystyrene beads. SEM images showed a half-coated asymmetric structure, achieving the needed asymmetry for self-diffusiophoresis. The diffusion of the Janus particles was measured by particle tracking. In the presence of H_2O_2, the mean squared displacement at long times was significantly enhanced, indicating a clear swimming behaviour. The Janus particles also formed doublet and triplet structures, and the former exhibited a persistent random walk in a preferred direction while the latter performed a spiralling rotational motion.
- We have demonstrated a wet-chemical approach to the synthesis of asymmetric catalytic nanoparticles that function as nanomotors. Asymmetric catalytic

particles can propel themselves by catalysing a reaction in liquid. However, achieving such asymmetry poses experimental challenges. So far, only a few artificial nanomotors have been reported, synthesised by top-down lithographic methods [42]. We developed a simple, scalable, wet-chemical alternative that allows fabrication of even smaller Pt-Au nanomotors of 15 nm diameter. We show that these asymmetric Pt-Au nanoparticles catalyse decomposition of hydrogen peroxide and exhibit enhanced diffusion consistent with chemical propulsion. Pt was grown on the surface of Au NP by a seeded-growth method and the resultant Pt-Au nanoparticles were characterised using HAADF-STEM, TEM, EDX, UV-vis and XPS. Pt-Au nanoparticles synthesised with low Pt precursor concentration formed asymmetric bimetallic nanoparticles; with higher precursor concentrations, more symmetric core-shell particles were obtained.

- Pt-Au nanoparticles catalyse the decomposition of hydrogen peroxide. We have used dynamic light scattering to demonstrate nanomotor activity of asymmetric particles in the presence of H_2O_2 fuel. Ballistic propulsion is manifest as an increase in the effective diffusion constant by up to 30% in hydrogen peroxide (2% v/v); an even greater enhancement was observed in a more viscous ionic liquid. The development of a higher degree of control over nanoparticle morphology can be envisaged. This work paves the way to large scale production of nanometre-scale active particles by wet-chemical methods. The practical application of such particles remains an open scientific and technological challenge.

- DNA conjugation was used to bind to polystyrene beads, via biotin-streptavidin conjugation and carbodiimide crosslinking. Aggregation and disassembly of polystyrene beads were achieved through strand displacement reactions. These methods were used to conjugate the platinum-coated Janus particles with dyed oligonucleotides and hybridise to smaller satellite beads on the polystyrene hemisphere. The successful bonding was shown by fluorescence microscopy.

In prior work, Howse et al. [12] fabricated Janus particles and studied their active Brownian motion. DNA-mediated colloidal assembly is an active area of research [188]. This work is the first of its kind to combine DNA-mediated colloidal interactions with self-propelled Janus particles.

- We developed novel DNA origami structures that allow flexible control of the effective valency and bond angles of encapsulated gold nanoparticles that can be reprogrammed through a small number of linker strands to create lattices of different symmetries. The hybrid structures were characterised by electron microscopy and the assembled lattices were analysed. It shows that by controlling the auxiliary strands in the DNA origami, the interparticle distance and lattice symmetry of Au NP can be well controlled. Unlike previous work in which gold nanoparticles have been positioned on independently-assembled DNA scaffolds, our lattices are true gold-DNA composites: interactions between the gold particles are mediated entirely by DNA, and the DNA origami will only fold into its designed form in the presence of the gold nanoparticles. DNA-guided nanoparticle lattices are promising model systems for exploration of the directed assembly of materials. Ordered arrays of gold nanoparticles, in particular, have the potential to create plasmonic metamaterials.

6

Design and assembly of self-propelled DNA nanostructures

6.1 Introduction: Chemically propelled nanomotors from the bottom-up

The focus of this chapter is the design and synthesis of chemically-powered nanomotors from a bottom-up approach using the tools of DNA nanotechnology. These nanomotors, which are subject to strong thermal fluctuations, are driven far-from-equilibrium by self-induced chemical reactions occurring at their catalytic sites and they are sustained by fuel in the environment. As described in chapter 2, the main mechanism of propulsion is *self-diffusiophoresis*. The following lines give a motivation as to how the tools of DNA nanotechnology could be used for a rational design and assembly of nanomotors.

In this chapter, a bottom-up approach to nanomotor synthesis is explored, implemented with the tools of structural DNA nanotechnology reviewed in chapter 1. *DNA Origami* [75] allows the synthesis of self-assembled nanostructures with designed morphology and it also offers a way to functionalise site-specifically with metallic or enzymatic catalysts. The goal of the present work is twofold: firstly, to endow DNA self-assembled nanostructures with catalytic activity (thereby providing self-propulsion capabilities) and secondly, to make the structure traceable, for example by single-molecule fluorescence methods. These goals are illustrated in Figure 6.1, which shows the assembly of a block 3D DNA origami functionalised with a catalyst and fluorophores. For the nanomotor design, two competing factors will be taken into consideration to increase the propulsion velocity: a high catalytic turnover rate to sustain a chemical concentration gradient across the nanomotor surface and a geometry that will reduce the hydrodynamic friction. The former can be altered by choosing different catalysts, the latter can be tuned by selecting cargoes of different molecular weight that can bind to the nanomotor.

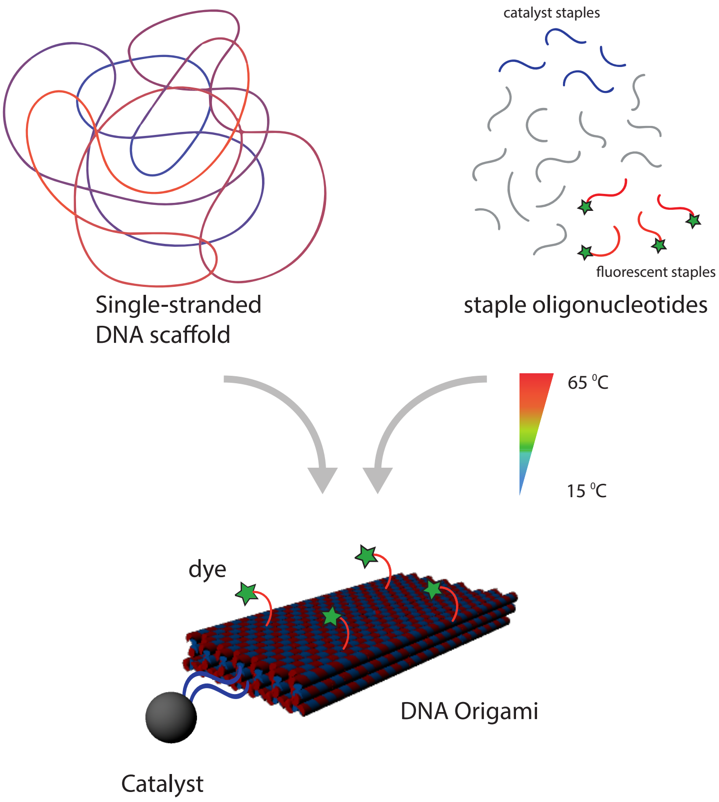

Figure 6.1: *Scheme of a DNA self-assembled nanomotor.* A 3D DNA Origami block structure self-assembles following a temperature annealing protocol, incorporating extended staple strands that serve to localise propulsive catalytic units, as well as traceable elements, such as fluorescent dyes.

This chapter first discusses the use of DNA as a structural component of the nanomotor, as well as its role as a cargo. A DNA origami monolith structure is presented capable of site-specific localisation of catalysts and fluorophores. Its design, assembly and purification are described. The structures are visualised and characterised by negative staining Transmission Electron Microscopy (TEM) and Atomic Force Microscopy (AFM). Then various choices of catalysts (metallic and enzymatic) are treated and their catalytic activity is assessed by electrochemical methods. Experimental techniques to synthesise DNA-catalyst hybrids follow, with a description of used bioconjugation and functionalisation methods. Cargoes of diverse molecular weight are then bound to enzymatic nanomotors and characterised. Finally, measurements of the diffusion of nanomotors bound to cargoes are presented using fluorescence correlation spectroscopy (FCS). Enhanced diffusion of catalase-based DNA structures in the presence of H_2O_2 is reported.

6.2 Structure design: 3D DNA Origami monolith

A rigid block 3D DNA Origami was chosen as the unit structure for a self-assembled nanomotor (see Figure 6.2). This block structure follows the design principles outlined in [201, 202] to create a multilayered DNA Origami on a square lattice. 14×3 DNA helix bundles are tightly packed in a square arrangement forming a rigid block. Each helix bundle extends 170 base pairs.

The block structure, named monolith hereafter, was assembled by mixing 198 short oligonucleotides (staple strands) to direct the folding of a larger strand of viral M13mp18 DNA (scaffold strand). Molecular recognition between base pairs (Watson-Crick pairing) assembles oligonucleotides into a rigid rectangular prism, as programmed by the staple strand sequences (full list of strands in appendix A.8). We introduced targeted deletions of base pairs to reduce the global twist of the structure [201].

The predicted 3D structure is shown in Figure 6.2, where estimated dimensions of the block ($57\,\mathrm{nm} \times 28\,\mathrm{nm} \times 6\,\mathrm{nm}$) have been calculated considering a helical diameter of double-stranded DNA of $2\,\mathrm{nm}$ and a base to base distance of $0.34\,\mathrm{nm}$. Figure 6.3 shows the two-dimensional representation of the structure, as designed

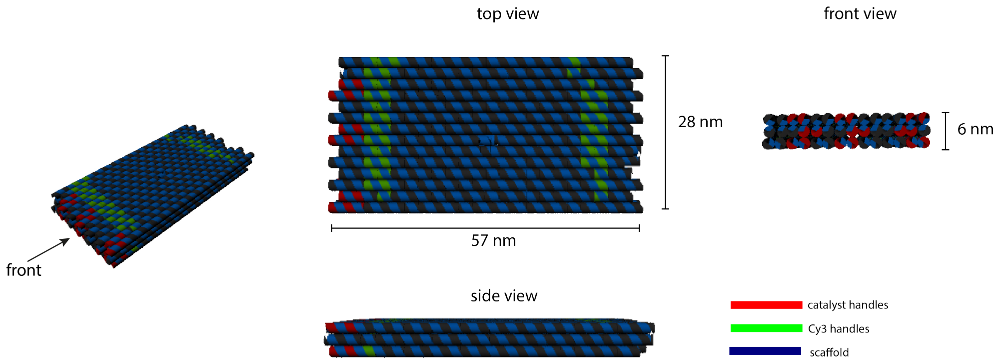

Figure 6.2: Illustration of the modified DNA Origami monolith structure with extended linkers for catalyst (red) and dye anchoring (green).

with the software caDNAno [74]. Extensions to staple oligonucleotides allow site-specific localisation of catalysts and fluorophores. These extensions (coloured in green and red in Figures 6.2 and 6.3) branch out of the main monolith structure as single stranded handles that serve as localised loading sites. The locations of the branching sites have been chosen to guarantee that staples extend outwards of the monolith. Any cargo conjugated with a complementary strand can then hybridise to the extended single-stranded handles. Table 6.1 lists the sequences of modified strands that bind to catalysts and fluorophores.

Table 6.1: List of strands that bind to catalysts and fluorophores (from Biomers Gmbh)

DNA strand name	Sequence	Description
Pt NP-oligo	5′-SH-TTTTTTTTTTTTTTTTTTTT-3′	thiolated poly-T
Catalase-oligo	5′-SH-AAGACGAATATTTAAGAA-3′	oligo for protein-DNA crosslinking
Cy3-oligo	5′-TTCTCTACCACCTACAT-3′	fluorescent oligo

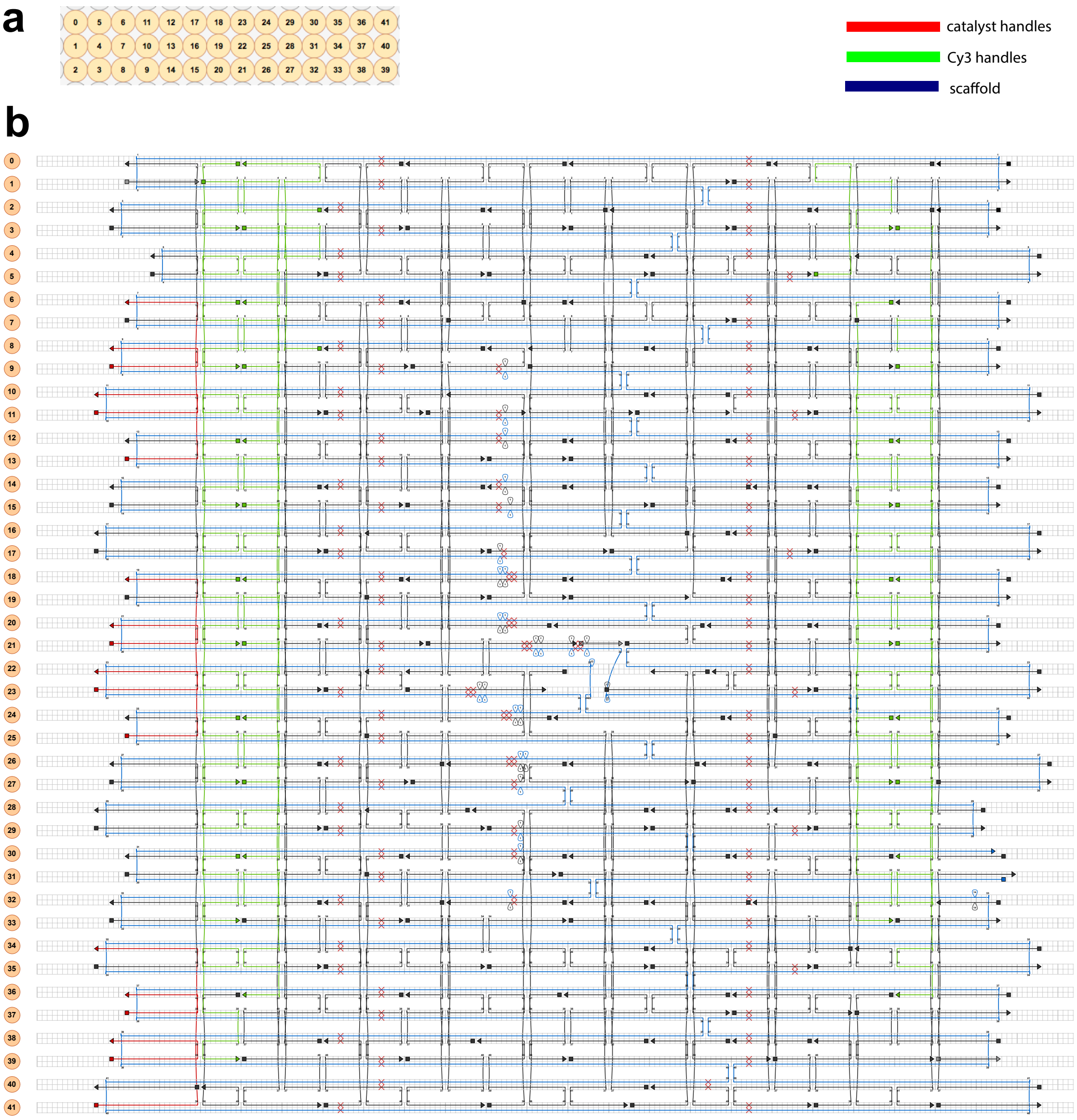

Figure 6.3: **a)** 14×3 helix-bundle cross-section. **b)** CaDNAno file showing the two-dimensional representation of the staple design. The routing of the scaffold is marked in blue. The staple strands are classified into three coloured categories: core staples (black), staples extended by linkers for hybridization with catalyst (red), staples extended by linkers for hybridization with a fluorescent complementary strand (green).

6.2.1 Assembly and purification of a DNA Origami monolith structure

All DNA origami structures in this work were folded according to the mixture protocol described in Table 6.2. 10 nM of scaffold strands (M13mp18 ssDNA, Affimetrix) were mixed with 100 nM of every staple strand in a buffer containing 10 mM Tris, 1 mM EDTA (pH 8) and 16 mM $MgCl_2$.This mixture was then subjected to a thermal-annealing ramp that cooled from 65 °C to 15 °C over the course of 16 hours in several steps illustrated in Figure 6.4.

Variations to this protocol involve the substitution of staple strands (marked with (*) in Table 6.2) by equivalent strands with no handles (control structures). In a similar fashion, handles responsible for Cy3 binding can be added or substituted. To create non-fluorescent monoliths it is sufficient to remove the fluorescent strand from the mixture in Table 6.2.

Two different methods were used to purify DNA origami monoliths from excess staple oligonucleotides. Agarose gel electrophoresis yielded solutions of 20 µl of 5 nM origami (see protocol in Materials and Methods A.5). For higher concentrations, Poly(ethylene glycol)-induced separation of staples was used (PEG precipitation). DNA molecules of different molecular mass are separable by precipitation with PEG. This technique is normally used in molecular biology to separate smaller DNA from larger fragments [203]. Higher molecular mass DNA precipitates at lower PEG concentrations than lower molecular mass DNA. Therefore, the purification threshold can be adjusted by changing the concentration of PEG. This is an effective purification method to separate DNA Origami from excess staples [204]. The protocol in appendix A.6 has been optimised for the DNA Origami monolith structure.

6.2.2 Visualisation of DNA Origami structures

Atomic Force microscopy (AFM) and negative stain transmission electron microscopy (TEM) are able to image DNA origami structures directly. Observation of monolith structures was done in Transmission Electron Microscopy (TEM) after uranyl

Table 6.2: Monolith Origami assembly protocol

	# of staples	**Concentration**	**Volume (µl)**	**Final concentration (nM)**
M13		464 nM	4.3	10
Core	164	609 nM	32.8	100
Cy3 handle (*)	24	4166 nM	4.8	100
Catalyst-handle (*)	10	10 μM	2	100
Cy3 complementary	1	100 μM	4.8	2400
$MgCl_2$		160 mM	20	16 mM
TE buffer			131.2	
		Total	200	

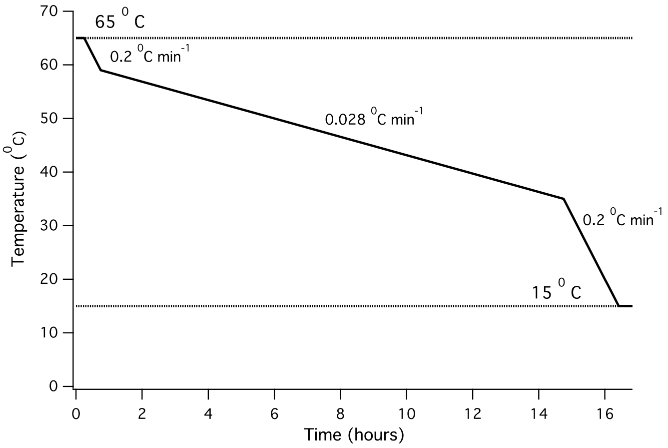

Figure 6.4: Thermal annealing ramp for the DNA Monolith assembly. The mixture was heated to 65 °C and cooled down to 15 °C over the course of 16 hours.

acetate staining of the sample (protocol in appendix A.7). Figure 6.5 a shows DNA Origami monolith structures on a TEM grid, after purification with PEG precipitation and sample preparation.

Characterisation of the monolith structure from TEM micrographs shown in Figures 6.5 a and b, yielded average dimensions of $58 \pm 6\,\text{nm} \times 30 \pm 3\,\text{nm}$. Atomic Force Microscopy allows profiling of the surface height, therefore, Figure 6.5 c shows the height of a representative monolith ($\approx$ 6 nm).

6.3 Nanomotor catalysts: metallic nanoparticles and enzymes

Once the structure of the motor has been established, a DNA compatible catalyst is required for the nanomotor to be propelled chemically. Two different types of catalysts are explored in this work, which are susceptible of DNA functionalisation:

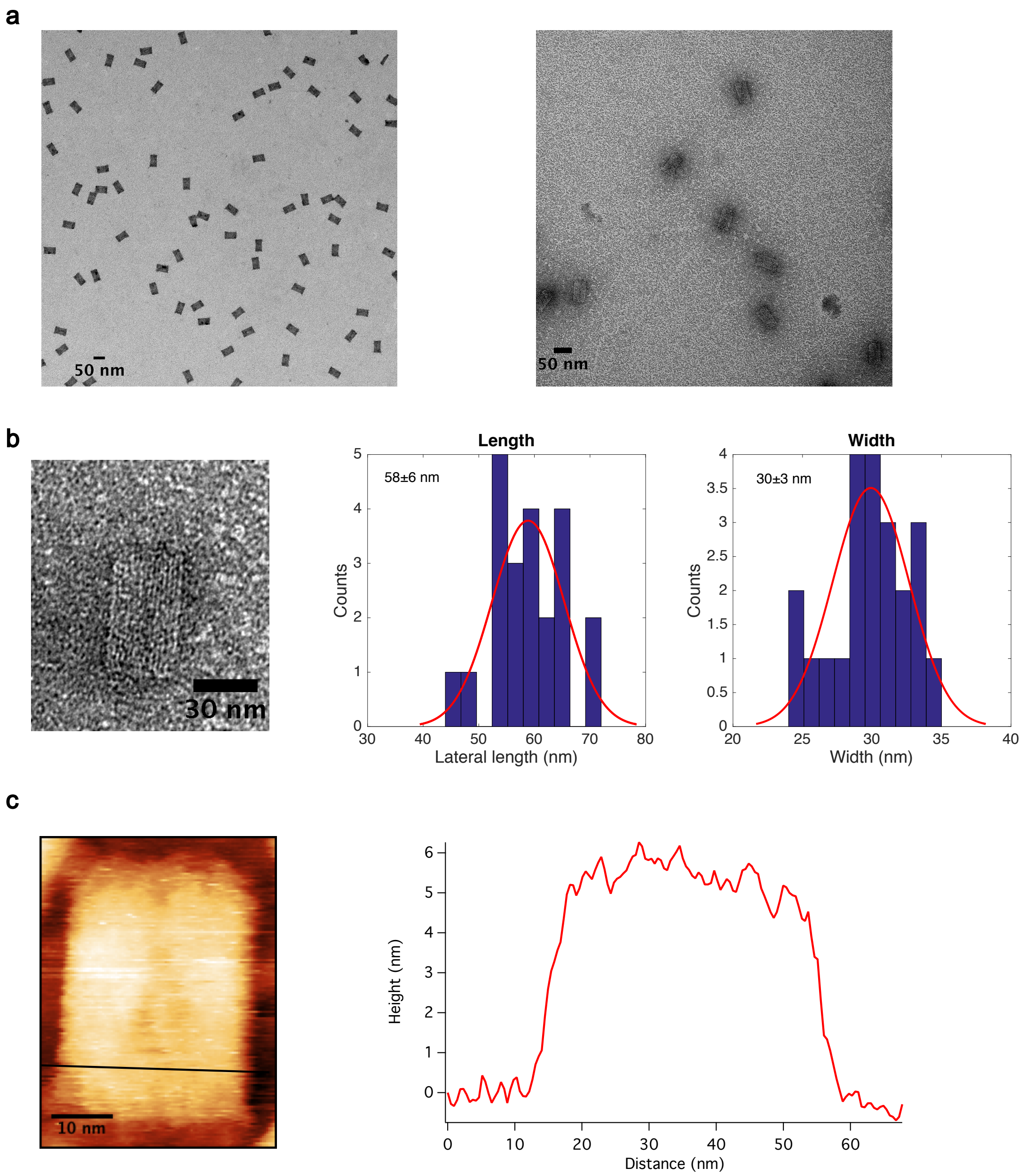

Figure 6.5: *Dimensions of the DNA Origami monolith* **a)** Transmission Electron Microscope micrographs of monolith structures, after negative staining with uranyl acetate. **b)** Length and width distributions of DNA Origami monolith structure as measured on TEM. Micrographs were evaluated with ImageJ to produce histograms and average dimensions of $(58 \pm 6\,\text{nm} \times 30 \pm 3\,\text{nm})$ nm. **c)** Atomic Force Microscopy image of DNA monolith. Height measurement along the indicated line is shown ($\approx$ 6 nm).

metallic nanoparticles and enzymes. The decomposition of hydrogen peroxide in aqueous solution is the standard chemical reaction used for all the catalysts studied in this chapter:

$$H_2O_2 \xrightarrow{k} H_2O + \frac{1}{2}O_2 \tag{6.1}$$

There is a broad range of inorganic and biological catalysts that decompose H_2O_2 at room temperature, making this fuel the preferred choice for micro and nanomotors. These include metals like Ag and Pt, and enzymes like catalase. In this section, the physical and catalytic properties of these potential nanomotor catalysts are analysed.

6.3.1 Physical and chemical properties of metallic nanoparticles and catalase

Three features of metallic nanoparticles are relevant for this study: optical properties due to their surface plasmon resonance, capability to bind to DNA and catalytic activity in the presence of H_2O_2.

Plasmonic nanoparticles -like gold, silver, and platinum – are highly efficient at absorbing and scattering light due to their local surface plasmon resonance. This allows an optical characterisation of shape, size and surface coating. Unlike gold or silver, platinum nanoparticles (Pt NPs) do not have visible-region plasmon absorption, as can be seen in Figure 6.6 (a), where the UV-Vis spectra of different nanoparticles are shown. The spectra with sharp surface plasmon absorption peaks correspond to Au NPs and Ag NPs, whereas the featureless spectrum corresponds to Pt NPs. Unlike Pt NPs, the resonant peaks of Au NPs and Ag NPs shift to the red and broaden as nanoparticles get bigger (Figure 6.6 (b)). Not having a distinguishable peak in the visible spectrum makes characterisation of Pt NPs using spectroscopic methods difficult.

Since the pioneering work of DNA-gold conjugated nanoparticles by Mirkin [76] and Alivisatos [83], efforts have been made to extend DNA conjugation to the surfaces of other metallic nanoparticles. However, low colloidal stability and the lack of strong chemical anchoring groups for other metals have prevented grafting

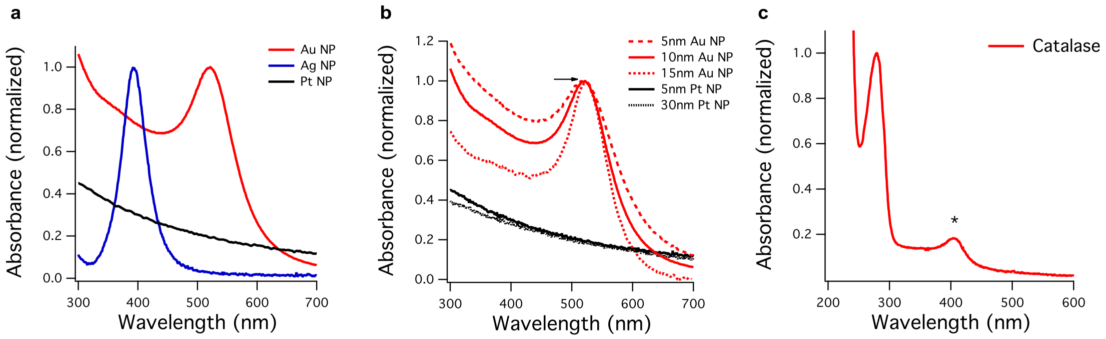

Figure 6.6: **a)** Absorption spectrum of 10 nm Au, Ag and Pt NPs measured with UV-Vis spectroscopy. **b)** Absorption peak of Au NPs and Pt NPs for different particle sizes. **c)** Optical spectrum of the catalase shows a Soret peak at 406 nm, which is a characteristic peak for the heme group.

strategies as robust as DNA-Au conjugation with alkyl-thiol moieties. In the case of gold, as discussed in section 5.5.1, DNA strands presenting 3′ or 5′ terminal thiol groups, in an ionic solution, are capable of forming a high density monolayer of oligonucleotides on the surface of Au NPs. Similar to Au, Ag and Pt also react with thiol groups to form self-assembled monolayers (SAM) on their surface. We use the thiol-to-metal interaction to bind oligonucleotides onto the surfaces of nanoparticles.

Finally, regarding the catalytic activity of Au, Ag and Pt, it is known that Ag and Pt are hydrogen peroxide catalysts, whereas Au is chemically inert. Whether this behaviour is also the case for nanoparticles is tested in the next section.

6.3.2 Catalytic activity measured by electrochemical methods

Chemically-propelled particles rely on specific chemical reactions that occur between the environment and their surface. In particular, the propulsion speed for phoretic particles is related to the chemical reaction rate (Eq. (2.15)). Therefore, when designing a nanomotor, it is of interest to characterise the chemical activity of the chosen catalyst.

Electrochemical methods offer a direct probe of the interfacial chemistry that takes place on the surface of catalytic motors. In this section, two electrochemical techniques (amperometry and cyclic voltammetry) are presented to measure the chemical activity of metallic and enzymatic catalysts in the presence of H_2O_2.

6.3.3 Electrochemical experimental setup

All electrochemical measurements were performed at room temperature (20 ± 2 °C) with a µ-AUTOLAB III potentiostat (Eco-Chemie, Netherlands). A three-electrode system as illustrated in Figure 6.7 was used, consisting of a working electrode, a Pt-wire counter electrode and a Ag/AgCl reference electrode.

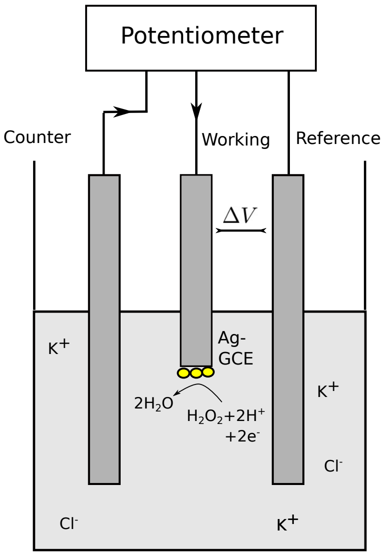

Figure 6.7: Three-electrode setup to measure H_2O_2 concentration in solution using a Ag modified glassy-carbon electrode.

In an amperometric experiment, the potential at the working electrode is held fixed and the generated current as a consequence of a redox reaction is recorded. To monitor H_2O_2 decomposition, a rotating disk electrode (RDE) of silver modified glassy carbon (Ag-GCE, $0.031\,\mathrm{cm}^2$) was used as a working electrode to allow an in-situ measurement of H_2O_2 concentration in solution. The Ag-GCE was prepared by dropping 10 µl Ag NP suspensions ($0.02\,\mathrm{mg\,mL^{-1}}$, size of 60 nm) onto the top of a glassy carbon electrode and it was dried for 40 min.

In cyclic voltammetry, a sweeping potential is applied at the surface of the working electrode and the resulting current is measured. For this experiment, glassy carbon electrodes were used as a substrate of working electrodes. For each experiment, the working electrode was prepared by coating the substrate with Ag, Au and Pt nanoparticles by dropping 10 µl suspensions ($0.01\,\mathrm{mg\,mL^{-1}}$) and drying for 20 min.

6.3.4 Amperometric measurement of H_2O_2 decomposition

This amperometric experiment aims to measure and compare the catalytic activities of catalase, Pt NPs and Ag NPs when catalysing the decomposition of H_2O_2 in the solution. It was performed at a fixed potential where silver reduces H_2O_2 (-0.6V), in a solution of 10 ml 0.1 M KCl and initial 25 mM H_2O_2, with a rotation speed of the working electrode of 1300 rpm, allowing an in-situ detection of H_2O_2. After the solution stabilised for 200 s, 10 µl of catalase (43 nM) was added into the beaker and the decrease in current was recorded, which corresponded to a decrease in H_2O_2 concentration. This experiment was repeated with equimolar additions of 5 nm Pt NPs and 10 nm Ag NPs and a 10× increased concentration of catalase in separate experiments [1]. The results are plotted together in Figure 6.8 (a), where $t = 0$ indicates the addition of catalyst to the solution. The H_2O_2 sensor works in the following way: H_2O_2 is reduced by silver on the electrode surface resulting in a current. As H_2O_2 is being consumed by a catalyst, fewer H_2O_2 molecules will be reduced on the electrode. Therefore fewer electrons will flow through the cell resulting in a decrease in current. For this sensor, a linear relationship exists between current and concentration given by the Levich equation $I \propto C$, which extends Faraday's law to the case of diffusion in RDE [205]. For the range between 0.1-100 mM [206] this linear relationship holds. Therefore, a decrease in current response can be translated into a decrease in H_2O_2 concentration in solution as shown in in Figure 6.8 (b). For this setup the conversion was $2.9\,\mathrm{\mu A\,mM^{-1}}$.

Ag NPs show catalytic activity ($3.21\,\mathrm{\mu M\,s^{-1}}$), but not as strong as Pt NPs ($10.53\,\mathrm{\mu M\,s^{-1}}$) or catalase ($12.54\,\mathrm{\mu M\,s^{-1}}$). A 10× increase in catalase concentration

---

[1] Nanoparticle concentrations were calculated from dilutions of stock samples as reported by the manufacturer. Catalase concentration was measured with UV absorption spectroscopy using extinction coefficient ϵ_{405}=324,000 $\mathrm{M^{-1}\,cm^{-1}}$.

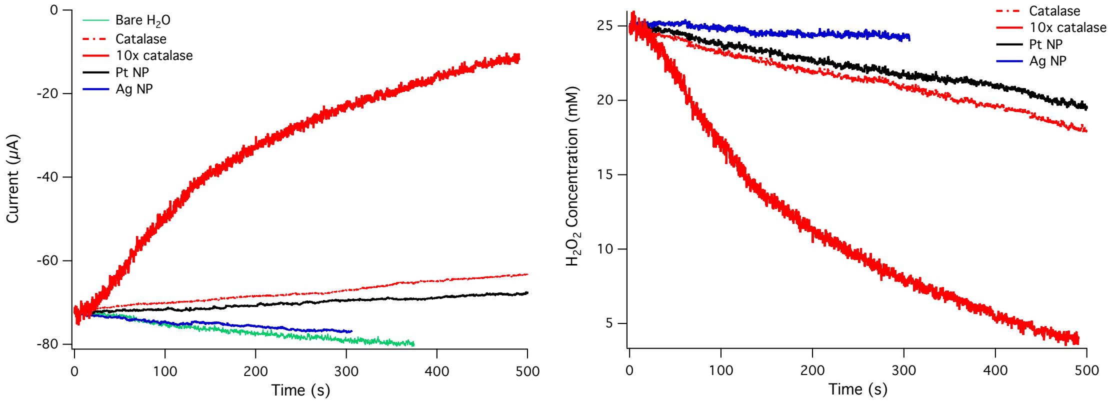

(a) Amperometric current response **(b)** H_2O_2 decomposition

Figure 6.8: a) Amperometric measurement of H_2O_2 reduction in a silver modified glassy carbon electrode at a fixed potential of -0.6 V in 10 mL of 0.1 M KCl and initial 25 mM H_2O_2 with the addition of equimolar concentrations of different catalysts (5 nm Pt NPs, 10 nm Ag NPs and catalase). **b)** Conversion of current to H_2O_2 concentration.

results in H_2O_2 decomposition which is linear at first, but as H_2O_2 is consumed the rate decreases gradually, following Michaelis-Menten enzyme kinetics.

From this experiment we conclude that catalase decomposes hydrogen peroxide at a higher rate than its metallic counterparts, although with a similar activity compared to equimolar 5 nm Pt NPs. Silver nanoparticles also display mild catalytic activity in H_2O_2.

6.3.5 Cyclic voltammetry of metallic nanoparticles in H_2O_2

Cyclic voltammetry is an electrochemical method that investigates the reaction kinetics between a solution and the electrode surface, by cycling the potential of a working electrode and measuring the resulting current.[2] Voltammetry can also be used to estimate activation energies, by identifying the so-called onset potential E_{on}, i.e. the lowest potential at which a reaction occurs. At the onset potential E_{on}, there is no current from the reaction and it can be assumed to be at equilibrium. The Nernst equation yields a direct relationship between the onset

---

[2] In a typical cyclic voltammetry experiment the voltage is swept between two values at a fixed rate, when the voltage reaches V_2 the scan is reversed and the voltage is swept back to V_1. This allows the study of oxidation and reduction of the analyte at the electrode surface [207].

potential and the Gibbs free energy change

$$\Delta G = -nFE_{on} \tag{6.2}$$

where n is the number of electrons transferred and F is Faraday's constant. This relationship could be directly translated into a catalytic rate k when the reaction is spontaneous under standard conditions, by means of Arrhenius law $k \propto e^{\frac{-\Delta G}{kT}}$. Therefore, a lower onset potential E_0 means a lower activation energy and a faster catalytic rate k.

In this experiment, a similar setup as in Figure 6.7 was used. The working electrodes were Pt NPs, Au NPs and Ag NPs modified glassy carbon electrodes. These were prepared by dropping 10 µl nanoparticle suspensions (0.01 mg/ml) onto the top of a glassy carbon electrode and dried for 30 min. As catalase is not conductive, this measurement was only limited to metallic nanoparticles. The obtained voltammograms are shown together in Figure 6.9.

To interpret these curves, we focus on the *onset potential*, starting potential E_{on} by identifying the beginning of H_2O_2 reduction[3] (these are labelled as 1 and 4 in Figure 6.9 for Ag and Pt respectively).The peak currents (2 and 3) represent the potentials with highest H_2O_2 reduction rate.

No significant peak at the Au NP electrode voltammogram is observed compared to an unmodified electrode. This indicates that Au NPs are inert to H_2O_2 in this potential range. For the Ag NP electrode, however, a reduction wave starts at E_{on}^{Ag} =-0.35 V and reaches the peak at about -0.7 V with a peak current value of 55 µA.

Finally, at the Pt NPs electrode, the onset potential for H_2O_2 reduction is at $E_{on}^{Pt} \approx 0$ V and the peak current value is about 236 µA for a scan rate of 100 mV/s. Lower scan rates v changed the peak current (as $I \propto v^{1/2}$ [207]), but did not alter the measured onset potential (see inset in figure 6.9). In comparison to Ag NPs, a lower onset potential $E_{on}^{Pt}<E_{on}^{Ag}$ suggests that it is easier for H_2O_2 to react at the surface of Pt NPs. In other words, the activation energy barrier that needs

---

[3] It is the potential at which the reaction current density significantly departs from the background for a given electrochemical reaction.

to be overcome is reduced in the case of Pt NPs, which directly translates into a higher catalytic rate (Arrhenius equation $k \propto e^{\frac{-E_a}{RT}}$).

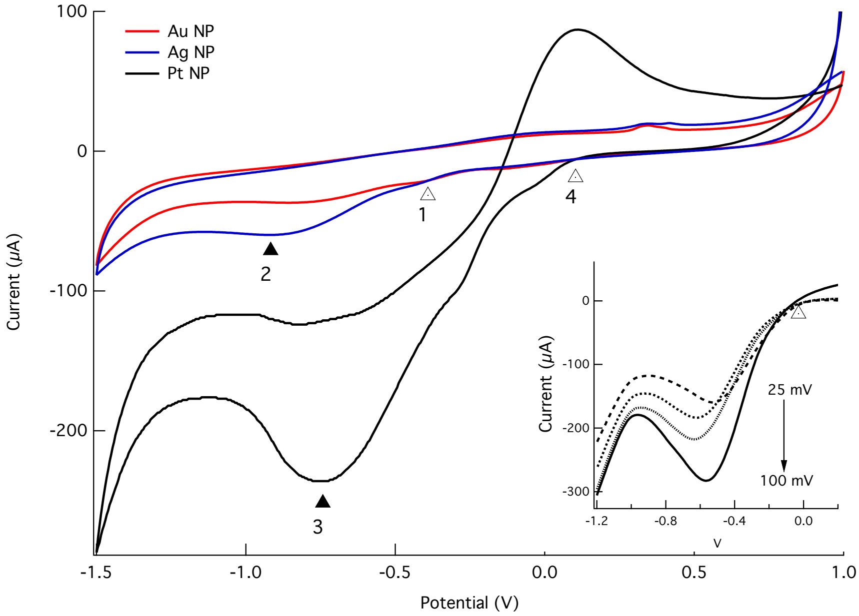

Figure 6.9: Voltammogram at Au NPs, Ag NPs and Pt NPs modified GCE in 10 mL of 0.1 M KCl and 25 mM H_2O_2 with scan rate of $100\,\mathrm{mV\,s^{-1}}$. Onset potentials E_0 (1 and 4) and current peaks (2 and 3) are labelled for Ag NPs and Pt NPs respectively. The inset shows voltammograms for Pt NPs at scan rates of 25, 50, 75 and $100\,\mathrm{mV\,s^{-1}}$.

These electrochemical experiments suggest that Au NPs, despite their appeal due to ease of functionalisation with DNA, display no catalytic activity and should be ruled out as potential catalysts in this project. Ag NPs show a mild activity when decomposing H_2O_2. In contrast, Pt NPs show much higher catalytic activity, making them the preferential choice as a metallic catalyst for a synthetic nanoswimmer. Finally, catalase displays the highest relative catalytic rate, as defined by the H_2O_2 decomposition rate in Figure 6.8 (b). This makes it a suitable choice for an enzymatically driven nanomotor.

6.4 Decoration of DNA structures with Pt nanoparticles

In order to localise Pt NPs on DNA origami monoliths, first DNA functionalisation of Pt NP is necessary. In this section, a ligand exchange reaction is described that facilitates binding of thiol-functionalised oligonucleotides to Pt surfaces. Then, Pt NPs conjugation to the DNA monolith structure and subsequent purification are discussed. Finally, transmission electron micrographs are reported, which show successful localisation of Pt NPs at desired locations on the DNA Origami structure.

6.4.1 Ligand exchange reaction of Pt nanoparticles with BSPP

5 ml of citrate-capped platinum nanoparticles (nanoComposix, 2 mM sodium citrate NanoXact ($0.05\,\mathrm{mg\,mL^{-1}}$)) were first mixed with 5 mg BSPP (Sigma Aldrich). The solution was stirred at room temperature and left overnight, allowing the phosphine ligands to replace the citrate ligands on the surface of the nanoparticles as illustrated in Figure 6.10.

The resulting solution was centrifuged at rcf of 21,500 g for 3 hours. The precipitate was resuspended in Milli-Q water containing BSPP at $2\,\mathrm{mg\,mL^{-1}}$. BSPP-capped Pt was stored at 4 °C for further use. The concentration of PtNP was determined by UV-Vis spectroscopy. Unlike Au NPs, Pt NPs do not have a distinguishable absorption peak, however, comparison with the known concentration of the source is possible at a wavelength different from DNA absorption (e.g. λ=500 nm).

Pt NPs stabilised in citrate showed a zeta potential of ζ=(-36.7 ± 0.1) mV, a mobility of μ=(-2.87 ± 0.01) µm cm/Vs, a hydrodynamic radius of (7.1 ± 0.2) nm and a diffusion constant (34.5 ± 0.4) $\mathrm{\mu m^2/s}$. After the ligand exchange reaction with BSPP, PtNPs showed a zeta potential of (-51 ± 1) mV, a mobility of (-4.0 ± 0.1) µm cm/Vs, a hydrodynamic radius of (8.8 ± 0.2) nm and a diffusion constant(27.9 ± 0.8) $\mu\mathrm{m}^2$/s. All measurements were repeated 3 times on a Nano Z Zetasizer (Malvern) apparatus using folded capillary cells. An increased zeta potential and mobility indicate that BSPP renders the PtNP solution more stable than citrate, due to an increased negative charge on the surface.

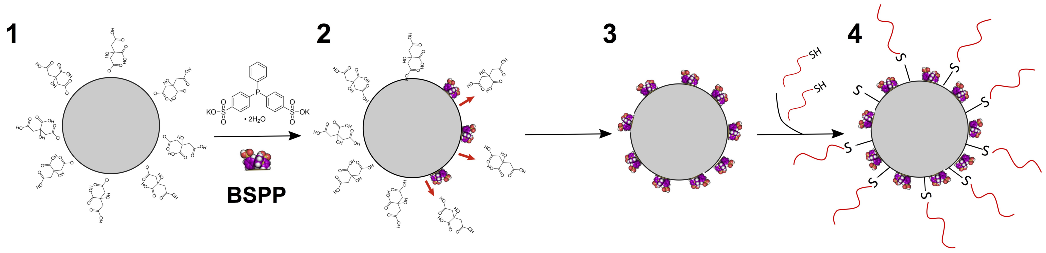

Figure 6.10: Ligand exchange reaction on Pt NP with BSPP: 1. Citrate coated Pt NP are exposed to BSPP 2. and 3. BSPP displaces citrate molecules 4. thiolated oligonucleotides bind to BSPP coated Pt NP forming a stable solution.

6.4.2 Functionalisation of Pt nanoparticles with oligonucleotides

Thiolated DNA normally forms disulfide bonds and one way to break these bonds is to use reducing agents, such as dithiothreitol (DTT) or tris(2-carboxyethyl)phosphine) (TCEP). Unlike DTT, TCEP does not contain any thiol groups, making it a preferred option, as it does not need further purification. Figure 6.11 illustrates the reduction of disulfide bonds by TCEP.

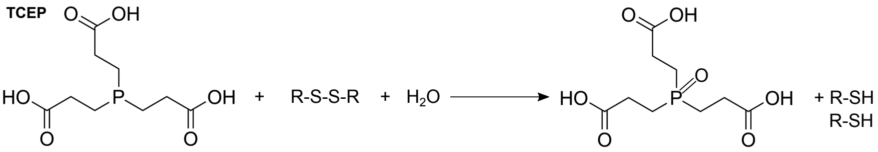

Figure 6.11: Reduction of disulfide bonds with TCEP.

Thiolated oligonucleotides (Biomers) with 19 thymines were first incubated with TCEP at 10 µM final concentration for 30 min. In 150 µl of buffer containing 0.5× TBE and 50 mM NaCl, a 100× molar excess of thiolated oligonucleotides was mixed with 1 µM BSPP-capped Pt NP. The mixture was left on a shaker for overnight incubation. Purification of nano particles from unreacted oligonucleotides was done with 100 kDa cutoff centrifugal filter (Amicon Ultra, Millipore) followed by 8 additional spinning steps (each 3 min, 10,000 rcf) with 500 µl buffer (0.5× TBE without $MgCl_2$) added to the centrifugal filter before each centrifugation step. UV-Vis spectroscopy was used to determine the new concentration. This protocol was performed immediately before incubation with origami structures to avoid disattachment of oligonucleotides from the surface of the nanoparticles.

One way to visually test the successful functionalisation of Au nanoparticles, is to mix them in a buffer with high $MgCl_2$ concentration (ideally the conjugates should be stable at $MgCl_2$ concentrations of up to 100 mM [78]). When excess salt is added to the gold solution, the surface charge of the nanoparticle is screened, causing nanoparticles to aggregate. Due to a smaller interparticle distance, the surface plasmon resonance shifts to lower energies, causing the absorption and scattering peaks to red-shift to longer wavelengths.

As Pt NPs do not have a visible plasmon resonance, one way to test successful functionalisation is to perform this test in gel-electrophoresis, shown in Figure 6.12 (b). Under origami salt conditions (11 mM $MgCl_2$), DNA coated nanoparticles migrate in the agarose gel, whereas uncoated ones aggregate and remain in the well. This variation of the magnesium test served as proof for successful DNA functionalisation. In addition, when no salt was added, a difference in mobility was observed for DNA coated Pt nanoparticles (shown in Figure 6.12 (a)).

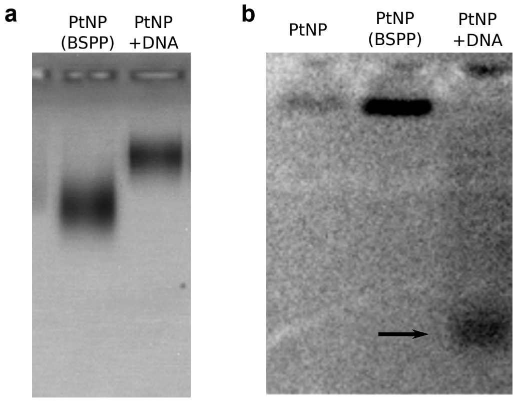

Figure 6.12: a) 2% Agarose Gel Electrophoresis at $16\,\mathrm{V\,cm^{-1}}$ of bare PtNPs and DNA functionalised Pt NPs. A difference in mobility is signature of successful functionalisation. **b)** 'Magnesium test': agarose gel electrophoresis in Origami buffer conditions (11 mM $MgCl_2$). Non-coated Pt NPs aggregate in wells in the presence of salt, whereas those grafted with DNA do not (marked with an arrow).

6.4.3 Immobilisation of DNA-Pt nanoparticles on DNA monolith structures

To demonstrate site-specific localisation of Pt NPs on the DNA monolith, three different monolith configurations were designed with extended staple strands containing single-base handles. These correspond to a single handle, cluster handles and side handles to allow for the three geometries shown in Figure 6.13. Each loading site for one nanoparticle consists of three handles with poly-A extension, complementary to the poly-T oligonucleotide bound to Pt NPs.

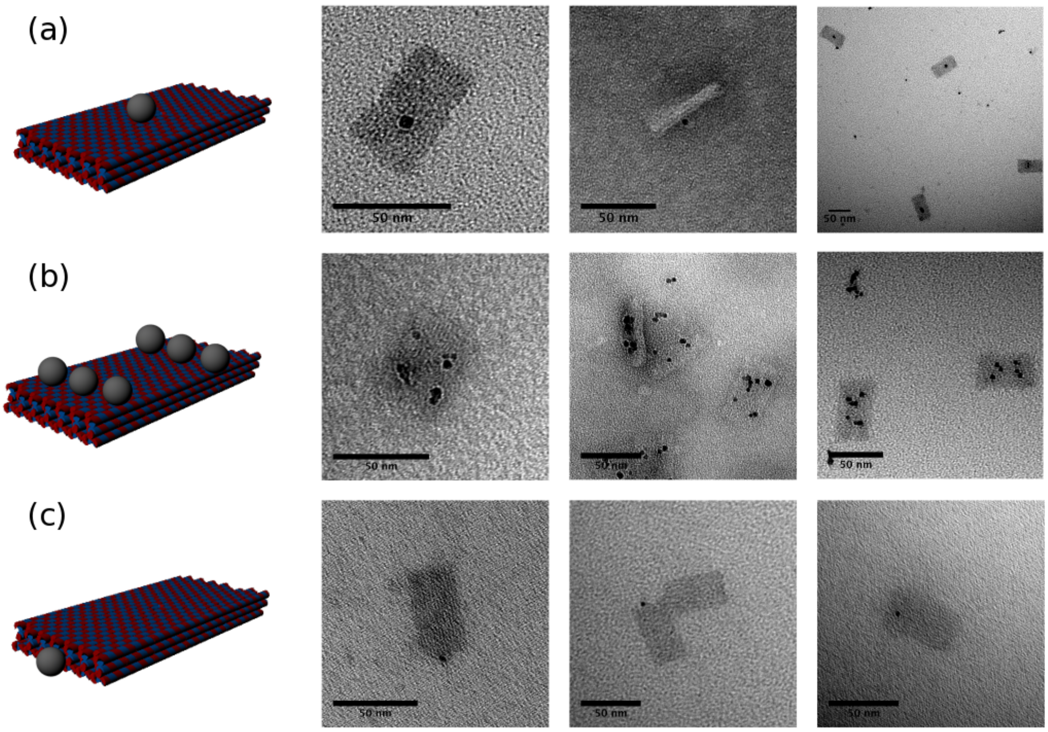

Figure 6.13: Transmission electron micrographs of 3 different DNA monolith designs functionalised with Pt NPs. **a)** monolith with single loading site in the centre of the structure **b)** monolith with 6 loading sites and **c)** monolith with single loading site on the side. All structures were purified with agarose gel electrophoresis prior to a TEM sample preparation with uranyl acetate. Side views in **a)** and (b) of monoliths confirm asymmetric localisation of Pt NPs.

The DNA Monolith structure was purified by agarose gel-electrophoresis (see materials and methods). The band corresponding to a monomer monolith was cut out and squeezed by the method described in the appendix A, resulting in 10-20 µl of 1 nM Origami. Next, a 1:20 excess of DNA coated Pt nanoparticles were mixed with DNA Origami in 0.5x TBE buffer with 11 mM $MgCl_2$. This mixture was left overnight on a shaker to allow for localisation of nanoparticles on the Origami.

The Origami/nanoparticle mixture was purified further by agarose gel electrophoresis and the corresponding fluorescent band was visualised in a gel scanner. The origami band was extracted for TEM visualization and FCS diffusion experiments. Figure 6.13 shows representative TEM micrographs of purified Pt NP-decorated DNA structures for three different configurations.

6.5 Decoration of DNA structures with catalase

Catalase from bovine liver (Sigma Aldrich) catalyses the decomposition of hydrogen peroxide in living tissue. It is a tetramer of four polypeptide chains, each over 500 amino acids long, with a total molecular weight of 250 kDa. It contains four heme groups (containing iron), which allow the enzyme to react with H_2O_2. Catalase is also an enzymatic nanomotor and its increased diffusion in the presence of H_2O_2 has been reported in [44, 45].

Figure 6.14 summarises relevant biochemical properties of the enzyme. Using the molecular visualization software *pyMol*, we can access the crystallographic data of bovine liver catalase and study the accessible surface functional groups (shown in Figure 6.14 (b)). Available lysine and cysteine residues can serve for cross-linking chemistry with modified oligonucleotides. An SDS PAGE gel in Figure 6.14 shows the purity of the lyophilised catalase protein used in these experiments. Finally, using dynamic light scattering, an average hydrodynamic radius of $5 \pm 1.6\,\text{nm}$ was measured.

In this section 4 types of cargoes are considered and conjugated to catalase, namely, rhodamine dye, streptavidin, fluorescent DNA (with complementary strands of different lengths) and the DNA monolith (illustrated in Figure 6.15). First, the conjugation steps and confirmation of successful binding are described. Then,

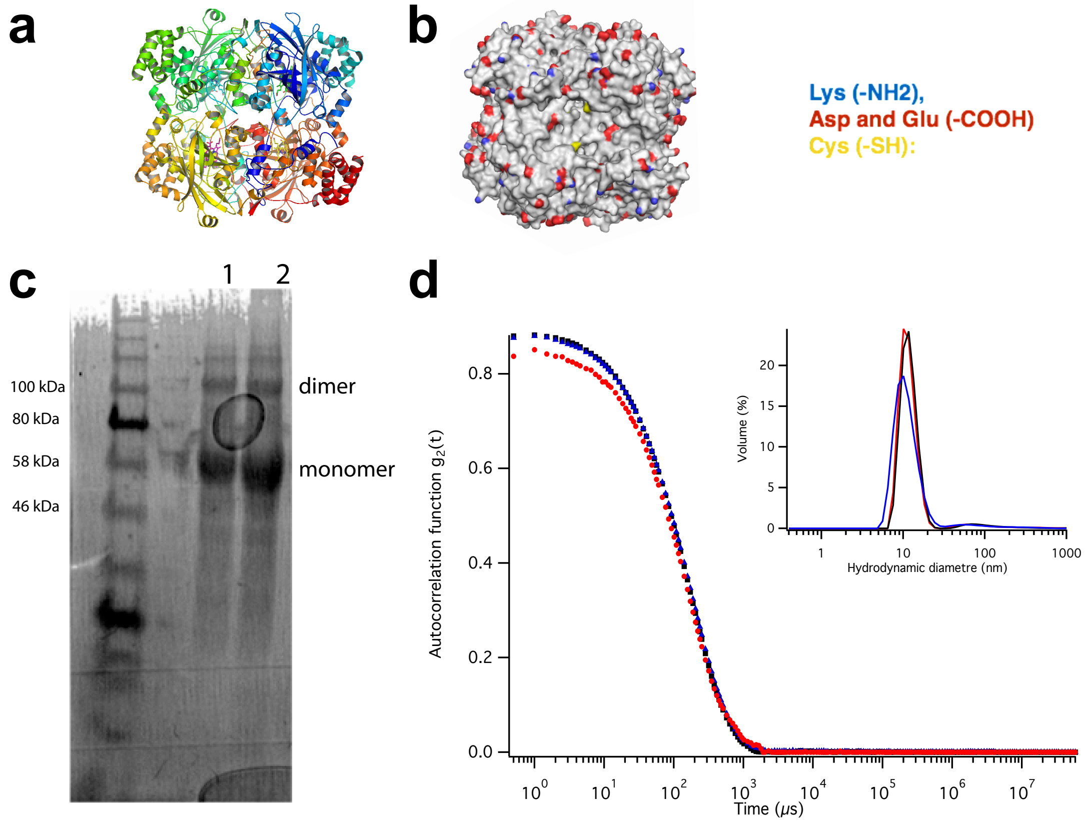

Figure 6.14: *Physico-chemical properties of catalase from bovine liver* **a)** Crystallographic data for the tetramer of bovine liver catalase (PDB ID: 1TGU) extracted from the Protein Data Bank. 4 heme groups are displayed. **b)** Only surface functional groups are displayed. **c)** SDS non reducing gel 4%-12% bis-tris glycine where, lane 1 is reconstituted protein in PBS buffer and lane 2 is after filtering. Monomer and dimer bands are shown after Coomassie staining. **d)** Dynamic Light Scattering (see section 3.2) of 1 mg/mL catalase in PBS. Average size distribution yields a hydrodynamic radius of $(5 \pm 1.6\,\mathrm{nm})$

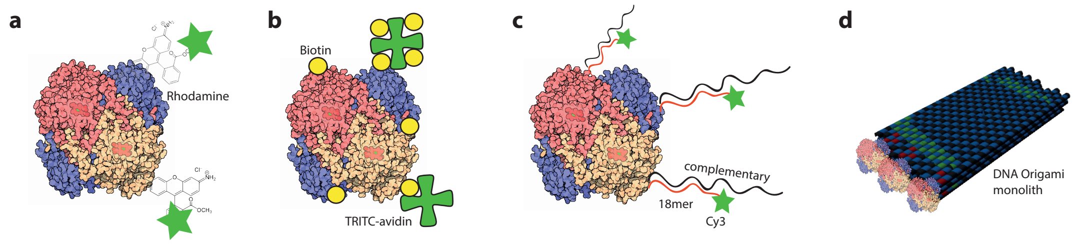

Figure 6.15: **a)** Catalase labelled with NHS-Rhodamine. **b)** Catalase conjugated to biotin and TRITC-avidin as fluorescent cargo. **c)** Catalase conjugated to a thiolated oligonucleotide with Cy3 and complementary strand as cargo. **d)** Catalase conjugated with thiolated oligonucleotide localised on fluorescent DNA origami monolith. Catalase illustration adapted from [208]

the changes in diffusion upon addition of H_2O_2 are measured with fluorescence correlation spectroscopy.

6.5.1 Bioconjugation of enzymes with DNA

There are multiple cross-linking strategies to bind oligonucleotides onto proteins, which are summarised in table 6.3.

Table 6.3: Protein/Oligonucleotide cross-linking strategies

Cross-linker	Protein functional group	DNA functional group
1. Biotin-streptavidin	Streptavidin conjugation	Biotin-oligo
2. Click-chemistry	Azide activated lysines (NHS-ester)	DBCO-oligo
3. sulfo-SMCC	Lysines (-NH_2)	Thiol-oligo
4. sulfo-SMCC	Cysteines (-SH)	Amine-oligo

In this work, the heterobifunctional cross-linker sulfo-SMCC (options 3 and 4) was used to address the lysine residues (-NH_2) of the protein to bind thiolated oligonucleotides (scheme (a) in Figure 6.16). Alternatively, the same cross-linker can be used to address the cysteine (-SH) residues of the protein, while using aminated oligonucleotides (scheme (b) in Figure 6.16). In both cases a thioether bond (C-S-C) forms between the maleimide group and the thiol [209].

Method b) only works if there are accessible cysteines on catalase. The Protein Data Bank (PDB) crystallographic analysis in Figure 6.14 (a) shows that there are at least 4 free cysteines. This was confirmed for the catalase used in this work by using Ellman's reagent (5,5'-Dithiobis(2-nitrobenzoic acid)) [210], a colourimetric method to quantify free sulfhydryls. A calibration with known concentrations of DTT allowed a direct quantification of free cysteines on catalase, indicating the availability of free cysteines to carry out the cross-linking chemistry.

Maleimide activation of catalase

Following the scheme in Figure 6.16 (a), $5\,\mathrm{mg\,mL^{-1}}$ solution of catalase was prepared in PBS buffer (corresponding to $\approx 20\,\mathrm{\mu M}$). 2 mg of sulfo-SMCC was dissolved in $200\,\mathrm{\mu l}$ MilliQ water and mixed while heating the sample in hot water for faster dissolution. $10\,\mathrm{\mu l}$ of this mixture was quickly added to 1 mL of protein solution

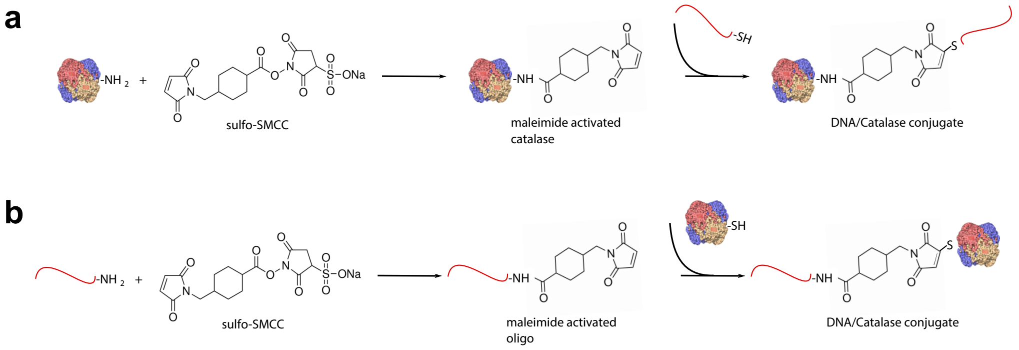

Figure 6.16: a) Cross-linking scheme for conjugating catalase with sulfo-SMCC to produce a maleimide-activated catalase. After excess non-reacted crosslinker and by-products are removed, the maleimide-activated catalase is reacted with oligonucleotides having sulfhydryl groups. **b)** Cross-linking scheme for conjugating aminated oligonucleotides with sulfo-SMCC to produce a maleimide-activated oligonucleotide. This is then reacted with catalase having reduced cysteines.

and left to react for 30 min at room temperature. A control reaction was prepared in which no sulfo-SMCC was added. In the meantime, thiolated oligonucleotides were mixed with TCEP (final concentration of 100 µM) to break disulfide bonds for at least 15 min. BioSpin columns (BioRad) were used to remove TCEP from the DNA/TCEP mixture and unreacted sulfo-SMCC from the conjugation solution. 50 µl of activated catalase was then mixed with 20 µl of 100 µM oligonucleotides in a total volume of 100 µl. The conjugation was left on a stirring plate overnight.

To confirm that the conjugation worked, an equimolar amount of Cy3 fluorescent complementary strand was mixed with the protein-DNA solution and with a control that had not been subjected to maleimide activation. A native 8% tris-glycine gel was run, visualised in the Cy3 channel and further stained with coomassie blue. Co-localisation of fluorescence and protein confirmed successful conjugation of proteins as shown in Figure 6.17 (a).

Maleimide activation of oligonucleotides

Following the scheme in Figure 6.16 (b), 1 mg mL^{-1} solution of catalase was prepared in PBS buffer (corresponding to $\approx$ 4 µM). 2 mg of sulfo-SMCC was dissolved in 200 µl MilliQ water and mixed while heating the sample in hot water for faster dissolution. 10 µl of this mixture were quickly added to 100 µl of aminated DNA solution at 20 µM and left to react for 30 min at room temperature. A control reaction was prepared where no sulfo-SMCC was added. In the meantime, catalase solution was mixed with TCEP (final concentration of 100 µM) to break disulfide bonds for at least 15 min. BioSpin columns (BioRad) were used to remove TCEP from the catalase/TCEP mixture and unreacted sulfo-SMCC from the conjugation solution. 50 µl of activated DNA were then mixed with 50 µl of catalase in a total volume of 100 µl. The conjugation was left on a stirring plate overnight.

An equimolar amount of Cy3 fluorescent complementary strand was mixed with the protein-DNA solution and with a control that had not been subjected to maleimide activation. A native 8% tris glycine gel in Fig 6.17 (b) shows successful conjugation of proteins following this strategy.

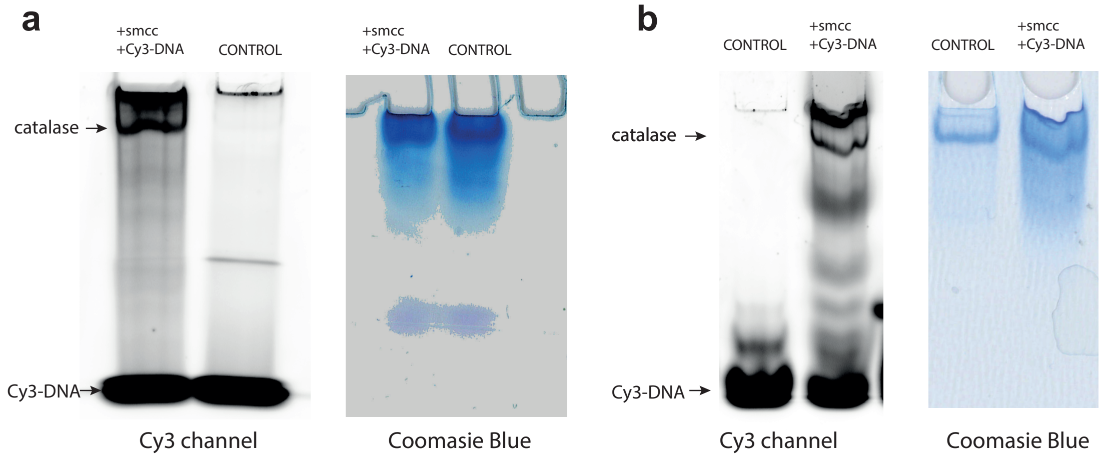

Figure 6.17: 8% Tris-glycine native gel showing co-localisation of fluorescent Cy3 strand and protein for maleimide activated catalase **a)** and maleimide activated oligonucleotides **b)** The control lane corresponds to catalase that has not undergone cross-linking chemistry. Co-localisation of fluorescence and protein (coomassie blue) indicates successful conjugation.

Bioconjugation of catalase with a fluorescent oligonucleotide

Catalase was cross-linked to an oligonucleotide (18mer) functionalised with Cyanine-3 and a thiol group on its 5' and 3' ends respectively. Maleimide activation of catalase was first performed using sulfo-SMCC following the protocol described in section 6.5.1. A SDS-PAGE gel shown in Figure 6.18 confirmed functionalisation of catalase, with a fluorescent band corresponding to the catalase monomer, also seen after coomassie blue staining.

After the bioconjugation reaction, the sample was purified from excess Cy3-oligonucleotides using desalting columns. This step is crucial to guarantee a single-species diffusion in FCS measurements. Best purification results were obtained with Illustra MicroSpin G-25 Columns (GE Healthcare). Even though there is a non-negligible amount of residual DNA, the SDS gel in Figure 6.18 b shows a 50% decrease in relative residual DNA concentration. To improve protein purification further, excess DNA was removed by 10 rounds of spin gel filtration (Millipore Amicon 100 kDa Ultra Centrifugal Filter Units). This yielded no observable residual DNA as marked by the red arrow in Figure 6.18 c.

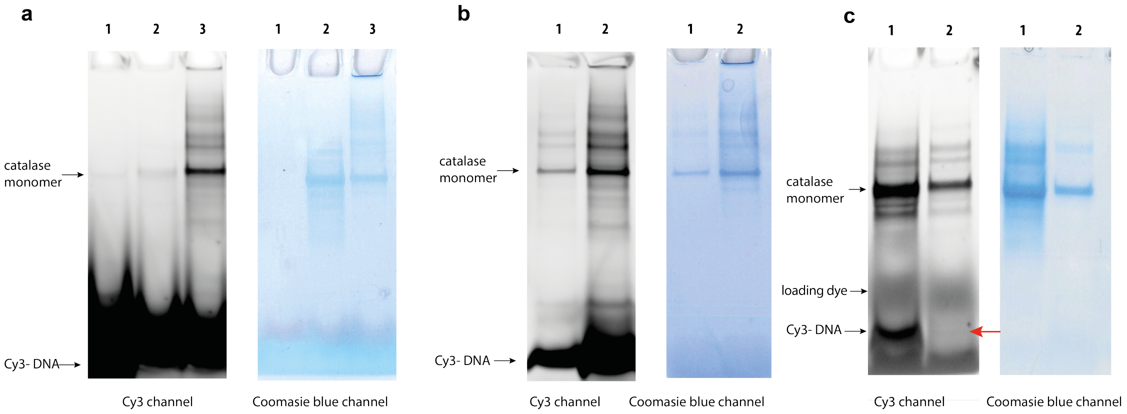

Figure 6.18: **a)** SDS-PAGE gels observed in Cy3 channel (left) and after coomassie protein staining (right) of (1) Cy3 oligonucleotide (2) control mixture of catalase and cy3 (no crosslinking) (3) catalase and Cy3 after crosslinking with sulfo-SMCC. **b)** (1) catalase-DNA crosslinked sample purified with size exclusion chromatography and (2) unpurified sample. **c)** (1) unpurified crosslinked catalase-DNA (2) purified 10 times with Amicon centrifugal filter unit (100kDa). The red arrow indicates the absence of DNA.

Strands with complementary sequences to the Cy3 strand on the catalase were hybridised to produce two types of cargoes (listed in table 6.4): a short strand (18 mer) and a long strand (60mer).

6.5.2 Bioconjugation of enzymes with streptavidin

ExtrAvidin-TRITC (Sigma Aldrich) is a variant form of streptavidin conjugated to tetramethylrhodamine isothiocyanate (TRITC), with a molecular weight of 67 kDa (approximately the size of a catalase monomer). To bind it as a cargo, catalase was first conjugated to biotin by addressing the free lysines with NHS-biotin esters.

Catalase was dissolved in PBS to a concentration of 5 mg/mL (20.8 µM). A 10 mM solution of NHS-biotin was prepared by dissolving 2 mg NHS-biotin in 590 µL of DMSO organic solvent. A volume of 31 µL of 10 m M NHS-biotin was added to 1 mL of catalase solution (15 fold biotin to protein molar excess). The samples were vortexed and incubated on ice for 2 hours in the dark. Unbound biotin was removed by using a NAP-5 desalting column (packed with Sephadex G-25, illustra, GE Healthcare).

To confirm biotynilation of catalase, the conjugate was mixed with streptavidinated beads (1 µm, Dynabeads MyOne Streptavidin C1, Thermo Fisher Scientific), and collected using a magnet. 30 µl of Dynabeads ($10\,\mathrm{mg\,mL^{-1}}$) were mixed with (10 µl) catalase conjugate (1 µM). The concentration of the catalase in solution was measured by UV-Vis spectroscopy. After incubation with streptavidinated beads for 30min and collected with a magnet, the concentration of protein in the supernatant reduced significantly, as shown in Figure 6.19. A control measurement with non-biotinylated catalase did not show a significant change in concentration after incubation with beads. Therefore, this experiment confirmed successful biotinylation of catalase.

Fluorescent streptavidin-catalase complexes were formed prior to FCS diffusion measurements, which are described in section 6.6.4. The modified catalase was

Table 6.4: List of strands that bind to catalysts and fluorophores (from Biomers Gmbh)

DNA strand name	Sequence	Description
Cy3-NH_2	5′-SH-AAGACGAATATTTAAGAA-3′	oligo for cystein binding
Cy3-SH	5′-Cy3-AAGACGAATATTTAAGAA-SH-3′	oligo for lysine binding
short cargo (18mer)	5′-TTCTTAAATATTCGTCTT-3′	complementary to catalase
long cargo (60mer)	5′-TTCTTAAATATTCGTCTT-42xT-3′	complementary to catalase

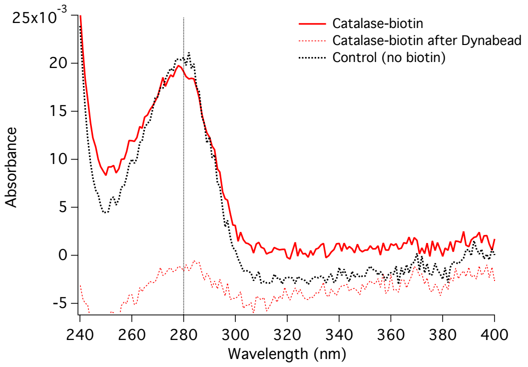

Figure 6.19: UV-Vis spectrum of the remainder of catalase solution after binding to streptavidinated magnetic beads. A reduction in concentration was measured for biotinylated catalase. No reduction in concentration was measured for non-conjugated catalase.

mixed with fluorescent streptavidin at various catalase:streptavidin molecular ratios of 1:1, 2:1, 3:1 and 4:1. To prevent multimer formation of catalase to streptavidin, free biotin was added to maintain total molecular ratio between streptavidin and biotin species (either in the form of free biotin or biotin-conjugated catalase) of 1:4. This is because streptavidin contains 4 binding sites for biotin.

The fraction of catalase bound to streptavidin vs. free streptavidin, can be determined by fitting the FCS autocorrelation curve to a two species model.

$$\begin{aligned} G(\tau_i) = \quad & \frac{F_1}{<N>}\left(\left(1+\frac{\tau}{\tau_1}\right)^{-1}\cdot\left(1+\frac{\tau}{SP^2\tau_1}\right)^{-1/2}\right) \\ & +\frac{(1-F_1)}{<N>}\left(\left(1+\frac{\tau}{\tau_2}\right)^{-1}\cdot\left(1+\frac{\tau}{SP^2\tau_2}\right)^{-1/2}\right) \end{aligned}$$

where τ_1, τ_2 are the diffusion times of the first species, second species, respectively and F is the fraction of the first species.

The diffusion time for species 1 (free streptavidin) was obtained from a mixture of biotin/streptavidin and that for species 2 (biotinylated catalase-streptavidin) was obtained from a mixture of catalase and streptavidin in a 10:1 molecular ratio (assuming all streptavidin bound). Figure 6.20 a shows FCS autocorrelation functions for solutions with different catalase to streptavidin ratios. By increasing this ratio, longer diffusion times are observed (autocorrelation curves shift to the right), which indicates the formation of more bound species.

The single-species fit used to determine the diffusion times for bare streptavidin (0:1 ratio in green) and mostly catalase-streptavidin conjugate (10:1 in black), resulted in diffusion times of 1.55 and 2.1 ms respectively. Using these values as fixed τ_1 and τ_2, a two-species fitting function was used to determine the value of F_1, namely the ratio of streptavidin to the total fluorescent particles (streptavidin+catalase-streptavidin complex). The results are shown in Figure 6.20b.

Assuming the binding of streptavidin to biotinylated catalase follows simple receptor-ligand kinetics ($[strep]+[cat] <=> [strep-cat]$), with dissociation constant K_d, the fraction of free streptavidin (F_1) follows a stoichiometric hyperbola $F_1 = \frac{[strep]}{[strep]+[strep-cat]} = \frac{K_d}{[cat]+K_d}$ (shown in Figure 6.20). The conclusion from this analysis is that at a 10:1 catalase:streptavidin molecular ratio, most of streptavidin is bound to biotinylated catalase. Therefore, FCS experiments can be done in this regime, assuming single-species diffusion.

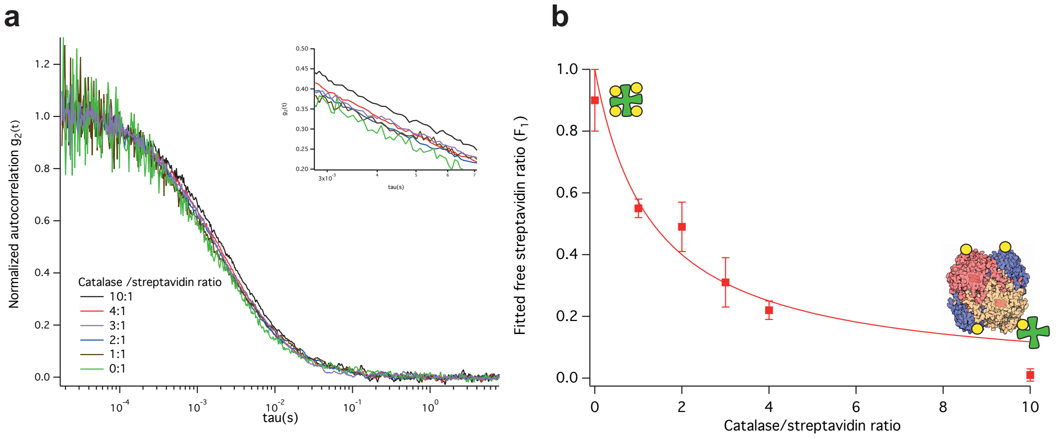

Figure 6.20: **a)** FCS normalised autocorrelation curves for catalase-streptavidin complexes mixed at shown ratios. At a fixed concentration of 2 nM streptavidin, increasing catalase concentration shifts autocorrelations curves to the right. **b)**Fraction of free streptavidin obtained by fitting a two-species autocorrelation function to data in a), while maintaining the diffusion times of free and bound streptavidin constant. The data has been fitted to a stoichiometric hyperbola as described in the text.

6.5.3 Immobilisation of DNA-conjugated catalase on DNA monolith

The assembly of catalase on DNA origami consisted in the hybridisation of DNA-conjugated catalase with the corresponding complementary strands that are displayed on the short edge of the DNA monolith (3 binding sites with 3 handles per site). To achieve this, first DNA-enzyme conjugation was done following the protocol in section 6.5.1 and purified with ultracentrifugation filters (Amicon, 100kDa). Then the assembled monolith structure was purified by PEG precipitation, mixed with the enzyme and incubated for one hour.

The as-prepared conjugated catalase was mixed with purified origami with an enzyme-to-origami molecular ratio of 3 in 0.5 x TBE buffer (11 mM $MgCl_2$) to achieve a final concentration of origami of 5 nM. The reaction mixture was annealed using a thermocycler with a temperature gradient from 37 °C to 10 °C (2 min per degree decrease).

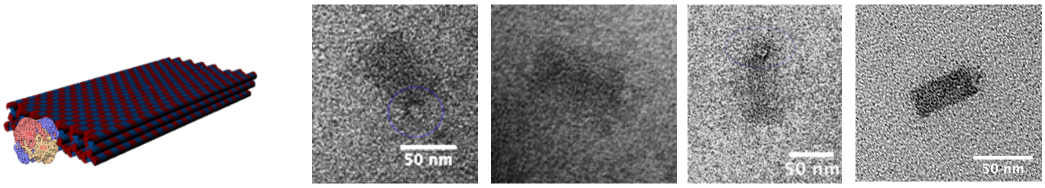

Figure 6.21: Transmission electron micrographs of DNA monolith with handles on the side functionalised with DNA-conjugated catalase.

The enzyme-assembled DNA monolith structures were visualised using Transmission Electron Microscopy and Atomic Force Microscopy. TEM micrographs in Figure 6.21 show catalase bound on DNA Origami monolith structures. Catalase (250 kDa, 5 nm radius) tetramer is distinguishable after uranyl staining.

Characterisation with AFM (Cypher S, Asylum research) was done after depositing 5 µl of 5 nM origami sample onto a freshly cleaved mica surface with an addition of 50 µl 1× TAE-Mg^{2+} 4 mM $NiCl_2$(pH 8) imaging buffer to enhance the adsorption of the DNA nanostructures on the mica surface. Another 50 µl was added on the cantilever in the liquid cell.

A low enzyme-to-origami ratio was used to obtain images not contaminated by background protein. As shown in Figure 6.22, the monolith DNA Origami and catalase are clearly identified under the AFM microscope. Bright spots indicate the presence of an assembled structure of approximately 10 nm (height profiles are shown in Figure 6.22 b) localised on one short side of the monolith, which can be identified as bound catalase. In order to guarantee a single-species FCS measurement by having most origami bound to catalase, FCS experiments were performed with a 10-fold excess of enzyme.

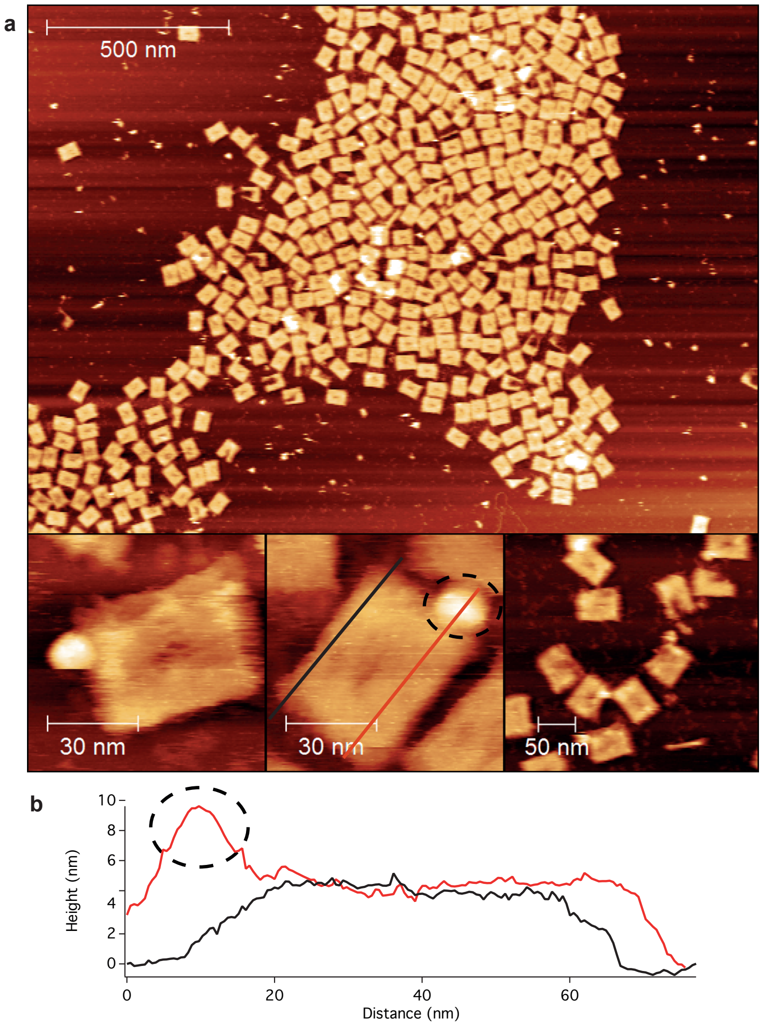

Figure 6.22: *Atomic Force Microscopy visualisation of the assembly of catalase on a DNA Origami monolith.* **a)**The assembled enzymes (≈ 10 nm) on the short side of the structure are higher than surrounding surface of the monolith, resulting in bright spots (increased height). **b)** Height profile along the red and black lines shown in a). The dashed circle represents catalase.

6.6 Diffusion measurements using Fluorescence Correlation Spectroscopy

The FCS experimental setup described in section 3.3 was used to measure the diffusion of DNA-based nanomotors. In this section experimental measurements are then reported for Pt and enzyme-based DNA nanostructures that were presented in sections 6.4 and 6.5.

6.6.1 Diffusion of Pt NP functionalised DNA structures

Pt NP bound to fluorescent DNA

To investigate the motility of 5 nm Pt NP functionalised with DNA, a complementary fluorescent strand was added to particles prepared by the protocol in section 6.4.2. Excess oligonucleotides were purified with 100 kDa cutoff centrifugal filter units (Amicon Ultra, Millipore). FCS measurements of metallic particles can pose a problem if we consider the scattering of nanoparticles. However, at low concentrations and with dichroic mirrors blocking any excitation light, only the contribution coming from emitted fluorescence intensity is detected at the photodiodes.

Figure 6.23 a shows FCS autocorrelation functions measured for Cy3 oligonucleotides and Pt-NP hybridised to Cy3 oligonucleotides. Figure 6.23 b shows increased diffusion in the presence of hydrogen peroxide. This effect changes with time as it can be seen in Figure 6.23 c. For different concentrations of H_2O_2 the diffusion time τ rapidly changes within minutes until a plateau is reached. Noticeably, addition of 30%(v/v) H_2O_2 results in diffusion times equivalent to those of the bare Cy3 strand. This leads to another possible cause for this effect, namely the release of thiolated-strands from Pt NP upon addition of high concentrations of H_2O_2. This would explain the quick reduction of diffusion time to values equivalent of freely diffusing DNA strand measured in Figure 6.23 c. It is known that the metal-sulphur bond is significantly compromised by adsorption of oxygen on its surface [211]. Large concentrations of an oxidising agent like H_2O_2 may lead to the break of the Pt-sulphur bond, which is weaker and more fragile than Au-sulphur bonds [212]. This effect is unlikely to happen for sulphur-carbon bonds (e.g.

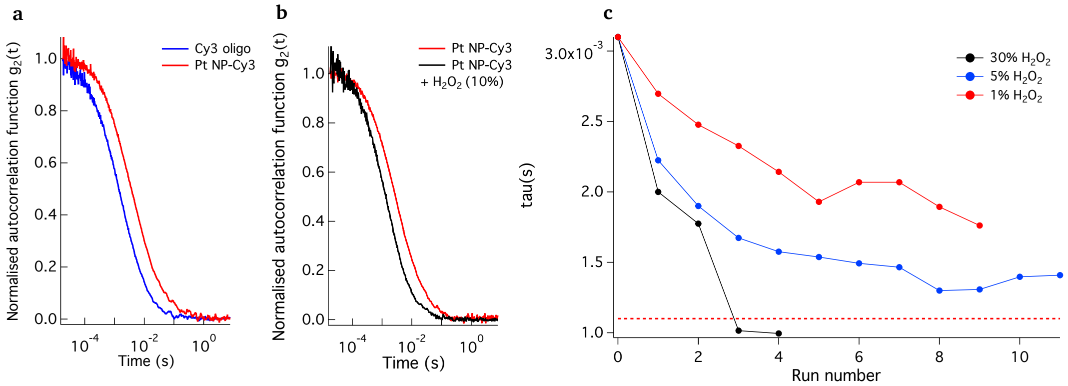

Figure 6.23: a) Autocorrelation function of Pt NP bound to a thiolated oligonucleotide hybridised to its complementary with Cy3. **b)** Autocorrelation functions showing more than a twofold increase in diffusion for Pt NP in the presence of H_2O_2. **c)** Change in diffusion as a function of time. Each run corresponds to 1 min and have been measured consecutively. The red line indicates the diffusion time of a single Cy3-strand.

thioether bond formed between maleimide and thiol groups), which are covalent and therefore much stronger, but reversible.

Another concern with Pt NP is thiol poisoning. *Catalyst poisoning* refers to the partial or total deactivation of a catalyst due to its exposure to certain compounds. Pt surface is highly susceptible to poisoning by sulphur-containing molecules, such as thiol groups. Sulfur is able to chemisorb onto the active sites of the catalyst and inhibit them. For example, *thiol poisoning* has been observed in Pt-based self-propelled catalytic microjets exposed to cysteine molecules in solution [213]. In the case of Pt NP binding to thiolated DNA, unbound oligonucleotides are removed from the solution using centrifugal filters. This also removes any free unreacted sulfhydryl group from the solution. The observation of oxygen bubbles after addition of H_2O_2 to the DNA modified Pt NP shows that nanoparticles are catalytically active and thiol poisoning, if any, occurs at a low level in these experiments.

Pt NP bound to DNA origami monolith

DNA monolith structures were functionalised with Pt NP following the protocols described in section 6.4. The final purification step is shown in Figure 6.24 (a), where Origami with and without Pt NP have been purified. These were extracted from the agarose gel and directly transferred to the FCS setup. The usual concentration of

Origami at this stage was at the nM range. Hence, no further dilution was needed and diffusion measurements were taken for DNA structures and fluorescent staples, shown in Figure 6.24 (b). There is a clear distinction between fast diffusing staple oligonucleotides and slower diffusing Origami structures, characterised by longer diffusion times. Experiments with H_2O_2 did not result in a significant change in diffusion constant compared with control measurements in the buffer. In light of the results in section 6.6.1, the lack of a significant enhanced diffusion could be due to the gradual loss of Pt NPs from the DNA structure in the presence of H_2O_2. An alternative explanation could be that the chosen monolith geometry cannot sustain a localised product gradient and therefore cannot self-propel by diffusiophoresis.

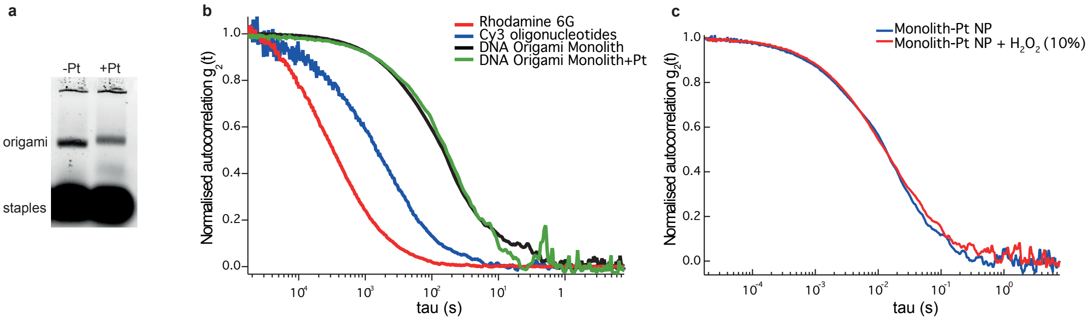

Figure 6.24: **a)** Agarose gel electrophoresis of DNA Origami Monolith without and with Pt NPs. **b)** FCS autocorrelation functions from bands extracted from gel in **a)**. The diffusion for staples and monolith can be extracted from fits to $g_2(t)$ which for 5 measurements yield, D_{staple} $=70 \pm 3\,\mu\mathrm{m}^2\,\mathrm{s}^{-1}$ and $D_{monolith}$ $=8.5 \pm 1\,\mu\mathrm{m}^2\,\mathrm{s}^{-1}$, respectively. **c)** Autocorrelation function of DNA Origami/Pt In the presence and absence of H_2O_2

.

6.6.2 Diffusion measurement of catalase

The change in the diffusion of catalase in the presence of H_2O_2 was measured by two different methods: fluorescence correlation spectroscopy (FCS) and nanoimpact voltammetry. Both methods are described in chapter 3.

For the FCS measurement, catalase from bovine liver (Sigma Aldrich) was dissolved in filtered PBS buffer at a concentration of $1\,\mathrm{mg\,mL}^{-1}$. NHS-Rhodamine, an amine-reactive dye was used to label catalase in 10:1 excess of dye (labelling protocol in appendix A.4). Labelling was performed at room temperature with gentle shaking for 2 hours. Gel filtration columns were used to purify the protein from the excess dye. After fluorescence labelling, catalase remained catalytically active.

A typical FCS experiment consists of mixing a 10 µL of twice the desired concentration of H_2O_2 together with 10 µL of labelled catalase at 1nM. Prior to performing the FCS experiment, these conditions were recreated in a cuvette to measure the change in concentration of H_2O_2 using UV-Vis absorption at 240 nm. After mixing 0.5 mM H_2O_2 within 2 min all H_2O_2 was consumed, as can be observed in Figure 6.25. This indicates the necessity of performing the FCS experiment immediately after addition of catalase.

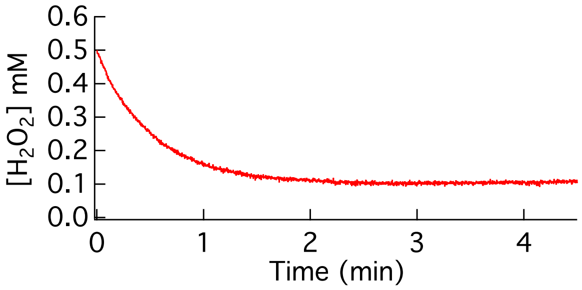

Figure 6.25: H_2O_2 decomposition of 0.5 mM mixed with 1 nM catalase, as recorded by UV-Vis spectroscopy (H_2O_2 extinction coefficient at 240 nm 43.6 $M^{-1}cm^{-1}$) reproducing the FCS experimental conditions. Within 2 min most of the H_2O_2 was consumed.

First, the experimental setup was calibrated with bare Rhodamine 6G (laser power 50 µW, $\lambda = 532$ nm). FCS measurements were done by mixing the enzyme solution in H_2O_2 at different concentrations. Each measurement was repeated 5 times to obtain the autocorrelation functions in Figure 6.26 (a) and the average diffusion time τ from data analysis. A comparison with the known diffusion coefficient of Rhodamine 6 G yields the results shown in Figure 6.26 (b). These indicate an increase in the diffusion coefficient of catalase of about 50% in the presence of fuel.

The change in diffusion of unmodified catalase was also characterised by nanoimpact voltammetry [4] (see section 3.5), which detected single-catalase collisions on the surface of a diamond ultramicroelectrode. In the present experiment a direct electron transfer between catalase and a boron-doped ultramicroelectrode results

---

[4] Work in collaboration with Dr. Luyun Jiang and Prof. John Foord.

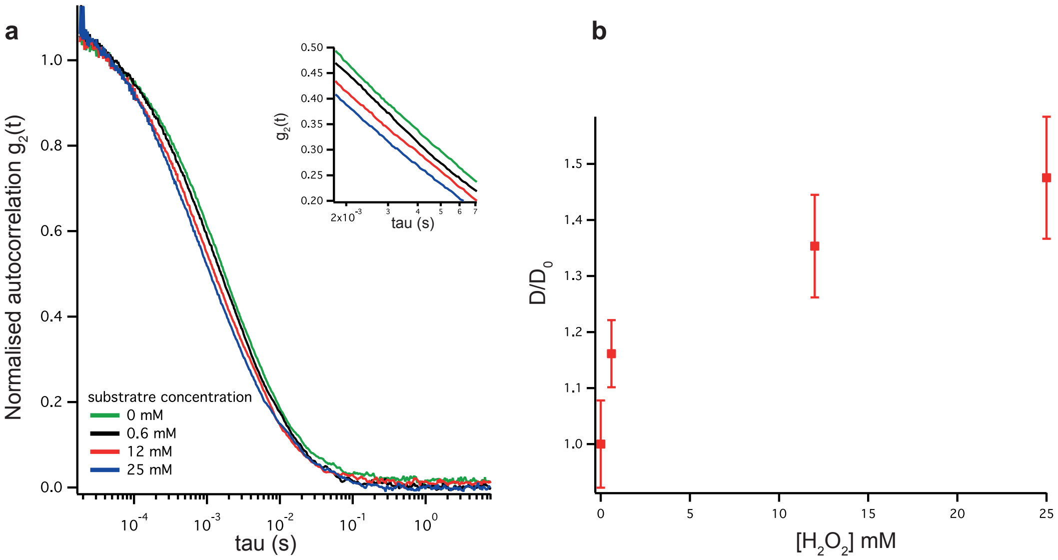

Figure 6.26: *FCS diffusion measurements of fluorescent catalase* **a)** Normalised autocorrelation $g_2(t)$ curves and diffusion coefficients of catalase in the presence of different H_2O_2. Zoom-in is shown in inset. **b)** Diffusion coefficients extracted by fitting $g_2(t)$ to a single-species model. Error bars show standard deviations from 5 independent measurements.

in characteristic current spikes as shown in Figure 6.27. The frequency of spikes is directly related to the diffusion of catalase.

We identified current spikes using a peakfinder algorithm (MATLAB, Mathworks). We observed an increase in number of spikes per unit time when hydrogen peroxide was added to a catalase solution. We measured an average spike count per 10 seconds of 3.8 (standard error of the mean 0.02) for 10 pM catalase and 8.6 (standard error of the mean 0.02) for 10 pM when 100 mM H_2O_2 was added. This corresponds to a change in the mean inter-spike time interval from 2.4 s to 1.1 s, in 10 pM catalase without and with H_2O_2 respectively (histogram and fitted exponential distribution are shown in Figure 6.27 (g-h)). This experiments suggests, in agreement with the FCS results, that addition of substrate results in an increase in diffusion of catalase.

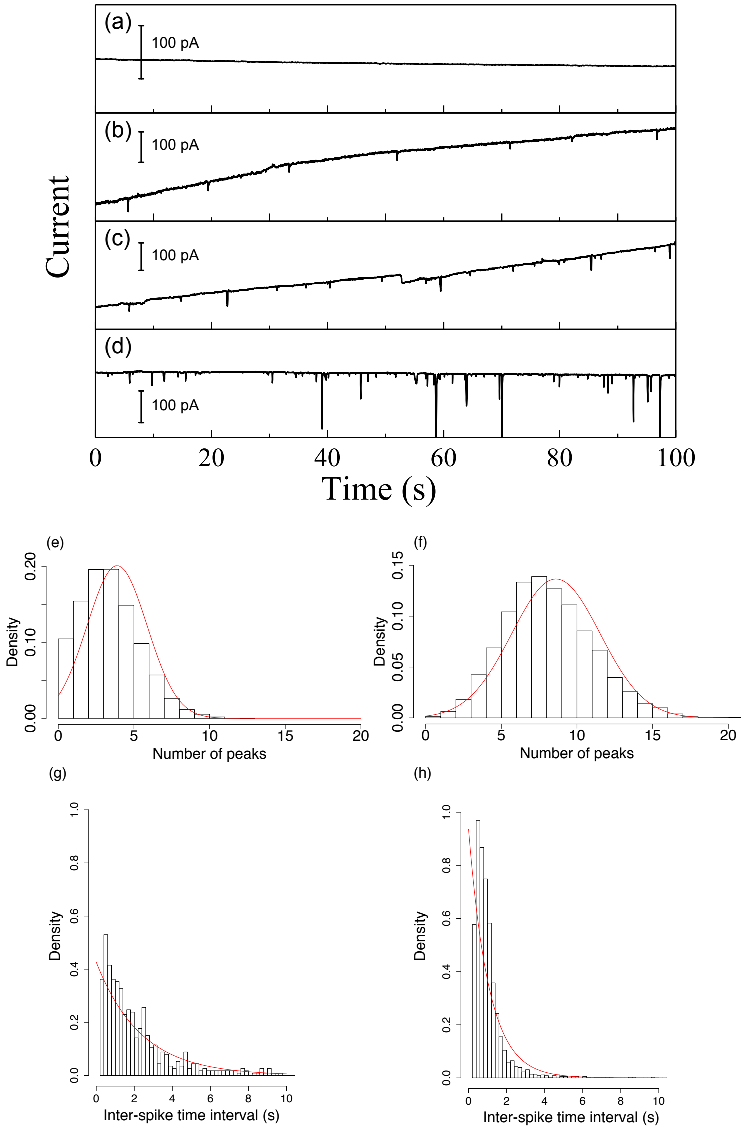

Figure 6.27: *Nanoimpact voltammetry of catalase on a diamond ultramicroelectrode* (a)-(d) Typical *i-t* curve at a boron-doped diamond ultramicroelectrode (BDD-ume) at -0.2 V in a solution containing **a)** 0.1 M PBS and **b)** 5 pM catalase; **c)**10 pM catalase; and **d)** 10 pM catalase mixed with 100 mM H_2O_2; (e)-(f) Histogram of detected number of spikes shows the average number of spikes per 10s, corresponding to a sample size of 1000 observations and 10000 replicates, randomly sampled over the duration of the experiment (2000 s). A fitted normal distribution yields an average spike count of 3.8 (standard error of the mean 0.02) for 10 pM catalase in **e)** and 8.6 (standard error of the mean 0.02) for 10 pM with H_2O_2 in **f)**. (g)-(h) Inter-spike interval histograms extracted by counting the number of inter-spike intervals falling in various time bins. Assuming collision events are independent of each other and follow a homogeneous Poisson distribution, the interspike interval is given by an exponential decay function e^{-rt}, with rate r= 0.42±0.01 s^{-1} and 0.93±0.02 s^{-1} for 10 pM catalase in the absence **g)** and presence of H_2O_2 **h)**. These rates correspond to a mean inter-spike time interval of 2.4 s and 1.1 s respectively.

6.6.3 Diffusion measurements of catalase functionalised with fluorescent DNA

First, FCS was used to measure the relative sizes of the conjugated enzymes. Figure 6.28 compares the diffusion of a reference dye (Rhodamine 6G), Cy3-DNA and catalase cross-linked with Cy3-DNA. Diffusion coefficients in Figure 6.28b were obtained by single-species fits to g_2 functions and by taking rhodamine as a reference. After conjugation with DNA, the diffusion coefficient of catalase reduced by 2/3, corresponding to an increase in hydrodynamic radius from 5 nm to 7.5 nm.

Then FCS was used to measure changes in diffusion in the presence of H_2O_2. A sample of catalase-DNA was prepared at 1 nM concentration, enough to give a detectable signal for a FCS measurement at a laser power of 50 µW. H_2O_2 mixtures were prepared at different concentrations and 10 µl was placed on a glass slide. 10 µl of catalase solution was added and recorded with a digital correlator for 30 s immediately afterwards. For high concentrations (>100 mM), the emergence of bubbles eventually disturbed the measurement.

Figure 6.29 a shows autocorrelations functions, indicating a shift towards faster diffusion, with increasing H_2O_2 concentrations. A single-species diffusion g_2 fitting function was used. The relative increase in diffusion of DNA functionalised catalase is shown in Figure 6.29 b. An increase of 50% in diffusion coefficient was observed. As control experiments, DNA was mixed with 10 mM H_2O_2 and no significant change was observed in its diffusion, as shown in Figure 6.30 a. This indicates that Cy3-DNA mixed with H_2O_2 does not contribute to shifts in autocorrelation functions. Similarly, the addition of unlabelled catalase to the previous solution did not result in an increase in diffusion (Figure 6.30 b). Also a control measurement was made of catalase-DNA before and 15 min after adding 1 mM H_2O_2 (6.31). First a shift toward faster diffusion was observed within 30 s of adding H_2O_2 and after 15 min a return to the original curve was measured. This is most likely due to the full consumption of H_2O_2. This control confirms that shifts in correlation functions are caused by catalysis of H_2O_2. In addition, short and long complementary strands were mixed with conjugated catalase at 10x excess. These strands acted

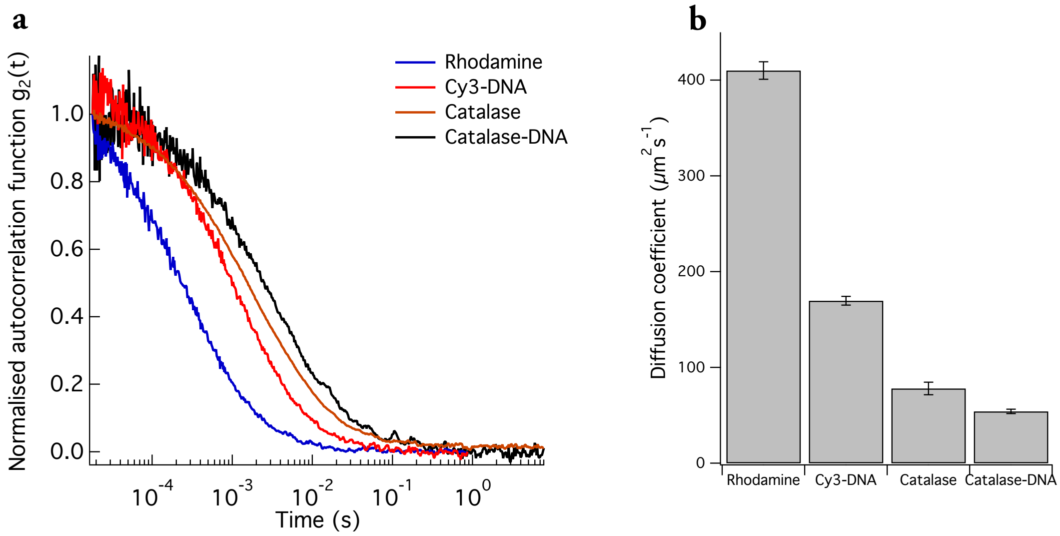

Figure 6.28: **a)** FCS normalised autocorrelation functions of reference dye rhodamine, 18mer functionalised with Cy3 and DNA crosslinked to catalase . Diffusion coefficients in **b)** are computed from fittings to g_2(t) functions. Error bars indicate standard deviations from three independent measurements.

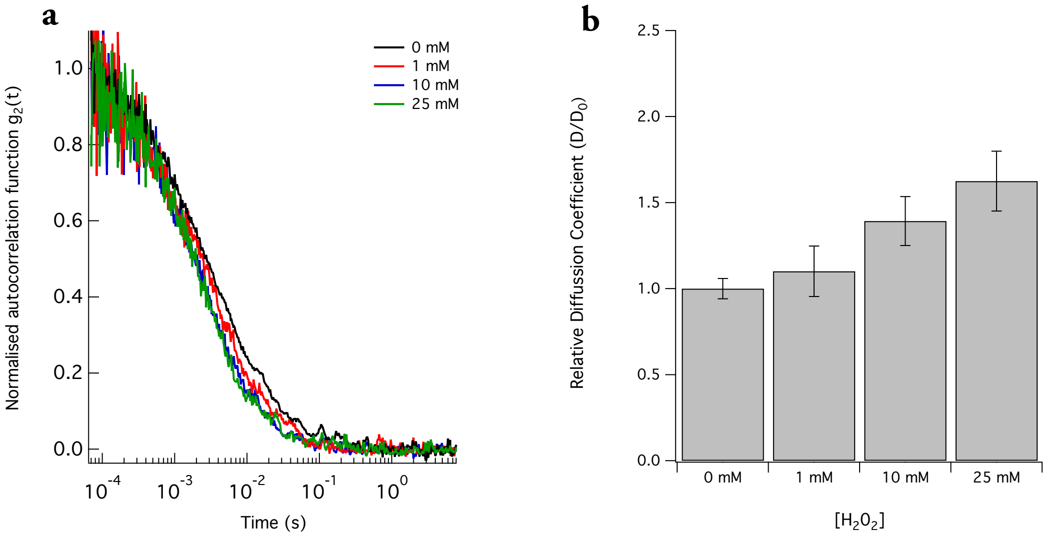

Figure 6.29: 4 **a)** FCS normalised autocorrelation functions of DNA functionalised catalase recorded for 30s after addition of 1 nM catalase to shown solvent-substrate concentrations. **b)** Relative diffusion coefficients of catalase obtained from fitting one-species diffusion model to $g_2(t)$ functions in a. Error bars indicate standard deviations from three independent measurements.

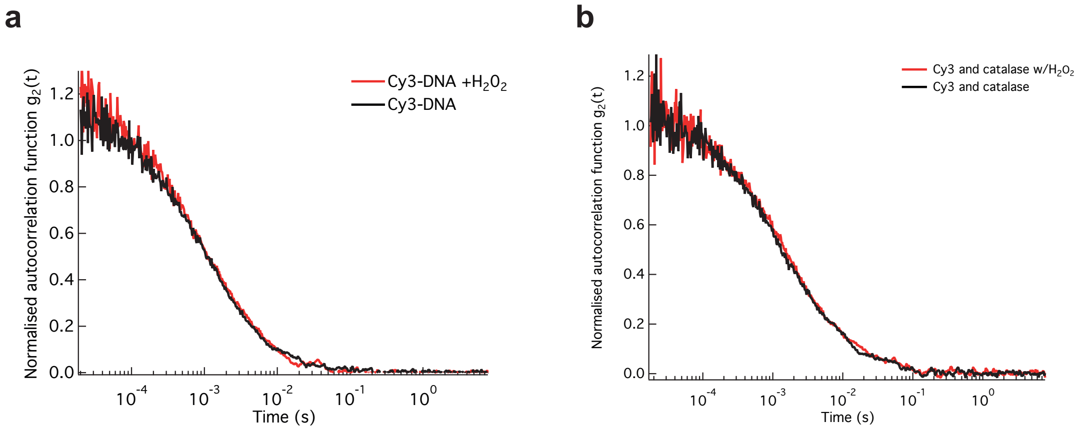

Figure 6.30: **a)** Control experiment of Cy3-DNA after addition of 10 mM H_2O_2. **b)** Control experiment of Cy3-DNA after addition of 10 mM H_2O_2 in the presence of unlabelled catalase.

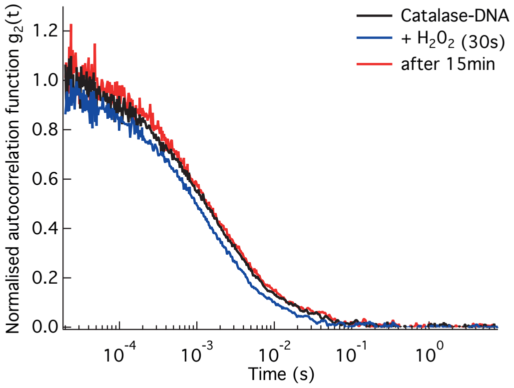

Figure 6.31: FCS measurement of catalase-dna sample after addition of 1 mM H_2O_2 and measured within 30 s and after 15 minutes.

as cargoes of 6 kDa and 18 kDa respectively. The unbound strands were not removed from the solution as they are not fluorescent and do contribute to the signal. Figures 6.32 and 6.33 show diffusion measurements of catalase bound to short and long cargoes, respectively. A maximum enhanced diffusion of $\frac{D}{D_0}$=1.4±0.2 was obtained for a short complementary cargo, which is similar to that obtained with only the fluorescent ssDNA. However,for the 60mer long strand a maximum enhanced diffusion of $\frac{D}{D_0}$=1.3±0.1 was measured. Together, these results suggest the possibility of using catalase to carry DNA as a cargo.

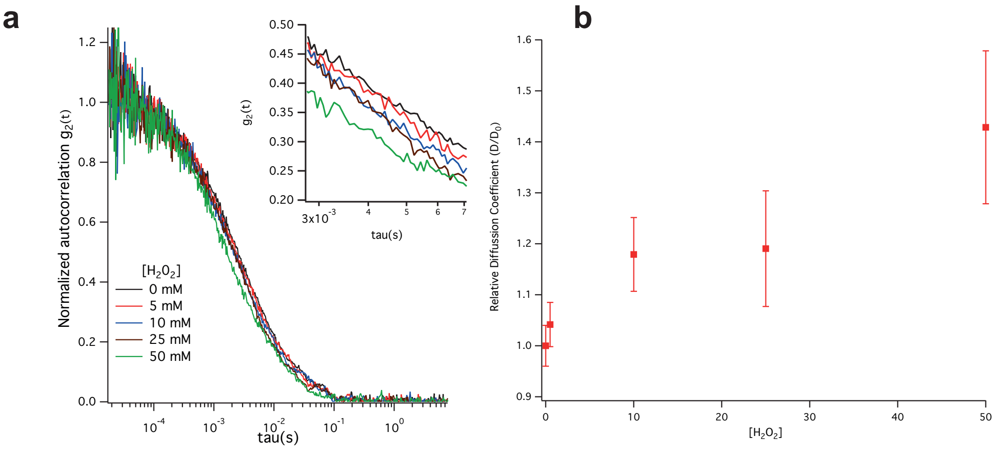

Figure 6.32: **(a)** FCS normalised autocorrelation functions of DNA functionalised catalase hybridised to a complementary 18mer. Intensity traces were recorded for 30s after addition of sample to shown solvent-substrate concentrations. **(b)** Relative diffusion coefficients of catalase-DNA-dsDNA obtained from fitting one-species diffusion model to $g_2(t)$ functions in a. Error bars indicate standard deviations from five independent measurements.

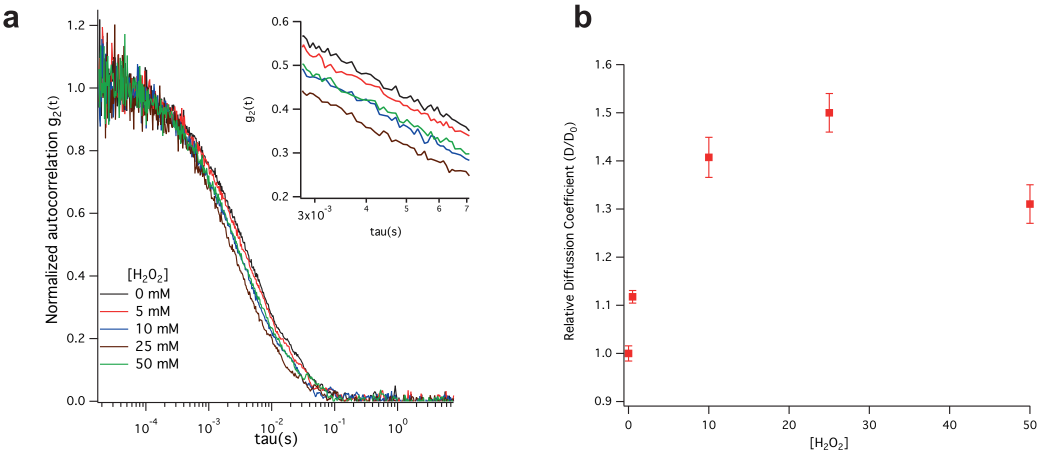

Figure 6.33: **a)** FCS normalised autocorrelation functions of DNA functionalised catalase hybridised to a complementary 60mer. Intensity traces were recorded for 30s after addition of sample to shown solvent-substrate concentrations. **b)** Relative diffusion coefficients of catalase-DNA-dsDNA obtained from fitting one-species diffusion model to $g_2(t)$ functions in a. Error bars indicate standard deviations from five independent measurements.

6.6.4 Diffusion measurements of biotinylated catalase bound to streptavidin

Biotinylated catalase was mixed in 10 fold excess with fluorescent streptavidin as described in section 6.5.2. The concentrations of catalase and streptavidin were measured in UV-Vis spectroscopy using extinction coefficients of $E_{280}^{1\%} = 36.5$ and 15.6 $(\mathrm{g}/100\mathrm{mL})^{-1}\mathrm{cm}^{-1}$ respectively. The sample was diluted in PBS buffer to reach 1 nM concentrations of catalase. FCS autocorrelation data was collected for 30 s at 0,1,10 and 25 mM H_2O_2 shown in Figure 6.34 a. A maximum relative change in diffusion of 20% was measured. A control sample with free streptavidin showed no enhanced diffusion. These results show that catalase is capable of acting as a nanomotor when bound to streptavidin as a cargo. Further, streptavidin can act as mediator and bind to other biotinylated cargoes.

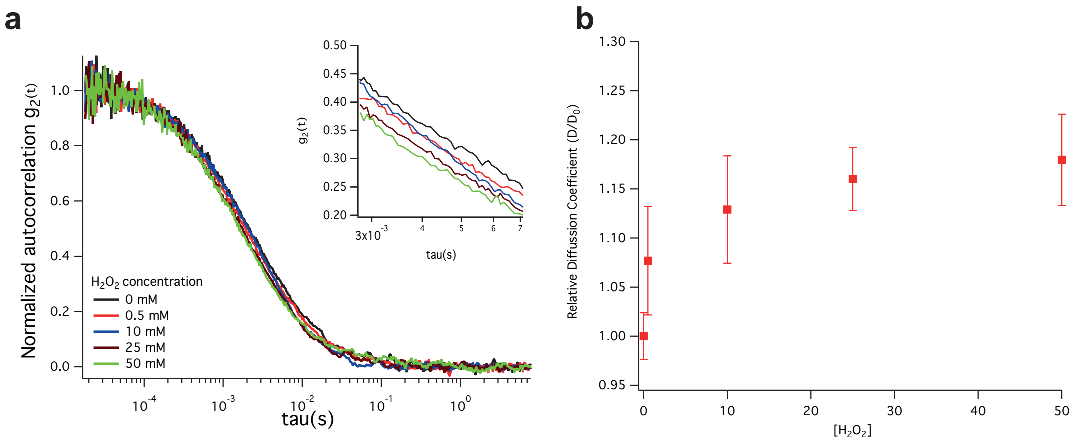

Figure 6.34: **a)** FCS normalised autocorrelation functions of biotin functionalised catalase bound to fluorescent streptavidin. Intensity traces were recorded for 30 s after addition of sample to shown solvent-substrate concentrations. **b)** Relative diffusion coefficients of catalase-streptavidin obtained from fitting one-species diffusion model to $g_2(t)$ functions in a. Error bars indicate standard deviations from five independent measurements.

6.6.5 FCS measurements of fluorescent DNA Origami

DNA Monolith and catalase conjugates were prepared as described in section 6.5.3. A 10:1 enzyme to origami ratio was used and the only fluorescent component was the DNA Origami monolith.

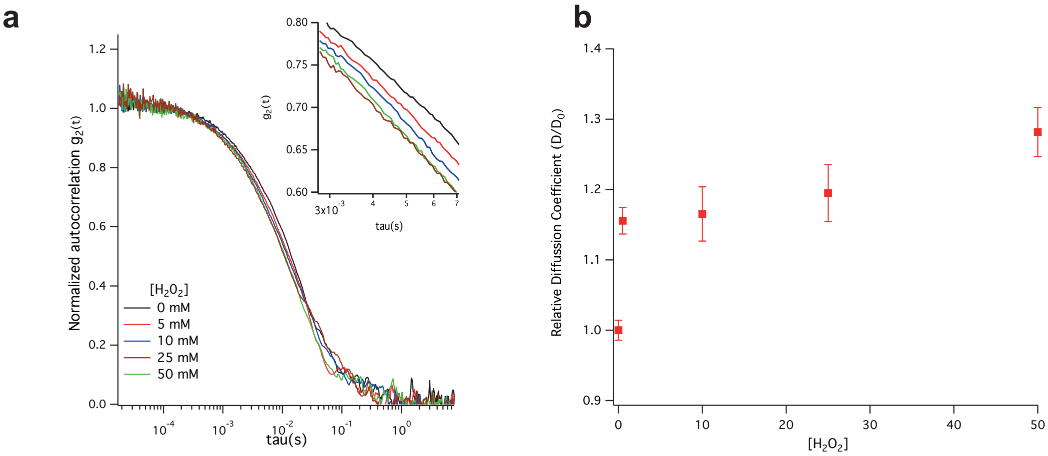

Figure 6.35: a) FCS normalised autocorrelation functions of fluorescent DNA Origami monolith functionalised with catalase. Intensity traces were recorded for 30s after addition of sample to shown solvent-substrate concentrations. **b)** Relative diffusion coefficients of catalase-monolith sample obtained from fitting one-species diffusion model to $g_2(t)$ functions in **a)**. Error bars indicate standard deviations from five independent measurements.

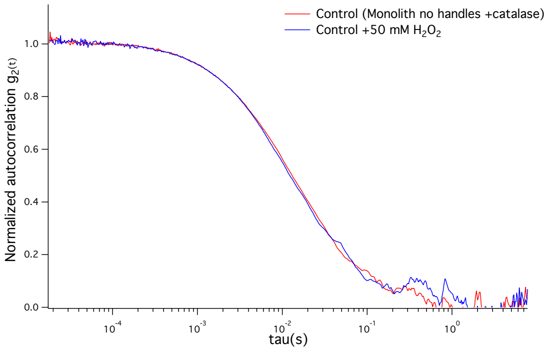

Figure 6.36: FCS normalised autocorrelation functions of fluorescent DNA Origami monolith physically mixed with catalase, before and after addition of 50 mM H_2O_2.

Figure 6.35 shows representative autocorrelation curves and the measured relative change in diffusion. A maximum enhanced diffusion of about 30% was observed in the presence of fuel. A control sample was prepared by physically mixing DNA Origami monolith with no side handles for protein localisation with catalase. Figure 6.36 shows the corresponding autocorrelation functions, which result in diffusion times of 13.6 ms and 13.8 ms in the absence and presence of 50 mM H_2O_2 respectively. Superposition of curves indicates a negligible shift in diffusion for this control measurement. The results above favour the hypothesis that catalase mediated decomposition of H_2O_2 is the cause of the observed enhanced diffusion.

6.6.6 Summary of diffusion measurements for various cargoes

Figure 6.37 shows the maximum relative increase in diffusion coefficient $\frac{D}{D_0}$ observed for cargoes of diverse molecular weight. The size of a cargo can contribute to two different effects on the nanomotor, namely an increased hydrodynamic drag and a change in the propulsive velocity. A hydrodynamic drag can hinder the formation of product gradient for self-diffusiophoretic particles and result in a smaller propulsive force. However it also reduces rotational diffusion, which results in increased diffusivity. From equation (2.15) we know that the velocity of a spherical Janus motor scales as $v \propto \frac{1}{R}$. This means that for a propeller moving at ballistic velocity v_0 the velocity of the cargo+propeller structure of size L would scale as $v \propto \frac{v_0 R}{L}$ (this is an estimate, as non-isotropic objects have a more complex dependency). Assuming that the catalase+cargo system follows a similar scaling law, the effect of a cargo of large molecular weight, and therefore larger hydrodynamic radius, contributes to a reduction in ballistic velocity in the presence of fuel. This means that larger cargoes will result in reduced enhanced diffusion [5]. However, the DNA monolith showed higher relative diffusion than expected, suggesting that other mechanisms might be at play. The location of the enzymes on the side of the structure and the reduction of rotational diffusion due the large size and anisotropy of the monolith might contribute to an increased rotational diffusion time τ_R, resulting in higher enhanced diffusion coefficient.

---

[5] Enhanced diffusion is related to ballistic velocity as $D = \frac{1}{3}V^2\tau_R + D_0$

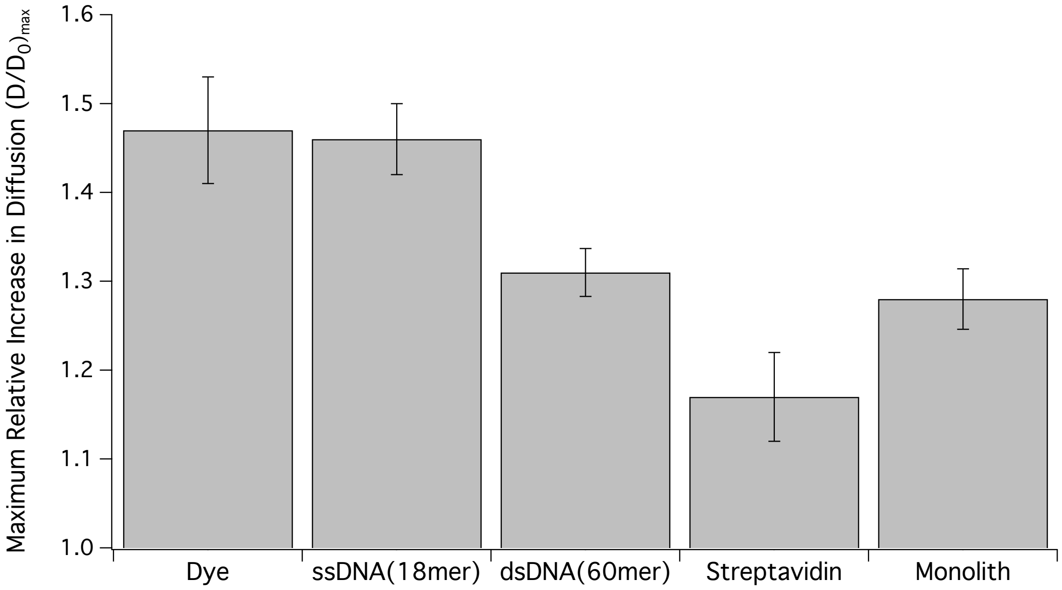

Figure 6.37: Maximum relative increase in diffusion coefficient $\frac{D}{D_0}$ measured for catalase bound to shown cargoes of diverse molecular weight in the presence of H_2O_2.

6.7 Conclusions

This chapter has presented the design process and the synthesis of nanomotors using DNA as a structural scaffold. This work constitutes the first use of a working enzymatic nanomotor to carry a cargo. The main conclusions of this chapter are summarised below:

A DNA Origami monolith was designed using open-source software (caDNAno) and optimised to produce a nanostructure for site-specific functionalisation with catalysts and fluorophores. In order to propel the designed DNA nanostructures, Pt NP and catalase were chosen as propellants due to their high catalytic activity for decomposition of H_2O_2. An electrochemical study of potential catalysts and their catalytic activity was measured (metallic nanoparticles and catalase). This permitted a comparison of particles of similar radius (5 nm). This measurement showed that Pt and catalase have the highest catalytic activity.

DNA was successfully functionalised to Pt and catalase using thiol-metal bond and amine-to-sulfhydryl crosslinker respectively. These catalysts were bound to DNA Origami by hybridisation, purified by gel electrophoresis and characterised by TEM and AFM. While localisation of Au NP [78] and enzymes [91] has been previously reported, site-specific localisation on 3D Origami of catalytic particles like Pt and catalase is a new result. In addition to DNA Origami, catalase was also bound to cargoes of different molecular weight, namely, DNA strands (long and short) and streptavidin. In order to measure their diffusivity, these cargoes were labelled with a fluorophore.

FCS was used to measure the diffusion behaviour of these particles in the presence of H_2O_2. The DNA-Pt-conjugate showed a reduced diffusion time with increasing H_2O_2, suggesting an enhanced diffusion. However this was not observed for the case of Pt bound to DNA monolith. The inconclusive results of experiments in which Pt nanoparticle were conjugated to DNA may be a result of the instability of the DNA-S-Pt bond in the presence of H_2O_2.

Catalase functionalised with a dye showed an enhanced diffusion up to 50% in the presence of H_2O_2. To act as a cargo, an 18mer strand functionalised with Cy3 dye was bound to catalase and purified successfully, as observed in SDS PAGE gels. The enzyme remained catalytically active after modification. An increase in diffusion of about 45% was observed in FCS for this DNA-catalyst nanostructure. Further, catalase bound to long and short DNA cargoes also exhibited enhanced diffusion of about 40% and 30% respectively. A similar measurement was carried out with streptavidin as a cargo of biotinylated catalase, which could be used as a mediator to bind to other biotin-modified cargoes. Finally, conjugated catalase-DNA monolith structure also showed increased diffusivity in the presence of H_2O_2. The relationship between the observed enhanced diffusion and the molecular weight of the cargo remains an interesting open question.

7

Control mechanisms using DNA

7.1 Introduction

After studying structural components and propulsion mechanisms for an autonomous swimmer, we now focus on the last characteristic of *E. coli* outlined in the introduction, namely chemosensing and computation. This chapter presents potential mechanisms of control over the swimming behaviour of DNA-based active particles with the tools of dynamic DNA nanotechnology. In the first part a mechanism of irreversible conformational change of a DNA structure is considered, which makes use of aptamers. A DNA aptamer is a strand selected from a random library that binds to a ligand [214], thereby inducing a structural change in the aptamer. The motivation behind this idea is to be able to control the shape and diffusivity of particles when placed in a gradient of chemicals.

However, a reversible sensor is more useful than an irreversible one. Therefore, the second part of this chapter is devoted to the design of a minimal adaptive system, similar to the *E. coli* chemotaxis network, that can respond to external signals and return to a set point in order to perform a new measurement. The discussion on adaptive dynamical systems is given in a general form and an experimental realisation of Lotka-Volterra oscillations with DNA is presented, together with a potential DNA implementation of a DNA adaptive system.

7.2 Adenosine aptamer for controlled shape changes of DNA structures[1]

Aptamers are oligonucleotide or peptide molecules that bind to a specific target molecule. The adenosine DNA aptamer developed by Huizenga et al. [101] consists of a 27 nucleotide strand that contains two binding sites for the ligand. It has a reported binding affinity of $K_D = 6 \pm 3$ µM. Here, we use a modified version of this aptamer as developed in [215]. This 27 nucleotide aptamer contains a FAM dye at the 5′-end. The sensor is formed by binding the aptamer to a partially complementary strand that contains multiple guanines at its 3′ end (quencher). The purpose of this strand is to quench the Fluorescein (FAM) fluorescence when the sensor is inactive.

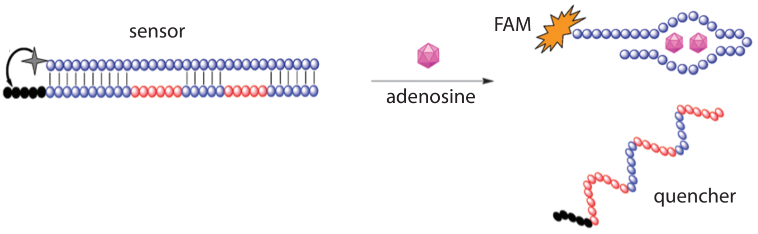

Figure 7.1: Scheme of the fluorescent aptamer sensor. When adenosine is present it binds to the FAM-labelled aptamer strand and promotes a conformational change, which results in the release of the quenching strand and recovery of FAM fluorescence. (The figure has been adapted from [215])

Table 7.1: List of DNA sequences for aptamer sensor

DNA strand name	Sequence
DNA aptamer	5′- FAM -AGAGAACCTGGGGGAGTATTGCGGAGGAAGGT -3′
quencher	5′-ACCTTCGAGGCCAATAGAGTGGCAGGTTCTCT-GGGGG-3′

Upon addition of adenosine (in 1x TE buffer with 50 mM NaCl and 10 mM $MgCl_2$), the strand is displaced and FAM fluorescence is recovered (see Figure 7.1). In order to characterise this system, we first performed a fluorescence measurement of the sensor and added adenosine at various concentrations. An increase in

---

[1] This project was done in collaboration with Luisa Kneer (LMU) and Dr. Jonathan Bath. The design of a shape-changing structure was suggested by Jonathan Bath and further developed by Luisa and the author. The contribution of the author consisted in identifying and characterising a working aptamer sensor, which is described in this section.

fluorescence is observed as the concentration of adenosine grows (Figure 7.2 (a)). Gel electrophoresis of the sensor before and after adenosine addition indicates that the duplex becomes single stranded upon addition of adenosine (Figure 7.2 (b)).

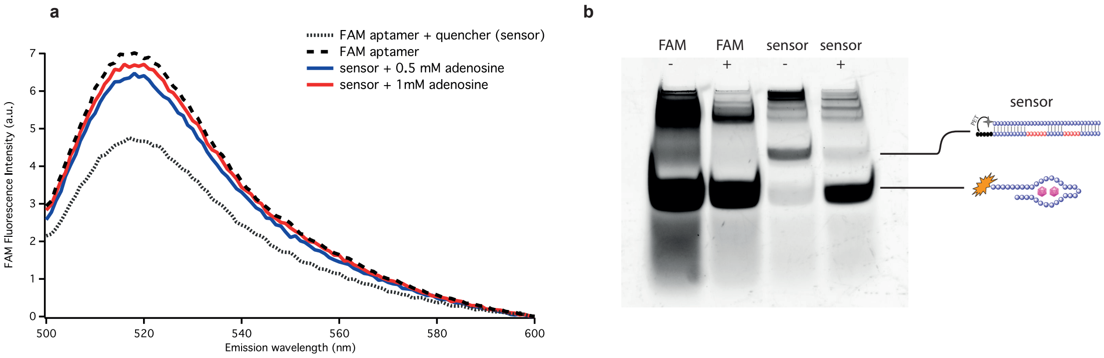

Figure 7.2: **a)** FAM Fluorescence emission of sensor with increasing adenosine concentration (incubated for 30 min at 37 °C). The sensor was assembled by mixing 0.5 µM FAM aptamer with 1.2 µM quencher. $\lambda_{excitation}$=490 nm. **b)** Gel electrophoresis (PAGE) scanned for FAM fluorescence. First and second lanes show bare FAM-aptamer strands, while the third and fourth lanes show the assembled sensor incubated without and with 1 mM adenosine, respectively. Increased mobility due to the addition of adenosine in the fourth lane signals successful opening of duplex structures. Slow moving bands suggest multimer formation.

This aptamer was used to implement a conformational change in the hinge structure shown in Figure 7.3 (a). The structure remains in a closed state but opens upon addition of adenosine. The hinge structure was annealed by heating a mixture with equal molarity of each strand (all 0.56 µM in solution) to 96 °C for 10 s and then cooling down with 3 °C/s. After adding the ligand (adenosine or ATP both bind to the aptamer), the solution was incubated at 37 °C for 35 min. Similar to the experiment in Figure 7.2 (b), the gel in Figure 7.3 (b) shows that the structure opens if adenosine or ATP is present in the solution.

One could incorporate the hinge mechanism in Figure 7.3 (a) in a larger and more complex DNA Origami structure. DNA assembled nanomotors could switch from a configuration with a higher diffusion constant to one with a lower diffusion constant in response to a signalling molecule, as shown in Figure 7.4. Conformational changes in response to stimuli could serve to control the direction of propulsion of DNA

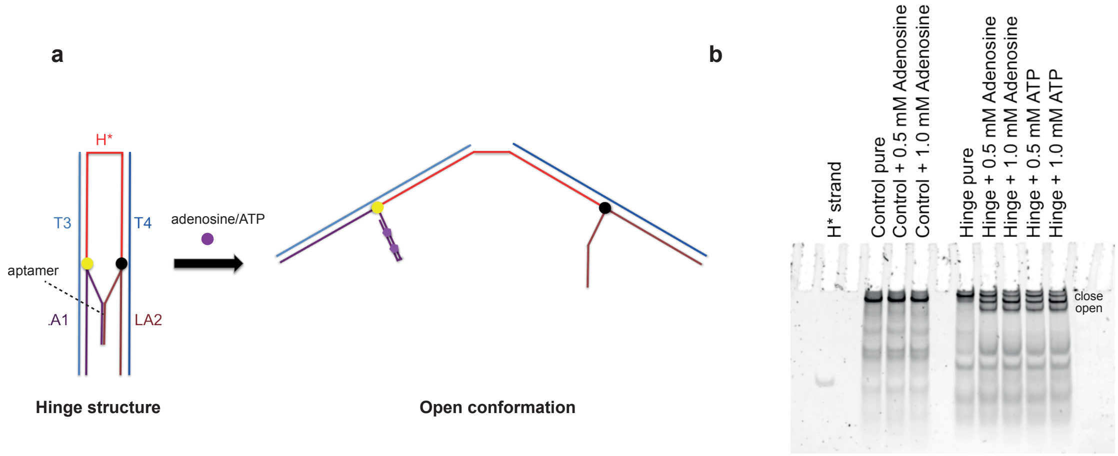

Figure 7.3: **a)** Hinge structure that incorporates an adenosine aptamer. The structure opens up in the presence of adenosine. **b)** Gel of the hinge structure with different ligands at different concentrations. The control is the hinge with the linkers, which does not change conformation. The hinge opens upon the presence of a ligand in the solution and two further bands can be observed. (15 % 29:1 1 xTAE, 45 min at 180 V at 4 °C)

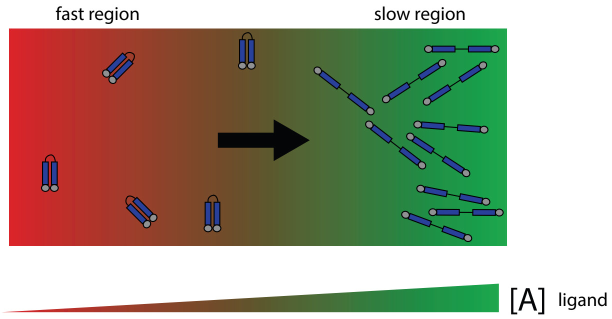

Figure 7.4: Schematic diagram showing accumulation of active particles in the presence of a gradient of ligand [A] that induces a change in shape. Swimmers accumulate in the region where they move slowest.

self-propelled devices. Accumulation would occur at low fuel concentration region (where diffusion is slowest) as discussed theoretically in [216, 217].

Using aptamers to sense the presence of ligands results in an irreversible conformational change that renders the sensor unusable for another measurement. The next section studies how to overcome this situation by using sensory adaptation, a dynamic property of many natural and engineered sensors that allows them to avoid saturation and return to a set point after a transient response to a signal.

7.3 Biomolecular mechanisms for robust adaptation

7.3.1 Model for adaptation in bacterial chemotaxis

Biological sensing devices are characterised by the ability to adapt to a persistent external stimulus. Sensory adaptation describes a situation in which after a transient response to a changing input signal, the system returns back towards the pre-stimulus state. Bacterial chemotaxis is an example that exhibits perfect adaptation to chemoattractants. The temporal gradient sensing of bacteria incorporates a desensitisation mechanism after a reaction to a stimulus has happened. Adaptation can be found in other sensory systems, such as human visual or olfactory systems.

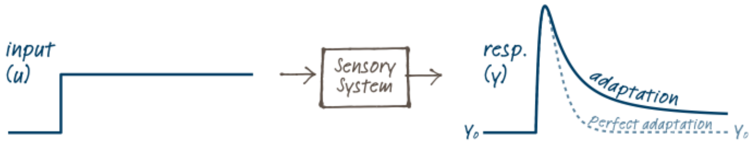

Figure 7.5: Scheme of an adaptive sensory system. A sensor reacts to an external signal and after a period of adjustment relaxes to a pre-stimulus value. Perfect adaptation refers to the case when the system relaxes back to the exact pre-stimulus value. (Figure adapted from [218])

Bacterial chemotaxis is possibly the most primitive and best-understood biological model of adaptation. There are two ways one can approach the phenomenon of perfect adaptation in this system: one approach by Spiro et al. considers that perfect adaptation in *E. coli* is the result of a *fine-tuning* or balancing between rate parameters of phosphorylation and methylation events [219]. This, however, is not robust, since any change in fine-tuned parameters can drive the system out of its adapted state. Another approach -the *Barkai-Leibler model*- considers fine-tuning unnecessary and shows that perfect robust adaptation is the result of a network property of the system [220].

Adaptation implies that the steady-state behaviour of the system is independent of the concentration of the input parameter u. This is illustrated in Figure 7.5, where the response relaxes back to its pre-stimulus state. In the language of control theory, adaptation is obtained with a feedback controller that takes the output signal and generates a “control action” signal, x, that is fed back into the original process and corrects it. The control variable x, which acts like a "memory", follows a dynamic that is independent of the input variable u and it only depends on the system output y, as expressed by:

$$\frac{dx}{dt} = f(y) \tag{7.1}$$

Negative-feedback is a minimal requirement for a system to self-regulate and have a stable point. Another requirement is that the system has a fixed set-point value, i.e. $f(y) = 0$ in (7.1) must have real roots, because imaginary roots give rise to oscillations. A general negative-feedback controlled system is shown in Figure 7.6. This simple form consists of two subsystems, the process P and the controller C. The former receives the input signal u and produces the response signal y. The output is then fed back to the controller C. Negative feedback indicates that changes compared with the reference (i.e. the error $e = y - y_0$) will be subtracted from the external input.

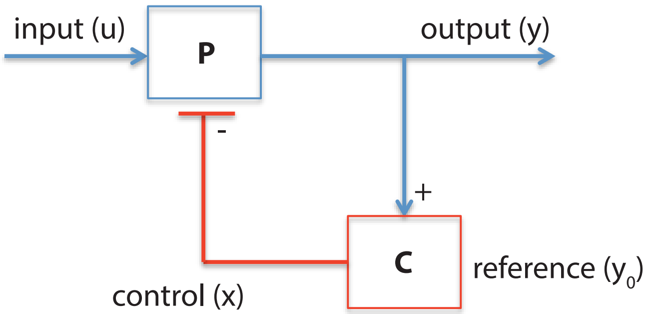

Figure 7.6: Diagram of a negative feedback-controlled system with an input signal, u, and an output signal, y. The error signal, e, is the difference between the current output and a reference value y_0, and this is fed back through a *controller* (C) which produces a control signal, x, that is subtracted from the external input signal.

From a control-engineering point of view, robust perfect adaptation is achieved through integral feedback control [221], which is a particular implementation of negative-feedback. Integral feedback assures that the output of a perturbed process is kept at a certain setpoint by integrating the associated error $e = y - y_0$, such that

e approaches zero [222]. Integral feedback is a necessary and sufficient condition for adaptation, which ensures that the output always approaches its desired set level despite step changes in the parameters and inputs. Yi et al. showed that adaptation in bacterial chemotaxis can be described in terms of an integral feedback control [223] and gave a proof of the necessary and sufficient conditions for adaptation.

Although integral control motifs can be found in genetic networks and other homeostatic regulatory mechanisms, the question addressed in this section is whether a synthetic biomolecular implementation of integral feedback control is possible. This would allow the creation of sensory devices that can adapt to their changing environment without compromising their sensitivity.

7.3.2 A primer on integral feedback control

The principle of integral feedback is illustrated in Figure 7.7. It contains features of the negative feedback loop described in Figure 7.6. In the context of a sensory swimmer like *E.coli*, the perturbation u is the chemoattractant, the output y is the receptor activity and the control x represents the receptor methylation levels. The description below is more general.

The error e between a reference signal y_0 and the output y is integrated, and then added to a perturbation and fed back to calculate the error again. This closed negative loop guarantees that the error e will approach to zero.

The system in Figure 7.7 obeys the following dynamics:

$$\begin{aligned} \frac{dx}{dt} &= f(y) \qquad (7.2)\\ f(y) &= y_0 - y \qquad (7.3)\\ &= y_0 - g(u+x) \qquad (7.4)\end{aligned}$$

Steady-state is achieved when $\frac{dx}{dt} = 0$, and $y = y_0$. Hence, the output y is independent of u, the external perturbation. In order for the equilibrium to be stable and that the perturbation in u drives the system back to the set-point y_0, the constant g must be positive $g > 0$.

We next study biomolecular implementations of adaptation.

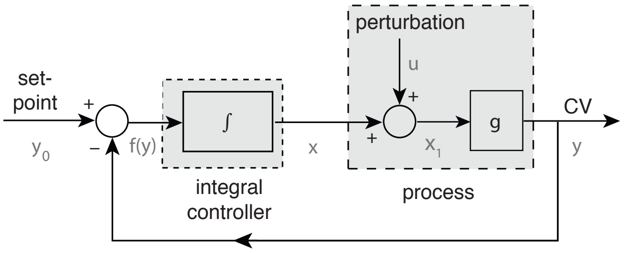

Figure 7.7: A basic block diagram representing a system with integral feedback. Circles represent summing junctions, such that the output arrow is a signal given by the sum of the signals associated with the input arrows (the molecular analogue would be activation and inhibition, respectively). The desired set point y_0 is compared to the actual output y and the resulting error is integrated to yield $x = \int_0^t f(y)d\tau$. This error is then used to change y. u is an external perturbation that alters the output y.

7.3.3 Minimal molecular implementation of adaptation

One way of achieving adaptive dynamics in a chemical reaction network is by balancing a zero-order reaction (e.g. synthesis of an element) against a first-order reaction (e.g. degradation). Here a simple example is chosen that consists of a single species with no intermediate components. Synthesis of a stable inactive form of a protein or DNA structure (P) is converted into an unstable form P_a, catalysed by an external signal (E). P_a is then degraded. Figure 7.8 (a) shows the coupled reaction, which in a simplified abstract form in Figure 7.8 (b) corresponds to an incoherent feedforward loop motif (IFFL).

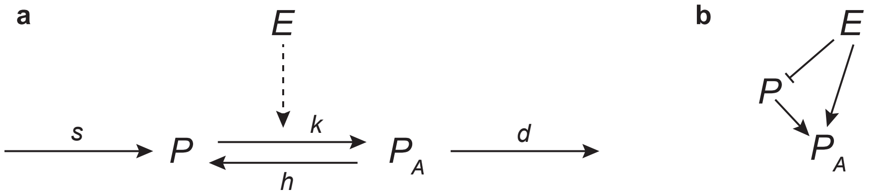

Figure 7.8: **a)** Minimal adaptive biochemical network, where a species P is catalysed by E into an active state P_a, while being synthesised and degraded. **b)** Abstract representation of the reaction, corresponding to the an incoherent feedforward loop motif (IFFL).

This example has been treated by Csikász-Nagy et al. in [224] and can be regarded as the minimal adaptive biochemical unit, as it only contains a single species and a catalyst. Robust adaptation is guaranteed by a zero-order reaction (the synthesis of P) that balances against a first-order reaction (the degradation of P_a). This can be visualised by writing the mass-action kinetic equation for this system, namely:

$$\frac{dP}{dt} = s - (k+E)\cdot P + h \cdot P_a \tag{7.5}$$

$$\frac{dP_a}{dt} = (k+E)\cdot P - (h+d)\cdot P_a \tag{7.6}$$

Solving for steady-state, the concentrations of P and P_a are given by:

$$\bar{P} = \frac{s \cdot (1+\frac{h}{d})}{k+E} \tag{7.7}$$

$$\bar{P_a} = \frac{s}{d} \tag{7.8}$$

As can be seen in equation (7.7), the steady-state concentration of P_a is independent of any input and depends only on the production and decay rates, s and d respectively. It should also be noted that removal of the inverse process h, which transforms P_a back into P does not alter the adaptive behaviour of the system, nor the addition of intermediate states [224].

Figure 7.9 shows numerical solutions for the ODEs in (7.5). Given a perturbation in the concentration of E of staircase form, the concentration of the active species P_a displays perfect adaptation. On the other hand, P follows an inverse trend to the time evolution of E.

This minimal adaptive system could have a molecular implementation in a two-state device that is constantly synthesised and degraded. There might be proteins that can satisfy these conditions (e.g. membrane receptors). However, in order to engineer a DNA based device we focus the attention on one of the main property that makes this system adaptive, namely the incoherent feedforward loop network topology (Figure 7.8 (b)).

In order to achieve this type of adaptive dynamic behaviour, we start from a simpler system that reproduces in vitro oscillations making use of the programmability of DNA interactions and the precise control of enzymatic catalysis.

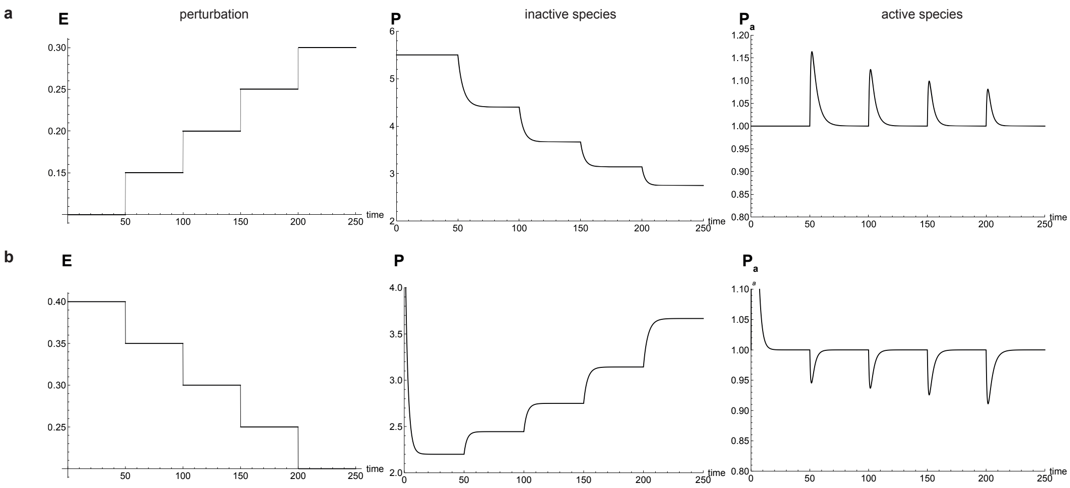

Figure 7.9: Solution to ODEs in (7.5) of the minimal adaptive system for $k = h = 0.1$ and $d = s = 1$, and initial conditions of $P(t = 0)$=5.5 and $P_a(t = 0)$=1. The time evolution of the external perturbation E is set to an increasing staircase function in **a)** and a decreasing one in **b)**.

7.3.4 Lotka-Volterra dynamics with DNA

This section presents experimental work on an engineered enzymatic system that can display oscillations, namely the DNA Predator-Prey system. It consists of the autocatalytic growth (self-growth) of a species that interacts between other species. When an autocatalyst (Prey, N) is consumed by another species (Predator, P), oscillations spontaneously form. The system alternates between a growth regime and a consuming regime, thus giving rise to oscillations in concentration following Lotka-Volterra dynamics.

Preys undergo autocatalytic growth (N → 2N), they are predated by predators (N + P → 2P), and both species decay (N or P → ∅). The system can be defined in terms of the coupled differential equations:

- Prey: $\frac{dN}{dt} = N - N \cdot P$ (the first term is the autocatalytic growth and the second term represents predation)
- Predator: $\frac{dP}{dt} = N \cdot P - P$ (The growth of predator is a function of its own population and the population of prey. Predators decay by natural death.)

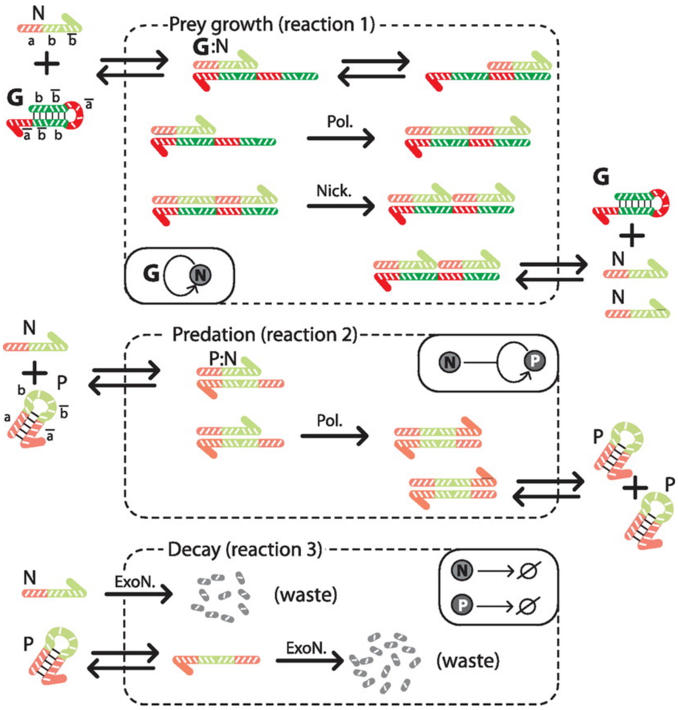

Figure 7.10: Design of the predator–prey reaction network. The reactions 1–3 are constructed from DNA polymerization and depolymerization reactions. The template G (in strong colours) is the only stable sequence in the system. Other strands (predator P and prey N, in light colours) are dynamically produced and degraded in the presence of a polymerase (Pol.), a nicking enzyme (Nick.), and an exonuclease (ExoN.). Sequences can be identified with colour-codes. (Figure extracted from [106])

Figure 7.10 shows how the corresponding chemical reactions of Prey and Predation can be compiled using DNA biochemistry. Autocatalytic growth is achieved through polymerisation and nicking of prey using a template (this type of reaction has been discussed in chapter 4). The predation reaction describes the growth of the predators through the consumption of prey and polymerisation. Finally, all of the species have a limited lifetime in the system as they decay by the action of exonuclease.

We reproduced this Predator-Prey dynamics with a DNA/enzyme system following the original work of Fuji & Rondelez [106]. EvaGreen Fluorescence was measured and sustained oscillations for 73 hours were obtained, before parasitic growth[2] of one species dominated and the reaction stopped, as shown in Figure

---

[2] These oscillations are unusually long, compared to work in [106]. Parasitic behaviour is the sudden dominance of one species, which ends the experiment. This effect has not been addressed in the literature.

Table 7.2: List of used oligonucleotides (from Biomers Gmbh)

DNA strand name	Sequence
prey	5′-CATTCGGCCG-3′
predator	5′-CATTCGGCCGAATG-3′
grass (DY635)	5′-*C*C*C*GGGAATGCCCGGGAATG-DY635-3′

7.12. FFT of the fluorescence signal (see Figure 7.13) reveals a period of 2.14 hours in the oscillations.

We used oligonucleotides in Table 7.2 in the experiment (buffers in appendix A.9). Titrations of polymerase gave different unstable behaviours, except for the following combination, which resulted in oscillations: grass template (50 nM), Predator (3 nM), Prey(3 nM), polymerase 0.5%, nickase 0.66%, exonuclease 0.4%.

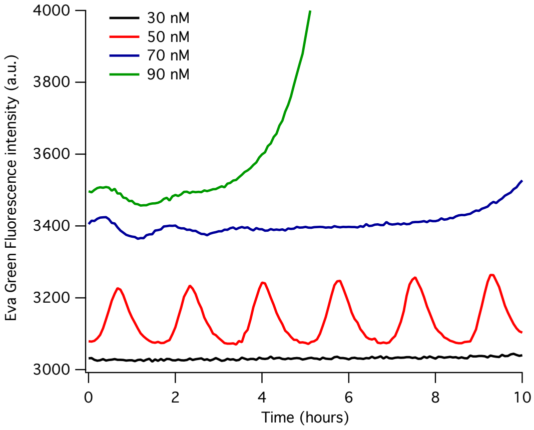

Figure 7.11: Predator-prey dynamics for increasing concentration of template (grass). The onset of oscillations was observed for 50 nM of grass template strand, while higher concentrations resulted in damped oscillations and eventual domination of prey species.

Quenching of Dy635 (the fluorophore of grass strands) occurs when prey grows and binds to template strands (grass). This gives a reporting mechanism for prey concentration, in addition to the intercalating dye EvaGreen, which reports mostly predator populations. In Figure 7.14 we observe oscillations for EvaGreen and Dy635 fluorescence and a characteristic phase plane trajectories for Lotka-Volterra dynamical systems. Increasing the concentration of grass template (above 50 nM) resulted in dampened oscillations, while lower concentrations did not sustain prey growth and thus did not give rise to oscillations (see Figure 7.11).

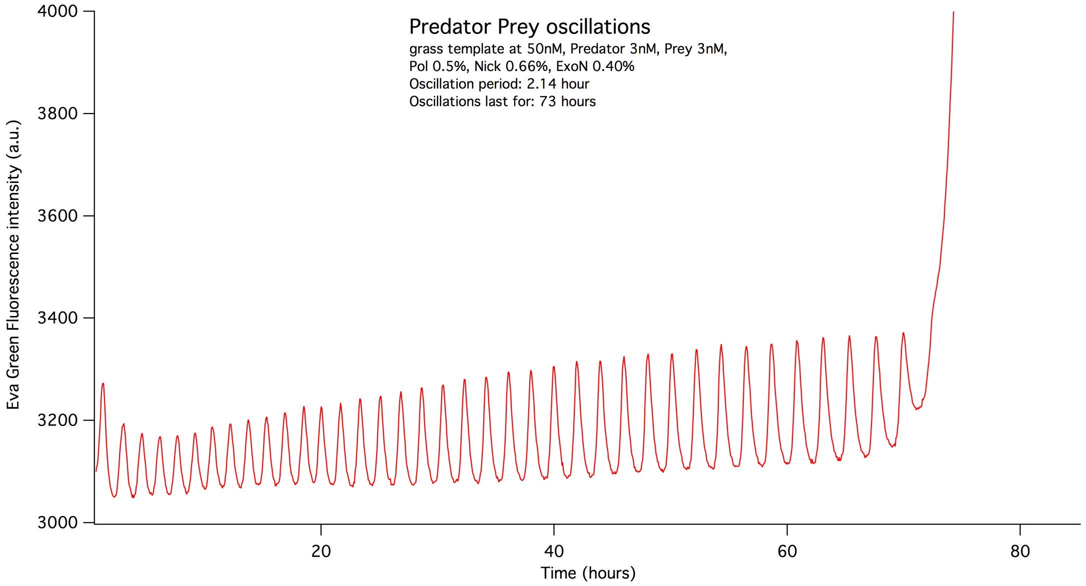

Figure 7.12: Predator-Prey oscillations recorded for 73 hours. Parasitic behaviour ends oscillations.

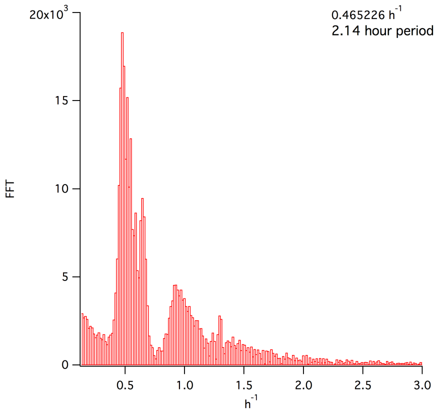

Figure 7.13: Fast Fourier Transformation of fluorescence signal indicating a period of 2.14 hours.

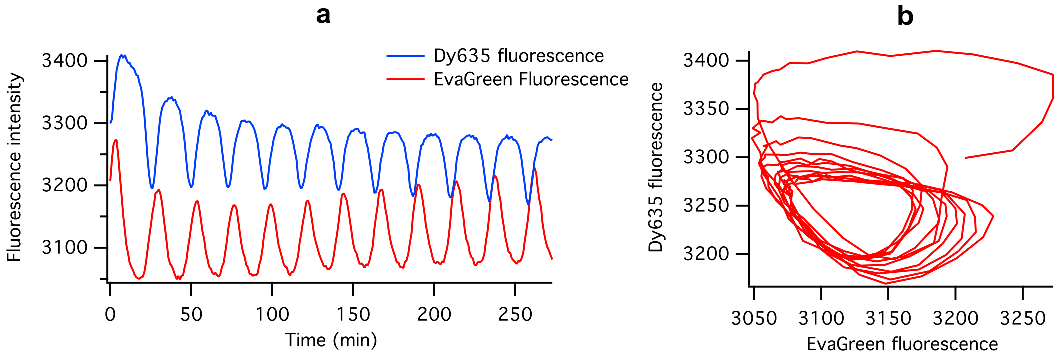

Figure 7.14: **a)** Two colour Predator-Prey system showing oscillations of EvaGreen and Dy635 fluorescence. **b)** Typical closed predator-pray trajectory in fluorescence space, which shows a limit cycle periodic oscillation.

The rich parameter-space this system offers makes it possible to explore spatio-temporal dynamics, when predators and preys are allowed to diffuse [159]. In addition, this system could act as a chemical clock and control other DNA-based processes.

The next section explores the use of a similar dynamical system to provide a robust adaptation mechanism based on DNA reactions. This is achieved by a molecular implementation of an IFFL motif, which exhibits adaptive behaviour under certain conditions.

7.3.5 Adaptive DNA chemical reaction network

The same tools that were used to create the oscillatory behaviour in section 7.3.4 can be used to implement more complex motifs, such the adaptive IFFL motif. The main ingredients of the DNA PEN toolbox (Polymerase Exonuclease Nickase, Dynamic Network assembly toolbox) [169], which are a generalisation of those used for the Predator-Prey system, are shown in Figure 7.15 (a). These combine oligonucleotides and the enzymes polymerase, exonuclease and nickase. Synthetic DNA templates act as regulators of the production of an output signal. Template strands are activated by ssDNA that allow DNA polymerase to extend the oligomer/template pair yielding a fully hybridised dsDNA. These are then nicked by nickase resulting in double-stranded complexes. Depending on the template and the activating ssDNA three type of reactions can occur, which are listed in Figure 7.15 (a): autocatalysis, activation and inhibition. A PEN-toolbox *in silico* realisation of a IFFL motif (Figure 7.15 (b)) was presented in [225]. This network is shown in Figure 7.15 (c) and it consists of three templates and an initial trigger U (it incorporates phosphorothioate to prevent degradation). Activation occurs in T1 by input U, which in turn activates both T2 and T3. Activation of T3 leads to the product oligomer Y, whereas activation of T2 leads to the production of an inhibitor *inh*, which inactivates T3.

The parameter space where such network exhibits robust adaptation is limited. Numerical simulations prescribe a set of dissociation constants and concentration

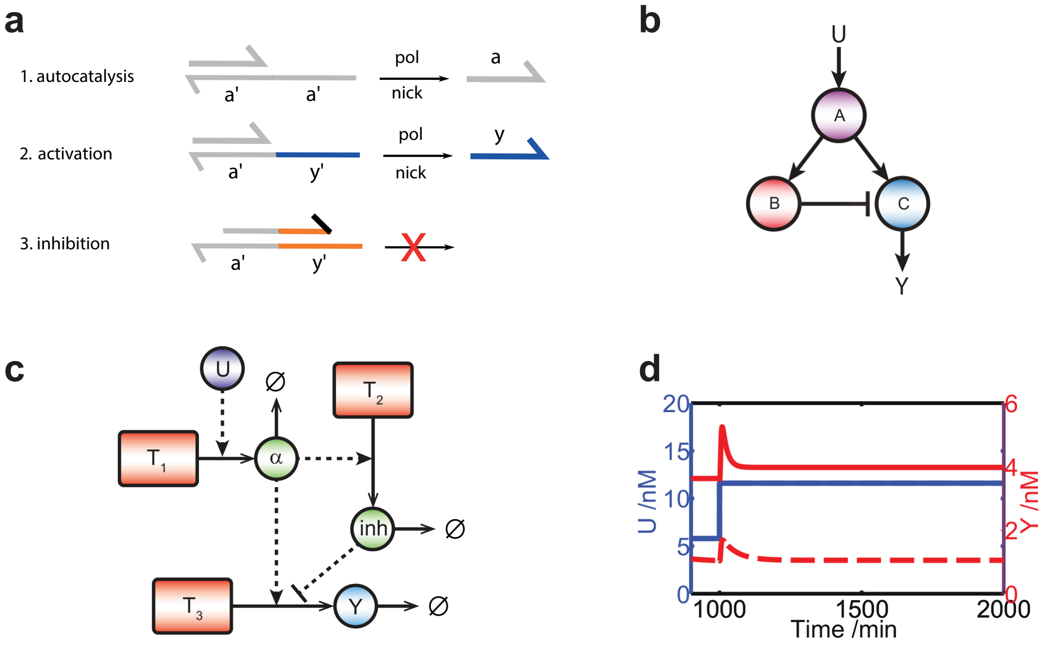

Figure 7.15: *Design of an adaptive biochemical network using the PEN toolbox.* **a)** Main ingredients of the PEN toolbox [169]. Activator ssDNA *a* primes the synthetic template, after which it is extended by DNA polymerase resulting in dsDNA. Nickase cleaves this dsDNA in the backbone of the newly formed strand, resulting in dissociation of a signal strand. Depending on the sequence of template, three types of reactions can occur, i.e. autocatalysis, activation and inhibition. **b)** Network topology of an incoherent feed-forward loop (IFFL). **c)** PEN-toolbox implementation of an IFFL as proposed in [225]. The input U is protected against degradation and templates T indicate the species they activate. The species Y is the final product. **d)** Solutions to full ODE described by c) for a set of parameters that supports adaptation [225]. Adaptation is observed in the concentration of oligomer Y for a step function in U. Perfect adaptation is shown in dashed lines.(Figures (b), (c) and (d) have been extracted from [225])).

ranges of all species involved where the system displays adaptive response [225]. One example is given in Figure 7.15 (d), where two different responses (in red) for the initial perturbation (in blue) are shown. This system, which exhibits adaptive behaviour, has not been implemented experimentally yet.

7.4 Conclusion

This chapter has introduced DNA-based sensing systems to employ them as control mechanisms in micro and nanoscale devices. The first part presents a DNA aptamer used to form a fluorescent sensor that was implemented in a larger DNA hinge structure. Upon addition of adenosine (or ATP) the structure opened, thereby also changing its diffusion constant, as observed in changes in mobility by gel electrophoresis.

The second part of this chapter studied adaptive sensory mechanisms implemented with DNA. The synthesis of a minimal adaptive biochemical network was presented, addressing the topic of synthetic chemotaxis. Minimal network motifs that exhibit adaptation were shown, including the incoherent feedforward loop (IFFL). Predator-prey dynamics with DNA and enzymes were reproduced experimentally, with persistent oscillations for more than 73 hours. The same DNA-enzyme toolbox that we have used to obtain oscillations could be modified to create DNA-based chemical reaction networks with adaptive behaviour in vitro.

8

Summary

This thesis is about using DNA nanotechnology to program the assembly of active matter at the micro and nanoscales. The introductory chapter motivated the combination of DNA nanotechnology and active matter. By using *E.Coli* as an example of an autonomous microswimmer, four main aspects of the thesis were introduced, namely structural and dynamic DNA nanotechnology, propulsion mechanisms, and active media. The main developments in the fields of both active matter and DNA nanotechnology were summarised and compared in detail.

Chapter 2 investigated the underlying physics behind self-diffusiophoretic propulsion of asymmetric catalytic colloids at two different regimes: continuum hydrodynamic of Janus microswimmer and multi-particle dynamic simulations of dimer nanomotors. These studies clarified the differences between passive nanoparticles and active nanomotors using simulated mean-squared displacements and average velocities. It was also pointed out that self-propulsion at the nanoscale results in enhanced diffusion which is experimentally observable. This chapter also summarised the motor activity of the micro and nanomotors studied in this thesis.

A full account of the experimental methods that were used throughout this work for probing self-propulsion for active micro and nanoparticles and enzymes was elaborated in chapter 3. These methods included dynamic light scattering (DLS), fluorescence correlation spectroscopy (FCS), dark-field optical microscopy with nanoparticle tracking analysis (NTA) and nanoimpact particle collision voltammetry. The detailed experimental setups were described, together with sample measurements and simulations for DLS and FCS that were carried out. Advantages and disadvantages of these methods for measuring enhanced diffusion were compared from theoretical and practical aspects. FCS was favoured as a relevant measurement tool for enzyme-based nanomotors, while DLS was chosen as the main tool to measure metallic nanomotors.

Chapter 4 introduced DNA as an active component, driven out-of-equilibrium by autocatalytic reactions. The mechanism of the autocatalytic reactions was analysed by using the Fisher-Kolmogorov-Piskunov reaction-diffusion equation. Then an autocatalytic DNA system of DNA/enzyme mixtures in microfluidic channels was studied and wave propagation behaviour was observed and studied theoretically. The velocity of the wave slowed down by changing the growth rate of the autocatalytic reaction. Later, a new implementation of this system with a gradient of template oligonucleotides was developed for two different forms of gradients: a sharp gradient in the form of a step-function and a more gradual exponential gradient. For both cases, the propagation velocity of the front slowed down in agreement with numerical simulations of the reaction-diffusion equation. The same phenomenon was observed for the system with gradients of inhibitor strand. These experiments showed that DNA itself acts as an active system and that by programming its kinetics the velocity of DNA chemical waves can be tuned, which is harder to achieve in conventional autocatalytic systems. In light of these results, this work constitutes a DNA-based programmable active system.

Chapter 5 focussed on the synthesis of active particles and the use of DNA as a “programmable glue” to mediate their interactions. Two different experimental approaches were developed to fabricate micro and nanomotors. First, Janus microparticles were half-coated with Pt by physical vapour deposition. Then, a wet-chemical approach was demonstrated to synthesise asymmetric catalytic Pt-Au nanoparticles that function as nanomotors. This is the first time in which chemical synthesis methods are used to fabricate catalytic nanomotors. The physical and chemical properties of the resulting motors were characterised by HAAD-STEM , EDX, XPS and SEM. Janus motor activity was shown by microscopy tracking, while DLS demonstrated the activity of the asymmetric particles in the presence of H_2O_2 fuel. Ballistic propulsion was manifested for Pt-Au NP as an increase in the effective diffusion constant by up to 30% in H_2O_2.

A second part of this chapter focussed on DNA conjugation on both micro and nanoparticles to control their colloidal assembly. For microparticles, aggregation and disassembly of polystyrene beads was achieved through DNA strand-displacement reactions. Small satellite colloids were assembled on larger Janus particles by DNA hybridisation. For nanoparticles, DNA Origami was used to provide directional bond between Au NP. The hybrid Origami/NP structures enabled control of the bonding valency and geometry for otherwise symmetric Au NP, allowing control over 2D lattice symmetry. The hybrid DNA Origami/Au NP structures formed assembled lattices of various symmetries (linear, square and hexagonal) and confirmed by TEM.

Chapter 6 concentrated on the design process and the synthesis of nanomotors using DNA as a structural scaffold. First, a DNA Origami monolith was designed and modified to produce a nanostructure for site-specific functionalisation with catalysts and fluorophores. In order to propel the designed DNA nanostructures, Pt NP and catalase were chosen as propellants due to their high catalytic activity for decomposition of H_2O_2, as shown by electrochemical experiments. DNA was successfully functionalised to Pt and catalase using crosslinking chemistry. These catalysts were bound to DNA Origami by hybridisation, purified by gel electrophoresis and characterised by TEM and AFM. Catalase was also bound to cargoes of different molecular weight, namely, DNA strands (long and short) and streptavidin. In order to measure their diffusivity, these cargoes were labelled with a fluorophore.

FCS was used to measure the diffusion behaviour of these particles in the presence of H_2O_2. The Pt conjugation of DNA showed a reduced diffusion time with increasing H_2O_2, suggesting an enhanced diffusion. However this was not observed for the case of Pt bound to DNA monolith. Catalase functionalised with a dye showed an enhanced diffusion up to 50% in the presence of H_2O_2. To act as a cargo, an 18mer strand functionalised with Cy3 dye was bound to catalase and purified successfully. An increase in diffusion of about 45% was observed in FCS for this DNA-catalyst nanostructure. Further, this DNA-modified catalase was bound to long and short DNA cargoes which also exhibited enhanced diffusion. A similar increase in diffusion in the presence of H_2O_2 was observed for catalase conjugated with streptavidin and also with DNA monolith. This work constitutes the first use of a working enzymatic nanomotor to carry a cargo.

Chapter 7 explored DNA-based sensing systems and the potential of employing them as control mechanisms in micro and nano scale machines. Firstly, a fluorescent DNA aptamer sensor that can bind a small biomolecule (adenosine) was shown. This aptamer was implemented in a larger DNA hinge structure and its shape change was proved by gel electrophoresis. Then, adaptive sensory systems based on DNA reaction networks were investigated and means of realising them with a DNA/enzyme system were shown. This system was used to demonstrate experimentally persistent oscillations in DNA predator-prey dynamical system.

Appendices

A
Materials and methods

A.1 UV-Vis measurement of DNA concentration

DNA concentrations were measured using the absorbance of single stranded DNA at 260 nm. Measurements were taken with a Varian Cary spectrophotometer (Varian Ltd, UK) and cuvettes with a path length of 1 mm. DNA concentration was calculated using the Beer-Lambert Law:

$$A = \epsilon_{260} c \cdot l \tag{A.1}$$

where A is absorbance, ϵ_{260} is the extinction coefficient of the DNA, c is the concentration and l is the path length. The extinction coefficient can be calculated from the sequence of the oligonucleotide. Figure A.1 shows the absorbance of DNA Origami monolith. The molar extinction coefficient of DNA Origami is equivalent to that of a fully double-stranded m13mp18 scaffold (ϵ=123 735 380 $\mathrm{M^{-1}\,cm^{-1}}$).

A.2 SYBR gold staining and gel visualization

SYBR Gold is an intercalating fluorescent dye that binds strongly to dsDNA. After gel electrophoresis, the gel is deposited in a tray containing approximately 20 mL of water. A 2 microlitre of stock SYBR Gold is added to the tray and left incubating for about 5 minutes. Then the tray is rinsed several times using MilliQ

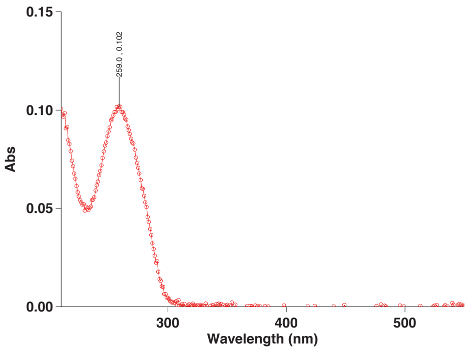

Figure A.1: UV-Vis absorbance spectrum of DNA Origami monolith.

water and the stained gel is imaged using a Pharox FX plus Molecular Imager (Bio Rad). If the DNA solution to be analysed contains fluorescent strands, then direct imaging is possible choosing the right excitation laser and filters. For protein staining Coomasie Blue R-250 dye was used.

A.3 DNA conjugation protocols

A.3.1 Streptavidin-biotin conjugation protocol

This protocol was used to bind bioninylated oligonucleotides to streptavidin coated microspheres.

1. Aliquot 100 µl streptavidin coated microspheres into a microcentrifuge tube.
2. Wash 2 times in 100 µL Binding / Wash Buffer (10 mM phosphate buffer, 50 mM NaCl, Poloxamer 407, 0.5%(w/w), pH 7.5) by centrifuging the streptavidin coated microspheres at 10 K rpm for 3 minutes, and decanting the supernatant.
3. Re-suspend the microspheres in 20 µL Binding / Wash Buffer and add 5-10µg biotinylated DNA. Keep bead concentration in the range of 10-50 mg/mL during the binding step.
4. Incubate 15 minutes at room temperature on a vortexer , then centrifuge and decant the supernatant.
5. Remove any unbound biotinylated oligonucleotide from the streptavidin- oligo beads by washing 2 times in 100µL Binding / Wash Buffer.
6. Re-suspend in 100 µL Binding / Wash Buffer.

A.3.2 EDC Bioconjugation protocol

The following protocol has been optimized for carboxylated polystyrene beads (Bangs laboratories)

1. Wash particles into coupling buffer (2-(N-morpholino)ethanesulfonic acid (MES) 50 mM pH 5.2)
2. Suspend 10 μl of source particles (10% (w/v)) in 150μl buffer.
3. Microsphere activation with EDC: Take a vial and measure 10 mg and add 50 µl of coupling buffer. For each reaction use 25µl EDC/MES.
4. Add 200 µl of DNA at 10 µM (higher concentration of DNA increases surface density)
5. Centrifuge at rcf of 9.1 10^3 g for 2 min. Resuspend in 100 µl
6. Resuspend in PBS/Tween-20 after washing.
7. Sonicate for 5 minutes.

A.4 Protein labelling protocol with NHS-Rhodamine

1. Prepare catalase solution a reaction tube in PBS buffer (1 mg/mL).
2. Dissolve NHS-Rhodamine at 10mg/mL in DMF or DMSO. Mix thoroughly. (e.g. 1 mg of NHS-Rhodamine in 100 µl of DMSO or DMF))
3. Transfer the appropriate amount of dye ($\approx$ 3 µl) to the catalase solution and mix well.
4. Incubate the reaction at room temperature for 1 hour or on ice for 2 hours.
5. Remove non-reacted NHS-Rhodamine by dialysis or gel filtration, or with a Dye Removal Column. Best results were obtained with a BioSpin column-3 (BioRad), equilibrated with PBS. Alternatively, Amicon filters (30kDa) remove excess dye effectively.
6. Store Rhodamine-labeled protein at 4°C protected from light until ready to use.

A.5 DNA Origami purification with Agarose gel electrophoresis

Agarose gel electrophoresis provides an effective method for high-resolution analysis and separation of well-folded DNA Origami nanostructures. The standard concentration of agarose used for purification was 1.2 % (w/v). More concentrated gels (2%) result in sharper bands and they were used only for structure characterisation purposes. Agarose was mixed in 100 ml 0.5x Tris-Borate-EDTA buffer, pH 8.3 (Sigma Aldrich) and heated in the microwave until a transparent liquid was obtained. 11 mM $MgCl_2$ was added to the agarose solution while cooled to room temperature. Additions of $MgCl_2$ in both the gel and running buffer promote tighter folding of the nanostructures. The agarose gel was cast and run at 3.5 V/cm for 2 hours.

The Origami band was visualised either with a gel scanner or with a UV transilluminator (an example is shown in Fig. A.3). The chosen band was cut and diced with a scalpel and placed on a parafilm surface as shown in Figure A.2. A parafilm covered glass was used to squeeze the diced agarose between two pieces of parafilm. A pipette was used to extract the droplet containing the origami structures. This purification method yields up to 20 μl of nM range concentrated solution, if the origami is initially assembled with 10 nM scaffold.

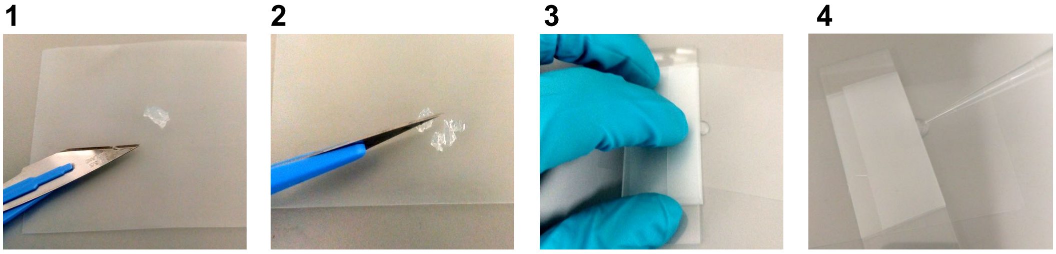

Figure A.2: 1. The band is extracted out of the agarose gel and placed on a parafilm surface. 2. A scalpel is used to dice the band. 3. Parafilm covered glass is used to squeeze the diced agarose. 4. The droplet is collected with a pipette.

A.6 Poly(ethylene glycol)-induced purification of DNA Origami

This protocol makes use of the excluded volume effect generated by long polymers. 30% (w/v) stock solution of Poly(ethylene glycol)-8000 (Fischer) was prepared in water by magnetic stirring. The solution was filtered through a 0.22 μm filter. 50 μl of DNA sample was mixed in 1xTE buffer with final concentrations of 7.5% (w/v) PEG-8000, 250 mM NaCl and 20 mM $MgCl_2$ in a total volume of 150 μl. The solution was spun at maximum speed in a tabletop centrifuge for 30 min. The supernatant was removed and the pellet was resuspended in a buffer of choice (0.5x TBE 11mM $MgCl_2$). This step is straightforward when the Origami is fluorescent, as a distinguishable pellet can be seen by bare eyes.

After PEG precipitation, a 1.2% agarose gel was run at 3.5 V/cm for 2 hours. A purification yield of 60% was measured by comparing the fluorescence intensity of Cy3 staple and origami bands for the purified samples and the source, shown in Fig A.3

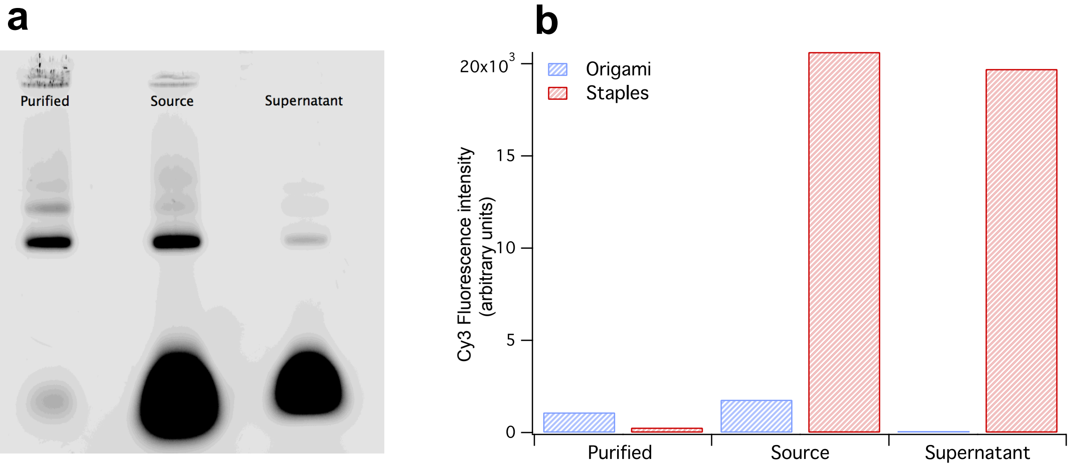

Figure A.3: a) Agarose gel electrophoresis (1.2% w/v) run at 3.5 V/cm for 2 hours and observed in Cy3 fluorescent channel. **b)** Cy3 fluorescence intensity of gel bands in (a) corresponding to DNA Origami and staple strands.

A.7 Uranyl acetate staining protocol for TEM sample preparation on grids

Formvar-carbon coated copper grids (01813-F Carbon type-B, 300 mesh, from TED Pella Inc) were made hydrophilic by glow discharge in a plasma cleaner using oxygen. The Formvar on these grids is deposited on the shiny side and a thin carbon layer is deposited on top of the Formvar. Therefore the glow discharge was applied on the shiny side of the grid.

We applied 10 µl DNA origami (at nM concentrations) to the surface of an electron microscope grid for ten minutes. Excess of DNA Origami was dabbed off with Whatman filterpaper. The grids were washed with a 2 % Uranyl acetate solution (10 µl) and subsequently stained for 10 s with additional 10 µl Uranyl acetate solution. Finally, excess of Uranyl acetate solution was dabbed off with Whatman filterpaper and air- dried for at least 10 minutes.

A.8 DNA Origami monolith

Table A.1: Staple sequences for a DNA Origami Monolith with Cy3 and catalyst handles.

Start	End	Sequence	Location
0[71]	2[56]	ATGCAGAGAGAATTAGAAACGATTTTTTGTGCTATTTTGGCTTAT	core
0[103]	8[96]	CAGACGACAGGGTAATAACAGCCAGGCATGATGTGGCAAC	core
0[143]	7[135]	AGAATATAAAGTACCACCTTTTTGACCTAAATTAGAGTG	core/Pt
1[136]	11[135]	AAAGCCAATCTTCTAACCTCCGAATAGTGAATTTATCAACAGAAA	core
2[87]	6[72]	ATAGCAAGCAAATCAGCTTTCCTTCCAAATAAACTGAACAAATAAGAG	core
2[111]	5[119]	TCGTAGGACCAAGTACACAAAATATGAGCGCTAATATTCT	core/Pt
2[151]	3[135]	GCGTTATACAAATTCTTACCCAAGGTTTGAA	core
4[119]	0[104]	TGCCAGTTCGCACTCAGTAAAGTAATTCTGTC	core
5[56]	3[71]	TAGACGGACGCGCCTTCAATAATCGGCTGTATATAGAAGCACCCA	core
5[88]	3[103]	AAAGTCAGGACAATAAAAGAACGGGTATTAAAATCATTACCCAACGCT	core
5[120]	1[135]	GAGAGACTGACAAAAGTCGAGAACAAGAGTAT	core
6[71]	15[71]	CAAGAAATCATCGGCTTACCATTTGAGGCACATACATGATTTCGG	core
6[95]	2[88]	TTGAGTTAAAAGAACTTATTATTTGAATCTTACGCGCCCA	core
7[80]	5[87]	AATACCCAAGCCCAATCCCTGAAC	core/Pt
7[160]	9[167]	TCGCTATTTTTTTTAACAAGAAAA	core/Pt
8[87]	0[72]	GAAACGCATTTATCCTATCCCAATATCATTCCACAACATGTTCAGCTA	core/Pt
8[119]	2[112]	AAATACATTCTTTCCAGAGCCAATGCCGTTTTTATTTTCA	core
8[151]	0[144]	GTACATAACCGTGTGATTAATTTCACGCTCAAGTAATAAG	core/Pt
9[73]	18[72]	GAAATTAGTAAGCGTGGTCAGACTCAGTACCCCTCAGAGACAAACTA	core/Pt
10[119]	6[104]	AATTAAGCCTTATTACAGGCAGAGAGATAACC	core
11[76]	16[64]	TCGGCCTCCCTCAGAGCCGACCGCCACAGGCGGAT	core
11[117]	4[120]	TTTGCACGTAAAAAATCATGCAGTATGTTTTAATT	core
11[152]	2[152]	GATTTTCAGACGCTGAGTAAATCGTATTTTAGTAAATAAGTATCATAT	core
14[55]	5[55]	ATGATACAAGGGAGGGCCGGAAACGAAGGAAATAGCAATAAAGCGCAT	core/Pt
14[151]	5[151]	TAAAAGTTATGATGAAGAATACCATTGCTTCTGAAGAGTCGCTTAGG	core/Pt
15[72]	22[72]	AACCTATTTCTCCAAAGCTAAACAAACCTAAA	core
17[56]	8[56]	CCTCAGACCACCCTCCAGGAGGTAGCAAGGAAGGTAAAAGTTTAT	core
17[152]	8[152]	CATCACCTTTCTGAATTCATCATAATTGCTTTACAAACATTGGAAACA	core
18[71]	22[64]	CAACGCCTGTCGAAAACGAAAG	core
19[64]	21[75]	GGATTTTAAAAAGGCACAACCATCGC	core
20[55]	11[55]	GGAGCCTTTTAATGCCGTCGAGAGAGCATTGAAGAACCGCGACTGTAG	core/Pt
20[151]	11[151]	CTGAAAGCTTGAGGATTTATCTAACGGAATTAAATGGAAGTTGCGTA	core/Pt
21[76]	19[87]	CCACGCATAACCAAGGCACCACTTTCAA	core
23[56]	14[56]	TAAATTGTGTAGCATTCTGTATGAAGTGCCCCCTGCCTGCTTTTG	core
23[72]	28[64]	TCCGCGACCGAACTGACCAACTTGTTTTGCCACATAACG	core
23[152]	14[152]	AACGAGGGGAGGTGAGCGAACTGAGAGGAAGGTTAGAAGTATTAATTT	core
25[144]	23[151]	TGAGGCCAGCTACAGAGCATCGG	core/Pt
26[55]	17[55]	GAATTACCTGCGCCGAGAATACACATGAATTTTCCACAGAACCGCCAC	core/Pt
26[151]	17[151]	GGATTTTATTACATTGGCAACAGGTTAATGCGGCGGTCAGTCTAAAG	core
29[56]	20[56]	AAAAGAATGAAAGAGATATTCATAGGCAAAACAATGACATCCAAAA	core
29[152]	20[152]	AAAGGGAGTAGCAACGCCGAGTAACAGCCATTGCAGATTCCTTCTGAC	core
30[71]	39[71]	GACCATAATAAAGCCTTTCATTTTCTAGCTTGTCAATCCGCATTA	core
30[103]	39[103]	CAAATGCTGTACCAAATCGCAAATGCTATTTTAGAATCGATTTAACCA	core

N.B. Staples annotated with core/Pt have been substituted with 15xA handles for Pt localisation in some experiments.

...continued from previous page

Start	End	Sequence	Location
30[135]	37[135]	GAGGTGCCCGTTGCGCGTGAGACGGTCCATAG	core
30[167]	34[160]	AACCATCAAAACCTGTTTGGGCGC	core
31[64]	33[71]	AATATCGATTGCTCCGTGTCTG	core
31[102]	36[103]	ACCGGAAAGTGATACATTAACATTATATTTCAACG	core
32[55]	23[55]	AAGAGGTCATAAAACGGAATTACGAGAACCGGGACAGATGTCGCCTGA	core/Pt
32[79]	36[72]	TACCTTTACGTTTTAAAGCTATATTCAGAGCACTCATATA	core
32[139]	38[136]	AAATCAAAAGAAGCTGATTGCCCTTCCGTAATC	core
33[40]	41[55]	TTTTAAATGATAATCAACCATCAACCGTAATGGAGGGGACGACGACAG	core
33[72]	41[87]	GAAGTTTCAACTAGCAGATAAATTGGATTCTCGATCGCACTCCAGCCA	core
33[104]	41[115]	ATTCTGCGCAAACAAGTGAGAGATCAACATTATCTGGTGCCGGA	core
35[56]	26[56]	TTAAGCAAATCAAAAAGACTTCACCAAAAGAACTAACGTCATTGT	core
35[152]	26[152]	CAGTCGGGCCCAAATCGTGGACTCGGAAGGGAGGGCGCGTGATTAAAG	core
36[71]	38[56]	TTTTAAACTCAGGAACGTGGGAACAAACGGTTAAAATTATATGTA	core
36[102]	38[86]	CAAGGATGCACCGCTAATGTGAGCGAGTAACGCTCATTTTGAACGGTAA	core
36[135]	40[120]	ATTAATTGCGCCATTCGCCTTCCTGTAGCCA	core
36[167]	38[152]	CCTGGGGTGGGAAGGGGCAAGGCGATTAAGTTTTGTAAAAGTACCGAG	core
37[136]	41[151]	CTGTTTCCCAGGGTTGCCATTCAGGCTGCG	core/Pt
38[55]	29[55]	CCCCGGTTATGCAACTGAGCTGAAAGCCCGAAATCAGGTCGCTTTTGC	core
38[119]	32[120]	GTCTGGAGAACGAGTAGATTTAACATAGCCCG	core
38[135]	39[143]	ATGGTATTCGCGTCTGTTCCCAG	core
39[40]	35[55]	AAACGTTAATATTTTGCGGATTGATATGATATCTGAGTAATAGCAAAA	core/Pt
39[72]	35[87]	AATTTTTGTTAAATCAAACCCGTCAATGCCGGTTAGAACCTAAAGCTA	core
39[104]	38[120]	ATAGGAACGCCATCAAAAATAATTGCCTGAGA	core
39[144]	35[151]	TCACGACGGGGTAACGCTGTGTGAAGTGAGCTCGCTTTC	core/Pt
40[119]	35[119]	GCTTTCATCTACAAAGAAGCCTTTGACCCTGT	core
41[56]	32[56]	TATCGGCTGCAATGCTCAACCGTGGGGCGCAAAGTACGTTTTGAT	core
41[88]	33[103]	GCTTTCCGAAAAATTTAGAGGGTAGGTCAATATAACAGTTGATTCCCA	core
41[116]	34[120]	AACCAGGCAAAGTGCGGGAGGCTATCAGGGCAGTTT	core
41[152]	37[159]	CAACTGTTGCCTAATGAATTGTTA	core
3[104]	13[103]	AACGAGCGACATAAAGTAAGACTCCATTTGGGAATTAGAGCACAAACA	core
10[135]	16[136]	AAATCGCGAACCACCAGAAGGAGAATATCT	core
13[88]	10[80]	TTGATATTCCAGCAAAATCACCAG	core
13[104]	19[103]	AATAAATCCAAGAGAAGGATTAGGGCGGAGTG	core
16[127]	10[120]	ACTAACAACTAATCCTCTCATTAAAACAAAGACAGAGGCG	core
19[88]	13[87]	CAGTTTCAATTAGCGGGGTTTTGCGATTGGCC	core
19[104]	19[127]	AGAATAGAAAGGAACATATTTTTG	core
22[103]	31[101]	ACGTAATGCAGTGAATAAGGCTTGTAGCGGTCATTTAGGAAACCAG	core
22[131]	28[136]	TGGATGTTTTTATAATCAGAAAGGAG	core
28[119]	22[120]	GGCAAGTGCCCTGACGCTGAGAAGAATACCTA	core
28[135]	36[136]	CGGGCGCTACAAGAGTCCACTATTTCACCATCACTGCCAACTCAC	core/Pt
34[119]	28[120]	GACCATTAGTTGTTCCAGTTTGGAAGGGCGCT	core
38[85]	28[85]	TCGTAAATTCCATAACCTGTTTTTCGAGCTTCAAAGCGATACCACATTC	core
0[175]	4[160]	TTAGGCAGAGGCATTTTATAACTATTCAAATA	core
1[32]	3[39]	AATTTACGGCGAGGCGTGAAGCCT	core/Pt
33[168]	41[175]	AGCAAGCGTCTAGAGGCAATTCCAGATGTGCTCGATCGGT	core
36[39]	40[32]	TAAAGATTGCCAGTTTGGATAGGT	core
37[160]	39[175]	TCCGCTCAATCCCCGGCGACGGCCAGTGCCAA	core/Pt
6[103]	12[104]	CACAAGAAAGCGTTTGCCATCTTTAATCACCG	core/Pt
9[96]	14[104]	TATCACCGTCACCGACTGGAAAGC	core
12[103]	17[111]	GAACCAGACAGGGATAGCAAGCCC	core
14[87]	8[88]	CCGTTCCATTCATTAAAGGTGAATATATAAAA	core
14[103]	15[119]	GCAGTCTCGTATTAAGAGGCTGAGACTAGATT	core
15[120]	8[120]	AGAGCCGTTTTTGCGGAGCCAGAATTGTTCATTTCAATTAAACGTAGA	core
17[88]	11[95]	CTCATTTTGCCACCACCGGAACCGTCATAGCCCCCTTATT	core
17[112]	11[116]	AATAGCGCTGAGAGCCTATCAAAATTAATCAATCATA	core
18[103]	17[87]	GTAACACTGAGTTTCGTCACCAGTCCACCACC	core/Pt
20[100]	14[88]	ATAATTTTTTCACGTTGAAAAATTCTGAAACATGAAATGAATTTA	core
24[134]	30[136]	GGACTAAGTAAAGCACTAAATCGTGGGGTC	core
26[103]	32[104]	GTAGTAAACAGTTGAGACGCTGCGTTGGCAAA	core

Table A.2: Continued from previous page

Start	End	Sequence	Location
27[73]	26[80]	TTATTACAGGTAGAAAGATTCATTTGGGCTTGAGATGGT	core
27[128]	28[144]	GCCGCGCTTAATGCGCCGCTACAAGAAAGCG	core
29[88]	30[104]	AAATGTTTAGACTGGATAGCGTCCATCCCCCT	core
32[103]	32[80]	CTCCAACAGGTCAGGATTAGAGAG	core
32[119]	27[127]	AGATAGGGCGTAACCACCACACCC	core
35[88]	29[87]	AATCGGTTTTAAACAGTTCAGAAATAATAGTA	core
35[120]	29[119]	AATACTTTCATAAATATTCATTGAAATACTGC	core
18[134]	18[104]	CCGCCTGCAACAGTGCCAGAACCCATGTACC	core
21[115]	20[101]	TGACGCTCAATCGACAGACAAACTAAAGGAATTGCGAATA	core
26[129]	26[104]	CGCCAGAATCAGAAACACCAGAACGA	core
29[120]	24[101]	GGAATCGTAGACTTTTTCATGAGGAAGTTGGCGCA	core
12[135]	18[135]	ACCTACCAAGCAGCAAATGAAAAATATTAACA	core/Pt
16[135]	24[135]	TTAGGAGCAATGGCTATTAGTCTAAAAACGGAAAGACAGGCTTTGA	core/Pt
24[100]	23[99]	GACGGTCAATCATAAGGGAACCTGCTCCATGTTACTTAGCC	core/Pt
14[139]	20[131]	TAACATTATCACAATAGATAATACATGTAAGAATACGT	core
20[130]	26[130]	GGCTCTGAAATGGATTATGACAGGAACGGTA	core
28[84]	21[105]	AACTAAACAAAGCTGCTCATTCCACTACGGATATATTCGGTCGCTGA	core
3[72]	11[75]	GCTACAATAAGACACCAATAACGGTAGCACCAATTT	core
7[136]	12[136]	AATAACCAGTTACATAAAGAAAGGTTAGA	core
26[79]	30[72]	TTAATTTCATCAACGTATGCAGATAGAGGGGGACGAGAAT	core/Pt
38[151]	29[151]	CTCGAATTACCGCCTGTTTTTCTTTAAAGAACAAGTTTTTGAACCCT	core/Pt
3[136]	14[140]	ATACCGAATCAATATATGTGCACCTGAGCAAAAGAAGTGAG	core
11[56]	9[72]	CGCGTTTCAATGAAACCGAGGAAACGCAATACGGAATATATTGACG	core
25[64]	27[72]	TACCCAAAACTTTAAGAACAACA	core
34[159]	32[140]	CAGGGTGGGCCCTGAGAAATCGGCAAAATCCCTTAT	core
0[190]	0[176]	CTGCCAACATGTAAT	core
1[17]	1[31]	CTAATATCCCATCCT	core
2[188]	2[176]	CTCCCATAATTACTA	core
3[14]	2[14]	CTGACTTGCGGGAGGTTTTTTTAGCGAACCTCCCTC	core
4[196]	1[190]	CTGCAAGACAAAGAACGCGAGCATATTTAACAACTC	core
5[22]	0[17]	CTAGAGAGAAGAACAAGAAAAATTC	core
6[190]	5[196]	CTCTTGAAAACATAGTGCTGATGCAAATCCAATCTC	core
7[17]	4[22]	CTAGTAAGCAGATAGGCCTTTACTC	core
8[188]	3[188]	CTCAATTTCATTTAACACCGGAATTC	core
10[196]	7[190]	CCTTTTACATCGGGAGAAACATTCCCTTAGAATCTC	core
12[190]	11[196]	CTCAATATAATCCTGAATATACAGTAACAGTACCTC	core
14[188]	9[188]	CTTCGTATTAAATATTACATTTAATC	core
15[14]	14[14]	CTAGTGCCTTGAGTAACAAAGTTTTAACGGGGTCTC	core
16[196]	13[190]	CTCTGGTCAGTTGGCAAATCAGATGGCAATTCATTC	core
17[11]	12[17]	CTCCGTACTCAGGAGGTTTAGACCCTCAGAGCCGTC	core
18[190]	17[196]	CTCGAACGAACCACCTCAAACCCTCAATCAATATTC	core
19[17]	16[11]	CTAGTTTTGTCGTCTGCCCGGAATAGGTGTATCATC	core
20[188]	15[188]	CTGACATTCTGGCAATTCGACAACTC	core
21[106]	22[132]	GGCTTGCAGGGAGTTAAAGGCCGCTTTTGCGGGATCGTCACCCTCAGCAGCCTCA	core
22[196]	19[190]	CTGGCCTTGCTGGTAATATCCCCATTAAAAATACTC	core
24[190]	23[196]	CCTTGTAGCAATACTTAGAAGAACTCAAACTATCTC	core
26[198]	21[188]	CTCCTCGTTAGAATCAGAGCGGGGTAATAAAAGGTC	core
27[14]	26[14]	CTAGTCAGGACGTTGGGAACTGGCTCATTATACCTC	core
27[176]	27[198]	CGAGCACGTATAACGTGCTTTCC	core
28[185]	25[190]	CTAAAGCCGGCGCAAATTAACCGTC	core
29[11]	24[17]	CCTTACCAGACGACGATAAAAGGCGCATAGGCTGTC	core
30[189]	29[185]	CTGGGCGATGGCCCTGACGGGGTC	core
31[17]	28[11]	CTAGCGGATTGCATCACACTATCATAACCCTCGTTC	core
32[188]	32[176]	CCTTTGCCCCAGCAGGCGAAAATCCTG	core
33[14]	32[14]	CTAATATAATGCTGTAGCTAGAGCTTAATTGCTGTC	core
34[196]	31[191]	CTAACGCGCGGGGAGAGGCGGAAAACCGTCTATCATC	core
35[11]	30[17]	CTAACATCCAATAAATCATACTAGTCAGAAGCAATC	core
36[190]	35[196]	CTCCGGAAGCATAAACTGCATTAATGAATCGGCCTC	core
38[188]	33[188]	CTTGCAGGTCGACGTCCACGCTGGTC	core
39[176]	39[188]	GCTTGCATGCCTCTC	core
40[31]	40[11]	CACGTTGGTGTAGATGGGCTC	core
40[196]	37[190]	CTCGCCAGCTGGCGAAAGGGGCACAACATACGAGTC	core

Table A.3: Continued from previous page

Start	End	Sequence	Location
2[55]	6[40]	CCGGTATTCTAAGAACAGCATGTAAAAAATGAAAACAGGGGCTATCTTATGTAGGTGGTAGAG	Cy3 handles
5[152]	3[167]	TTGGGTTATCGAGCCACAGTAGGGCTTAATTGCTGTTTAGGCGTTAAAATGTAGGTGGTAGAG	Cy3 handles
6[167]	15[167]	TAGATTAAGGTTTAACTTCGCCTGTTCCTGATCGAACGTTATTAGACTATGTAGGTGGTAGAG	Cy3 handles
8[55]	0[40]	TTTGTCACGATTAGTTTTAACGTCGAAACCAAGTTTATCAACAATAGAATGTAGGTGGTAGAG	Cy3 handles
12[167]	21[167]	GATTATACTGCTGAACAAGGAATTTAGCCCTAATAGAACCACCAGTCAATGTAGGTGGTAGAG	Cy3 handles
15[40]	24[40]	ATAAACAGTAATTGTAGTTAGTAATAAAACACTTGTATCAAACGGTGTATGTAGGTGGTAGAGGAG	Cy3 handles
24[167]	33[167]	TAGTAATACCCCCGATGCGAGAAACAACGTCATGGTTCCGAGAGTTGCATGTAGGTGGTAGAG	Cy3 handles
18[167]	27[167]	ATAAAACAACATCACTATTACCGCAAGAGTCTAGGAGGCCACTATGGTATGTAGGTGGTAGAG	Cy3 handles
21[40]	30[40]	CCGATAGTTTATGCGATCTTGACAAGGCATAGAGCGAGAGTTTACCCTATGTAGGTGGTAGAG	Cy3 handles
27[40]	36[40]	CTACGTTAATTTTTGCTAAGAGGAAAGGTGGCCAAAGAATTGTGTAGGATGTAGGTGGTAGAG	Cy3 handles
0[39]	9[39]	TAAGTCCTTAACATAAAAATAGCACCGAACAAGAAAATTCGACATTCAATGTAGGTGGTAGAG	Cy3 handles
1[32]	3[39]	GAAAAAGCAGAATCGCAAAACTTTTATGTAAACGATAGCTATGTAGGTGGTAGAG	Cy3 handles
3[40]	12[40]	TAAATCAAAATCAATAAGTTACCAGTCACCAATAGCGTCACACCCTCAATGTAGGTGGTA	Cy3 handles
3[168]	12[168]	TAAGAATAGAATTACCAATTAATTATAACGGAGTCAGATGATTGTTTGATGTAGGTGGTAGAG	Cy3 handles
6[39]	15[39]	ACCGAAGCTTTGCCTTTGAAACCACACCAGAGCTGGTAATGTGCCCGTATGTAGGTGGTAGAG	Cy3 handles
9[168]	18[168]	CAAAATTACCTTTGCCTATCAGATACAGTTGACTCAAATAAGCAGAAGATGTAGGTGGTAGAGGAG	Cy3 handles
12[39]	21[39]	GAGCCACCTACCGCCATAAGTATATTCCAGACTCGGTTTAGCTTGATAATGTAGGTGGTAGAG	Cy3 handles
15[168]	24[168]	TTACAAACCAACAGAGAAACATCGAGAACAATTGCCTGAGTCTTTGATATGTAGGTGGTAGAGGAG	Cy3 handles
18[39]	27[39]	ATAGTTAGACGGAGATTCATCTTTAAGAGTAATTTTAAGAAGAAAAATATGTAGGTGGTAGAG	Cy3 handles
9[40]	18[40]	ACCGATTGGGAGTGTACCGCCGCCGGTTGATACCCTCAGACAGCCCTCATGTAGGTGGTAGAGGAG	Cy3 handles
21[168]	30[168]	CACGACCAAGCTAAACGTCCATCACGAACGTGTTAGAGCTACTACGTGATGTAGGTGGTAGAG	Cy3 handles
24[39]	33[39]	ACAGACCAACCAAAATTAAGAGCAAAAAAGATGGATGGCTTCAACATGATGTAGGTGGTAGAG	Cy3 handles
27[168]	36[168]	TGCTTTGATTTGATGGAAGGGCGATTTGCGTACGTGCCAGGTGTAAAGATGTAGGTGGTAGAG	Cy3 handles
30[39]	39[39]	GACTATTAAGGCAAGGATCAATTCGTCAAATCGAAAAGCCTAAATTGTATGTAGGTGGTAGAG	Cy3 handles
9[14]	8[14]	CTCCAAAGACAAAAGGGCATATGGTTTACCAGCGTCTTCTTAAATATTCGTCTT	Catalyst handles
11[11]	6[17]	CTCAGTAGCGACAGAATCAAGCCTTTTTAAGAAATCTTCTTAAATATTCGTCTT	Catalyst handles
13[17]	10[11]	CTCCACCAGAACCACTCGATAGCAGCACCGTAATTCTTCTTAAATATTCGTCTT	Catalyst handles
21[14]	20[14]	CTGTGAATTTCTTAAACATCAGCTTGCTTTCGAGTCTTCTTAAATATTCGTCTT	Catalyst handles
23[11]	18[17]	CTAAGCGCGAAACAAAGTACACGTAACGATCTAATCTTCTTAAATATTCGTCTT	Catalyst handles
25[17]	22[11]	CTGCTGACCTTCATCGACCCCCAGCGATTATACCTCTTCTTAAATATTCGTCTT	Catalyst handles
37[17]	34[11]	CTAAGGCCGGAGACATACTAATAGTAGTAGCATTCCTTCTTAAATATTCGTCTT	Catalyst handles
39[14]	38[14]	CTTGTATAAGCAAATATTCCAAAAACAGGAAGATTCTTCTTAAATATTCGTCTT	Catalyst handles
41[11]	36[17]	CTGCATCGTAACCGTGCATCTCAAAAGGGTGAGATCTTCTTAAATATTCGTCTT	Catalyst handles

A.9 Mixture protocols for DNA wave and Predator-Prey experiments

The following master-mix was used for Predator-Prey and DNA wave experiments in chapter 4.

A.9.1 Predator-Prey buffermix (universal)

Predator-Prey mix			
	Stock	Vol (μl)	Final (4X)
Thermopol buffer	10x	400	4X
NaCl	5M	40	0.2 M
$MgSO_4$	1 M	24	0.02M
Symperonic	4%	100	0.40%
dNTP	10 mM	160	1.6mM
Netropsin	200uM	20	4uM
H_2O		256	
	Total	1000	

A.9.2 Autocatalytic reaction Master Mix

Table A.4: Mastermix for all reaction in this report

Master mix (2X)	vol (μL)	final conc in reaction tube (%)
H_2O	11.88	
PPBuffer (4X)	33.00	25 %
EVaGreen 20X	6.60	5
DTT (300 mM)	1.32	1 %
d autocatalyst (1 uM)	0.00	0 %
Template (10 uM)	1.32	10% (or 0 if functionalised on surface)
BSA (AET 100 X, 10 mg/mL)	6.60	5 %
Bst/5	1.32	1 %
Nt.Bst NBI	3.96	3 %
ttRecJ	0.00	0 %
Total reaction vol (uL)	66.0	
Total reaction vol (uL)	132.0	

B

Codes

B.1 Simulation of Dynamic Light Scattering

This code written in MATLAB simulates the far-field intensity of diffusing scatterers. The autocorrelation function is calculated with the built-in "xcorr" function. References: [226, 227]

```matlab
% Simulation Parameters (SI units)
lambda=830e-9;% lambda of the scattering light
countPoints=50;%number of diffusing particles
Steps = 100000;
tDel = 1.0e-5; %time steps in seconds
R = 0.2e-6; %radius
vis = 0.001002;%viscosity of water
kB = 1.3806488e-23;%Boltzmann constant
temp = 293;% Room temperature in K
D = (kB * temp)/(6*pi*vis*R);
q = 4*pi*1.33*sin(pi/2)/lambda;%q scattering wave vector for theta=90 degrees
decayC = D * q^2; %decay constant [1/s]
Time = Steps*tDel; %[s]
n=1.33
sq = sqrt(2*D*tDel);
%Generate an array of uniformly distributed random numbers
ptRandArr = rand(3,countPoints);
xInitial = 1e-6 - (2e-6) * ptRandArr(1,:);
yInitial = 1e-6 - (2e-6) * ptRandArr(2,:);
zInitial = 1e-6 - (2e-6) * ptRandArr(3,:);
ptArray = [xInitial; yInitial; zInitial];
%Find the intensity due to the initial positions of the particles
intenTime = zeros(1,Steps+1);
```

```
intenTime(1,1) = simIn(ptArray,lambda,n);
%At each timeStep, follow Brownian motion
%and calculate the intensity from  new arrangemente
for t = 1:Steps
%Array of normally distributed random numbers
randArr = randn(3,countPoints);
%Updating the xyz-coord
ptArray(1,:) = ptArray(1,:) + sq.*randArr(1,:);
ptArray(2,:) = ptArray(2,:) + sq.*randArr(2,:);
ptArray(3,:) = ptArray(3,:) + sq.*randArr(3,:);
%Finding the intensity from new arrangement
intenTime(1,t+1) = simIn(ptArray,lambda,n);
end
%Plot the intensity versus time
figure(1)
tm = 0:tDel:Time; %Setting a time axis
plot(tm,intenTime,'-')
%Plot the autocorrelation function
intenTime=intenTime-mean(intenTime);
figure(2)
[ac,lags]=xcorr(intenTime,'unbiased');
ac=ac/ac(Steps);
plot(lags(Steps:(Steps+2000))*1e-5,ac(Steps:(Steps+2000)), '*')
%%%
function [ ptIntensity ] = simIn(ptArray, wavelength, n)
%Calculate the intensity at far field
ii = sqrt(-1); pha=((2*pi*n)/wavelength)*(ptArray(3,:)+ptArray(1,:));
Etotal=sum(exp(ii*pha));
ptIntensity = Etotal * conj(Etotal);
end
```

B.2 Fluorescence Correlation Spectroscopy Data Analysis

R code for extraction of autocorrelation data from the digital correlator (Flex, Correlator). The data is then fitted to a a 3D diffusion model in a confocal volume and diffusion times are extracted from the fits and presented on a table. The Levenberg-Marquard algorithm fitting package (minipack.lm) and a standard R plotting packages (ggplot) are needed to run this code.

```
############################################################
# Fluorescence Correlation Spectroscopy Data Analysis (written in R)
# Read, debug and analyse .SIN files from Digital Correlator (Flex)
# Ibon Santiago
# January 2015
```

```
#
library(minpack.lm)            # Levenberg-Marquard algorithm
library(gsubfn)                # To import specific rows from the SIN file

#READ FILES FROM INPUT FOLDER
wd = "working directory"
namefiles = dir("")
n_files = length(namefiles)
setwd(wd)
exp_data = NULL

### Read ".SIN" file
#   Regular expression of the rows to be extracted
pat="^([0-9]*\\.[0-9]+[e][-+]?[0-9]+)\\s+([0-9]*\\.[0-9]+[e][-+]?[0-9]+)$"

for (f in 1:n_files)
{
    read_data <- read.pattern(namefiles[f],pattern = pat, as.is = TRUE )
    names(read_data) <- c("tau", "Obs_corr")
    read_data$Obs_corr = read_data$Obs_corr-1
    read_data$exp <- f
    exp_data = rbind(exp_data,data.frame(read_data))
}
### change directory to Output
wd = "Output directory"
setwd(wd)

DATA1 <- subset(exp_data, tau>0.00001)
# Delete negative values Obs_corr= -1
DATA1 <- subset(DATA1, !(Obs_corr==-1))

results_fits = NULL
table_fits = NULL
for (f in 1:n_files)
{
    DATA2 <- subset(DATA1, exp == f)
    mod <- nlsLM(Obs_corr ~ 1/(a*(1+ tau/b)*sqrt(1+tau/(SP*SP*b))),
    data = DATA2, start=c(a=0.8,b=0.0003),trace=TRUE)
    #
    # Results and Normalization
    #
    DATA2$Obs_norm = DATA2$Obs_corr*coef(mod)[1]
    DATA2$Fit_norm = fitted(mod)*coef(mod)[1]
    # Include expected values in the data frame
    results_fits = rbind(results_fits,DATA2)
    table_fits = rbind(table_fits,data.frame(f,coef(mod)[1],coef(mod)[2],
    confint(mod)[1,1], confint(mod)[1,2], confint(mod)[2,1], confint(mod)[2,2],
    summary(mod)$parameters[1,2],summary(mod)$parameters[2,2],
    logLik(mod),df.residual(mod),
    row.names=NULL))
}
#
# RESULTS - Figures
#
library(ggplot2)
```

```
# Raw data
jpg("scatterplot.jpg",width = 10, height = 6, units = 'in', res = 500)
p1 <- qplot(tau, Obs_norm, data = results_fits,
colour = factor(exp), geom="point")+geom_point(aes(size=1)
p1 <- p1 + scale_x_log10()
p1 <- p1 + scale_y_continuous(limits = c(0,1))
print(p1)
dev.off()
# Fitted curves
png("fits.jpg",width = 6, height = 6, units = 'in', res = 300)
p2 <- qplot(tau, Fit_norm, data = results_fits,
colour = factor(exp),geom="path")
p2 <- p2 + scale_x_continuous(limits = c(0,1))+ scale_x_log10()
p2 <- p2 + scale_y_continuous(limits = c(0,1))
print(p2)
dev.off()
#
# RESULTS - Table
#
names(table_fits) <- c("fit number","M","tau_diff", "LL-M",
"UL-M", "LL-tau_diff", "UL-tau_diff",
"Std. Error-M","Std. Error-tau_diff", "logLik", "df_residul" )
write.table(table_fits, file = "Table Fits.csv", sep = ",")
tau_diff_MEAN =mean(table_fits$tau_diff)
tau_diff_SD =sd(table_fits$tau_diff)
```

B.3 Fast Fourier Transform

The code below, written in MATLAB gives the 2D FFT of a 15 nm diameter disk. The second part of the code can be used to calculate the 2DFFT of an image (imageA). This section reproduces Figures 5.26 and 5.25.

```
%%2D Fast Fourier Transform of a 15 nm diameter disk
%%Ibon Santiago

u_FFT = @(N) single((-1/2):(1/N):(1/2 - 1/N)); % centered unity
% ==== START:  Inputs
N = 2^10;       % FFT size
L = 200;      % Total spatial size [nm]
D = 15;          % Diameter of specified spatial pattern [nm]
% ==== END:    Inputs
% Establishing coordinates and resolutions
dx = L/N;                     % spatial resolution [nm]
x = ( N*u_FFT(N) )*dx;        % 1D spatial coordinate [nm]
df = 1/N/dx;                  % resolution in frequency plane [1/nm]
f = ( N*u_FFT(N) )*df;        % 1D spatial freq. coordinate [1/nm]
funit=1:N;
funit=funit.*1/(N*dx)
dx2 = 1/N/df;                 % inverse-transformed spatial resolution [nm]
```

```
 x2 = (N*u_FFT(N) )*dx2;     % inverse-transformed spatial coordinate [nm]
 f_Nyq = 1/2/dx;             % max observable (+/-) spatial freq. [1/nm]
 % Establishing input spatial function, and performing transformations
 [X,Y] = meshgrid(x,x);      % 2D spatial coordinates [nm]
 rho = sqrt(X.^2 + Y.^2);    % 2D radius [nm]
 g = zeros(size(X));         % Initialize amplitude matrix
 g(rho<=D/2) = 1;            % Specify amplitude pattern.
 F = dx^2*fftshift(fft2(g)); % Perform Fourier Transform: spatial->freq
 G = dx^2*fft2(g);
 % Plot FFT
plot(1)
 imagesc(f,f,(abs(F).^2).^.2);axis('square');
 xlabel('f_x [1/mm]'); ylabel('f_y [1/mm]');

%%%%%FFT of TEM image %%%%%%

pix2nm=1/1.952;  %Enter here how many pixels per nanometer
nx = size(imageA, 2);%Size of x axis (same as original image)
ny = size(imageA, 1);%Size of y axis (same as original image)

dFx = 1/(pix2nm*nx);              % cycles per nanometer
dFy = 1/(pix2nm*ny);

Fx=(-nx/2:nx/2-1)*(1/nx)
Fy=(-ny/2:ny/2-1)*(1/ny)
%calculate magnitude of fft2 and shift low frequency components of fft2 to
%the center by using "fftshift"
F=fft2(imageA);
F=abs(fftshift(F));
%calculate log of output to get data below 1.
F=log(F);
F = mat2gray(F); % Use mat2gray to scale the image between 0 and 1
imagesc(Fx,Fy,F);
```

B.4 Radial Distribution Calculation (RDF)

This code is to be used with TEM micrographs converted into a binary image using ImageJ (NIH; Bethseda, USA). This MATLAB routine locates centroids of nanoflowers and generates a list of distances. Running a peakfinder algorithm on this list, nearest-neighbour peaks can be located.

```
%RADIAL DISTRIBUTION FUNCTION (RDF) CALCULATION
%Lattice analysis Nanoflower paper
Scale=0.512;  %Enter scale of image
Neighbour=165; %Threshold distance in pixe for neighbour
Neighbour=Neighbour/Scale;
n=4   %Connectivity. E.g. for square lattice
%Please insert binary image with nanoparticles
```

```
ImgTEM=imread('square_lattice.tif');
[Ilabel,numObjects] = bwlabel(ImgTEM,n);% Find particles
particle=regionprops(Ilabel, 'centroid'); %Computes centroid
[SizeY SizeX] = size(Ilabel);
%SHOWS CENTROIDS AND IMAGE
imshow(Ilabel); hold on;
for x = 1: numel(particle)
plot(particle(x).Centroid(1),particle(x).Centroid(2),'ro');
end
%CALCULATE INTERPARTICLE DISTANCE IN A GIVEN NEIGHBOURHOOD
npar=numObjects
%DOUBLE LOOP
contador=1;
for i=1:npar-1
for j=i+1:npar
Distance=sqrt( ( particle(i).Centroid(1) - particle(j).Centroid(1) )^2
+ ( particle(i).Centroid(2) - particle(j).Centroid(2) )^2 );
if (Distance<=Neighbour)
Dist(contador)=Distance;
contador=contador+1;
end
end
end
%FORM HISTOGRAM WITH DISTANCE list
[HistCont, xout] = hist(Dist,200);
%FINDPEAK ALGORITHM, e.g.
[pks,loc]=findpeaks(HistCont,4,'MinPeakDistance',10)
```

B.5 Peak frequency analysis

B.5.1 Average number of spikes

This code takes the list of peak counts, generates a histogram of number of peaks per 1000 observations and resamples 10000 times (bootstrapping method).

```
library(fitdistrplus) # fitdist
spikes0 <- read.table("filename",header=TRUE, sep=",", dec=".") #no fuel
spikesH <- read.table("filename",header=TRUE, sep=",", dec=".")#with fuel

#Sample with sample size = n / m times ---------
#
n <- 1000   # Sample size
m <- 10000   # Number of replicates
#change to spikesH or spikes 0
s <- replicate(m,sum(sample(spikes0$peak, n, replace = TRUE, prob = NULL)))
sH <- replicate(m,sum(sample(spikesH$peak, n, replace = TRUE, prob = NULL)))
#
##
# Fit normal distribution
```

```
fitg0 <- fitdist(s, "norm")
fitgH <- fitdist(sH, "norm")
par(mfrow=c(2,1))

denscomp(fitg0, xlim=c(0, 20), xlab="Number of peaks",main="",
cex.lab=1.8, cex.axis=1.8,label="")
mtext("(e)", side=3, adj=0, line=1.2, cex=2, font=0.5);

denscomp(fitgH, xlim=c(0, 20),ylim=c(0, 0.15),
xlab="Number of peaks",main="",cex.lab=1.8, cex.axis=1.8,label="")
mtext("(f)", side=3, adj=0, line=1.2, cex=2, font=0.5)
```

B.5.2 Interspike interval

Inter-spike interval histograms are extracted by counting the number of inter-spike intervals falling in various time bins. Assuming collision events are independent from each other and follow a homogeneous Poisson distribution, the interspike interval is given by an exponential decay function e^{-rt}.

```
library(fitdistrplus) # fitdist
intervals <- read.table("Desktop/intervals.csv",header=TRUE, sep=",", dec=".")

int1 <- round(intervals$peakintervals1[!is.na(intervals$peakintervals1)],2)
int2 <- intervals$peakintervals2[!is.na(intervals$peakintervals2)]

nint1<-int1[int1>0.3]
nint2<-int2[int2>0.3]


fitg1 <- fitdist(nint1,"exp")
fitg2 <- fitdist(nint2,"exp")
par(mfrow=c(1,2))


denscomp(fitg1, xlim=c(0, 10),nclass=200,ylim=c(0,1),
xlab="Inter-spike time interval (s)",main="",cex.lab=1.5, cex.axis=1.5)
mtext("(a)", side=3, adj=0, line=1, cex=2, font=0.5);

denscomp(fitg2, xlim=c(0, 10),nclass=100,ylim=c(0,1),
xlab="Inter-spike time interval (s)",main="",cex.lab=1.5, cex.axis=1.5)
mtext("(b)", side=3, adj=0, line=1, cex=2, font=0.5);
```

B.6 Numerical solutions to the FKP equation

For given initial conditions and rate equation, this code produces numerical solutions to the Fisher-Kolmogorov-Piskunov (FKP) equation (4.21). By changing the functional form of the rate $k(x)$, the numerical solution in Figure 4.9 are reproduced. Code written in ‘Mathematica’.

```
(*Experimental parameters*)
(***********************)
L=LMaxMM = 20; (* size in x in mm*)
tMaxMin=600; (*time in min*)
polPerCent = 1; (*Polymerase concentration*)
T1= 200;        (*(nM)Template conc *)
T2 = T1;
k1    = 0.067;   (*(min-1) growth rate*)
(*3 growth rate fitted by logarithm equal to k1*T*pol*)
b = 1/500;
mm2m = 1*^-3; sec2min = 1/60;
Nl = 11 ; (*Number of bases in lapin*)
scalingDiffusion20Cto45C = 1.95;
D1rt = 7.8*^-3; (*mm2/min measurement of strand diffusion @ 20C*)
D1 = D1rt*scalingDiffusion20Cto45C ;

Monitor[S=NDSolve[
{(*First autocatalyst pde*)
D[d[x,t],t]==k1*(d[x,t])*(1 -b*d[x,t]) + D1*D[d[x,t],x,x],
(*For inhomogenoeus media
D[d[x,t],t]=k1*(keff[x]*d[x,t])*(1 -b*d[x,t]) + D1*D[d[x,t],x,x]*)
(*Second autocatalyst pde*)
d[x,0]==100*(1-1/(1+Exp[-100*(x-1)])), (*Approximates a heaviside function*)
(*dbit boundary conditions*)
(d^(1,0))[0,t]==0,(d^(1,0))[LMaxMM,t]==0},
{d},{x,0,LMaxMM},{t,0,tMaxMin} ,Compiled->True,
MaxStepFraction->.001,AccuracyGoal->3,Method->{"MethodOfLines",
"SpatialDiscretization"-> {"TensorProductGrid",
"MinPoints"->100,"DifferenceOrder" ->4}},
StepMonitor:>(sol=d[x,t]; time=t)],
Plot[sol,{x,0,LMaxMM},PlotRange->{0,1000},PlotLabel->time]];
Animate[Plot[{Evaluate[{d[x,t]}/.S]},{x,0,LMaxMM},
Filling->Axis,PlotRange->{0,1000},
PlotLabel->t], {t,0,tMaxMin},AnimationRate->20,AnimationRepetitions->1]
DensityPlot[Evaluate[d[x,t]/.S],{x,0,LMaxMM},{t,0,400},PlotPoints->80]
```

References

1. Miller, S. L. *et al.* A production of amino acids under possible primitive earth conditions. *Science* **117,** 528–529 (1953).
2. Brown, R. A Brief account of microscopical observations made in the months of June, July and August 1827 on the particles contained in the pollen of plants (1828).
3. Boltzmann, L. *Vorlesungen über gastheorie* (JA Barth, 1896).
4. Einstein, A. Über die von der molekularkinetischen Theorie der Wärme geforderte Bewegung von in ruhenden Flüssigkeiten suspendierten Teilchen. *Annalen der Physik* **322,** 549–560 (1905).
5. Von Smoluchowski, M. Zur kinetischen theorie der brownschen molekularbewegung und der suspensionen. *Annalen der physik* **326,** 756–780 (1906).
6. Perrin, J. L'agitation moléculaire et le mouvement brownien. *Comptes rendus hebdomadaires des séances de l'académie des sciences* **146,** 967–970 (1908).
7. Bustamante, C., Chemla, Y. R., Forde, N. R. & Izhaky, D. Mechanical processes in biochemistry. *Annual review of biochemistry* **73,** 705–748 (2004).
8. Marchetti, M. *et al.* Hydrodynamics of soft active matter. *Reviews of Modern Physics* **85,** 1143 (2013).
9. Balzani, V., Credi, A., Raymo, F. M. & Stoddart, J. F. Artificial molecular machines. *Angewandte Chemie International Edition* **39,** 3348–3391 (2000).
10. Bath, J., Green, S. J. & Turberfield, A. J. A free-running DNA motor powered by a nicking enzyme. *Angewandte Chemie* **117,** 4432–4435 (2005).
11. *Microswimmers – From Single Particle Motion to Collective Behaviour - Lecture Notes of the DFG SPP Summer School 2015* (eds Gompper, G. *et al.*) (Forschungszentrum Jülich GmbH Zentralbibliothek, Verlag, Jülich, 2015).
12. Howse, J. R. *et al.* Self-motile colloidal particles: from directed propulsion to random walk. *Physical review letters* **99,** 048102 (2007).
13. Dreyfus, R. *et al.* Microscopic artificial swimmers. *Nature* **437,** 862–865 (2005).
14. Bregulla, A. P., Yang, H. & Cichos, F. Stochastic Localization of Micro-Swimmers by Photon Nudging. *ACS Nano,* 6542–6550 (2014).
15. Palacci, J., Sacanna, S., Steinberg, A. P., Pine, D. J. & Chaikin, P. M. Living crystals of light-activated colloidal surfers. *Science* **339,** 936–940 (2013).
16. Berg, H. C. & Brown, D. A. Chemotaxis in Escherichia coli analysed by three-dimensional tracking. *Nature* **239,** 500–504 (1972).
17. Phillips, R. & Quake, S. R. The biological frontier of physics. *Physics Today* **59,** 38–43 (2006).

18. Webre, D. J., Wolanin, P. M. & Stock, J. B. Bacterial chemotaxis. *Current Biology* **13,** R47–R49 (2003).

19. Young, K. D. The selective value of bacterial shape. *Microbiology and molecular biology reviews* **70,** 660–703 (2006).

20. Dusenbery, D. B. *Living at Micro Scale: The Unexpected Physics of Being Small* (Harvard University Press, 2009).

21. Mitchell, J. G. The energetics and scaling of search strategies in bacteria. *The American Naturalist* **160,** 727–740 (2002).

22. Schreiber, R., Santiago, I., Ardavan, A. & Turberfield, A. J. Ordering Gold Nanoparticles with DNA Origami Nanoflowers. *ACS nano* **10,** 7303–7306 (2016).

23. Purcell, E. Life at low Reynolds number. *American Journal of Physics* **45,** 3–11 (1977).

24. Najafi, A. & Golestanian, R. Simple swimmer at low Reynolds number: Three linked spheres. *Physical Review E* **69,** 062901 (2004).

25. Turner, L., Ryu, W. S. & Berg, H. C. Real-time imaging of fluorescent flagellar filaments. *Journal of bacteriology* **182,** 2793–2801 (2000).

26. Bray, D. *Cell Movements: From Molecules to Motility* (Garland Pub., 2001).

27. Qiu, T. *et al.* Swimming by reciprocal motion at low Reynolds number. *Nature Communications* **5,** 5119 (2014).

28. Elgeti, J., Winkler, R. G. & Gompper, G. Physics of microswimmers—single particle motion and collective behavior: a review. *Reports on progress in physics* **78,** 056601 (2015).

29. Ghosh, A. & Fischer, P. Controlled propulsion of artificial magnetic nanostructured propellers. *Nano letters* **9,** 2243–2245 (2009).

30. Tierno, P., Golestanian, R., Pagonabarraga, I. & Sagués, F. Controlled swimming in confined fluids of magnetically actuated colloidal rotors. *Physical review letters* **101,** 218304 (2008).

31. Tierno, P., Güell, O., Sagués, F., Golestanian, R. & Pagonabarraga, I. Controlled propulsion in viscous fluids of magnetically actuated colloidal doublets. *Physical Review E* **81,** 011402 (2010).

32. Anderson, J. L. Colloid transport by interfacial forces. *Annual review of fluid mechanics* **21,** 61–99 (1989).

33. Cates, M. & Tailleur, J. When are active Brownian particles and run-and-tumble particles equivalent? Consequences for motility-induced phase separation. *Europhysics Letters* **101,** 20010 (2013).

34. Ismagilov, R. F., Schwartz, A., Bowden, N. & Whitesides, G. M. Autonomous Movement and Self-Assembly. *Angewandte Chemie* **114,** 674–676 (2002).

35. Sanchez, S., Soler, L. & Katuri, J. Chemically Powered Micro-and Nanomotors. *Angewandte Chemie International Edition* **54,** 1414–1444 (2015).

36. Paxton, W. F. *et al.* Catalytic nanomotors: autonomous movement of striped nanorods. *Journal of the American Chemical Society* **126,** 13424–13431 (2004).

37. Golestanian, R., Liverpool, T. B. & Ajdari, A. Propulsion of a molecular machine by asymmetric distribution of reaction products. *Physical review letters* **94,** 220801 (2005).

38. Jiang, H.-R., Yoshinaga, N. & Sano, M. Active motion of a Janus particle by self-thermophoresis in a defocused laser beam. *Physical review letters* **105,** 268302 (2010).

39. Ebbens, S. J. & Howse, J. R. In pursuit of propulsion at the nanoscale. *Soft Matter* **6,** 726–738 (2010).

40. Golestanian, R. Viewpoint: Debut of a hot "fantastic voyager". *Physics* **3,** 108 (2010).

41. Sengupta, S. *et al.* Enzyme molecules as nanomotors. *Journal of the American Chemical Society* **135,** 1406–1414 (2013).

42. Lee, T.-C. *et al.* Self-propelling nanomotors in the presence of strong Brownian forces. *Nano letters* **14,** 2407–2412 (2014).

43. Kapral, R. Perspective: Nanomotors without moving parts that propel themselves in solution. *The Journal of chemical physics* **138,** 020901 (2013).

44. Riedel, C. *et al.* The heat released during catalytic turnover enhances the diffusion of an enzyme. *Nature* **517,** 227–230 (2014).

45. Sengupta, S. *et al.* Enzyme molecules as nanomotors. *Journal of the American Chemical Society* **135,** 1406–1414 (2013).

46. Golestanian, R. Enhanced Diffusion of Enzymes that Catalyze Exothermic Reactions. *Phys. Rev. Lett.* **115,** 108102 (2015).

47. Bai, X. & Wolynes, P. G. On the hydrodynamics of swimming enzymes. *The Journal of chemical physics* **143,** 165101 (2015).

48. Ma, X., Hahn, K. & Sanchez, S. Catalytic mesoporous Janus nanomotors for active cargo delivery. *Journal of the American Chemical Society* **137,** 4976–4979 (2015).

49. Ma, X. *et al.* Enzyme-Powered Hollow Mesoporous Janus Nanomotors. *Nano letters* **15,** 7043–7050 (2015).

50. Dey, K. K. *et al.* Micromotors Powered by Enzyme Catalysis. *Nano letters* **15,** 8311–8315 (2015).

51. Pantarotto, D., Browne, W. R. & Feringa, B. L. Autonomous propulsion of carbon nanotubes powered by a multienzyme ensemble. *Chemical Communications,* 1533–1535 (2008).

52. Muddana, H. S., Sengupta, S., Mallouk, T. E., Sen, A. & Butler, P. J. Substrate catalysis enhances single-enzyme diffusion. *Journal of the American Chemical Society* **132,** 2110–2111 (2010).

53. Mikhailov, A. S. & Kapral, R. Hydrodynamic collective effects of active protein machines in solution and lipid bilayers. *Proceedings of the National Academy of Sciences* **112,** E3639–E3644 (2015).

54. Colberg, P. H., Reigh, S. Y., Robertson, B. & Kapral, R. Chemistry in Motion: Tiny Synthetic Motors. *Accounts of Chemical Research* **47,** 3504–3511 (2014).

55. Illien, P. *et al.* Exothermicity is not a necessary condition for enhanced diffusion of enzymes. *Nano Letters* (2017).

56. Sengupta, S. *et al.* Self-powered enzyme micropumps. *Nature chemistry* **6,** 415–422 (2014).

57. Zhao, X. *et al.* Enhanced Diffusion of Passive Tracers in Active Enzyme Solutions. *Nano Letters* (2017).

58. Pavlick, R. A., Dey, K. K., Sirjoosingh, A., Benesi, A. & Sen, A. A catalytically driven organometallic molecular motor. *Nanoscale* **5,** 1301–1304 (2013).

59. Dey, K. K. *et al.* Chemotactic separation of enzymes. *ACS nano* **8,** 11941–11949 (2014).

60. Franklin, R. E. & Gosling, R. G. Molecular configuration in sodium thymonucleate. *Nature* **171,** 740–741 (1953).

61. Phillips, R., Kondev, J., Theriot, J. & Garcia, H. *Physical Biology of the Cell, Second Edition* (Taylor & Francis Group, 2012).

62. Chargaff, E. Chemical specificity of nucleic acids and mechanism of their enzymatic degradation. *Experientia* **6,** 201 (1950).

63. Watson, J. D., Crick, F. H., *et al.* Molecular structure of nucleic acids. *Nature* **171,** 737–738 (1953).

64. Tinland, B., Pluen, A., Sturm, J. & Weill, G. Persistence length of single-stranded DNA. *Macromolecules* **30,** 5763–5765 (1997).

65. Seeman, N. C. Nucleic acid junctions and lattices. *Journal of theoretical biology* **99,** 237–247 (1982).

66. Chen, J. & Seeman, N. C. Synthesis from DNA of a molecule with the connectivity of a cube. *Nature* **350,** 631–633 (1991).

67. Goodman, R. P. *et al.* Rapid chiral assembly of rigid DNA building blocks for molecular nanofabrication. *Science* **310,** 1661–1665 (2005).

68. Seeman, N. C. Nanotechnology and the double helix. *Scientific American* **17,** 30–39 (2007).

69. Seeman, N. *Structural DNA Nanotechnology* (Cambridge University Press, 2015).

70. Bath, J. & Turberfield, A. J. DNA nanomachines. *Nature nanotechnology* **2,** 275–284 (2007).

71. Rothemund, P. W. Folding DNA to create nanoscale shapes and patterns. *Nature* **440,** 297–302 (2006).

72. Douglas, S. M. *et al.* Self-assembly of DNA into nanoscale three-dimensional shapes. *Nature* **459,** 414–418 (2009).

73. Geary, C., Rothemund, P. W. & Andersen, E. S. A single-stranded architecture for cotranscriptional folding of RNA nanostructures. *Science* **345,** 799–804 (2014).

74. Douglas, S. M. *et al.* Rapid prototyping of 3D DNA-origami shapes with caDNAno. *Nucleic acids research,* gkp436 (2009).

75. Castro, C. E. *et al.* A primer to scaffolded DNA origami. *Nature methods* **8,** 221–229 (2011).

76. Mirkin, C. A., Letsinger, R. L., Mucic, R. C., Storhoff, J. J., *et al.* A DNA-based method for rationally assembling nanoparticles into macroscopic materials. *Nature* **382,** 607–609 (1996).

77. Maune, H. T. *et al.* Self-assembly of carbon nanotubes into two-dimensional geometries using DNA origami templates. *Nature nanotechnology* **5,** 61–66 (2010).

78. Schreiber, R. *et al.* Hierarchical assembly of metal nanoparticles, quantum dots and organic dyes using DNA origami scaffolds. *Nature nanotechnology* **9,** 74–78 (2014).

79. Li, Y., Zheng, Y., Gong, M. & Deng, Z. Pt nanoparticles decorated with a discrete number of DNA molecules for programmable assembly of Au–Pt bimetallic superstructures. *Chemical Communications* **48,** 3727–3729 (2012).

80. Elghanian, R., Storhoff, J. J., Mucic, R. C., Letsinger, R. L. & Mirkin, C. A. Selective colorimetric detection of polynucleotides based on the distance-dependent optical properties of gold nanoparticles. *Science* **277,** 1078–1081 (1997).

81. Jin, R., Wu, G., Li, Z., Mirkin, C. A. & Schatz, G. C. What controls the melting properties of DNA-linked gold nanoparticle assemblies? *Journal of the American Chemical Society* **125,** 1643–1654 (2003).

82. Geerts, N., Geerts, N. & Eiser, E. DNA-functionalized colloids: Physical properties and applications. *Soft Matter* **6,** 4647–4660 (2010).

83. Alivisatos, A. P. *et al.* Organization of'nanocrystal molecules' using DNA. *Nature* **382,** 609–611 (1996).

84. Rogers, W. B., Shih, W. M. & Manoharan, V. N. Using DNA to program the self-assembly of colloidal nanoparticles and microparticles. *Nature Reviews Materials* **1,** 16008 (2016).

85. Nykypanchuk, D., Maye, M. M., van der Lelie, D. & Gang, O. DNA-guided crystallization of colloidal nanoparticles. *Nature* **451,** 549–552 (2008).

86. Wang, Y. *et al.* Colloids with valence and specific directional bonding. *Nature* **491,** 51–55 (2012).

87. Xing, H. *et al.* DNA-directed assembly of asymmetric nanoclusters using Janus nanoparticles. *ACS nano* **6,** 802–809 (2011).

88. Kuzyk, A. *et al.* DNA-based self-assembly of chiral plasmonic nanostructures with tailored optical response. *Nature* **483,** 311–314 (2012).

89. Edwardson, T. G., Lau, K. L., Bousmail, D., Serpell, C. J. & Sleiman, H. F. Transfer of molecular recognition information from DNA nanostructures to gold nanoparticles. *Nature chemistry* **8,** 162–170 (2016).

90. Wilner, O. I. *et al.* Enzyme cascades activated on topologically programmed DNA scaffolds. *Nature nanotechnology* **4,** 249–254 (2009).

91. Fu, J., Liu, M., Liu, Y., Woodbury, N. W. & Yan, H. Interenzyme substrate diffusion for an enzyme cascade organized on spatially addressable DNA nanostructures. *Journal of the American Chemical Society* **134,** 5516–5519 (2012).

92. Biancaniello, P. L., Kim, A. J. & Crocker, J. C. Colloidal interactions and self-assembly using DNA hybridization. *Physical review letters* **94,** 058302 (2005).

93. Park, S. Y. *et al.* DNA-programmable nanoparticle crystallization. *Nature* **451,** 553–556 (2008).

94. Rosi, N. L. & Mirkin, C. A. Nanostructures in biodiagnostics. *Chemical reviews* **105,** 1547–1562 (2005).

95. Macfarlane, R. J. *et al.* Nanoparticle Superlattice Engineering with DNA. *Science* **334,** 204–208 (2011).

96. Monod, J. *Le hasard et la nécessité. Essai sur la philosophie naturelle de la biologie moderne* (Seuil, 2014).

97. Adleman, L. M. Molecular computation of solutions to combinatorial problems. *Science* **266,** 1021–1024 (1994).

98. Yurke, B., Turberfield, A. J., Mills, A. P., Simmel, F. C. & Neumann, J. L. A DNA-fuelled molecular machine made of DNA. *Nature* **406,** 605–608 (2000).

99. Zhang, D. Y. & Seelig, G. Dynamic DNA nanotechnology using strand-displacement reactions. *Nature chemistry* **3,** 103–113 (2011).

100. Seelig, G., Soloveichik, D., Zhang, D. Y. & Winfree, E. Enzyme-free nucleic acid logic circuits. *science* **314,** 1585 (2006).

101. Huizenga, D. E. & Szostak, J. W. A DNA aptamer that binds adenosine and ATP. *Biochemistry* **34,** 656–665 (1995).

102. Liu, J. & Lu, Y. Fast colorimetric sensing of adenosine and cocaine based on a general sensor design involving aptamers and nanoparticles. *Angewandte Chemie* **118,** 96–100 (2006).

103. Douglas, S. M., Bachelet, I. & Church, G. M. A logic-gated nanorobot for targeted transport of molecular payloads. *Science* **335,** 831–834 (2012).

104. Wickham, S. F. *et al.* Direct observation of stepwise movement of a synthetic molecular transporter. *Nature nanotechnology* **6,** 166–169 (2011).

105. Howard, J. *et al. Mechanics of motor proteins and the cytoskeleton* (Sinauer Associates Sunderland, MA, 2001).

106. Fujii, T. & Rondelez, Y. Predator–Prey Molecular Ecosystems. *ACS Nano* **7,** 27–34 (2012).

107. Marchetti, M. C. *et al.* Hydrodynamics of soft active matter. *Reviews of Modern Physics* **85,** 1143–1189 (3 2013).

108. Kapral, R. Nanomotors Propelled by Chemical Reactions. *Engineering of Chemical Complexity* **11,** 101 (2012).

109. Poon, W. From Clarkia to Escherichia and Janus: The physics of natural and synthetic active colloids. *Proceedings of the International School of Physics 'Enrico Fermi', Course CLXXXIV "Physics of Complex Colloids",* 317–386 (2013).

110. Derjaguin, B., Sidorenkov, G., Zubashchenkov, E. & Kiseleva, E. Kinetic phenomena in boundary films of liquids. *Kolloidnyi zhurnal* **9,** 335–347 (1947).

111. Churaev, N. V., Derjaguin, B. V. & Muller, V. M. *Surface forces* (Springer Science & Business Media, 2013).

112. Happel, J. & Brenner, H. *Low Reynolds number hydrodynamics: with special applications to particulate media* (Springer Science & Business Media, 2012).

113. Ebbens, S., Tu, M.-H., Howse, J. R. & Golestanian, R. Size dependence of the propulsion velocity for catalytic Janus-sphere swimmers. *Physical Review E* **85,** 020401 (2012).

114. Collins, F. C. & Kimball, G. E. Diffusion-controlled reaction rates. *Journal of colloid science* **4,** 425–437 (1949).

115. Ruckner, G. & Kapral, R. Chemically Powered Nanodimers. *Physical Review Letters* **98,** 150603 (2007).

116. Berg, H. *Random Walks in Biology* (Princeton University Press, 1993).

117. Palacci, J., Cottin-Bizonne, C., Ybert, C. & Bocquet, L. Sedimentation and effective temperature of active colloidal suspensions. *Physical Review Letters* **105,** 088304 (2010).

118. Padding, J. & Louis, A. Hydrodynamic interactions and Brownian forces in colloidal suspensions: Coarse-graining over time and length scales. *Physical Review E* **74,** 031402 (2006).

119. Malevanets, A. & Kapral, R. Mesoscopic model for solvent dynamics. *The Journal of chemical physics* **110,** 8605–8613 (1999).

120. De Buyl, P. & Kapral, R. Phoretic self-propulsion: a mesoscopic description of reaction dynamics that powers motion. *Nanoscale* **5,** 1337–1344 (2013).

121. De Buyl, P., Mikhailov, A. S. & Kapral, R. Self-propulsion through symmetry breaking. *Europhysics Letters* **103,** 60009 (2013).

122. Colberg, P. H. & Kapral, R. Ångström-scale chemically powered motors. *Europhysics Letters* **106,** 30004 (2014).

123. Rahman, A. Correlations in the motion of atoms in liquid argon. *Physical Review* **136,** A405 (1964).

124. Astumian, R. D. Enhanced Diffusion, Chemotaxis, and Pumping by Active Enzymes: Progress toward an Organizing Principle of Molecular Machines. *ACS nano* **8,** 11917–11924 (2014).

125. Berne, B. J. & Pecora, R. *Dynamic light scattering: with applications to chemistry, biology, and physics* (Courier Corporation, 1976).

126. Goodman, J. W. Some fundamental properties of speckle∗. *Journal Optical Society of Amera* **66,** 1145–1150 (1976).

127. Shetty, A. M., Wilkins, G. M., Nanda, J. & Solomon, M. J. Multiangle depolarized dynamic light scattering of short functionalized single-walled carbon nanotubes. *The Journal of Physical Chemistry C* **113,** 7129–7133 (2009).

128. Provencher, S. W. CONTIN: a general purpose constrained regularization program for inverting noisy linear algebraic and integral equations. *Computer Physics Communications* **27,** 229–242 (1982).

129. Digman, M. A. & Gratton, E. Lessons in fluctuation correlation spectroscopy. *Annual review of physical chemistry* **62,** 645–668 (2011).

130. Bacia, K., Haustein, E. & Schwille, P. Fluorescence correlation spectroscopy: principles and applications. *Cold Spring Harbor Protocols* **2014,** 709–725 (2014).

131. Rigler, R., Mets, Ü., Widengren, J. & Kask, P. Fluorescence correlation spectroscopy with high count rate and low background: analysis of translational diffusion. *European Biophysics Journal* **22,** 169–175 (1993).

132. Sauer, M., Hofkens, J. & Enderlein, J. *Handbook of Fluorescence Spectroscopy and Imaging: From Ensemble to Single Molecules* (Wiley, 2010).

133. Schätzel, K. Correlation techniques in dynamic light scattering. *Applied Physics B* **42,** 193–213 (1987).

134. Gendron, P.-O., Avaltroni, F. & Wilkinson, K. Diffusion coefficients of several rhodamine derivatives as determined by pulsed field gradient–nuclear magnetic resonance and fluorescence correlation spectroscopy. *Journal of fluorescence* **18,** 1093–1101 (2008).

135. Perrin, J. Mouvement brownien et molécules. *J. Phys. Theor. Appl.* **9,** 5–39 (1910).

136. Wilson, D. A., Nolte, R. J. & Van Hest, J. C. Autonomous movement of platinum-loaded stomatocytes. *Nature chemistry* **4,** 268–274 (2012).

137. Hole, P. *et al.* Interlaboratory comparison of size measurements on nanoparticles using nanoparticle tracking analysis (NTA). *Journal of Nanoparticle Research* **15,** 1–12 (2013).

138. Krueger, A. B., Carnell, P. & Carpenter, J. F. Characterization of Factors Affecting Nanoparticle Tracking Analysis Results With Synthetic and Protein Nanoparticles. *Journal of pharmaceutical sciences* **105,** 1434–1443 (2016).

139. Cheng, W. & Compton, R. G. Electrochemical detection of nanoparticles by 'nano-impact' methods. *TrAC Trends in Analytical Chemistry* **58,** 79–89 (June 2014).

140. Sokolov, S. V., Eloul, S., Kätelhön, E., Batchelor-McAuley, C. & Compton, R. G. Electrode–particle impacts: a users guide. *Physical Chemistry Chemical Physics* **19,** 28–43 (2017).

141. Xiao, X. & Bard, A. J. Observing Single Nanoparticle Collisions at an Ultramicroelectrode by Electrocatalytic Amplification. *J. Am. Chem. Soc.* **129,** 9610–9612 (Aug. 2007).

142. Zhou, Y.-G., Rees, N. V. & Compton, R. G. The electrochemical detection and characterization of silver nanoparticles in aqueous solution. *Angewandte Chemie International Edition* **50,** 4219–4221 (2011).

143. Kim, B.-K., Boika, A., Kim, J., Dick, J. E. & Bard, A. J. Characterizing Emulsions by Observation of Single Droplet Collisions—Attoliter Electrochemical Reactors. *J. Am. Chem. Soc.* **136,** 4849–4852 (Mar. 2014).

144. Cheng, W. & Compton, R. G. Investigation of Single-Drug-Encapsulating Liposomes using the Nano-Impact Method. *Angewandte Chemie International Edition* **53,** 13928–13930 (Dec. 2014).

145. Dick, J. E., Renault, C. & Bard, A. J. Observation of single-protein and DNA macromolecule collisions on ultramicroelectrodes. *Journal of the American Chemical Society* **137,** 8376–8379 (2015).

146. Dick, J. E., Hilterbrand, A. T., Strawsine, L. M., Upton, J. W. & Bard, A. J. Enzymatically enhanced collisions on ultramicroelectrodes for specific and rapid detection of individual viruses. *PNAS* **113,** 6403–6408 (June 2016).

147. Moo, J. G. S. & Pumera, M. Self-Propelled Micromotors Monitored by Particle-Electrode Impact Voltammetry. *ACS Sensors* (2016).

148. Ross, J., Muller, S. C. & Vidal, C. Chemical Waves. *Science* **240,** 460–465 (1988).

149. Luther, R. Räumliche Ausbreitung chemischer Reaktionen. *Zeitschrift für Elektrochemie* **12,** 596–600 (1906).

150. Turing, A. M. The chemical basis of morphogenesis. *Philosophical Transactions of the Royal Society of London B: Biological Sciences* **237,** 37–72 (1952).

151. Tsien, R. W. & Tsien, R. Y. Calcium channels, stores, and oscillations. *Annual review of cell biology* **6,** 715–760 (1990).

152. Martiel, J.-L. & Goldbeter, A. A model based on receptor desensitization for cyclic AMP signaling in Dictyostelium cells. *Biophysical journal* **52,** 807–828 (1987).

153. Ishihara, K. *et al.* Organization of early frog embryos by chemical waves emanating from centrosomes. *Philosophical Transactions of the Royal Society B* **369,** 20130454–20130454 (2014).

154. Kauffman, S. *At home in the universe: The search for the laws of self-organization and complexity* (Oxford university press, 1996).

155. Murray, J. D. *Mathematical Biology I: An Introduction* (Springer, New York, NY, USA, 2002).

156. Zaikin, A. & Zhabotinsky, A. Concentration wave propagation in two-dimensional liquid-phase self-oscillating system. *Nature* **225,** 535–537 (1970).

157. Epstein, I. R. Predicting complex biology with simple chemistry. *Proceedings of the National Academy of Sciences* **103,** 15727–15728 (2006).

158. Zadorin, A. S., Rondelez, Y., Galas, J.-C. & Estevez-Torres, A. Synthesis of Programmable Reaction-Diffusion Fronts Using DNA Catalyzers. *Physical Review Letters* **114,** 068301 (2015).

159. Padirac, A., Fujii, T., Estévez-Torres, A. & Rondelez, Y. Spatial waves in synthetic biochemical networks. *Journal of the American Chemical Society* **135,** 14586–14592 (2013).

160. Plasson, R., Brandenburg, A., Jullien, L. & Bersini, H. Autocatalysis: At the root of self-replication. *Artificial life* **17,** 219–236 (2011).

161. Scott, S. K. & Showalter, K. Simple and complex propagating reaction-diffusion fronts. *The Journal of Physical Chemistry* **96,** 8702–8711 (1992).

162. Kolmogorov, A., Petrovsky, L. & Piskunov, N. An investigation of the diffusion equation combined with an increase in mass and its application to a biological problem. *Bulletin of Moscow University Ser Int A* **1,** 1–26 (1937).

163. Aronson, D. G. & Weinberger, H. F. in *Partial differential equations and related topics* 5–49 (Springer, 1975).

164. Fisher, R. A. The wave of advance of advantageous genes. *Annals of Human Genetics* **7,** 355–369 (1937).

165. Showalter, K. & Tyson, J. J. Luther's 1906 discovery and analysis of chemical waves. *Journal of Chemical Education* **64,** 742–744 (1987).

166. Venegas-Ortiz, J., Allen, R. J. & Evans, M. R. Speed of invasion of an expanding population by a horizontally transmitted trait. *Genetics* **196,** 497–507 (2014).

167. Van Saarloos, W. Front propagation into unstable states. *Physics reports* **386,** 29–222 (2003).

168. Virgo, N., Ikegami, T. & McGregor, S. Complex Autocatalysis in Simple Chemistries. *Artificial life* (2016).

169. Montagne, K., Plasson, R., Sakai, Y., Fujii, T. & Rondelez, Y. Programming an in vitro DNA oscillator using a molecular networking strategy. *Molecular systems biology* **7** (2011).

170. Zadorin, A. S., Rondelez, Y., Galas, J.-C. & Estevez-Torres, A. Programmable reaction-diffusion fronts. *arXiv preprint arXiv:1407.4152* (2014).

171. Taylor, G. Dispersion of Soluble Matter in Solvent Flowing Slowly through a Tube. *Proceedings of the Royal Society of London. Series A, Mathematical and Physical Sciences,* 186–203 (1953).

172. Selvin, P. R. & Ha, T. *Single-molecule Techniques* (CSHL Press, 2008).

173. Rulands, S., Klünder, B. & Frey, E. Stability of localized wave fronts in bistable systems. *Physical review letters* **110,** 038102 (2013).

174. Fleck, N., McMeeking, R. M. & Kraus, T. Convective assembly of a particle monolayer. *Langmuir* **31,** 13655–13663 (2015).

175. Jiang, P. & McFarland, M. J. Large-scale fabrication of wafer-size colloidal crystals, macroporous polymers and nanocomposites by spin-coating. *Journal of the American Chemical Society* **126,** 13778–13786 (2004).

176. Sabapathy, M., Christdoss Pushpam, S. D., Basavaraj, M. G. & Mani, E. Synthesis of Single and Multipatch Particles by Dip-Coating Method and Self-Assembly Thereof. *Langmuir* **31,** 1255–1261 (2015).

177. Micheletto, R., Fukuda, H. & Ohtsu, M. A simple method for the production of a two-dimensional, ordered array of small latex particles. *Langmuir* **11,** 3333–3336 (1995).

178. Campbell, A. I. & Ebbens, S. J. Gravitaxis in spherical Janus swimming devices. *Langmuir* **29,** 14066–14073 (2013).

179. Israelachvili, J. N. *Intermolecular and surface forces: revised third edition* (Academic press, 2011).

180. Buttinoni, I. *et al.* Dynamical clustering and phase separation in suspensions of self-propelled colloidal particles. *Physical review letters* **110,** 238301 (2013).

181. Ebbens, S. *et al.* Self-assembled autonomous runners and tumblers. *Physical Review E* **82,** 015304 (2010).

182. Alarcón-Correa, M., Walker, D., Qiu, T. & Fischer, P. Nanomotors. *The European Physical Journal Special Topics* **225,** 2241–2254 (2016).

183. Bradley, M. J., Read, C. G. & Schaak, R. E. Pt–Au nanoparticle heterodimers as seeds for Pt–Au–metal sulfide heterotrimers: thermal stability and chemoselective growth characteristics. *The Journal of Physical Chemistry C* **119,** 8952–8959 (2015).

184. He, J. *et al.* A general approach to synthesize asymmetric hybrid nanoparticles by interfacial reactions. *Journal of the American Chemical Society* **134,** 3639–3642 (2012).

185. Yu, T., Zeng, J., Lim, B. & Xia, Y. Aqueous-Phase Synthesis of Pt/CeO2 Hybrid Nanostructures and Their Catalytic Properties. *Advanced Materials* **22,** 5188–5192 (2010).

186. Guo, S., Li, J., Dong, S. & Wang, E. Three-dimensional Pt-on-Au bimetallic dendritic nanoparticle: one-step, high-yield synthesis and its bifunctional plasmonic and catalytic properties. *The Journal of Physical Chemistry C* **114,** 15337–15342 (2010).

187. Phibbs, M. & Giguère, P. A. Hydrogen peroxide and its analogues. I. Density, refractive index, viscosity, and surface tension of deuterium peroxide-deuterium oxide solutions. *Canadian journal of chemistry* **29,** 173–181 (1951).

188. Michele, L. D. & Eiser, E. Developments in understanding and controlling self assembly of DNA-functionalized colloids. *Physical Chemistry Chemical Physics* **15,** 3115–3129 (9 2013).

189. Leunissen, M. E. *et al.* Switchable self-protected attractions in DNA-functionalized colloids. *Nature materials* **8,** 590–595 (2009).

190. Holmberg, A. *et al.* The biotin-streptavidin interaction can be reversibly broken using water at elevated temperatures. *Electrophoresis* **26,** 501–510 (2005).

191. Feng, L., Dreyfus, R., Sha, R., Seeman, N. C. & Chaikin, P. M. DNA patchy particles. *Advanced Materials* **25,** 2779–2783 (2013).

192. Kanaras, A. G., Wang, Z., Bates, A. D., Cosstick, R. & Brust, M. Towards Multistep Nanostructure Synthesis: Programmed Enzymatic Self-Assembly of DNA/Gold Systems. *Angewandte Chemie International Edition* **42,** 191–194 (2003).

193. Rogers, P. H. *et al.* Selective, Controllable, and Reversible Aggregation of Polystyrene Latex Microspheres via DNA Hybridization. *Langmuir* **21,** 5562–5569 (2005).

194. Tison, C. K. & Milam, V. T. Programming the kinetics and extent of colloidal disassembly using a DNA trigger. *Soft Matter* **6,** 4446–4453 (2010).

195. Hurst, S. J., Lytton-Jean, A. K. & Mirkin, C. A. Maximizing DNA loading on a range of gold nanoparticle sizes. *Anal. Chem* **78,** 8313–8318 (2006).

196. Yi, G.-R., Pine, D. J. & Sacanna, S. Recent progress on patchy colloids and their self-assembly. *Journal of Physics: Condensed Matter* **25,** 193101 (2013).

197. Solomon, C. & Breckon, T. *Fundamentals of Digital Image Processing: A Practical Approach with Examples in Matlab* (Wiley, 2011).

198. Maier, S. A. *et al.* Local detection of electromagnetic energy transport below the diffraction limit in metal nanoparticle plasmon waveguides. *Nature materials* **2,** 229 (2003).

199. Pendry, J. B. Negative refraction makes a perfect lens. *Physical review letters* **85,** 3966 (2000).

200. Auyeung, E. *et al.* Controlling Structure and Porosity in Catalytic Nanoparticle Superlattices with DNA. *Journal of the American Chemical Society* **137,** 1658–1662 (2015).

201. Ke, Y. *et al.* Multilayer DNA origami packed on a square lattice. *Journal of the American Chemical Society* **131,** 15903–15908 (2009).

202. Schreiber, R. *et al.* DNA origami-templated growth of arbitrarily shaped metal nanoparticles. *Small* **7,** 1795–1799 (2011).

203. Lis, J. T. & Schleif, R. Size fractionation of double-stranded DNA by precipitation with polyethylene glycol. *Nucleic acids research* **2,** 383–390 (1975).

204. Stahl, E., Martin, T. G., Praetorius, F. & Dietz, H. Facile and scalable preparation of pure and dense DNA origami solutions. *Angewandte Chemie International Edition* **53,** 12735–12740 (2014).

205. Compton, R. G. & Banks, C. E. *Understanding voltammetry* (World Scientific, 2007).

206. Zhu, Y.-J. & Chen, F. Microwave-assisted preparation of inorganic nanostructures in liquid phase. *Chemical Reviews* **114,** 6462–6555 (2014).

207. Bard, A. J., Faulkner, L. R., Leddy, J. & Zoski, C. G. *Electrochemical methods: fundamentals and applications* (Wiley New York, 1980).

208. Goodsell, D. Catalase. *Molecule of the Month. RCSB Protein Data Bank. doi* **10,** 2210 (2004).

209. Hermanson, G. *Bioconjugate Techniques* (Elsevier Science, 2013).

210. Ellman, G. L. Tissue sulfhydryl groups. *Archives of biochemistry and biophysics* **82,** 70–77 (1959).

211. Nuzzo, R. G. & Allara, D. L. Adsorption of bifunctional organic disulfides on gold surfaces. *Journal of the American Chemical Society* **105,** 4481–4483 (1983).

212. Ulman, A. *An Introduction to Ultrathin Organic Films: From Langmuir–Blodgett to Self–Assembly* (Academic press, 2013).

213. Zhao, G., Sanchez, S., Schmidt, O. G. & Pumera, M. Poisoning of bubble propelled catalytic micromotors: the chemical environment matters. *Nanoscale* **5,** 2909–2914 (2013).

214. Wilson, D. S. & Szostak, J. W. In vitro selection of functional nucleic acids. *Annual review of biochemistry* **68,** 611–647 (1999).

215. Fan, X. *et al.* A simple adenosine fluorescent aptasensor based on the quenching ability of guanine. *New Journal of Chemistry* **36,** 2260–2265 (2012).

216. Ebbens, S. J., Buxton, G. A., Alexeev, A., Sadeghi, A. & Howse, J. R. Synthetic running and tumbling: an autonomous navigation strategy for catalytic nanoswimmers. *Soft Matter* **8,** 3077–3082 (2012).

217. Ghosh, P. K., Li, Y., Marchesoni, F. & Nori, F. Pseudochemotactic drifts of artificial microswimmers. *Physical Review E* **92,** 012114 (2015).

218. Ang, J. & McMillen, D. R. Physical constraints on biological integral control design for homeostasis and sensory adaptation. *Biophysical journal* **104,** 505–515 (2013).

219. Spiro, P. A., Parkinson, J. S. & Othmer, H. G. A model of excitation and adaptation in bacterial chemotaxis. *Proceedings of the National Academy of Sciences* **94,** 7263–7268 (1997).

220. Alon, U., Surette, M. G., Barkai, N. & Leibler, S. Robustness in bacterial chemotaxis. *Nature* **397,** 168–171 (1999).

221. Wilkie, J., Johnson, M. & Katebi, R. *Control Engineering: An Introductory Course* (Palgrave, 2002).

222. Ni, X. Y., Drengstig, T. & Ruoff, P. The control of the controller: molecular mechanisms for robust perfect adaptation and temperature compensation. *Biophysical Journal* **97,** 1244–1253 (2009).

223. Yi, T.-M., Huang, Y., Simon, M. I. & Doyle, J. Robust perfect adaptation in bacterial chemotaxis through integral feedback control. *Proceedings of the National Academy of Sciences of the United States of America* **97,** 4649–4653 (2000).

224. Csikász-Nagy, A. & Soyer, O. S. Adaptive dynamics with a single two-state protein. *Journal of The Royal Society Interface* **5,** S41–S47 (2008).

225. Van Roekel, H. W. *et al.* Automated design of programmable enzyme-driven DNA circuits. *ACS synthetic biology* **4,** 735–745 (2014).

226. Volpe, G. & Volpe, G. Simulation of a Brownian particle in an optical trap. *American Journal of Physics* **81,** 224–230 (2013).

227. Mullen, R. *Simulation of light scattering from Brownian particles* (California Polytechnic State University, 2015).